Numerical Analysis and Modelling of Liquid Turbulence in Bubble Columns at Various Scales by Computational Fluid Dynamics

Zur Erlangung des akademischen Grades

Doktor der Ingenieurwissenschaften (Dr.-Ing.)

von der KIT-Fakultät für Maschinenbau des
Karlsruher Instituts für Technologie (KIT)

genehmigte

Dissertation

von

M. Sc. Sercan Erdoğan

Acknowledgements

Abstract

This dissertation focuses on the development of improved statistical models for bubble-induced turbulence (BIT) (also called pseudo-turbulence). For this purpose, an integrated methodology is applied involving different computational methods such as Direct Numerical Simulations (DNS) and Euler-Euler (E-E) approach (two-fluid model). The investigations are conducted for various scales such as single bubbles, bubble swarms, lab-scale and pilot-scale bubble columns. The simulation results are verified with experiments and correlations. The applicability of models is demonstrated for engineering computations of an industrial bubble column using Computational Fluid Dynamics (CFD) codes that rely on E-E approach.

For the model development, extensive direct numerical simulations for bubble swarms within a sub-region of a flat bubble column are performed with an in-house code TURBIT-VOF. The transport equation for the liquid phase turbulence kinetic energy, k_L, which is the cornerstone in many statistical turbulence models, is analyzed by using the DNS data. It is deduced that the main source term for the turbulence kinetic energy (TKE) is due to interfacial effects, while the production due to shear stresses is negligible for the conditions examined here. The production and dissipation terms are not in local equilibrium. Instead, the excess of k_L production from areas with high local gas content is redistributed by diffusion into areas with low gas content. This shows that for a reliable calculation of flows in bubble columns with the E-E approach, an adequate modeling of the interfacial term in the k_L equation is of great importance. Model approaches from literature for closure of this term are analyzed by comparison with the DNS data and two suitable models for the interfacial term are selected.

An industrial bubble column is computed using an OpenFOAM® solver based on the k-ε two-fluid approach. The influence of models for the interfacial term is examined. It is found that the turbulence model has a very slight influence on the local gas holdup and the velocity profiles of phases at normal pressure while the influence is noticeable at 18.5 bar. In general, at high pressures, the local gas holdup is significantly overestimated by the simulation for a water system measured by project partners. For an organic system, numerical and experimental results are very close. Using the turbulence model that is identified and implemented during this study, the overall gas holdup data for the water system from the experiments is estimated with a deviation of 9 – 13 %. Based on correlations from literature, one approach is identified that is able to predict the CFD data for the overall gas holdup closely in organic system at 18.5 and 36 bar and in water system at 18.5 bar. The TKE profiles are analyzed for different liquid properties, pressure, gas superficial velocities and temperature. A linear relation of TKE with local gas holdup and mean gas velocity is identified for the examined cases.

This work contributes to turbulence modelling in bubbly flows and the advancement of CFD as a tool for design of industrial scale bubble columns. The implemented systematic procedure is essential for the development of statistical models to engage numerical simulations in practical applications.

Kurzfassung

Diese Doktorarbeit beschäftigt sich mit der Entwicklung verbesserter statistischer Modelle für die Blasen-induzierte Turbulenz (Pseudo-Turbulenz). Es wird eine Skalen-übergreifende Herangehensweise gewählt, die sowohl Direkte Numerische Simulationen (DNS) als auch Euler-Euler (E-E) Simulationen umfasst. Die dabei betrachteten Skalen umfassen Einzelblasen und Blasenschwärme sowie Blasensäulen im Labor- und Pilotmaßstab. Die Simulationsergebnisse werden jeweils anhand von Experimenten und Korrelationen verifiziert. Die Anwendbarkeit von Modellen für die ingenieurtechnische Berechnung von einem industriellen Blasensäulenreaktor auf Basis von numerischen Strömungssimulationen mit dem E-E Ansatz (Zwei-Fluid-Modell) wird nachgewiesen.

Zur Modellentwicklung werden umfangreiche DNS Berechnungen für Blasen-schwärme durchgeführt. Hierfür wird das am KIT entwickelte Rechenprogramm TURBIT-VOF verwendet und ein Teilgebiet einer flachen Blasensäule betrachtet. Mittels der DNS-Daten wird die Transportgleichung der turbulenten kinetischen Energie (TKE) der Flüssigphase (k_L) analysiert, die den Grundstein der ingenieurtechnischen Turbulenz-modellierung darstellt. Es zeigt sich, dass der dominierende Quellterm auf Grenzflächen-effekte zurückzuführen ist, während die Produktion aufgrund von Scherspannungen für die betrachteten Bedingungen gering ist. Produktions- und Dissipationsterm sind nicht im lokalen Gleichgewicht. Der Überschuss der Produktion von k_L in Bereichen mit hohem lokalem Gasgehalt wird durch Diffusion in Bereiche mit geringem Gasgehalt umverteilt. Für die zuverlässige Berechnung von Strömungen in Blasensäulen mit dem E-E Ansatz ist eine adäquate Modellierung des Grenzflächenterms in der k_L-Gleichung daher von großer Bedeutung. Ansätze aus der Literatur zur Schließung dieses Terms werden durch Vergleich mit den DNS-Daten analysiert und zwei tragfähige Modelle ausgewählt.

Mit dem k-ε Zwei-Fluid-Modell in OpenFOAM® wird eine industrielle Blasensäule berechnet und der Einfluss des Grenzflächenterms in der k_L-Gleichung untersucht. Das Turbulenzmodell hat bei Normaldruck nur einen sehr geringen, bei 18,5 bar Druck aber einen merklichen Einfluss auf den Gasgehalt und die Gas- und Flüssigkeitsgeschwindigkeit. Bei hohem Druck wird der gemessene Gasgehalt für ein Wassersystem in der Simulation deutlich überschätzt. Für ein organisches System liegen die numerischen und experimentellen Ergebnisse sehr nahe beieinander. Unter Verwendung des innerhalb dieser Arbeit implementierten Turbulenzmodells wird für das Wassersystem der Gasgehalt in Experimenten mit einer Abweichung von 9 – 13% berechnet. TKE-Profile werden für unterschiedliche Bedingungen analysiert und es wird eine lineare Beziehung zwischen TKE und lokalem Gasgehalt und mittlerer Gasgeschwindigkeit identifiziert.

Die in dieser Arbeit verwendete skalenübergreifende Herangehensweise trägt zur verbesserten Turbulenzmodellierung in Blasenströmungen und damit zur Etablierung der numerischen Strömungssimulation für die Auslegung von industriellen Blasensäulen bei.

Table of Contents

1. Introduction

This Chapter introduces the motivation for studying the modelling of liquid phase turbulence in bubbly flows and the background information for numerical methods to perform this research.

1.1. Motivation

Bubble columns are widely used as multiphase reactors in chemical, biochemical and petrochemical industries [1, 2]. In bubble columns as multiphase reactors, the gas phase is dispersed into a continuous phase [3] and moves in one of the two characteristic regimes depending upon the nature of dispersion [4]. The flow regime can be homogeneous or heterogeneous (with a wide bubble size distribution). The ascending gas-phase creates an unsteady buoyancy-driven flow and induces large recirculation loops in the liquid phase (with up-flow in the center and down-flow near the wall). Experience, empirical correlations, one-dimensional convection-dispersion models and compartment models form usually the basis for the design of industrial scale bubble columns. Such approaches remain somewhat limited when increase of the reactor performance is sought. Multidimensional Computational Fluid Dynamics (CFD) methods are potentially attractive for this purpose, however, their use is nowadays often limited to lab scale bubble columns and aqueous liquids and not yet used as tool for design of industrial scale bubble columns [5, 6].

During the years bubbly flows were analyzed experimentally [7-9] as well as numerically [10-12]. Several papers in literature investigated the suitability and limitations of different modeling concepts for bubble columns by comparing computed mean profiles for gas-holdup, gas and liquid velocity, and turbulence kinetic energy (TKE) with experimental data from dedicated lab-scale bubble column experiments. It was observed that modification of carrier flow by bubbles depends on the flow conditions (e.g. flow Reynolds number) and on the characteristics of the bubbles (e.g. bubble size and total gas hold-up) [13]. Though the conclusions are not definite, several authors report that predictions of the mean flow (mean velocities, mean gas-hold-up) and the turbulence kinetic energy obtained by using the $k-\varepsilon$ models are comparable to those obtained by using Reynolds stress model (RSM) or Large eddy simulation (LES) (at least away from the sparger where the performance of LES is clearly superior) [14-17]. However, all model approaches have deficiencies concerning turbulence quantities, which often do not compare well with experiments. This deficit is of special importance for population balance approaches where turbulence data

enter in breakup and coalescence kernels [5, 6]. Therefore, improved closure relations for k and ε which are necessary for bubble-driven flows are one of the focus in this study.

In bubble columns, the rising bubbles create an unsteady buoyancy-driven flow and induce large recirculation loops in the liquid phase. This generates shear-induced turbulence (especially near the walls) and bubble-induced turbulence (BIT or pseudo-turbulence) [6]. Some researchers showed the significance of BIT by measuring turbulence intensities in a flow before and after the addition of bubbles [7, 18]. In various industrial processes involving slow dispersed two-phase flows no shear turbulence occurs [19] and the main flow features such as phase distribution and mixing are controlled only by the bubble-induced turbulence. Neither pure pseudo-turbulence is fully understood nor its inherent non-linear interaction with shear-induced turbulence. For reliable mathematical modeling of pseudo-turbulence in bubbly flows, it is essential to understand the underlying physics [5, 6].

Among several engineering approaches commonly used to predict the bubble-induced turbulence, far the most popular concept is based on the balance equation for turbulence kinetic energy of the liquid phase (k_L equation) [20]. Turbulence modelling in bubbly flows can also be identified based on the basic equations of turbulence in gas-liquid flow. Kataoka and Serizawa [21] derived the exact equations for k, the turbulence kinetic energy (TKE), and ε, the dissipation rate of TKE, for a gas-liquid flow consisting of two incompressible phases. The formulation they derived employs a single-phase flow representation but includes the influence of the bubbles by means of additional interfacial source terms in the balance equations [13]. In the exact k_L equation, the terms representing the shear production, diffusion, dissipation and interfacial momentum transfer must be modeled to close the system of equations. Experimentally, it is difficult to obtain data about the terms in the k_L equation especially under non-dilute conditions. However, direct numerical simulations (DNS) on sufficiently fine grids can provide such data [5]. The turbulence in the dispersed gas phase is commonly neglected due to the low density of the gas and the small dimensions of bubbles [13].

Several authors used the formulation of Kataoka and Serizawa [21] for modelling the BIT of bubbly flow and proposed models with source terms to represent BIT [22-25]. Ilic [26] performed DNS studies of laminar bubbly flow in a narrow vertical channel in rather viscous liquids (Morton number $M > 3 \times 10^{-6}$) and evaluated all terms in the k_L equation for a single bubble [19] and a swarm consisting of up to eight bubbles [27]. For all closure terms, they compared the DNS profiles with model predictions. Ilić found

that for the production by shear stresses all models yield a strong overestimation, while for the turbulent diffusion all models used in engineering codes result in an underestimation. For the interfacial term, Ilic [26] analyzed a number of models and identified a promising one [5]. However, all the other closure terms in the kinetic energy equation need further improvement for bubbly flows [26].

In the recent studies, since 2016, Santarelli and Fröhlich [28] and Santarelli et al. [29] analyzed the turbulence kinetic energy budget for bubble swarms in a turbulent channel flow configuration with realistic density difference and used the DNS data from vertical turbulent channel flow laden with finite-size bubbles. Ma et al. [30], [31] and Ma [13] extended those works by using the DNS data of two-fluid system to model the interfacial terms of BIT and help modelling for E-E and LES simulations. They presented a BIT model that is valid for small bubbles in contaminated fluid and a closure for the BIT terms in an E-E RANS model based on DNS data.

An industrial scale validation has not been achieved so far. An up-to-date detailed review for the simulation of bubble columns by Mühlbauer et al. [32] in 2019 concludes that there is still a need for research in the field of multi-phase turbulence and for bubbly flow applications with high gas holdup. They emphasize that one deficit in the literature is to bring the use of numerical simulation closer to practical applications and for this purpose, a solution procedure involving a systematic validation of the models is essential. This should be supported with DNS on the small scale to resolve the transfer from single to bubble swarm models in detail and to determine closures for large-scale models [32].

The current research has been performed under a joint project of the Federal Ministry of Education and Research in Germany (BMBF: Bundesministerium für Bildung und Forschung). The BMBF project "Multi-Phase" seeks to optimize multiphase reactors utilizing scale-independent models, measurement techniques and apparatuses. The project members link their competences in academic fundamental research, small and medium-sized companies with expertise on measurement technologies and design and operation of industrial processes. Evonik Industries AG transfers the laboratory data and models to industrial scale and provides the results to the project partners. Significant energy efficiency as well as reduced CO_2 emissions are expected [33]. One main goal of the project is the development of reliable multi-scale models that allow the numerical investigation and optimization of industrial scale multiphase reactors.

In this context, this study aims on the development and validation of improved statistical models for bubble-induced turbulence. The applied strategy is to use the

DNS data as basis for improving and testing the models for the main source term of BIT and to employ the improved models for the E-E approach.

1.2. Direct numerical simulations (DNS)

Direct numerical simulations (DNS) of bubbly flow provides the full information on instantaneous three-dimensional flow field and phase interface topology based on computational grids fine enough to resolve all flow scales and auxiliary algorithms to track the gas–liquid interface. In spite of serious limitations concerning the magnitude of Reynolds number of the liquid flow and number of bubbles that can be tracked, DNS is a promising way to get a detailed insight into mechanisms governing the turbulence in bubbly flows [19]. Steady-state and transient simulations of single bubbles enable an isolated investigation of effects such as bubble rise, shape and oscillation [32].

In early studies, authors [34-39] investigated the DNS of bubbles in fully periodic computational domains. As the bubbles originally inside the domain leave through one boundary, new ones come in through the opposite boundary [26]. Such an unbounded, steady and homogeneous bubbly flow with uniformly sized bubbles and no bubble coalescence approximated by infinite arrays of identical monodisperse bubble-swarms [39] doesn't allow quantitative analysis of mechanisms of the liquid turbulence. This is because the imposed spatial uniformity excludes the wall effects and the related considerations of the diffusion transport and the transfer of energy between the mean and fluctuating liquid flow [26].

In this study, the DNS computations are performed with the in-house computer code TURBIT-VOF, which uses a volume-of-fluid method with piecewise linear interface reconstruction for describing the interface evolution [5]. The in-house computer code TURBIT-VOF was developed at the Research Centre Karlsruhe (today Karlsruhe Institute of Technology) to perform direct numerical simulations of incompressible gas-liquid flows within a domain confined with two or four rigid walls [40, 41]. It is used and proved through the studies for the analyses of single bubbles [41-46] and bubble swarms [26]. In the latter work, the code is further improved for the quantitative analysis of balance equation for liquid turbulence kinetic energy and a non-homogeneous developed gas-liquid flow within a flat bubble column is simulated to provide the data for the analyses of mechanisms governing the liquid turbulence kinetic energy. The TURBIT-VOF is therefore used in this study to simulate a sub-region of a bubble-column with consideration of column wall effects, which is appropriate for a quantitative analysis of k_L equation. The numerical method and the related equations are further discussed in Section 2.5.4.

4

1.3. CFD Methods for simulation of bubbly flows

Mono-disperse bubble-driven gas-liquid flows in industrial scale bubble columns are of interest in this work. In gas-liquid flow and for the flow of two immiscible liquids, the phases are separated by an interface. In order to handle the length scales, the simulation methods which do not resolve details of the interface are usually used for such problems [47]. Two CFD approaches are mainly adequate for capturing the flow in bubble columns: two-fluid model (the Euler-Euler (E-E) method) [4, 16, 48-50] and particle-based methods (the Euler-Lagrange (E-L) method) [51-55]. The E-E method can be applied in principle to any two-phase flow pattern and it is favored over the E-L method with its advantage for lower computational costs considering high gas fractions due to the model's capability to apply a quite rough spatial resolution of the flow domain [47, 56, 57]. While the E-L method is suitable for bubbly flows with low gas holdup (below 5% [58]), the E-E method is much more general and is also suitable for churn-turbulent flows. Therefore, it is commonly used for the numerical simulation of flows in even large industrial-scale reactors. Within the E-E approach one can distinguish two-fluid models (with a prescribed mean bubble diameter d_{B}) and multi-fluid models which consider bubble-size distributions, e.g. by population balance models [32, 59, 60] or the MUSIG (MUltiple SIze Group) model [61]. In the E-E approach [12], separate balance equations with additional modelling terms are solved for the different phases [13]. Different approaches in multiphase fluid dynamics including the turbulence modeling and the population balance to determine bubble size distributions are reviewed and the potential as well as the deficits of the models are evaluated in the course of numerous published examples in a recent work by Mühlbauer et al. [32].

In Eulerian multi-fluid simulations of flows in bubble columns, there are model limitations regarding three main aspects [62]: i) closure relations accounting for turbulence effects, ii) closure laws defining interfacial interaction forces between gas and liquid phases, iii) determination of local bubble-size distribution, which affects in return both turbulence phenomena and interfacial forces. Turbulence (which we are interested in here) can be described either by statistical models, which are based on the Reynolds-Averaged Navier-Stokes (RANS) equations, or by Large-Eddy Simulation (LES). The unsteady recirculating flow with coherent structures suggests that LES is more suitable. However, the dimensions of industrial bubble columns (diameters of several meters and height of tens of meters) do not allow a sufficient fine discretization and it is not possible to simulate sufficient long times necessary for a reliable statistical evaluation. Hence, the only viable approach seems to be RANS. Here, one can distinguish eddy-viscosity models (such as the $k-\varepsilon$ and $k-\omega$ models) and Reynolds stress models (RSM) which can better account for the inherent an-

isotropy of the buoyancy-driven flow in bubble columns [6].

Among RANS approaches, RSM leads to additional constitutive relations and the associated modeling uncertainties [63]. The $k - \varepsilon$ approach is commonly used for predicting the mean flow parameters of turbulent two-phase flows in bubble columns by several researchers and presented reasonable results in comparison to more precise LES and RSM methods [14-17]. The interested readers are referred to recent studies for a detailed review and comparison of turbulence models for bubble column reactors [64] and for a review of bubble-induced turbulence modeling for vertical bubbly flows [63]. The E-E method and the $k - \varepsilon$ approach used in the current study are further discussed in Chapter 2.

1.4. Objectives and procedure

In this research, the turbulence kinetic energy in immiscible, incompressible two-phase flows of Newtonian fluids with focus on rising gas bubbles in a surrounding liquid is investigated for deducing improved closure relations to be further used in Eulerian-Eulerian Two-Fluid Models. For this purpose, comprehensive DNS investigations for bubble swarms with a wide range of parameters are performed and the closure terms in the k_{L} equation for bubbly swarms are evaluated. The DNS profiles are compared with model predictions and the promising models for the interfacial term are identified (A-priori testing). These turbulence models are used in the Euler-Euler simulation with the CFD code OpenFOAM® and verified for the bubble columns within the Multi-Phase Project (A-posteriori testing).

In order to reach the goal, the following procedures and objectives arise from the above discussions. An overview of the workflow is presented as a sketch in Fig. 1.

1. Preliminary study:

   The study of Ilic [26] over mono-disperse bubble swarms is considered as a reference and extended to higher gas hold-up values (higher number of bubbles) in a wider range of parameters, i.e. for lower values of the Morton number and a variety of the Eötvös number. Preliminary study is performed for single bubbles and bubble swarms to understand the influence of non-dimensional parameters on the exact k_{L} equation and closure relations for the interfacial term (the main source term of the bubble-induced turbulence). The investigation under such conditions provides valuable information for testing the engineering models in real life applications and later for using those models in CFD tools for industrial applications.

2. Comparison and validation:

    The DNS results with TURBIT-VOF are analyzed to understand the influence of physical features such as surface contamination and side walls on hydrodynamics of a rising bubble. The results are also verified via a literature study, a code-to-code comparison and validation with experiments.

3. A-priori testing:

    Closure terms in the k_L equation are evaluated and compared with model predictions in the literature.

4. A-posteriori testing:

    The useful model approaches for the interfacial term are then implemented in the CFD software OpenFOAM® and the simulations results are compared with experiments within the Multi-Phase Project.
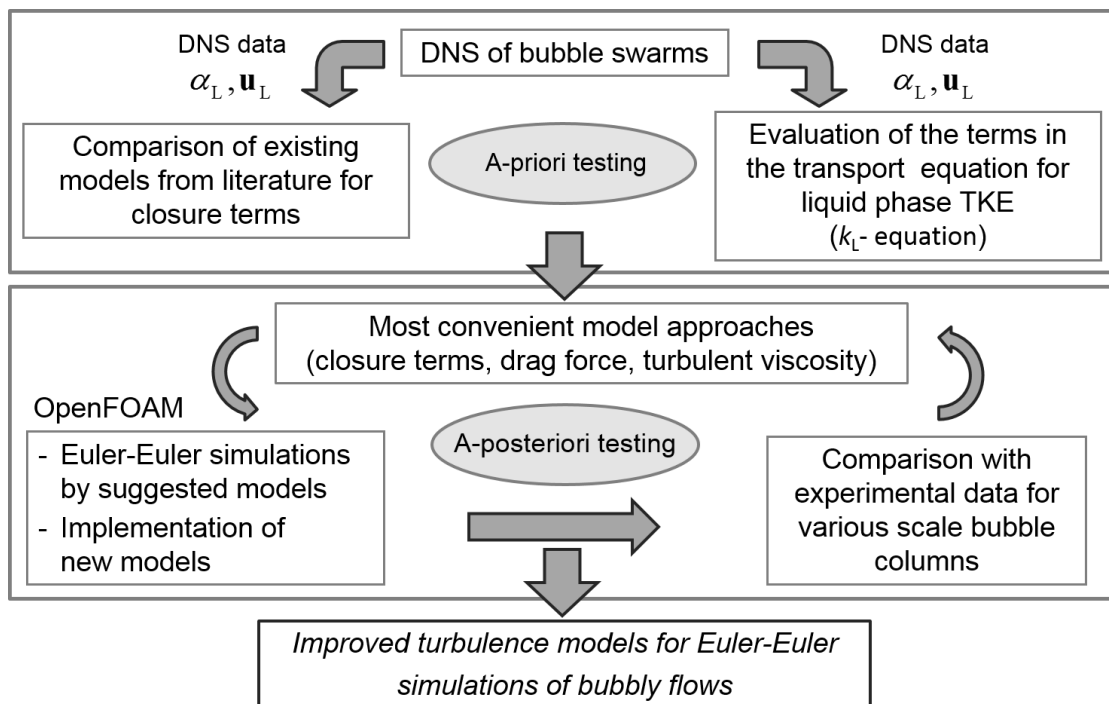
Fig. 1:   Sketch of the workflow.

1.5. Outline

This dissertation is organized as follows:

Chapter 2 reports methodology and theoretical background required for performing this research.

Chapter 3 presents the DNS results for the preliminary and comparative investigations, the verification of the DNS results for single bubbles by experimental data and further simulations of bubble swarms, which are used for evaluation of the liquid phase turbulence kinetic energy.

Chapter 4 is devoted to the analysis and assessment of the liquid phase turbulence kinetic energy, and discusses various concepts for closure of the k_{L} equation based on different simulation cases and presents the suitable models for the interfacial term in the k_{L} equation.

In Chapter 5, the results of Euler-Euler simulations with OpenFOAM® are analyzed and validated with the approaches from the literature as well as the experimental data for the test bubble column developed by Evonik Industries within the Multi-Phase Project.

2. Fundamentals and Methodology

2.1. Bubble induced turbulence

Experiments show that statistical features of bubble induced turbulence (pseudo-turbulence) considerably differ from those in conventional shear turbulence [6]. In a bubbly flow, relative motion between bubbles and liquid causes velocity fluctuations in the liquid, producing Reynolds stresses and other phenomena inherent to fluctuations [65]. For reliable mathematical modeling of pseudo-turbulence in bubble swarms, the velocity fluctuations play an essential role. This Section presents the special features of bubble-induced turbulence which have been published in Wörner and Erdogan [6] as a part of this research. A detailed overview on the physics of BIT is given in [65].

2.1.1. Liquid velocity fluctuations

Velocity fluctuations in BIT are often characterized by the probability distribution function (PDF) and the energy spectrum. In BIT, the PDFs are non-Gaussian and exhibit a self-similar behavior when scaled with $\alpha_G^{0.4}$ [66-68]. The spectrum differs from that in shear-driven turbulence and follows in a certain range a power law with a slope close to -3 of the wave number [7, 66, 69] (in contrast to the Kolmogorov -5/3 law for homogeneous single-phase turbulence). The difference in scaling is attributed to the immediate dissipation of eddies in the bubble wake in pseudo-turbulence [7, 70]. The slope -3 and its origin have been recently confirmed by DNS [71] while E-L simulations based on the point-particles approach do not give the correct scaling observed in experiments [72]. This indicates that resolving the finite size of the bubble in the DNS is essential [6].

The evaluation of spectra from experimental or numerical data is not trivial since signals arise as segments of different length. In general, spectra are computed from signals which are interpolated during the intervals when bubbles are present at the measuring point; therefore the kind of interpolation has an impact on the spectra themselves [73]. To circumvent this problem, spectra are sometimes measured behind the rising bubble swarm [6, 66].

2.1.2. Bubble clustering

The clustering of bubbles modifies the rise behavior of the swarm as compared to an isolated bubble (hindering or cooperative rise) and changes the local volume fraction. Hence, it is important for consideration of swarm effects in the bubble forces.

At the same time, the interaction of the bubble wakes modifies the liquid velocity fluctuations as compared to single bubbles. Bubble clustering is often characterized by the pair correlation function [37, 69] or radial probability distribution functions [74]. Experiments show that PDFs of all components of the bubble velocity have non-Gaussian form [69]. DNS investigations [37, 38] suggest that the bubble deformability and the associated inversion of the lift force play a crucial role in determining the orientation of the clustering; close to spherical bubbles have a higher probability of aligning horizontally [74] while non-spherical preferentially align in the vertical direction [6].

2.2. Hydrodynamics of a rising bubble

In numerical study of a single bubble, a broad range of bubble hydrodynamics can be investigated, such as bubble shape, terminal velocity of bubble, liquid velocity, and flow formation in the wake and inside of bubble. Bubbles in free rise in liquid under the influence of gravity adopt different shapes. The change of bubble shape modifies the velocity profiles and thus the flow formation. For interested readers, a detailed investigation of bubble hydrodynamics is given in Clift et al. [75]. The relation between bubble shapes, velocity and properties of gas and liquid can be explained by non-dimensional numbers. This Section, firstly, looks over those numbers that are often utilized in this study. Further, in this Section, the terminal velocity phenomena in the existing literature are reviewed focusing on the attempts to discover generic correlations for the estimation of the terminal velocity.

The experimental study of a single bubble within the Multi-Phase project provides data for terminal velocity of the rising bubble. For comparison of the terminal velocity with the experiments in the Multi-Phase project, the numerical conditions must correspond to the experimental conditions. However, imponderable factors always bring about some severity and complexity for validation studies and may affect bubble hydrodynamics, therefore must be examined as well. One of the most important characteristics influencing the shape and terminal velocity of a bubble is the surface contamination. Purifying the system is a general problem in experimental studies. Despite all the intention and attempt, the system often remains somehow contaminated. Moreover, the walls of the container modify the shape of bubbles rising in bounded channels and accordingly change the terminal velocity. A corresponding literature review of those factors is also presented in this section.

2.2.1. Non-dimensional numbers

The flow of bubbles rising freely in liquid is represented by three non-dimensional numbers: Eötvös number ($E\ddot{o}$), Morton number (M), Reynolds number (Re). The book of Clift et al. [75] presents a generalized graphical correlation based on those numbers. This diagram is given in Section 3.2 together with the cases considered in this study. The definition of the non-dimensional numbers is explained here.

The Eötvös number ($E\ddot{o}$) is defined as the ratio of buoyancy and capillary forces (surface tension). The change of bubble size is strongly related to the $E\ddot{o}$ since it is characterized mainly by the bubble diameter. For bubble rising in liquid it is defined as

$$E\ddot{o} \equiv \frac{g \cdot \Delta\rho \cdot d_{\text{B}}^2}{\sigma}$$

(1)

Here, $\Delta\rho = (\rho_{\text{L}} - \rho_{\text{G}})$ with a unit of (kg/m^3) is the density difference of the surrounding fluid and gas phase, d_{B} (m) is the bubble diameter, σ (N/m) is the surface tension coefficient and g is the gravity (g = 9.81 m/s^2).

The Morton number (M) adopts its name from a paper of Haberman and Morton [76] and consists of the physical parameters of gas and liquid as

$$M \equiv \frac{g \cdot \Delta\rho \cdot \mu_{\text{L}}^4}{\rho_{\text{L}}^2 \cdot \sigma^3}$$

(2)

The Morton number is dominated by the liquid properties, primarily by the dynamic viscosity of the liquid μ_{L} (N·s/m^2 or kg/m·s). It can also be defined as a ratio of forces as

$$M \equiv \frac{F_{\text{buoyancy}} \cdot F_{\text{viscous}}^4}{F_{\text{inertia}}^2 \cdot F_{\text{surface tension}}^3}$$

(3)

The Morton number can also be written as

$$M \equiv \frac{g \cdot \mu_{\text{L}}^4}{\rho_{\text{L}} \cdot \sigma^3} \frac{\Delta\rho}{\rho_{\text{L}}}$$

(4)

According to Brauer [77], the first factor here in Eq. (4) can be interpreted as a dimensionless liquid number, which represents the ratio of acceleration due to gravity g and molecular motion $\rho_{\text{L}}\sigma^3/\mu_{\text{L}}^4$ (m/s^2). Mobility of molecules is higher with the increment of this molecular acceleration. It therefore makes sense that the bubble rise velocity U_{T} must increase with decreasing values of Morton number [77].

The Reynolds number (Re) is defined as the ratio of inertial forces to friction forces (viscous forces) and for bubbles rising in liquid given as

$$Re_B \equiv \frac{U_T \cdot d_B}{v_L} = \frac{\rho_L \cdot U_T \cdot d_B}{\mu_L}$$ (5)

where v_L (m²/s) the kinematic viscosity and μ_L (kg/m·s) is the dynamic viscosity of the liquid. The Reynolds number is dominated by viscous forces for laminar flow and by inertial forces for turbulent flow.

2.2.2. Terminal velocity

As being a fundamental topic in the field of gas-liquid two-phase flows, several studies sought for an approach to estimate the terminal velocity of freely rising single bubbles. Much of the previous research has developed empirical, semi-empirical and theoretical formulation for the terminal velocity, which many times remain subjective to a narrow range of parameters since the rise velocity shows varying nature with the system properties [78]. Tomiyama et al. [79] reviewed on the related approaches in literature and investigated the terminal velocity (U_T) of a single bubble rising through an infinite stagnant liquid. They found number of studies (e.g., [75, 80]) conducted to establish a reliable U_T model. For small spherical bubbles [81] and large spherical-cap bubbles [82], some reliable theoretical models are available. However, no theoretical U_T models have been proposed for a bubble of intermediate size, in which the surface tension force plays a dominant role [79].

An extended review on bubble rise velocity is given in [78]. Kulkarni and Joshi [78] assorted the approaches for estimation of U_T under three categories, i.e. the fundamental approach based on simple force balance, empirical approaches based on dimensional analysis and semi-empirical ones through Wave Analogy. In order to have a quick overview, those approaches from [78] are summarized here.

The force balance approach is based on the earliest investigations in the bubble rise, where the balance of buoyancy, gravity and drag forces form the bubble movement. When a bubble is small enough to be spherical and $Re_B < 1$, U_T can be evaluated by using the Hadamard–Rybczynski solution [81]. The Stokes drag model can be utilized for the evaluation of U_T [79] when the bubbles do not have any internal circulation [78] and no slip exists at the bubble surface so that the bubble behaves as if it were a rigid sphere [79]. In a comprehensive study of bubble dynamics, Clift et al. [75] identifies that the internal circulation occurs if $Re > 20$ while the "Bond criterion" suggests that internal circulation could only occur for $E\ddot{o} > 4$.

Peebles and Garber [83] analyzed the velocity of air bubbles in twenty-two liquids in a wide range of physical properties and defined different correlations for four distinct regions in terms of range of applicability depending on Re and M whereas Mendelson

[84] categorize similar four regions depending on d_B, based on the data of Haberman and Morton [76]. Table 1 summarizes those regions considering both authors' approach. According to extensive experimental measurements from Peebles and Garber [83], the Stokes solution is adequate to predict the rise velocity of small bubbles with $Re \leq 0.2$ in the Region-1. The Region-2 covers the range of $2 \leq Re \leq 4.02M^{-0.214}$ or $0.7\text{mm} < d_B < 1.4\text{mm}$ while Region-3 includes bubbles ranging in $4.02M^{-0.214} \leq Re \leq 3.1M^{-0.25}$ or $1.4\text{mm} < d_B < 6\text{mm}$.

In the experiments within the Multi-Phase Project, d_B was obtained in the range of 1.6 mm – 1.9 mm. These values, as most of bubbles in practical applications, fall into the Region-3 where the bubbles are distorted in time (no longer spherical) and tend to follow non-rectilinear trajectory such as a zigzag and helical path. The U_T is widely scattered [79] and the drag is increased by the vortex formation in the wake. However, with respect to the criterion $2 \leq Re \leq 4.02M^{-0.214}$, the experiments belong in Region-2. This is not very surprising because the criterion depending on physical properties (viscosity, surface tension, density) of the phases may differ from strictly drawn borders by bubble diameter values, the transition region of the bubbles from rigid to fluid spheres or fluid spheres to ellipsoidal may occur.

According to Peebles and Garber [83], the terminal velocity in Region-2 is correlated by

$$U_T = \frac{0.33g^{0.76}\rho_L^{0.52}(d_B/2)^{1.28}}{10\mu_L^{0.52}}$$

(6)

The terminal velocity in Region-3 is given by

$$U_T = 1.35\sqrt{\frac{2\sigma}{d_B\rho}}$$

(7)

and in general, it predicts the data very well for $M > 10^{-8}$.

Clift et al. [75] discuss some other approaches for higher Re from the authors Haas et al. [85], Levich [86] and Moore [87-89]. The correlation of Moore [88] is valid only for $M < 10^{-7}$ whereas the prediction of Levich [86], and Moore [89] who extended Levich [86]'s work, are valid for spherical bubbles for $Re > 60$ [90]. The formula from Levich [86] can be used to estimate the terminal velocity for a bubble in potential flow (Region-2) is given by

$$U_T = \frac{\Delta\rho g d_B^2}{36\mu_L}$$

(8)

However, this correlation may be somewhat limited since it was calculated by using drag coefficient (C_D) and Re, both of which contain velocity and viscosity term. Maxworthy et al. [91] performed experiments on the rise of air bubbles in distilled water mixed with different content of pure glycerin (0-100 wt.%) in an unbounded channel and proposed a correlation for M in the range of $7.71 \times 10^{-12} < M < 78$ as

$$U_T = \frac{\mu_L}{d_B \rho_L} \left(0.526 Mo^{-0.142} E\ddot{o}^{0.5} \right)^3$$

(9)

Raymond and Rosant [92] improved the correlation of Maxworthy et al. [91] and found a better approximation, but only for $M > 10^{-6}$.

The second type of approach is based on dimensional analysis [78]. This category includes the approaches where the correlations for the bubble size and rise velocity are determined from the parameters that govern the bubble motion such as density, viscosity, surface tension, gravity, equivalent diameter and finally a relation between drag coefficient and Reynolds number is obtained. For practical predictions, it is useful to have the terminal velocity correlated explicitly in terms of system variables [93]. One of the initial attempts, Abou-El-Hassan [94] found correlations independent on flow regimes and the bubble shapes, and applicable for the range of Re from Stokes region to Newton's law region [78]. Following the approach of Abou-El-Hassan [94], Rodrigue [95] developed a general correlation and Rodrigue [96] further extended it to predict the velocity for any bubble volume in any Newtonian fluid. The latest correlation derives the bubble rise velocity in terms of the velocity number (V) and the flow number (F) as

$$V = \frac{F}{12} \left[\frac{\left(1 + 1.31 \times 10^{-5} M^{11/20} F^{73/33} \right)^{21/176}}{\left(1 + 0.020 F^{10/11} \right)^{10/11}} \right]$$

(10)

Here

$$V = U_T \left(\frac{\rho^2 d_B^2}{\sigma \mu} \right)^{1/3}$$

(11)

and

$$F = g \left(\frac{\rho^5 d_B^8}{\sigma \mu^4} \right)^{1/3} = E\ddot{o} \left(\frac{Re}{Ca} \right)$$

(12)

Grace et al. [97] also determined the terminal velocity for a rising bubble with a correlation including dimensionless groups for contaminated drops and bubbles. In the

formulae of Grace et al. [97] and Rodrigue [96], the dependence of the terminal velocity on the viscosity and density of the internal fluid is neglected. Tomiyama et al. [79] also proposed an approach with projection of bubble shape and it gives a way of understanding the trends in rise velocity for different liquid properties and for different bubble shapes. However, it is only valid for high bubble Reynolds numbers.

The third category is the approach through Wave Analogy [78]. Mendelson [84] proposed the wave theory for prediction of bubble rise velocity assuming that the behavior of rising bubbles is similar to the behavior of surface waves propagated over deep water. The terminal rise velocity of a bubble correlated by Mendelson [84] in terms of the fluid properties and bubble size d_B is given by

$$U_T = \sqrt{\frac{2\sigma}{d_B \rho_L} + \frac{g d_B}{2}} \qquad (13)$$

This analogy is mainly valid in the Region-2 and 3 proposed by Peebles and Garber [83] for bubbles in low viscosity (low M) but only tested for high velocities. The wave analogy is later modified by Maneri [98] for special cases of rise of a planar bubble and the rise in a rectangular duct but the model applicability is restricted. Jamialahmadi et al. [99] also modified the wave analogy and combined with the correlation of Hamadard, and obtained a good fit for pure liquids over a wide range of gas-liquid properties [78]. However this model is an extension of Mendelson [84] for small bubble sizes doesn't apply for the cases here.

As can be seen from broad approaches discussed above, there is no exact universal correlation to predict the terminal velocity. Each correlation is valid in a limited range of bubble size and flow conditions. Table 1 summarizes the appropriate models picked out for prediction of U_T to use in comparison study. U_T correlation of Peebles and Garber [83] in Eq. (7) is valid in a certain range of non-dimensional numbers whereas the correlation of Mendelson [84] in Eq. (13) covers a range of all values of $d_B > 0.7\,\text{mm}$ and $M > 10^{-8}$ for ellipsoidal fluid particles. The correlation from Levich [86] is chosen among similar approaches as the only one with indicated velocity correlation. It is valid for spherical bubbles at large Reynolds numbers. Rodrigue [96] in Eq. (10) is the most general approach to predict the velocity for any bubble volume in any Newtonian fluid considering the effect of Morton number. Maxworthy et al. [91] in Eq. (9) is also considered on the ground of the given correlation depending on the experiments for Water - Glycerin mixtures for the range of $7.71 \times 10^{-12} < M < 78$.

Table 1: Classification of single bubble flow behavior and correlations for estimating C_D and U_T from literature. Bubble shape illustrations are taken from Bothe and Schlüter [100].

	Range of applicability	Characteristics				Possible applicable correlations	
	a) Mendelson [84] b) Peebles and Garber [83]	Bubble shape	Internal circulation	Path	Dominant force	C_D	U_T
Region 1	a) $d_B < 0.7\,\mathrm{mm}$ b) $Re \leq 0.2$	Rigid Sphere	No	Rectilinear	Viscous force	Stokes' law $C_D = 24/Re_B$	Stokes' law $U_T = \dfrac{g d_B{}^2 \Delta\rho}{18\mu}$
Region 2	a) $0.7\,\mathrm{mm} < d_B < 1.4\,\mathrm{mm}$ b) $2 \leq Re \leq 4.02 M^{-0.214}$	Fluid Sphere	Yes	Rectilinear	Viscous force and Inertial forces	$C_D = 48/Re_B$ [86] C_D from Eq. (63) [101] $C_D = 14.9 Re_B^{-0.78}$ [85] C_D from Eqs.(64),(65) [102]	Eqs. (6),(8),(9),(13),(18)
Region 3	a) $1.4\,\mathrm{mm} < d_B < 6\,\mathrm{mm}$ b) $4.02 M^{-0.214} \leq Re \leq 3.1 M^{-0.25}$	Ellipsoidal	Yes	Tendency for zigzag and helical	Surface tension force	$C_D = 2\sqrt{E\ddot{o}_B}\big/3$ [103] C_D from Eqs.(64),(65) [102]	Eqs. (7),(9),(13)
Region 4	a) $d_B > 6\,\mathrm{mm}$ b) $3.1 M^{-0.25} \leq Re$	Irregular form	Yes	Irregular	Inertial force	$C_D = 0.44$ C_D from Eqs.(64),(65) [102]	$U_T = 1.18 \left(\sigma g/\rho\right)^{1/4}$ [83]
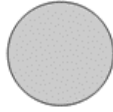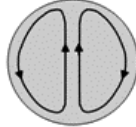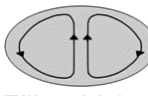
2.2.3. Surface contamination effect

The surfactant effects on bubble dynamics, primarily on the bubble rise velocity, are discussed in this section. In general, one of the main difficulties for comparing the experimental data with simulations is that the influence of impurities is very hard to avoid. The liquid may always be contaminated [95]. Traces of surface-active contaminants may have a profound effect on the behavior of drops and bubbles. If surfactants are accumulated on bubble surface, the so-called Marangoni effect makes the interface immobile (no slip exists at the bubble surface) and thereby the bubble behaves as if it were a rigid sphere [79] and do not have any internal circulation [78]. The immobile surface modifies the wake formation and consequently the turbulence induced by bubbles related to its modified eddies in the bubble wake. The possible influence of surfactants on the recirculation inside of a bubble can be observed from the pictures in Fig. 2.

Clift et al. [75] discusses the surfactant effect on bubbles and refers to Frumkin and Levich [104] and Levich [86] as the most reasonable explanation for the absence of internal circulation for small bubbles and drops. Surface-active substances tend to accumulate at the interface between two fluids, thereby reducing the surface tension. When a drop or bubble moves through a continuous medium, adsorbed surface-active materials are swept to the rear, leaving the frontal region relatively uncontaminated and this causes a tendency to retard surface motion. The surface contamination theory implies that all bubbles and drops, no matter how small, will show internal circulation if the system is sufficiently free of surface-active contaminants [75].
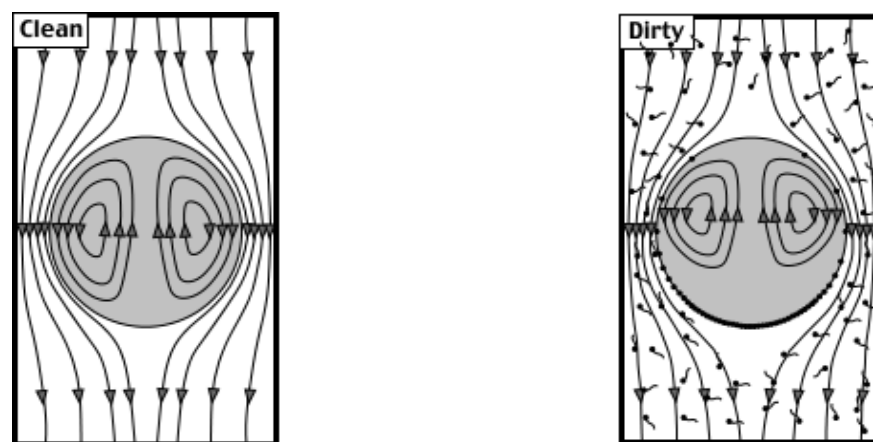
Fig. 2:   Effect of contamination on internal recirculation (Source: [105]).

Tomiyama et al. [79] summarized the primal role played by surfactants in bubble dynamics. In viscous force dominant regime (small spherical bubble), the immobile bubble interface changes the boundary condition on the interface from free-slip to no-slip, which results in the increase in the viscous drag and the decrease in U_T. In surface tension force dominant regime (intermediate bubble), surfactants damp down the shape oscillation, by which the mean aspect ratio increases, and thereby U_T becomes close to that for a clean bubble with small initial shape deformation. Consequently, the scatter of U_T caused by initial shape deformation becomes much smaller than that in a pure system.

In 2010 edition of VDI Heat Atlas, Räbiger and Schlüter [106] presented the formation and movement of bubbles and drops. The authors reported that the relative velocity of single bubbles is dominated by the shape, whereas the influence of impurities and surface-active agents play an important role due to the larger difference in density and negligible inertia of the gas phase. They established the differentiation for the characterization of bubble shapes according to Peebles and Garber [83] with four different general shapes and presented four characteristic regimes (A, B, C, D) depending on the properties of the continuous phase.

Mersmann [107] developed an overall description for a rough estimation of the terminal velocity of single bubbles and drops [106]

$$U_T^* = U_T \cdot \sqrt[3]{\frac{\rho_L^2}{\mu_L \cdot g \cdot \Delta\rho}} = \sqrt[3]{Re_B Fr} \tag{14}$$

in dependency of the dimensionless bubble diameter [106]

$$d_B^* = d_B \cdot \sqrt[3]{\frac{\rho_L \cdot g \cdot \Delta\rho}{\mu_L^2}} = \sqrt[3]{Ar} \tag{15}$$

Here, the Reynolds number Re_B is as given in Eq. (5), the Froude number is defined as $Fr \equiv U_T^2 / d_p \cdot g$ and the Archimedes number Ar is defined as the ratio of external forces to internal viscous forces [106] as $Ar \equiv d_B^3 \cdot g \cdot \rho_L \cdot \Delta\rho / \mu_L^2$. Eq. (14) and Eq. (15) together with the logarithm of the dimensionless modified liquid number (reciprocal to Morton-number) [106]

$$\log\left(K_{F,\Delta\rho}\right) = \log\left(\frac{\rho_L \cdot \sigma^3}{g \cdot \mu_L^4}\right)\frac{\rho_L}{\Delta\rho} \tag{16}$$

allow a convenient estimation of the terminal velocity of single drops and bubbles. The liquid number helps to differentiate between four characteristic regimes (A, B, C and D). The single bubble cases in this study fall into the Regime-B of the four regimes by

fulfilling the condition of $7.2 \leq Ar < 125 \cdot K_F^{0.25}$. In this regime, the forces of inertia are more dominant with increasing Ar and the drag coefficient can be calculated by empirical equation of Haas et al. [85] as given in [106]

$$C_D = 14.9 Re_B^{-0.078} \tag{17}$$

Within the Regime-B, the dimensionless terminal velocity is calculable by the empirical correlation

$$U_{T,Ar}^* = 0.136 Ar^{0.4266} \tag{18}$$

A number of studies [79, 108-110] have been conducted to account for surface contamination in the estimation of bubble shape and U_T. However, it is very difficult to develop a mathematically closed model of U_T for contaminated systems. A modified correlation from Grace et al. [97] to estimate the pure U_T from contaminated U_T by using a correction factor (Γ) [75] is given by

$$U_{T,\,pure} = U_{T,\,cont} \left[1 + \frac{\Gamma}{1 + (\mu_G / \mu_L)} \right] \tag{19}$$

Here, the correction factor (Γ) can be approximately estimated from Fig. 3 for a certain value of ψ that is given as

$$\psi = \frac{E\ddot{o}\left[1 + 0.15 (\mu_G / \mu_L) \right]}{1 + (\mu_G / \mu_L)} \tag{20}$$

The contaminated U_T can be calculated in an easier form by defining a contamination coefficient κ_{cont} as

$$U_{T,\,cont} = U_{T,\,pure} \kappa_{cont} = U_{T,\,pure} \left[1 + \frac{\Gamma}{1 + (\mu_G / \mu_L)} \right]^{-1} \tag{21}$$

and by substituting the value of Γ into Eq.(21).
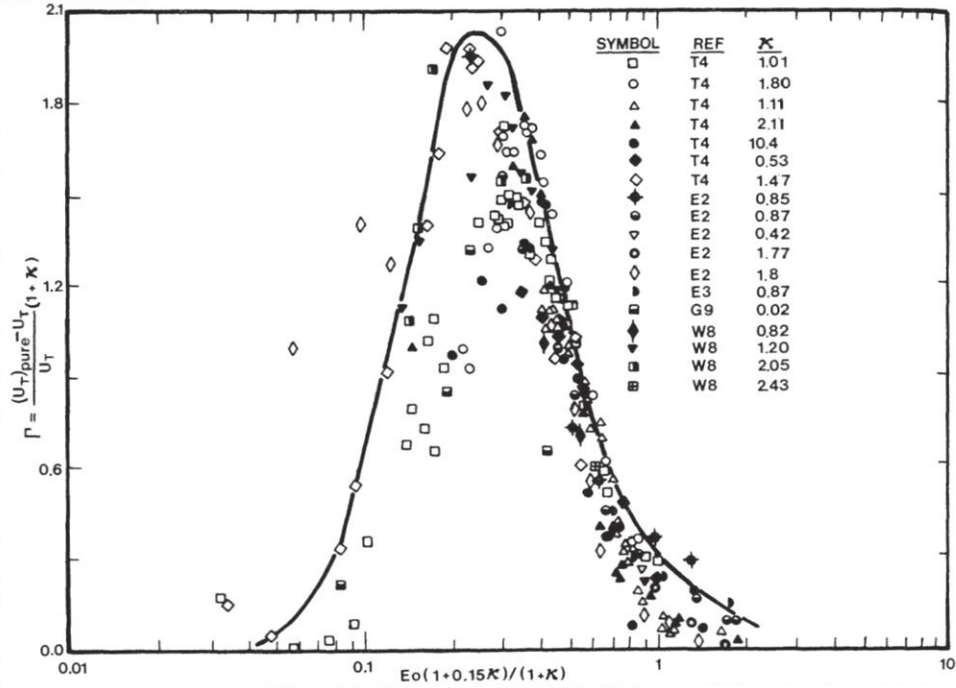
Fig. 3:   Correction factor Γ relating terminal velocity in pure systems to value in corresponding contaminated systems. Taken from Clift et al. [75].

2.2.4. Wall effect

The solid wall effect is an important factor affecting the bubble shape and the terminal velocity of rising bubble. It must be accounted for comparison of correlations for so-called unbounded channels with the results from the experiments and the simulations that are obtained in bounded channels. In the prior studies, researchers aimed to determine the influence of the ratio of equivalent bubble diameter of the fluid particle to the diameter of channel with cylindrical containing walls (λ) on the terminal velocity

$$\lambda = d_{\mathrm{B}} / D \tag{22}$$

Using the wall distance as hydraulic channel diameter for vertical parallel plates, λ can be assumed as a ratio of equivalent bubble diameter to the wall distance

$$\lambda = \lambda_z \equiv d_{\mathrm{B}} / L_{\mathrm{ref}} \tag{23}$$

It is known that the containing walls tend to cause elongation of fluid particles in the vertical direction, suppress secondary motion, and alter the wake structure. Yet there are not sufficient experimental evidence to allow useful quantitative generalizations to be drawn [75].

The correlations for estimation of terminal velocity of single bubbles discussed before are defined for so-called unbounded channels. In reality, they could be described as the channels where the wall distance is large enough to minimize the wall effects. Clift et al. [75] quantified this definition as $\lambda < 0.1$. This ratio is $\lambda \approx 0.4-0.5$ for the simulations in this study so that wall effects on bubble rise velocities are expected. A certain limit of wall effects dependent on λ was not seen in the literature for spherical and ellipsoidal bubble whereas for spherical-caps in low M systems the wall effects are negligible for $\lambda < 0.125$ [75].

In one of the first studies for the walls effect, Uno and Kintner [111] proposed a formula depending on a constant related to tube diameter but invalid for small tubes. Another correlation is given in Collins [112] for Water-Air system with $E\ddot{o} > 40$. Clift et al. [75] present simple correlations to obtain a coefficient for circular ducts to consider retarding effects of the walls for rigid particles, and bubbles and drops at different range of Reynolds number. For intermediate size drops and bubbles where $E\ddot{o} < 40$, if $Re > 200$ and $\lambda \leq 0.6$ then they recommend the equation [75]

$$U_T / U_T^\infty = \left[1 - \lambda^2 \right]^{3/2} \tag{24}$$

If $1 \leq Re \leq 200$ and $\lambda \leq 0.6$ then the velocity correction factor for rigid spheres at higher Reynolds numbers in Fig. 4 should be used. The correction factor is defined as the velocity ratio [75]

$$K_U = U_T^\infty / U_T \tag{25}$$

where U_T^∞ is the terminal velocity which the bubble would have in an infinite container. Fig. 4 shows the terminal Reynolds number and $\left(K_U - 1 \right)$ as a function of $N_D^{1/3}$. N_D is a term called "Best number" and given as [75]

$$N_D = C_D \, Re_B^2 = 4\rho \Delta \rho g \, d_B^3 / 3\mu_L^2 \tag{26}$$

K_U can be estimated as a function of $N_D^{1/3}$ and λ of the system from Fig. 4.
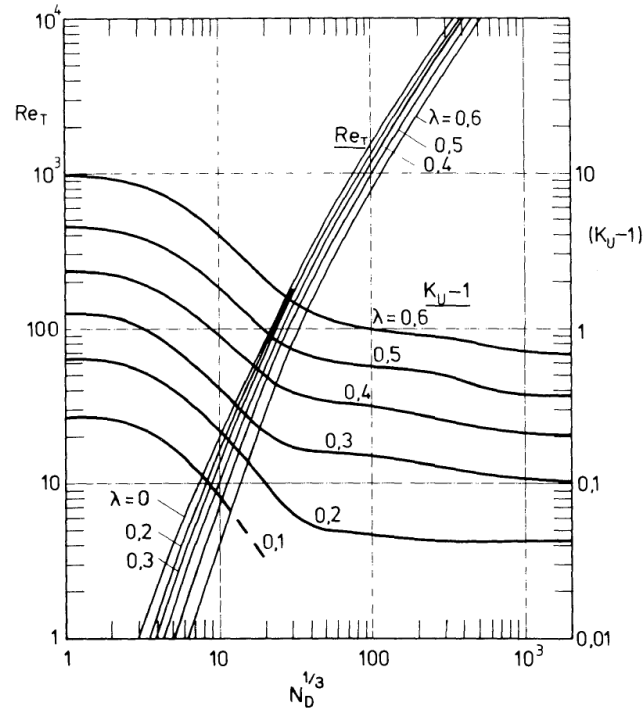
Fig. 4: Terminal Reynolds number and velocity correction factor for rigid spheres on the axis of circular ducts. Taken from Clift et al. [75].

2.3. Turbulence modelling

The turbulence models for CFD simulations of flows in bubble columns are the main interest in this dissertation. This Section starts with an introduction of the basic definitions used for the modelling of turbulent flow for a better understanding of the formulations. After an introductory overview on the modelling approaches for the BIT, the balance equation for turbulence kinetic energy of the liquid phase (k_L equation) and its closure are discussed in detail. Furthermore, the k-ε type approach is elaborated here since the E-E simulations in the present study are based on this method. At the end, the approaches for estimating the turbulent viscosity are presented. Part of this Section is based on Wörner and Erdogan [6] where the shortcomings of common concepts for closure of the liquid phase turbulence kinetic energy equation have been published as a part of this research.

2.3.1. Basic definitions

The chaotic and random nature of turbulent flow compels an indirect and detailed solution strategy. The appearance of turbulence reveals itself as random fluctuations of the measured velocity component and a mean (averaged) value. The flow variables are then required to be characterized in terms of the mean values of flow properties

($u_{x,mean}$, $u_{y,mean}$, $u_{z,mean}$ etc.) and some statistical properties of their fluctuations (u'_x, u'_y, u'_z etc.). This is called the Reynolds decomposition. The velocity is decomposed into a steady mean value u and a fluctuating component $u'(t)$ [113]:

$$u(t) = u_{\mathrm{mean}} + u'(t) \tag{27}$$

All other flow variables will also exhibit this additional time-dependent behavior. The Reynolds decomposition defines flow property φ at this point as the sum of a steady mean component Φ_{mean} and a time varying fluctuating component $\varphi'(t)$ with zero mean value:

$$\varphi(t) = \Phi_{\mathrm{mean}} + \varphi'(t) \tag{28}$$

The mean Φ of flow property φ is defined as follows [113]:

$$\Phi_{\mathrm{mean}} = \frac{1}{\Delta t} \int_0^{\Delta t} \varphi(t)\, dt \tag{29}$$

The time average of the fluctuations φ' is, by definition, zero:

$$\overline{\varphi'} = \frac{1}{\Delta t} \int_0^{\Delta t} \varphi'(t)\, dt \equiv 0 \tag{30}$$

The descriptors used to indicate the spread of the fluctuations φ' about the mean value are the variance

$$\overline{(\varphi')^2} = \frac{1}{\Delta t} \int_0^{\Delta t} (\varphi')^2\, dt \tag{31}$$

and root mean square (r.m.s.)

$$\varphi_{\mathrm{rms}} = \sqrt{\overline{(\varphi')^2}} = \left[\frac{1}{\Delta t} \int_0^{\Delta t} (\varphi')^2\, dt \right]^{1/2} \tag{32}$$

The root mean square (r.m.s.) values of the velocity components are of particular importance since they are generally most easily measured and express the average magnitude of velocity fluctuations. A larger u_{rms} indicates a higher-level turbulence. Records at different points may have the same mean velocity while each record may have a different level of turbulence (different u_{rms} values). One-half times the variances of velocity fluctuations have a further interpretation as the mean kinetic energy per unit mass contained in the respective velocity fluctuations. The total kinetic energy per unit mass k of the turbulence at a given location can be found as follows [113]:

$$k = \frac{1}{2}\overline{u'^2} = \frac{1}{2}\left(\overline{u_x'^2} + \overline{u_y'^2} + \overline{u_z'^2}\right)$$ (33)

2.3.2. Model approaches for bubble induced turbulence

In general, one can distinguish (seldom-adopted) models that account for the turbulence in both phases, and (more common) models that neglect the turbulence in the disperse phase (as it is considered as laminar) and model the turbulence in the continuous phase only. In the former case, usually no separate transport equation for k_G is solved [6].

I.   The modeled k_L and k_G equations are solved (with or without interfacial term).

II. The modeled k_L equation (with or without interfacial term) is solved while the turbulence in the gas phase is neglected.

For closure of the k_L equation it is common practice to adopt for the single-phase like terms closure relations and model coefficients from the standard single-phase k-ε model. Two approaches exist for considering the pseudo-turbulence. In the more general one, the interfacial term is explicitly modeled. For this BIT source term, several closure relations have been proposed in literature (e.g. [14, 26]). In the second approach, the interfacial term is neglected, i.e. set to zero, so that the single-phase k-ε equation is solved for the continuous phase. The BIT is taken into account by a two-phase multiplier for the shear-induced turbulence kinetic energy [8] or by an extra (linearly superposed) contribution to the eddy viscosity, e.g. by the model of Sato [114, 115]. The latter approach has two main drawbacks. First, it can only increase the turbulent viscosity in bubbly flow and is, thus, unable to reproduce the attenuation of turbulence observed in several bubbly flow experiments. Second, the influence of the bubbles on the turbulence kinetic energy and its dissipation rate are neglected [6].

2.3.3. Turbulence kinetic energy of liquid phase

The turbulence kinetic energy (TKE) is an important quantity for the analysis of turbulence and provides statistical information. In bubble columns operated with gas-liquid flows, the turbulence is mainly based on the fluctuations of liquid phase quantities induced by the bubbles. The transport equation of the TKE which was proposed by [21, 116] contains the related formulations for the analysis of the mechanisms in such turbulence modification or the bubble induced turbulence (BIT) in bubbly flows. The transport equation of the liquid phase turbulence kinetic energy, k_L is the cornerstone in k - ε type turbulence models which are commonly employed for industrial applications [26].

Kataoka & Serizawa [21] derived the exact conservation equations of turbulence for k and ε for a gas-liquid flow consisting of two incompressible phases. The formulation uses a single-phase flow representation and involves the effects of the bubbles through additional terms in the basic equations. In non-dimensional form, the transport equation for the liquid phase turbulence kinetic energy k_L can be written as [6, 19]

$$\frac{\partial}{\partial t}\left(\alpha_L k_L\right) + \nabla\cdot\left(\alpha_L k_L \overline{\overline{\mathbf{u}_L}}\right) = \frac{1}{Re_{\mathrm{ref}}}\nabla\cdot\left(\alpha_L \overline{\overline{\tau_L'\cdot\mathbf{u}_L'}}\right) - \nabla\cdot\left[\alpha_L\left(\overline{\overline{p_L'\mathbf{u}_L'}} + \frac{1}{2}\overline{\overline{\mathbf{u}_L'^2\mathbf{u}_L'}}\right)\right] - \alpha_L\overline{\overline{\mathbf{u}_L'\mathbf{u}_L'}}:\nabla\overline{\overline{\mathbf{u}_L}}$$

$$\underbrace{\phantom{\frac{1}{Re_{\mathrm{ref}}}\nabla\cdot\left(\alpha_L \overline{\overline{\tau_L'\cdot\mathbf{u}_L'}}\right) - \nabla\cdot\left[\alpha_L\left(\overline{\overline{p_L'\mathbf{u}_L'}} + \frac{1}{2}\overline{\overline{\mathbf{u}_L'^2\mathbf{u}_L'}}\right)\right]}}_{\textit{DIFFUSION}} \qquad \underbrace{\phantom{-\alpha_L\overline{\overline{\mathbf{u}_L'\mathbf{u}_L'}}:\nabla}}_{\textit{PRODUCTION BY SHEAR}}$$

$$-\frac{1}{Re_{\mathrm{ref}}}\alpha_L\overline{\overline{\tau_L':\nabla\mathbf{u}_L'}} + \overline{\left[\frac{1}{Re_{\mathrm{ref}}}\tau_{L,i}' - p_{L,i}'\mathbf{I}\right]\cdot\mathbf{u}_{L,i}'\cdot\hat{\mathbf{n}}_{L,i}a_i}$$

$$\underbrace{\phantom{-\frac{1}{Re_{\mathrm{ref}}}\alpha_L\overline{\overline{\tau_L':\nabla\mathbf{u}_L'}}}}_{\textit{DISSIPATION}} \qquad \underbrace{\phantom{\overline{\left[\frac{1}{Re_{\mathrm{ref}}}\tau_{L,i}' - p_{L,i}'\mathbf{I}\right]\cdot\mathbf{u}_{L,i}'\cdot\hat{\mathbf{n}}_{L,i}a_i}}}_{\textit{PRODUCTION BY INTERFACIAL TERM}}$$

$$(34)$$

Here, subscript i denotes liquid phase quantities at the gas-liquid interface. The detailed background mathematical formulation of liquid turbulence in bubbly-flows is given in [26].

For an arbitrary physical quantity φ_L, the conditionally averaged value and the fluctuation with respect to this average are given by [6]

$$\overline{\overline{\varphi_L}} = \overline{\varphi_L X_L} / \overline{X_L} \tag{35}$$

$$\varphi_L' = \varphi_L - \overline{\overline{\varphi_L}} \tag{36}$$

Here X_L is the characteristic function (also called the indicator function) of the liquid phase. It takes the value 1 in the liquid phase and the value 0 in the gas phase. The single overbar indicates averaging while the double overbar denotes phase-weighted (conditional) averaging. By applying this notation, the turbulence kinetic energy of the liquid is written as $k_L = \overline{\overline{\mathbf{u}_L'^2}}/2$. In Eq. (34), the terms involving the mean liquid volumetric fraction $\alpha_L = \overline{X_L}$ have essentially the same form and meaning as in the single-phase k equation. The last term in Eq. (34) contains the specific interfacial area a_i and is specific for two-phase flows as it represents a source/sink of turbulence due to the presence of interfaces [6]. This term is mentioned in the literature as the interfacial term.

In the context of the combination of the two-fluid approach with the k - ε turbulence model, all terms of the right-hand side in Eq. (34) (i.e. shear production term,

diffusion term, dissipation term and interfacial term) must be modeled to close the system of equations. However, some correlations between fluctuating quantities can hardly be measured so that detailed information is missing in literature. All terms from instantaneous, spatially resolved data obtained via DNS must be evaluated in order to gain insight in statistical features of bubble-induced turbulence and to develop improved models.

The performance of variants of the $k - \varepsilon$ model (standard, realizable, RNG, SST) in the E-E approach has been investigated in several papers [48, 62, 117-120]. In such numerical studies it is important to use higher order schemes since low order schemes (like upwind) have a large amount of numerical diffusion, which masks the eddy viscosity of the turbulence model [62, 117]. Despite their apparent similarities, the Standard, RNG and Realizable versions perform different when applied to flows in bubble columns (with the RNG model being the best) [62]. The impact of the BIT term, despite being negligible on the computation of velocity fields and gas holdup, is significant on the estimation of turbulence quantities [62]. While the above comparative studies are useful to identify which model performs best for a certain experiment, there are hardly useful for development of improved closure relations [6].

The transport equations of the standard $k\text{-}\varepsilon$ model contain adjustable constants [121], whose values were calculated by numerous iterations of data fitting for a wide range of turbulent flows [113] or determined by various relations [122]. Hence, these constants are not universal, even in case of single-phase flow. Furthermore, statistical features of BIT differ from that of shear turbulence (cf. Section 2.1). It is therefore obvious that for two-phase flows specific models and coefficients should be developed for closure of Eq. (34). Experimentally it is difficult to obtain detailed information about the terms in the k_{L} equation especially under non-dilute conditions. By applying molecular tagging velocimetry to a turbulent bubbly flow in a vertical square duct, Hosokawa et al. [123] studied the effect of bubbles on the TKE budget and carried out a priori tests of closure assumptions of the standard and low Reynolds number $k - \varepsilon$ model. They found that the $k - \varepsilon$ model can reasonably predict the production rate of TKE but fails in evaluating the diffusion rate in the near wall region [6].

However, more detailed and complete information about the TKE budget can be obtained by DNS, where the governing equations are solved numerically on sufficiently fine grids so that every continuum length and time scales are fully resolved. In order to ensure that DNS results are of relevance for bubble columns, it is - for two reasons - essential to consider a computational domain with walls [6]. First, in triple periodic computational domains the possibility of occurrence of large-scale recirculating flow

structures that are typical for bubble columns is reduced [71]. Second, statistical quantities (i.e. all terms in the k_L equation) depend on the wall distance. DNS investigations of turbulent bubbly flow in a vertical channel were performed both for up-flow [124] and down-flow [125] by Lu & Tryggvason.

Ilić [26] performed DNS studies of laminar bubbly flow in a narrow vertical channel in rather viscous liquids (Morton number $M = g(\rho_L - \rho_L)\mu_L^4 / \rho_L^2\sigma^3 > 3 \cdot 10^{-6}$) and evaluated all terms in Eq. (34) for a single bubble [19] and a swarm consisting of eight bubbles [27]. The budget of k_L shows that, for the parameters investigated, a gain of k_L is mainly due to the interfacial term while the production by shear stresses is almost negligible. The interfacial term and the dissipation are not in local equilibrium. Therefore, the redistribution of k_L by diffusive transport is very important. Besides giving insight in the TKE budget, the DNS data are used for a priori testing of closure assumptions. For this purpose, the wall-normal profile of any closure term in Eq. (34) as evaluated from the DNS data is compared with the profile predicted by a model for this closure term, where all flow quantities entering into the model are taken by the respective profiles evaluated from the DNS data. In [27], it was found that all models yield a strong overestimation for the production by shear stresses, while for the turbulent diffusion all models used in engineering codes result in an underestimation. For the interfacial term, a large number of models have been analyzed and one promising model could be identified. However, all the other closure terms in the kinetic energy equation need further improvement for bubbly flows [6].

Most of the above references consider monodisperse flows. For polydisperse flows, literature indicates that bubble population balances cannot be applied in a satisfactory manner because of the inability of $k - \varepsilon$ models to predict the turbulent dissipation rate correctly, thus causing a large underestimation of bubble break-up rates [50, 59, 60]. To solve this issue, further developments of coalescence [126] and break-up kernels [127] seem to be required on the one hand, while on the other hand improved closure relations for k and ε are necessary for bubble-driven flows [6].

It is noted [6] that for closure of the two-phase source/sink term in the ε equation, it is common practice to relate it to the two-phase source/sink term in the k_L equation by means of a time scale – for which essentially four options exist, see [128]. Simulations with the MUSIG model clearly show that the kind of turbulence modeling affects sensitively the bubble coalescence and break-up so that different bubble size distributions are obtained for different turbulence models [129].

2.3.4. The k-ε type models

The Eulerian conservation equations for each phase may be averaged in various ways (i.e. time averaging, volume averaging, ensemble averaging). The result is known as the two-fluid model [23]. Because of the averaging, the Reynolds stress tensor $\overline{u'_{i,L} u'_{j,L}}$ appears in the averaged Navier-Stokes equation. It is an additional stress term due to turbulence (fluctuating velocities) [122]. The modelling of Reynolds stress term is of practical interest in bubbly flows.

In eddy viscosity turbulence models the Reynolds stresses are linked to the velocity gradients via the turbulent viscosity by using the Boussinesq [130] hypothesis [122]. The Reynolds stress in this concept is given by [26]

$$\overline{u'_{i,L} u'_{j,L}} = v_{L}^{t}\left(\nabla \overline{u}_{ij,L} + \nabla \overline{u}_{ij,L}^{T}\right) - \frac{2}{3}\mathbf{I}k_{L} \tag{37}$$

where v_{L}^{t} represents the turbulent viscosity of the liquid phase as it is given in Eq. (40), k_{L} is the liquid turbulence kinetic energy as given in Eq. (33), $\mathbf{I}$ denotes the unit tensor and superscript T indicates transposition.

Two-equation models formulate the stress term by solving two transport equations derived for the turbulence kinetic energy k and its dissipation ε [122]. The standard k-ε model from Launder and Spalding [121] and the mixture k-ε model from Behzadi et al. [131] are adopted in this study. The standard k-ε model [121, 132] is commonly applied and widely used by many authors, the transport equations are given in [23, 133, 134]. They modelled the turbulent stress-strain relation analogous to the constitutive relation of a viscous fluid based on the Boussinesq hypothesis [130]. In the frame of two-fluid modelling, the turbulent viscosity is related to the fluid's turbulence kinetic energy k and its dissipation rate ε, which are governed by their own transport equations [135]. The standard k-ε model approach has been developed originally for turbulence modeling in single-phase flows, and thus solely accounts for turbulence within the liquid phase [56]. This means the turbulence is dictated by the continuous phase. The presence of the dispersed phase is accounted for by the additional terms. Thus, only the transport equation for the continuous phase turbulence kinetic energy k_{L} needs to be solved while k_{G} is obtained directly from k_{L} via a response coefficient [131].

Such "standard" methods based on the k-ε model exclusively considering the turbulence within the liquid phase are then limited in application to dilute systems. As the gas holdup increases, the dominance of the continuous phase on turbulence diminishes, in the limit the turbulence of the dispersed phase becomes the sole factor

[131]. Thus, the turbulent fluctuations can no longer be assumed to be dominated by the liquid phase [56, 131, 135].

In Behzadi et al. [131] a mixture k-ε model is proposed where the disperse phase turbulence is algebraically related to that of the continuous phase through a turbulence response coefficient, C_t [6]. This turbulence model based on the k-ε equations for the mixture of the two phases, i.e. k_m and ε_m, is formulated in [131, 135]. The mixture k-ε model is suitable for computations at all phase fraction values and reverts to the single-phase form in the extreme limits of zero when only one or other of the phases is present. k_m and ε_m quantities are defined as follows

$$k_m = \left(\alpha_L \frac{\rho_L}{\rho_m} + \alpha_G \frac{\rho_G}{\rho_m} C_t^2 \right) k_L \tag{38}$$

$$\varepsilon_m = \left(\alpha_L \frac{\rho_L}{\rho_m} + \alpha_G \frac{\rho_G}{\rho_m} C_t^2 \right) \varepsilon_L \tag{39}$$

where $\rho_m = \alpha_L \rho_L + \alpha_G \rho_G$ is the mixture density and C_t is a turbulence response function representing the ratio of the dispersed to continuous phase fluctuations. The variation of C_t with phase fraction is determined from experimental data which suggest that as phase fraction increases beyond a certain limit, which could be as small as 6%, C_t approaches a constant value close to unity [131].

2.3.5. Turbulent viscosity

Many authors considered different approaches to evaluate the turbulent viscosity of liquid phase for two-fluid model calculations [20]. The effective viscosity v_L^{eff} is introduced here as a broad definition for the turbulent viscosity. For the k-ε two-equation model, in the basic approach [22, 25] the usual (turbulent) eddy viscosity [7] is evaluated as v_L^{eff} solely

$$v_L^{eff} = v_L^t = C_\mu \frac{k_L^2}{\varepsilon_L} \tag{40}$$

Here $C_\mu = 0.09$ is a constant and commonly adapted by many studies. ε_L represents the magnitude of the dissipation rate. The second approach accounts for the molecular viscosity of the liquid additional to the eddy viscosity [136, 137] as

$$v_L^{eff} = v_L^t + v_L^{mol} \tag{41}$$

Sato [114, 115] introduced an additional eddy viscosity due to bubble existence. The model of Sato [114, 115] v_L^b presents the perturbations induced by bubbles, namely BIT, taking account of "drift" phenomena of liquid due to liquid displacement by the

bubbles [13] and given as

$$v_L^b = 0.6\alpha_G d_B \left| u_{rel} \right| \tag{42}$$

Here u_{rel} is the mean relative velocity between phases, d_B is the equivalent bubble diameter α_G is the mean gas volumetric fraction. The approach which takes the model of Sato [114, 115] into consideration [24] is then as follows

$$v_L^{eff} = v_L^t + v_L^{mol} + v_L^b \tag{43}$$

For the mixture k-ε model [131] the effective viscosity is compromised from the mixture viscosities as:

$$v_m^{eff} = v_m^t + v_m^{mol} \tag{44}$$

Here, v_m^t is the mixture turbulent viscosity given as

$$v_m^t = \frac{\left(\alpha_L \mu_L^t + \alpha_G \mu_G^t C_t^2\right)}{\alpha_L \rho_L + \alpha_G \rho_G C_t^2} \tag{45}$$

where μ_G^t is given with the molecular viscosity as

$$\mu_G^t = C_t^2 \left(\frac{v_L^{mol}}{v_G^{mol}} \frac{\rho_G}{\rho_L} \right) \mu_L^t \tag{46}$$

2.4. DNS methodology

This Section introduces the mathematical formulation and the solution strategy for direct numerical simulations in this study.

2.4.1. Governing equations

The locally volume-averaged conservation equations for mass and momentum describing the flow of two immiscible incompressible Newtonian fluids with constant material properties (density, viscosity and surface tension) are given in the non-dimensional form as follows [43, 46]:

Zero divergence condition for center-of-mass velocity:

$$\nabla \cdot \mathbf{v}_m^* = 0 \tag{47}$$

The advection equation for liquid volumetric fraction f within a mesh cell to account for the phase-interface evolution:

$$\frac{\partial f}{\partial \theta} + \nabla \cdot f \mathbf{v}_m^* = 0 \tag{48}$$

The non-dimensional Navier-Stokes equation in single field formulation with surface tension term with constant physical properties (density, viscosity and surface tension):

$$\frac{\partial(\rho_m^* \mathbf{v}_m^*)}{\partial \theta} + \nabla \cdot \left(\rho_m^* \mathbf{v}_m^* \mathbf{v}_m^*\right) = -\nabla P^* + Re_{ref}^{-1}\nabla \cdot \left[\mu_m^*\left(\nabla \mathbf{v}_m^* + \left(\nabla \mathbf{v}_m^*\right)^T\right)\right]$$
$$-(1-f)E\ddot{o}_{ref}We_{ref}^{-1}\hat{\mathbf{e}}_g + Fr_{ref}\hat{\mathbf{e}}_g + \frac{Eu_{ref}}{L_{axial}^*}\hat{\mathbf{e}}_{axial} + We_{ref}^{-1}A_i^*\kappa^*\hat{\mathbf{n}}_i \tag{49}$$

Here, θ is the is the non-dimensional time, A_i^* the non-dimensional interfacial area concentration, κ^* is the non-dimensional interface curvature, $\hat{\mathbf{n}}_i$ is the unit normal vector to interface pointing from gas into liquid. The last term in Eq. (49) expresses the contribution of the surface tension force. P^* is the dimensionless "reduced pressure" [43, 46] which is related to the dimensional physical pressure p and defined to allow for the use of periodic boundary conditions. L_{axial}^* is the non-dimensional axial length of the computational domain, $\hat{\mathbf{e}}_{axial}$ is the unit normal vector in axial direction. The buoyancy force in Eq. (49) is represented by terms which involve the unit vector in direction of gravity $\hat{\mathbf{e}}_g$. It appears together with the gravity vector $\mathbf{g} = g\hat{\mathbf{e}}_g$ where the gravity g = 9.81 m/s². The non-dimensional mixture density ρ_m^*, the non-dimensional mixture viscosity μ_m^* and the non-dimensional center-of-mass velocity $\mathbf{v}_m^*$ are given by

$$\rho_m^* \equiv \frac{f\rho_L + (1-f)\rho_G}{\rho_L} \tag{50}$$

$$\mu_m^* \equiv \frac{f\mu_L + (1-f)\mu_G}{\mu_L} \tag{51}$$

$$\mathbf{v}_m^* \equiv \frac{1}{U_{ref}}\frac{f\rho_L\mathbf{v}_L + (1-f)\rho_G\mathbf{v}_G}{f\rho_L + (1-f)\rho_G} \tag{52}$$

Here, $\mathbf{v}_L$ and $\mathbf{v}_G$ represent the mean liquid and gas velocity within the mesh cell, obtained by volume averaging over the region occupied by the respective phase.

The non-dimensional numbers are defined based on reference scales L_{ref} and U_{ref}. The definitions of the reference Reynolds number (Re_{ref}), reference Eötvös number ($E\ddot{o}_{ref}$), reference Weber number (We_{ref}), reference Froude number (Fr_{ref}) and reference Euler number (Eu_{ref}) are

$$Re_{ref} = \frac{\rho_L L_{ref} U_{ref}}{\mu_L} \tag{53}$$

$$E\ddot{o}_{ref} \equiv \frac{(\rho_L - \rho_G)g\ L_{ref}^2}{\sigma} \tag{54}$$

$$We_{\mathrm{ref}} = \frac{\rho_{\mathrm{L}} L_{\mathrm{ref}} U_{\mathrm{ref}}^2}{\sigma} \tag{55}$$

$$Fr_{\mathrm{ref}} = \frac{g\ L_{\mathrm{ref}}}{U_{\mathrm{ref}}^2} \tag{56}$$

$$Eu_{\mathrm{ref}} = \frac{\bar{p}_0 - \bar{p}_{L_{\mathrm{axial}}}}{\rho_{\mathrm{L}} U_{\mathrm{ref}}^2} \tag{57}$$

2.4.2. Numerical method

The flow considered for the DNS in this work involves two immiscible fluids that are separated by a phase interface. The description of the temporal and spatial evaluation of the phase interface is performed by using the Volume of Fluid method (VOF). In VOF method [138] a local volume fraction f represents one of the phases and the interface position is captured by introducing this volume fraction. For a certain instant in time, $f = 1$ for mesh cells entirely filled with liquid, $f = 0$ for mesh cells entirely filled with gas, and $0 < f < 1$ for mesh cells that contain both phases. Wörner [47] presents a comprehensive review of numerical methods and models for interface resolving simulations of multiphase flows, including the VOF method and the solution strategy applied in this study.

VOF methods can be divided into two groups based on the interface evolution approaches [47]: Interface-Reconstruction (IR) VOF [139] where the interface thickness is zero (sharp interface) and Color-Function (CF) VOF [140] where the interface is finite (diffusive interface). CF-VOF method relies on a smooth color function that is an approximation of the f function in classical IR-VOF method. The color function equation is solved by a difference scheme that yields smeared interface. Instead, in IR-VOF method, the f-equation is solved in an advection step where the flux of f across the faces of any interface mesh cell is calculated in a geometrical manner that yields a sharp interface. In principle, an inherent volume (and mass) conservation is secured by the IR-VOF method, since all volume fluxes across mesh cell faces in the entire computational domain are supposed to sum up to zero [47]. The IR-VOF method is used to describe the phase distribution in this study.

Advection schemes applied in the IR-VOF method can be classified in two different categories [139]: operator split schemes and multidimensional (unsplit) schemes [47]. The split method consists of a sequence of one-dimensional advection steps. In an unsplit method [141], which is of interest in this work, only one reconstruction step and one advection step per time step is used [47]. State-of-the-art method for interface reconstruction is the Piecewise Linear Interface Calculation

(PLIC) method [139, 140] where in any mesh cell with $0 < f < 1$ the interface is approximated by a line (in 2D) or a plane (in 3D) [47]. An example for 2D interface approximation is exhibited in Fig. 5 a). In 3D, the location and orientation of the plane representing the interface inside each mesh cell is reconstructed from the discrete distribution of the volumetric fraction f of the continuous fluid. After the first step, the surface integrals can then be evaluated in the advection step, which is illustrated for a 2D case in Fig. 5 b). In the advection step, the flux of the liquid phase crosses through the mesh cell face (the right-hand face of a cell) within a time step Δt and the total flux of fluid is evaluated by $u.\Delta t$, where u is the velocity component normal to the mesh cell face [47, 138]. If the interface is approximated by a plane (in 3D) then the volume fluxes of the liquid phase per unit cross sectional area are taken into account.

a)   b)
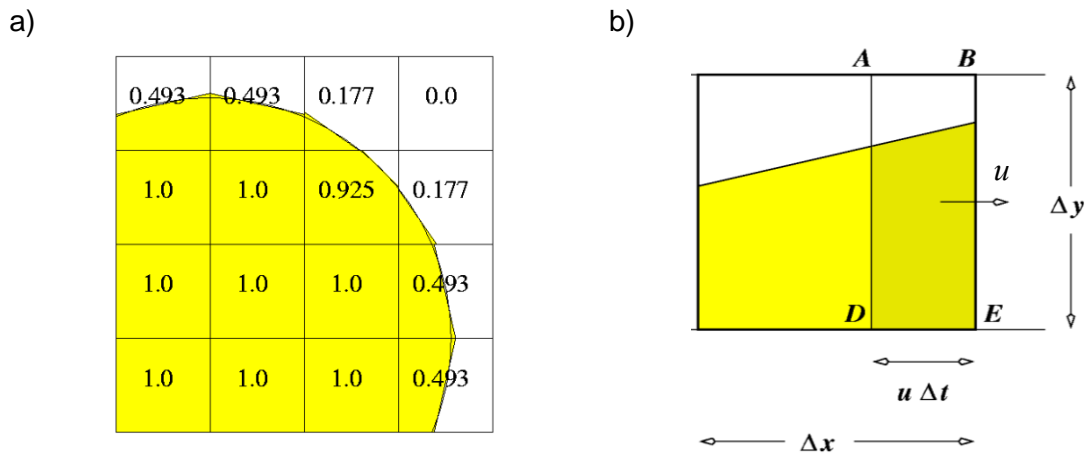
Fig. 5:   a) Interface approximation with PLIC, b) Geometric flux evaluation (advection step) in interface reconstruction based volume-of-fluid method (Figures are provided by Dr. Martin Wörner, KIT).

2.4.3. Numerical code: TURBIT-VOF

The direct numerical simulations (DNS) are performed with the in-house computer code TURBIT-VOF developed at the Karlsruhe Institute of Technology (KIT) [40, 41]. TURBIT-VOF solves the locally volume-averaged Navier-Stokes equations with surface tension term in a so-called single-field-formulation for two incompressible immiscible Newtonian fluids on a Cartesian grid via a finite volume method under assumption of constant fluid properties (i.e. density, viscosity, surface tension). The single-field formulation accounts for the proper momentum jump conditions across the gas liquid interface. The equations in Section 2.4.1 are implemented in TURBIT-VOF. The solution strategy for the momentum equation Eq.(49) and the continuity condition Eq.(47) is based on a projection method, by which a divergence free velocity field is

ensured at the end of each time step. Time integration of the momentum equation Eq.(49) is performed by an explicit third order Runge–Kutta method, where all derivatives in space (spatial derivatives) are approximated by second order central differences schemes. Discretization in space is based on a finite volume method, where a regular Cartesian staggered grid is used.

The IR-VOF method (cf. Section 2.4.1) is used for computing the evolution of the deformable interface, which separates the two immiscible fluids. In the VOF method, the liquid volumetric fraction f is advected by using the transport equation Eq.(48), which governs the temporal and spatial evolution of the phase distribution for f [46]. Eq.(48) is solved in a geometrical manner based on the unsplit advection method (cf. Section 2.4.1) in two steps. At first, the (infinitely thin) phase interface is locally approximated by a PLIC plane in each mesh cell that instantaneously contains the components of both phases. The location and orientation of this plane is determined and reconstructed by an in-house PLIC algorithm called EPIRA [40]. On a 3D structured orthogonal fixed grid, it reconstructs a planar interface of any orientation exactly (therefore its name stands for Exact Plane Interface Reconstruction Algorithm) [142]. In the second step, fluxes of the liquid are geometrically evaluated over all faces of the mesh cells (cf. Section 2.4.1). Further details on TURBIT-VOF can be found in [40-43, 142, 143]. The code has been applied for the DNS of bubbly flows in different configurations of small channels [27, 43, 45, 46, 144-150], validated with other codes [44] and experiments [142] and also used for analyzing the bubble induced turbulence [5, 19, 20, 73].

2.4.4. Statistical evaluation of DNS data

The statistical evaluation of the k_{L}-equation requires appropriate averaging of the instantaneous flow field within the computational domain. The averaging procedure applied for the statistical analysis of DNS results in the frame of this study have been explained in Erdogan and Wörner [5]. For the bubbly flow between vertical parallel plates, the vertical and span-wise directions can be considered as homogeneous, which allows the spatial averaging over vertical slabs of mesh cells parallel to the channel walls [20, 26]. This yields profiles of statistical quantities, which depend on the wall-normal coordinate z. In addition, the data over different instants in time within the statistically steady regime is also averaged. The respective plane and time averaging is denoted by a double overbar [5].

For the evaluation of the closure terms in Ilic [26], the local instantaneous data for phase distribution, velocity field and pressure field are averaged over wall-normal

planes and additionally in time. By this averaging procedure, the wall-normal profile of the budget of k_{L} is obtained; it indicates the relative importance of the various terms in Eq. (34) [6].

The DNS data of the bubble swarm simulations are averaged to evaluate all terms on the right hand side in Eq. (34). For the present set-up, since the vertical and span-wise directions can be considered as homogeneous, and analogous to [20, 26], the averaging of DNS data of one time step takes place over all mesh cells on vertical planes with identical wall distance parallel to the side walls.

$$\overline{\varphi}_{\mathrm{L};k} = \frac{1}{N_x N_y} \sum_{i=1}^{N_x} \sum_{j=1}^{N_y} f_{i,j,k} \varphi_{\mathrm{L};i,j,k} \qquad \overline{\overline{\varphi}}_{\mathrm{L};k} = \frac{\displaystyle\sum_{i=1}^{N_x} \sum_{j=1}^{N_y} f_{i,j,k} \varphi_{\mathrm{L};i,j,k}}{\displaystyle\sum_{i=1}^{N_x} \sum_{j=1}^{N_y} f_{i,j,k}} \tag{58}$$

where $f_{i,j,k}$ and $\varphi_{i,j,k}$ are the liquid volume fraction and the averaged physical quantity in the mesh cell (i, j, k). This spatial averaging yields one-dimensional wall-normal profiles. These are additionally averaged over different instants in time where the DNS is statistically steady.

2.5. Two-fluid model methodology

The k-ε approach of two-fluid modelling is the most adequate method for CFD simulations of the bubbly flow in the bubble columns examined in this work (cf. Section 1.3). The k-ε type models are discussed in Section 2.3. The current Section gives an overview on the governing equations of two-fluid model and the numerical methodology in CFD software OpenFOAM® where the two-fluid simulations are performed. The closure relations for the terms interfacial momentum transfer and turbulence effects (including bubble induced turbulence) in Eulerian conservation equation are presented here.

2.5.1. Governing equations

In the two-fluid model, both phases are described using Eulerian conservation equations. Hence, the model is also referred to as the Euler-Euler model [135]. The capability of two-fluid model method to apply a quite rough spatial resolution of the flow domain benefits for numerical simulation of flows even in large scale reactors for relatively low computational costs [56]. Each phase is considered as interacting and interpenetrating continua [56] and represented by averaged conservation equations [135]. So-called interpenetrating field equations which are valid in the entire domain

are obtained by the averaging procedure [10, 12, 47, 151]. In the framework of a two-fluid model, for incompressible two-phase flow without phase change, the following conservation equations have to be solved [56, 152, 153]:

$$\frac{\partial \alpha_\varphi}{\partial t} + \nabla \cdot \left(\alpha_\varphi \bar{\mathbf{u}}_\varphi \right) = 0 \tag{59}$$

$$\frac{\partial \alpha_\varphi \bar{\mathbf{u}}_\varphi}{\partial t} + \nabla \cdot \left(\alpha_\varphi \bar{\mathbf{u}}_\varphi \bar{\mathbf{u}}_\varphi \right) + \nabla \cdot \left(\alpha_\varphi \bar{\mathbf{R}}_\varphi^{\text{eff}} \right) = -\frac{\alpha_\varphi}{\bar{\rho}_\varphi} \nabla \bar{p} + \alpha_\varphi \mathbf{g} + \frac{\sum \mathbf{F}_\varphi}{\bar{\rho}_\varphi} \tag{60}$$

Here, α_φ is the volumetric phase fraction and $\bar{\mathbf{u}}_\varphi$ denotes the (averaged) velocity of a phase, which has the density $\bar{\rho}_\varphi$. $\bar{\mathbf{R}}_\varphi^{\text{eff}}$ is the (averaged) effective Reynolds stress tensor and the term $\sum \mathbf{F}_\varphi$ represents the sum of all interfacial forces [56] (cf. Section 2.5.2). The averaging process introduces the phase fraction α_φ into the equation set, which is defined as the probability that a certain phase is present at a certain point in space and time [135, 154].

The applied averaging procedure is based on a single averaging process (the conditional averaging) [154], whereby the effects of the discontinuities and the turbulence are treated at the same time and the derivation of the conservation equation is easier. As a consequence of averaging, some detailed information about the local flow conditions disappear while some additional terms ($\sum \mathbf{F}_\varphi$, $\bar{\mathbf{R}}_\varphi^{\text{eff}}$) appear in the momentum equation Eq.(60) for each phase. Thus, an additional modeling of closure terms is required in order to fully describe a two-phase flow [56]. These extra terms are the interfacial momentum transfer terms $\sum \mathbf{F}_\varphi$ (cf. Section 2.5.2) and the effective Reynolds stresses $\bar{\mathbf{R}}_\varphi^{\text{eff}}$ which represents turbulence effect (cf. Section 2.5.3). Closure relations for bubble-induced turbulence are typically described as extensions of turbulence modeling approaches (cf. Section 2.5.3).

2.5.2. Interfacial forces

The term $\sum \mathbf{F}_\varphi$ is known as the averaged interfacial momentum transfer term and accounts for the average effect of the forces acting at the interface between continuous and dispersed phase due to their relative motion [135]. These terms are not directly related to turbulence, although they may be affected by it [154]. The modelling of these terms are discussed in [153, 154] in detail. Marschall et al. [56] present an overview on the main models in the literature. In this section, the models related to the E-E simulations in the course of this study are summarized.

Interfacial interaction can be explained in two categories as drag force and non-drag forces. For bubbly flows the non-drag forces basically encompass the lateral lift

force $\mathbf{F}_L$, the turbulent dispersion force $\mathbf{F}_{TD}$, and the virtual mass force $\mathbf{F}_{VM}$ and the closure term results [56] in

$$\sum \overline{\mathbf{F}}_\varphi = \overline{\mathbf{F}}_D + \overline{\mathbf{F}}_L + \overline{\mathbf{F}}_{VM} + \overline{\mathbf{F}}_{TD} \tag{61}$$

a) Drag force

In a two-fluid model the drag force $\overline{\mathbf{F}}_D$ is given as [56]

$$\overline{\mathbf{F}}_D = \frac{3}{4} C_D \frac{\alpha_G \rho_L}{d_B} |\overline{\mathbf{u}}_L - \overline{\mathbf{u}}_G| (\overline{\mathbf{u}}_L - \overline{\mathbf{u}}_G) \tag{62}$$

There are various models in literature for the modeling of the drag coefficient C_D. Clift et al. [75] list the equations that have been proposed to approximate C_D. Among them, the Schiller-Naumann drag coefficient [101] is considered as the closest correlation to the standard drag curve. It accounts for small spherical bubbles at low bubble Reynolds numbers $Re_B \leq 1000$ and given as

$$C_D = \frac{24}{Re_B} \left(1 + 0.15 Re_B^{0.687} \right) \tag{63}$$

However, none of these correlations appears to consider all available data.

Tomiyama et al. [102] developed a drag coefficient model for single bubbles by using a balance of forces acting on a bubble and available theoretical and empirical correlations of terminal rising velocity. This model covers a wide range of fluid properties, gravity and bubble diameter as well as the contamination of the liquid phase. The first term represents the standard drag curve for pure systems and Schiller-Naumann model for the contaminated systems. The second term stands for potential flow for spherical fluid particles and the third term is valid for deformed and spherical cap bubbles. It is given for pure, slightly contaminated and contaminated gas-liquid systems by the following formulations:

For a pure system (e.g. pure water and air bubbles):

$$C_D = \max \left\{ \min \left[\frac{16}{Re} \left(1 + 0.15 Re^{0.687} \right), \frac{48}{Re} \right], \frac{8}{3} \frac{E\ddot{o}}{E\ddot{o} + 4} \right\} \tag{64}$$

For a slightly contaminated system (e.g. air bubbles in tap water):

$$C_D = \max \left\{ \min \left[\frac{24}{Re} \left(1 + 0.15 Re^{0.687} \right), \frac{72}{Re} \right], \frac{8}{3} \frac{E\ddot{o}}{E\ddot{o} + 4} \right\} \tag{65}$$

For a contaminated system (e.g. high concentration of tracers in liquid):

$$c_{\mathrm{D}} = \max\left\{ \frac{24}{Re}\left(1+0.15Re^{0.687}\right), \frac{8}{3}\frac{E\ddot{o}}{E\ddot{o}+4} \right\} \tag{66}$$

b) Non-Drag Forces

The performance of a two-fluid CFD study significantly depends on the underlying closure models. As a consequence of the averaging procedure, the flow structure and topology is not explicitly resolved, thus, additional modeling of closure terms is required in order to fully describe a two-phase flow and subsequently solve a corresponding two-fluid model [56].

Lateral Lift Force ($\overline{\mathbf{F}}_{\mathrm{L}}$):

For bubbly flows this is the most important non-drag force, since the lateral lift force acts perpendicularly to the drag force [56] and is given as

$$\overline{\mathbf{F}}_{\mathrm{L}} = \alpha_{\mathrm{G}}\rho_{\mathrm{L}}C_{\mathrm{Lift}}\left(\overline{\mathbf{u}}_{\mathrm{L}} - \overline{\mathbf{u}}_{\mathrm{G}}\right)\times\nabla\times\overline{\mathbf{u}}_{\mathrm{L}} \tag{67}$$

Two approaches from Tomiyama [155] and Legendre and Magnaudet [156] are widely used for calculating the lift coefficient. In Tomiyama's correlation, C_{Lift} takes a negative value for large bubbles. Consequently, those bubbles move toward the centerline, while smaller bubbles move toward the wall of a bubble column. It is also noted that this correlation should be applied with care when considering systems different from air / water [56, 157]. On the other hand, the correlation of Legendre and Magnaudet is derived by numerically solving the Navier-Stokes equations assuming a smooth and pure bubble surface where no particle rotation was induced and is valid for $0.1 \leq Re \leq 500$ [56], which corresponds to the cases in this study where BIT is dominating the flow. Therefore, the correlation from Legendre and Magnaudet is used for the E-E simulations in this work.

Turbulent Dispersion Force ($\overline{\mathbf{F}}_{\mathrm{TD}}$):

The turbulent dispersion force accounts for turbulent fluctuations in the flow field acting on the fluid particles. The corresponding dispersion coefficient is assumed constant, taking a value between 0.1 and 1.0 [56]. In the course of this study, a constant value of 0.5 is set based on internal discussions and experience of OpenFOAM® users.

Virtual Mass Force ($\overline{\mathbf{F}}_{\mathrm{VM}}$):

The virtual mass force accounts for the effect that accelerating particles always entrain a certain amount of surrounding fluid. For spherical single bubbles, it reads a constant

value of 0.5 [56]. It must also be defined although the effective influence of the virtual mass force coefficient in bubbly flows is rather small [14].

Wall Lubrication Force:

This force has first been introduced by Antal et al. [158] in order to take into account the repulsive force between bubbles and the pipe wall in a bubbly pipe flow [159]. However, in their numerical investigation for turbulent bubbly flow, Hosokawa and Tomiyama [159] found that though the wall force tends to shift the void peak toward the pipe center, the predictions without the wall force are better than those with the wall force. In their simulations for the bubble columns with OpenFOAM®, Marschall et al. [56] neglected the wall lubrication force since models are subject to various restrictions and constraints. In this study, the two-fluid simulations are also performed without consideration of the wall lubrication force.

2.5.3. Turbulence models

The two-fluid model requires closure relations for the effective Reynolds stresses $\bar{\mathbf{R}}_\varphi^{\text{eff}}$, which relate to the effects of velocity fluctuations on the mean transport of the phases. The velocity fluctuations arise from single-phase turbulent fluctuations (shear induced – true – turbulence) and other two-phase flow factors that induce turbulence. For a two-phase flow in a bubble column, as in this study, the latter factors involve the fluctuations induced by the bubbles (bubble induced – pseudo – turbulence, BIT) which is the main source of the turbulence. The unknown terms need to be modeled in terms of known quantities to obtain a closed equation set.

$\bar{\mathbf{R}}_\varphi^{\text{eff}}$ term in the momentum equation contains the phase viscous stress tensor (laminar stress term) and the phase Reynolds stress ($\bar{\mathbf{R}}_\varphi$). The Reynolds stresses for the gas phase are small in comparison with the pressure gradient and the interfacial forces, so they can be neglected [23]. Hence, the Reynolds stresses correspond to the liquid phase and given as $\overline{u'_{i,\text{L}} u'_{j,\text{L}}}$. The closure of this term represents the turbulence closure. The Reynolds stress term is related to the gradient of mean velocity through a turbulent (eddy) viscosity [133]. The laminar stress term on the other hand is proportional to the molecular viscosity ($v_{\text{L}}^{\text{mol}}$) of the liquid. From the definition of effective Reynolds stresses, the effective viscosity of the continuous phase $v_{\text{L}}^{\text{eff}}$ is then calculated from $v_{\text{L}}^{\text{eff}} = v_{\text{L}}^{\text{t}} + v_{\text{L}}^{\text{mol}}$. For the purpose of this study, the Reynolds stresses are modelled by means of k-ε type models [152]. The adopted models are the standard k-ε model from Launder and Spalding [121] and the mixture k-ε model from Behzadi et al. [131] (cf. Section 2.3.4).

The BIT term is significant for the estimation of turbulence quantities [62]. The k - ε models are extended with an interfacial term to incorporate the effects of the dispersed phase on the turbulence. The modelling of BIT is one of the cornerstones in this study. The model approaches for the interfacial term are investigated in detail by means of a-priori-testing (cf. Chapter 4) and the identified suitable models are then tested in the two-fluid model computations (cf. Chapter 5).

2.5.4. Numerical methodology

The two-fluid model computations in this work are performed with the Open Source CFD software OpenFOAM® (Open Field Operation and Manipulation; registered trademark from OpenCFD Limited, www.opencfd.co.uk) [160-162]. OpenFOAM® is a C++ library, providing numerous numerical algorithms, methods, and solvers for solving continuum mechanics problems in the field of chemical and process engineering [157]. The developers of the code explain in Weller et al. [160] that their intention was to make it as easy as possible to develop reliable and efficient computational continuum-mechanics codes. They applied various object-orientation techniques to allow mimicking data types and operators [160]. The types and associated operations that are part of the verbal and mathematical languages used in science and engineering are declared by using the object-oriented mechanism (classes) and the solver applications are written using these classes [163]. An extensive portfolio of solvers are available for a wide range of physical processes such as turbulence, multiphase flows, heat transfer, combustion, molecular dynamics, solid mechanics, electromagnetics and acoustics [164]. The conservation equations are discretized using the finite-volume method [165, 166] on unstructured meshes [135]. A mesh of arbitrary polyhedral cells in 3-D, bounded by arbitrary polygonal faces (*polyMesh*) is defined by default [163]. The system of algebraic equations obtained from the discretization is solved using an iterative solver [166]. OpenFOAM® does not have a generic solver applicable to all cases. Instead, users must choose a specific solver for a class of problems to solve [167]. For more details about the code and the numerical methodology please see the following studies [135, 153, 166, 168].

OpenFOAM® can be considered as a flexible and efficient development platform for a variety of continuum models in the field of reactor design [157]. In this dissertation, the two-fluid simulations in a bubble column are performed with the development line of OpenFOAM® (OpenFOAM-dev). The top-level solver *twoPhaseEulerFoam* is used in this study. Some authors [169-171] proved the capability of the solver for studying bubbly flows. The algorithm of *twoPhaseEulerFoam* is an extension of the solver

bubbleFoam, which was developed for bubble flow. The solution algorithm is explained in Rusche [135].

The twoPhaseEulerFoam solves the conservation equations of a two-phase flow using the conditional averaging procedure [154]. The resulting averaged equations are given in Eqs.(59) and (60). The conditional averaging is described in Hill [154] and has been modified and applied by Weller [152] into the algorithm of OpenFOAM®. The unstructured *polyMesh* is used for discretization of the averaged conservation equations. The hybrid PIMPLE algorithm [163] is employed for pressure-velocity coupling. The solver composes a set of classes from the OpenFOAM® library to model the interfacial forces ($\sum \mathbf{F}_{\varphi}$) and the stress tensor ($\bar{\mathbf{R}}_{\varphi}^{\text{eff}}$) in Eq. (60). Several models for $\sum \mathbf{F}_{\varphi}$ have already been implemented to the solver, many of them in the frame of the study of Otromke [172] in Evonik Industries. The models used in this study are given in Section 5.1.4. For the closure of $\bar{\mathbf{R}}_{\varphi}^{\text{eff}}$, the $k\text{-}\varepsilon$ type models are employed from the OpenFOAM® library. For the influence of the turbulence induced by bubbles, two models for the interfacial term are utilized (cf. Section 5.1.4), one of those models is implemented based on the mixture $k\text{-}\varepsilon$ model in the framework of Euler-Euler simulations within this study.

In the course of the Multi-Phase Project, as a part of agreement between the OpenCFD Ltd (and later CFD Direct Ltd) and Evonik Industries, the test simulation results have been shared with OpenFOAM® developers and during this research the solver was improved, and a more stable version was provided.

3. Numerical investigation based on DNS

For the analysis of the transport equation for the liquid phase turbulence kinetic energy in Eq. (34), the DNS data must be obtained through bubble swarm simulations. To this end, this Chapter is divided into five sections:

Section 3.1 is dedicated to a brief explanation of computational setup.

Section 3.2 explains the cases used for single bubble simulations.

Section 3.3 discusses the results of the single bubble simulations by means of the influence of numerical aspects and physical effects. In this dissertation, initially the DNS study of Ilic [26] on BIT in mono-disperse bubble swarms is extended on lower values of the Morton number. Besides the influence of the Eötvös number and gas hold-up on the k_L equation and closure relations for the interfacial term is investigated. The preliminary studies examine the influence of those non-dimensional numbers as well as different related physical (density and viscosity ratio) and numerical parameters (grid resolution, domain size, time step width).

Section 3.4 further discusses the results of the single bubble simulations and focuses on comparison of the results with the correlations from the literature as well as the reference experimental data and the simulations with another code provided in the frame of the Multi-Phase project. In this part, the results are analyzed in terms of the terminal velocity of a rising bubble, which is a fundamental topic that regulates a rising bubble in the liquid. The surfactant factor that contributes to hydrodynamics of a rising bubble and the drag coefficient that is an important phenomenon for modelling are discussed. The last part of this part presents the numerical results in comparison to the reference experiments and the simulations based on an algebraic VOF method from the project partner.

Section 3.5 at last presents the bubble swarm simulations. The results are discussed in terms of common issues for DNS of bubble swarms. The simulation cases and the drag models to be used for the analysis of turbulence kinetic energy are identified in this part. The method for duplication of computational domain is also introduced here.

3.1. Computational setup

The cubic computational domain represents a sub-region of a flat bubble column (see Fig. 6). In vertical (x) and span-wise (y) direction, periodic boundary conditions are specified whereas in z-direction the domain is bounded by two vertical sidewalls

(distance $L_z = L_{wall} = L_{ref}$) with no-slip condition. The length scales are normalized by a reference length L_{ref}. Thus, the size of the computational domain is given in relation to $L_z = L_{ref}$, i.e. in the form $L_x / L_{ref} \times L_y / L_{ref} \times 1$. The no-slip side walls are placed at $z = 0$ and $z = 1$. The wall distance is about 4 to 6 bubble diameters (which is of the order of millimeters). The liquid and gas are initially at rest. The bubbles rise due to buoyancy in the center of the channel, whereas near the sidewalls a downward liquid flow occurs. The velocity scales are normalized by a reference velocity U_{ref}. The reference velocity is taken as 0.1 m/s for the simulations in this work. The resulting time scale is $t_{ref} = L_{ref} / U_{ref}$.
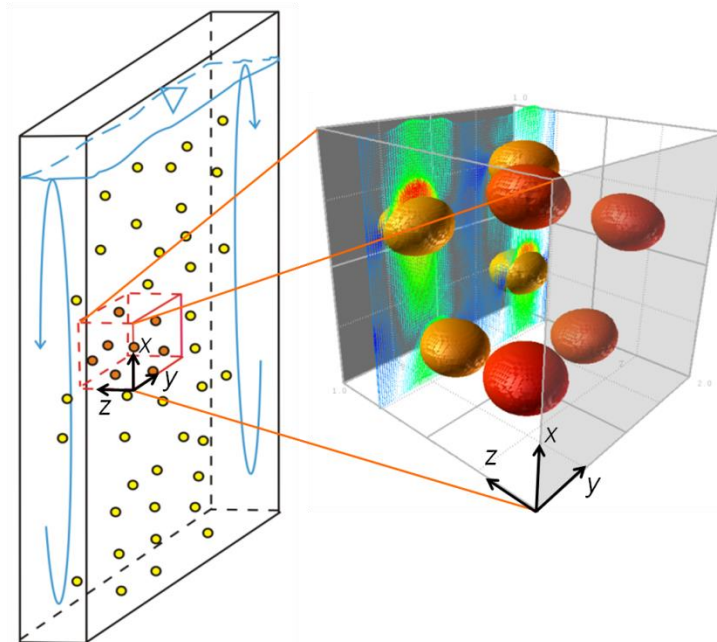

Fig. 6:   Sketch of a flat bubble column and a sub-region representing the computational domain (with no-slip conditions at the two lateral side walls and periodic boundary conditions in vertical (*x*) and span-wise (*y*) direction). Taken from Wörner and Erdogan [6].

The simulations are performed with TURBIT-VOF (cf. Section 2.4.3), which accounts for the dimensions $L_x \times L_y \times L_z$ in non-dimensional form. The grid is equidistant in vertical (*x*) and span-wise (*y*) direction and optionally equidistant or not in wall (*z*) direction. The number of mesh cells is calculated by $N_{cell} = N_x \times N_y \times N_z$. By a non-equidistant grid, it is easier to ensure that the liquid film between the bubble and the wall is well resolved. Due to the downward liquid flow near the sidewalls, the lift force acts away from the wall; this avoids an unwanted contact of bubbles with the walls during the simulation [5]. The equidistant grid is mainly considered for the preliminary studies of bubble swarm simulations. For statistical analysis with the

purpose of model improvement scenarios, the non-equidistant grid is also applied.

Fig. 7 presents two sketches of the numerical set-up for single bubble simulations. On the left side, it is a cubic domain bounded in z-direction by two lateral no-slip walls and periodic boundary conditions apply in vertical (x) and span-wise (y) directions. This set-up with two parallel walls is mainly used as the numerical set-up in this work. The cubic domain represented on the right side of Fig. 7 is bounded in z and y directions by lateral no-slip walls and periodic boundary conditions apply only in vertical (x) direction. This second set-up is used to understand the walls effects and for the code validation (cf. Section 3.4.4).
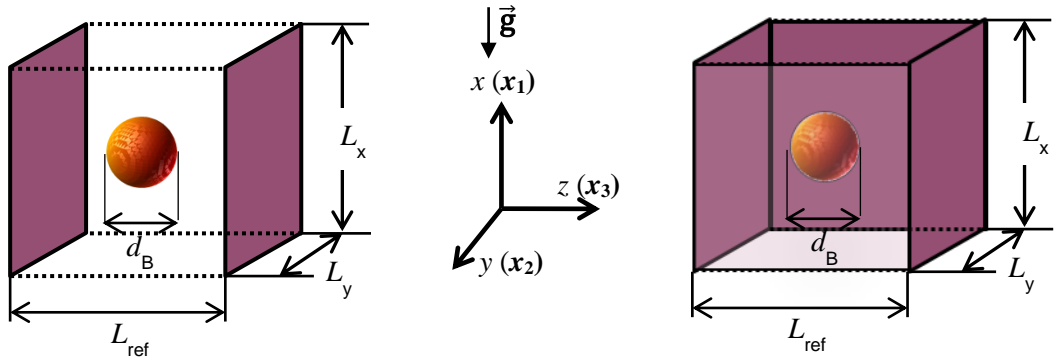
Fig. 7:   The numerical set-up for single bubble simulations. The rising bubble between parallel walls (p.b.c in x (x_1) and y (x_2) direction) (left) and in a rectangular domain (p.b.c in x (x_1) direction) (right).

In this study, the initial bubble shape is always considered as spherical on the DNS simulations. The cluster of bubble arrays are thought out with different variations and utilized based on the study of Ilic [26]. The initial clustering of bubble arrays for a case with 6 bubbles at t = 0 in a 1 × 1 × 1 computational domain represented in Fig. 8 as an example. This six bubble placement is applied for the cases where d_B / L_{wall} = 1 / 5 and gas content in the domain ε_G = 2.5% from Table 15 in the Appendix A.1, among others for example Case No.6, Case A4, B-M7 and B-M8 which are examined in Section 3.4.5.
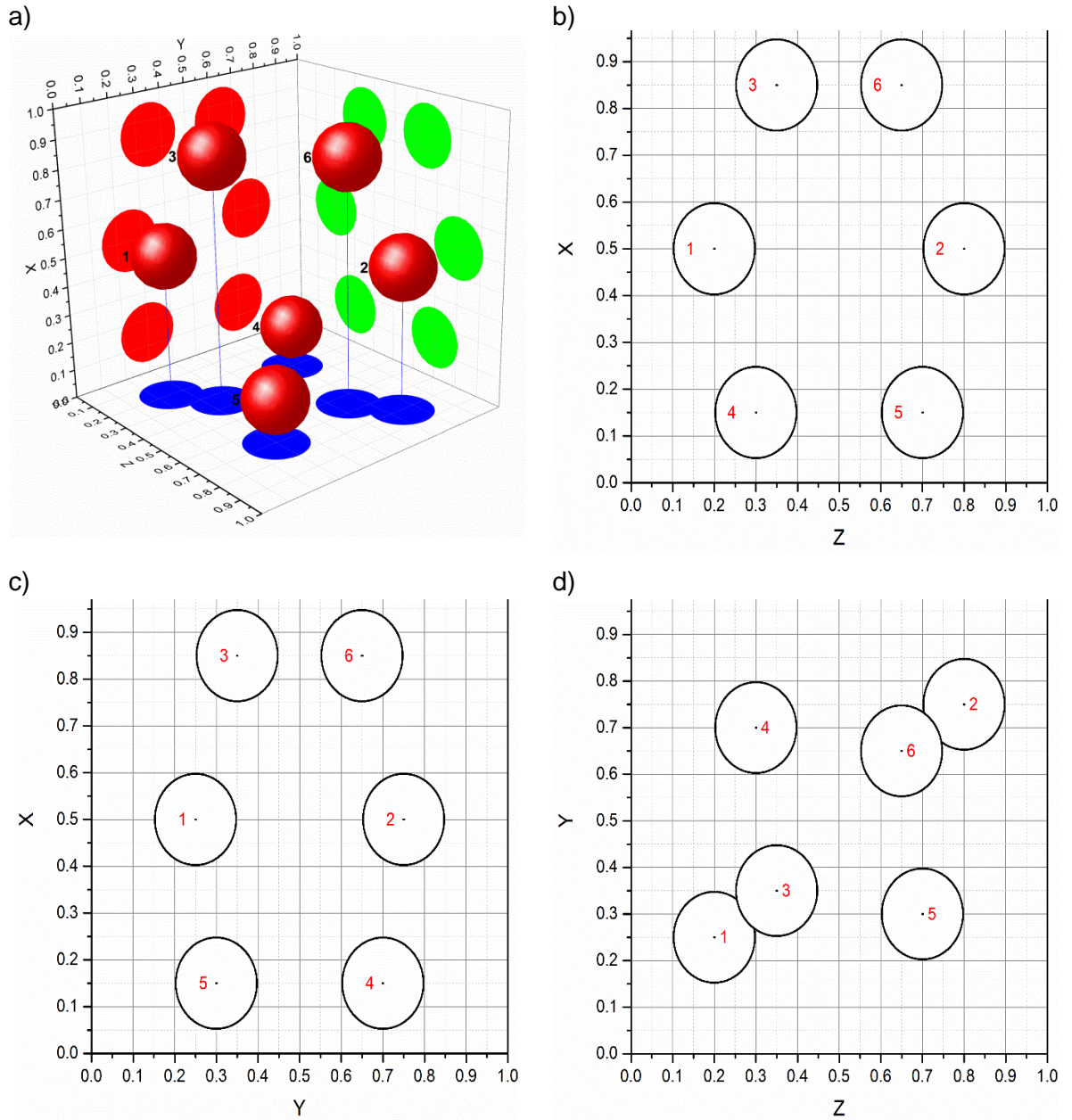
Fig. 8: A representation of initial clustering of bubble arrays for a case with 6 bubbles at $t = 0$ in a 1 × 1 × 1 computational domain. $d_B / L_{wall} \approx 1/5$ (X is flow direction; Z is wall direction). a) 3D view with projection of bubbles b) The view between two walls c) The view looking through the walls d) The view from above

3.2. Simulation cases for single bubble simulations

The direct numerical simulations of the single bubbles are performed for a wide range of physical and numerical parameters. The simulations are conducted for the gas to liquid viscosity ratio $0.02 \leq \Gamma_\mu \leq 1$, the gas to liquid density ratio $0.00167 \leq \Gamma_\rho \leq 0.04$, bubble Eötvös number $0.253 \leq E\ddot{o} \leq 2.539$, Morton number $2.2 \times 10^{-10} \leq M \leq 3.86 \times 10^{-7}$ and Reynold number $50 \leq Re \leq 187$. The ratio of bubble diameter to channel

size is in the range of $0.167 \leq d_B / L_{wall} \leq 0.476$. Here, d_B is varied from 1 mm to 1.907 mm and L_{wall} from 4 mm to 6 mm. Different equidistant (N_{cell}=64×64×64, 80×80×80, 100×100×100) and non-equidistant (N_{cell}=64×64×80) grid resolutions are tested.

The usage of organic liquids is one of the focus points in the Multi-Phase Project. One of the considered systems is nitrogen (N_2) in cumene. Therefore, Cumene-N_2 is selected as a base system for the preliminary simulations. The bubble diameter is chosen as d_B = 1 mm and the wall distance between parallel plates (that is also taken as reference length) as L_{ref} = 4 mm, thus their ratio is $\lambda = d_B / L_{ref}$ = 1/4. The gas-to-liquid density ratio is $\Gamma_\rho \approx 1/600$ and the viscosity ratio is $\Gamma_\mu \approx 1/50$. The surface tension of the real Cumene-N_2 system (σ = 0.028 N/m) is obtained from the measurements performed by project partners under varied pressure and temperature. As a result, Morton number and Eötvös number are calculated respectively: M = 2.2×10^{-10} and $E\ddot{o}$ = 0.253. Afterwards, the range of M and $E\ddot{o}$ is extended to $2.2\times10^{-10} \leq M \leq 2.2\times10^{-7}$ and $0.253 \leq E\ddot{o} \leq 2.539$ based on the physical properties of Cumene and N_2. For a reliable and target focused comparison, those values are obtained via reducing the surface tension of the real Cumene-N_2 system with the factor of 2.5, 5 and 10. Thus, the possible effects, which may occur by changing other physical parameters, are prevented. The single bubbles simulations are performed for the resulted cases that are given in Table 2. Extended data for these cases are given in Table 14 in Appendix.A.1, where the Case M7 is mentioned as M7-SB1.

Table 2: The non-dimensional numbers for the cases with adapted surface tension values. Number of mesh cells N_{cell}=100×100×100, L_{ref} = 4 mm, d_B = 1 mm.

		M10	**M9**	**M8**	**M7**
Surface tension	Definition	$\sigma_{\text{Cumol-}N_2}$	$\sigma_{\text{Cumol-}N_2} / 2.5$	$\sigma_{\text{Cumol-}N_2} / 5$	$\sigma_{\text{Cumol-}N_2} / 10$
	[N/m]	28×10^{-3}	11.2×10^{-3}	5.6×10^{-3}	2.8×10^{-3}
Morton number		2.22×10^{-10}	3.47×10^{-9}	2.77×10^{-8}	2.22×10^{-7}
Bubble Eötvös number		0.253	0.632	1.265	2.529
Bubble Reynolds number		~187	~137	~131	~130

In the Multi-Phase Project, the experimental group at Institute for Multiphase Flow (IMS) of the Hamburg University of Technology (TUHH) performed experiments for single bubbles and these data are used to assess the numerical methods. At the TUHH IMS, two series of experiments were carried out for a rising regular bubble chain in a

vertical column with a wall distance of 4 mm. In the first series of experiments, the rise of air bubbles in a tap water-glycerin mixture with the addition of the surfactant Triton-X was investigated, where the interface is immobile ("contaminated system"). In the second experiment, the rise of nitrogen bubbles in a tap water-glycerin mixture without the addition of Triton-X was investigated, so that it behaves like a nominally "pure system" with a fully mobile interface. The "Water-Glycerin / Air" system with Triton-X (WGA) is tested under 1.1 bar absolute pressure. It consists of 49.5% of the volume water, 49.5% glycerin and 1% Triton-X surfactant as liquid phase and synthetic air as gas phase. The pure "Water-Glycerin / Nitrogen" system (WGN) experiments are performed at ambient pressure with volumetric 50% water and 50% glycerin as liquid phase and nitrogen as gas phase. The smallest possible bubbles obtained in the experiments have d_B in the range of 1.6 – 1.9 mm. The non-dimensional numbers for the WGA and WGN cases are shown in Table 3.

Table 3:   The properties of the cases used for comparison.

	WGA (with Triton-X)	WGN (pure)
Bubble diameter [mm]	1.907	1.67
Surface tension [N/m]	0.0307	0.0687
Morton number	$3.86x10^{-7}$	$3.5x10^{-8}$
Bubble Eötvös number	1.295	0.432
Bubble Reynolds number	~60	~50

The simulations are performed for cases WGA and WGN in the numerical set-up as it is illustrated in Fig. 7. In WGA system, the real density ratio is $\Gamma_\rho \approx 1/950$ and the real viscosity ratio is $\Gamma_\mu \approx 1/330$. For the simulations, the viscosity and density ratio are set to $\Gamma_\rho \approx 1/100$ and $\Gamma_\mu \approx 1/3.3$. The bubble diameter is d_B = 1.907 mm and the wall distance of 2 parallel plates (reference length) is L_{ref} = 4 mm so that the ratio $\lambda \approx 0.476$. In WGN system, the real density ratio is $\Gamma_\rho \approx 1/980$ and the real viscosity ratio is $\Gamma_\mu \approx 1/350$. For the simulations, the viscosity and density ratio are set to $\Gamma_\rho \approx 1/50$ and $\Gamma_\mu \approx 1/5$. The bubble diameter is d_B = 1.675 mm and the wall distance is L_{ref} = 4 mm so that the ratio $\lambda \approx 0.417$.

Clift et al. [75] established a diagram (Fig. 9) which provides rough estimation of physical parameters of two-phase systems for single bubbles rising with an unbounded domain filled with quiescent liquid. This diagram is useful for preliminary estimation of bubble parameters on the numerical pre-study of wall-bounded application such as

bubble rise velocity, and bubble shape and deformation. In Fig. 9, the single bubble simulations in Table 2 and Table 3 are highlighted and compared on the "Clift Diagram". The real Cumene-N_2 system (M10 in Table 2) is placed, depending on its $E\ddot{o}$, near the border of the undefined region (above the line of $M = 10^{-12}$) on the Clift diagram given in Fig. 9.The bubble shapes from simulations are consistent with the prediction of the Clift Diagram.
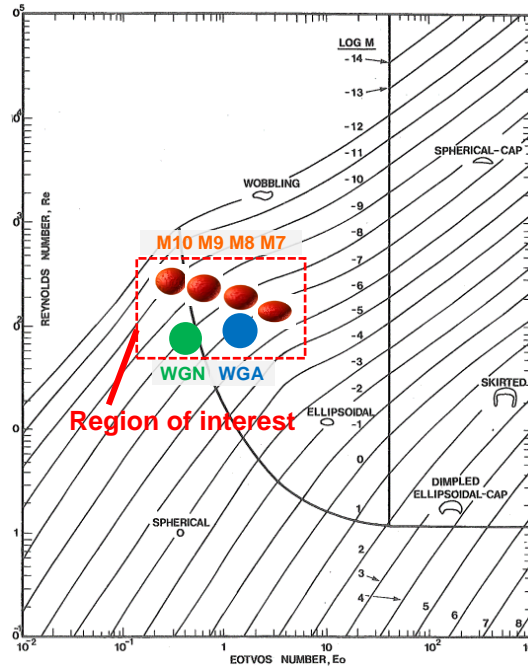

Fig. 9:   Diagram of Clift et al. [75]. Cases from Table 2 and Table 3 used for the preliminary study are approximately placed in the diagram and marked as the region of interest. The bubble shapes of the cases from Table 2 (M10, M9, M8, M7) are extracted from the direct numerical simulations for single bubbles.

3.3. Preliminary investigations

In order to identify suitable numerical parameters which allow efficient simulations for the time consuming simulations of bubble swarms without compromising the physics, comprehensive numerical preliminary studies are carried out using single bubble simulations (Table 14 in Appendix.A.1). The simulations are performed in an equidistant isotropic grid. First, the numerical aspects such as grid resolution, time step width and domain size are discussed. Later in this section, the physical effects on the numerical results are presented, i.e. density / viscosity and Morton / Eötvös numbers.

3.3.1. Influence of grid resolution

Fig. 10 shows comparison of different equidistant (N_{cell}=64×64×64, 80×80×80, 100×100×100) and non-equidistant (N_{cell}=64×64×80) grid resolutions to understand the effective grid resolution to be considered in this study. The non-equidistant grid has different mesh size in wall direction. U_T is tested for different domain sizes for the equidistant grid. L_x×L_y×L_{ref} as 1×1×1 and 2×1×1. The simulations of Case M7 from Table 2 are performed for a single bubble with d_B = 1 mm rising between two parallel planes with a wall distance L_{ref} = 4 mm. The computational setup is given in Fig. 7. The density ratio is set to Γ_ρ = 1/25 and the viscosity ratio to Γ_μ = 1 (Influence of viscosity and density ratio is discussed in Section 3.3.4 and Section 3.3.5, respectively). The ratio d_B / L_{ref} = 1/4 for an equidistant grid resolution 64×64×64 means that one bubble is resolved with 64/4 = 16 mesh cells per bubble diameter (N_B=16). N_B is used as the abbreviation for the number of mesh cells per initial bubble dimeter. For an 80×80×80 grid N_B=20 and for a 100×100×100 grid N_B=25. For a 64×64×80 grid the maximum resolution occurs in the middle of channel as a mesh size of the value of 1/64 so that one bubble is resolved with minimum 16 cells per d_B, N_B=16.

The bubble rise velocity profiles in Fig. 10 a) shows that the neither equidistant nor non-equidistant grid resolution has any significant influence on the terminal velocity of bubble. However, according to the bubbles shapes shown inside Fig. 10 a), it has significant influence on the interface reconstruction. In IR-VOF methods, Piecewise Linear Interface Calculation (PLIC) method is used for interface reconstruction where in any mesh cell with $0 < f < 1$ the interface is approximated by a line (in 2D) or a plane (in 3D). Interface approximation with PLIC is discussed in Section 2.4.2 and an example for 2D interface approximation is exhibited in Fig. 5 b).

In Fig. 10 a), the bubble surface is smoother for a finer mesh (N_B=25) than the bubbles with N_B=16, as expected. The "rough" surface influences the normal vector and curvature calculation on the interface. If the curvature of the interface in the momentum equation (Eq. (49)) is not accurately computed, the spurious currents may occur and dominate the solution [47]. This numerical artifact may also be the reason of the results obtained from the analysis of local velocity profiles (u_1) in flow direction (x_1) within the wake and inside of bubbles in Fig. 10 b). Comparison of three different grid sizes showed that the velocity profiles for two finer grids are in good agreement in the wake whereas the profiles for the coarse grid deviate from other cases in the bubble and in the wake close to the interface. The combination of findings with the results of bubble interface reveals that using 80 mesh cells per unit length (L_x, L_y, L_{ref}) so that N_B=20 is sufficient to obtain results that are independent on the mesh size.
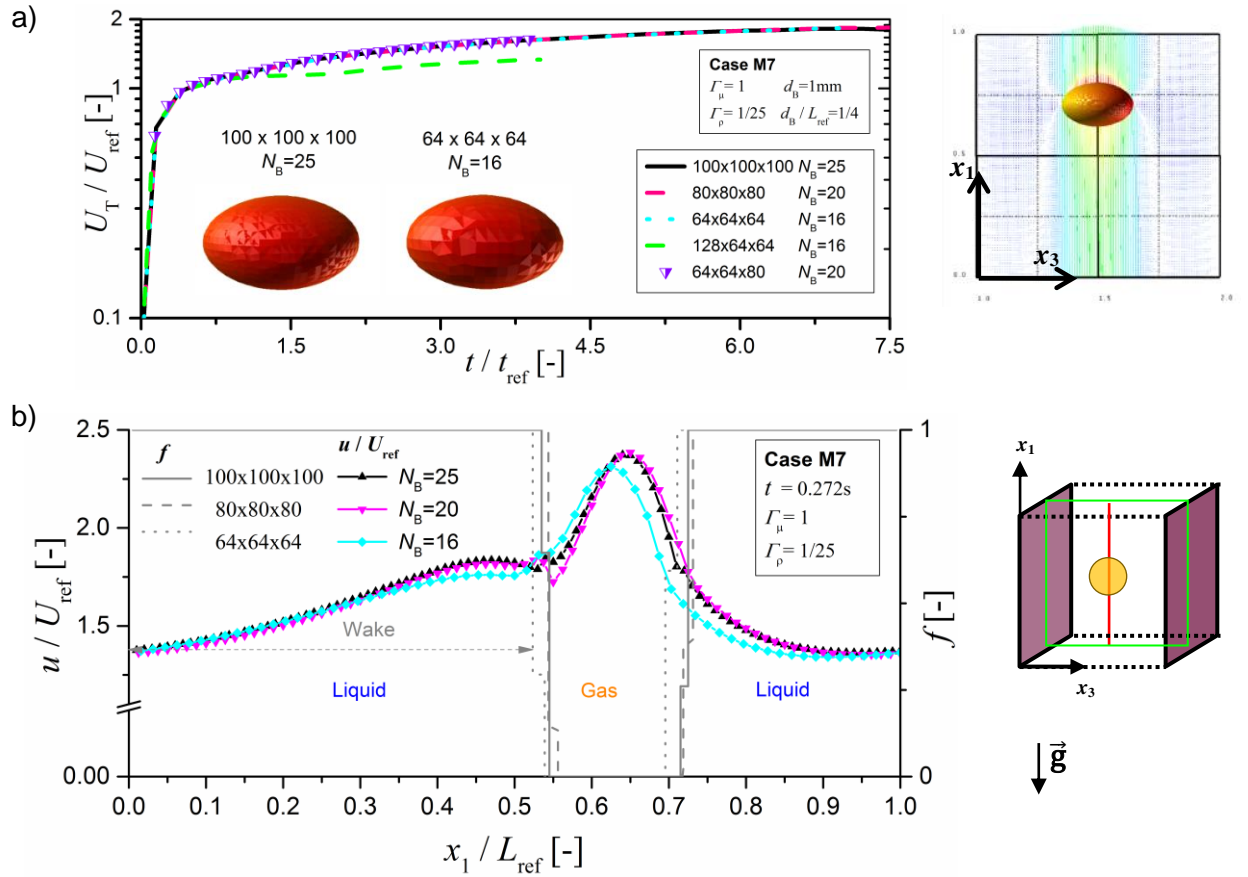
Fig. 10: Influence of grid resolution on bubble rise velocity. The profiles are evaluated for variations of Case M7 in Table 2 and given in Table 14 as M7-SB1. a) Left: Bubble rise velocity profiles and bubble shapes. Right: Simulation result in 2D view with velocity vectors (steady state). b) The vertical profile of the vertical velocity component in the middle of the computational domain in the wake and inside of bubbles in 1×1×1 domain. Right side: The profiles are evaluated along the channel a mid-vertical line (red) on a mid-vertical plane (green). f is the volume fraction, $f = 0$ (gas) and $f = 1$ (liquid).

A coarse grid may result an inaccurate calculation of the interface normal vector and curvature, and severe errors regarding velocity calculation. Because the velocity is approximated by the volume averaged solution of the single field momentum equation with surface tension term (see Eq. (49)) on a staggered grid. Therefore, setting a tolerance above the limit and using N_B=25 is still a safer choice. However, the required one million mesh cells (100×100×100) cause very high CPU time. This disadvantage of high grid resolution can be balanced by choosing a non-equidistant grid where the mesh size is becoming finer in wall direction, which is of high importance. Having such a discretization reduces the CPU time and still provides enough mesh size for smooth interface. Therefore, the 80×80×100 grid size is the most optimal choice. It provides a grid resolution of minimum sufficient N_B=20 cells per d_B for independent results on the mesh size and even finer grid near the wall.

3.3.2. Influence of time step width

Many numerical works suffer from one common obstacle: long CPU time. The low viscosity and density ratio of the Cumene-N_2 system require low time step width $\Delta t \leq 10^{-6}$ that causes high CPU time. For reliable results, the velocity profiles ideally should reach quasi-steady state condition where the mean velocity of the liquid phase and the bubble rise velocity can be considered approximately constant. In some cases, 4-6 weeks CPU time was required to reach steady state.

In an unsplit method, as used in TURBIT-VOF, during the advection step the liquid volume fluxes cross through all the mesh cell faces during a time step of duration Δt and the total flux of fluid (V) crossing the right cell face per unit cross sectional area is calculated as $V = u.\Delta t$. At this point, too small Δt values (i.e. $\Delta t \leq 10^{-6}$) may cause unreliable results by estimating the volume flux transferred through cells incorrectly. Besides, there is also an upper limitation for the determination of Δt. The main advantage of IR-VOF methods is the volume conservation property [47]. However, some discrepancies such as loss of volume of bubbles were observed in case of using high values of Δt ($\Delta t > 2\times10^{-4}$). As a matter of collective experience on TURBIT-VOF code in the past and during this study, the optimal time step width is determined as $\Delta t = 10^{-4}$ for reasonable CPU time as well as for reliable results. In some cases when convergence problems occur during simulations, Δt was decreased down to the value of 5×10^{-6} for sustaining convergence and then again were set to possible closest value to 10^{-4}.

Primarily, the numerical stability must be sustained for further steps. The density and viscosity of the gas phase are changed for better numerical stability. The influence of these changes on the simulation results is examined. For this purpose, test simulations for single bubbles are performed and feasible values are determined in Section 3.3.4 and 3.3.5.

3.3.3. Influence of domain size

Two different computational domains are considered for single bubble simulations. The mainly used one is bounded with two parallel walls, and unbounded and periodical in vertical and lateral directions. Another one used for experimental validation is a rectangular channel bounded with four walls and periodical in vertical direction (cf. Section 3.1). Physically, the single bubble rising between parallel walls or in a rectangular channel in a domain with periodic boundary condition (p.b.c.) in flow direction can be defined as a chain of identical single bubbles with a well-defined vertical distance. The frequency of bubble passage is an important parameter since

the passage of consecutive bubbles modifies the mean velocity profile of the liquid and influences the vortices in bubble wake [173]. The wake effect leads to an increased bubble rise velocity and more bubble – bubble and bubble – wake interactions [174] which may lead to a non-rectilinear trajectory of bubble [175]. Consequently, the turbulence is enhanced by the frequency of bubble formation [176]. In the literature, the wake effect is taken into consideration by modelling the drag force. Chai [177], Chai et al. [178] and Chai and Cheng [174] proposed drag force model approach to consider the wake acceleration effect on spherical bubbles using the relationship between the reduced drag force and the wake velocity together with the bubble diameter and the vertical distance between bubbles. For numerical investigations in the current study, the frequency of bubbles depends solely on the channel length due to p.b.c. in flow direction. Therefore, the channel length must be investigated to identify appropriate distance between bubbles for a minimized bubble frequency effect on the bubble rise velocity (U_T). In the experiments, the bubbles are injected when the liquid in the wake becomes almost stagnant. Thus, the injection frequency of single bubbles is high enough to reduce the influence of bubbles chain (or the wake effect).

Fig. 11 shows the influence of the domain size on local velocity field for different channel sizes such as 2×1×1 with a grid of 100×50×50, 3×1×1 with a grid of 150×50×50, 5×1×1 with a grid of 250×50×50 and 3×2×1 with a grid of 150×100×50. The Water-Glycerin-Air (WGA) case with d_B = 1.907 mm is considered for simulations. Table 4 presents the corresponding diameter to length ratio for WGA and WGN cases.

Table 4: The domain size applied for the cases in the simulations.

|	$\lambda_x^{-1} = L_x / d_B$		$\lambda_y^{-1} = L_y / d_B$		$\lambda_z^{-1} = L_{wall} / d_B$	
	WGA	WGN	WGA	WGN	WGA	WGN
2×1×1	≈ 4.2	≈ 4.8	≈ 2.1	≈ 2.4	≈ 2.1	≈ 2.4
3×1×1	≈ 6.3	≈ 7.2				
5×1×1	≈ 10.5	≈ 12				
3×2×1	≈ 6.3	-	≈ 4.2	-		
4.5×2.5×1	-	≈ 10.7	-	≈ 6		

a)

b)
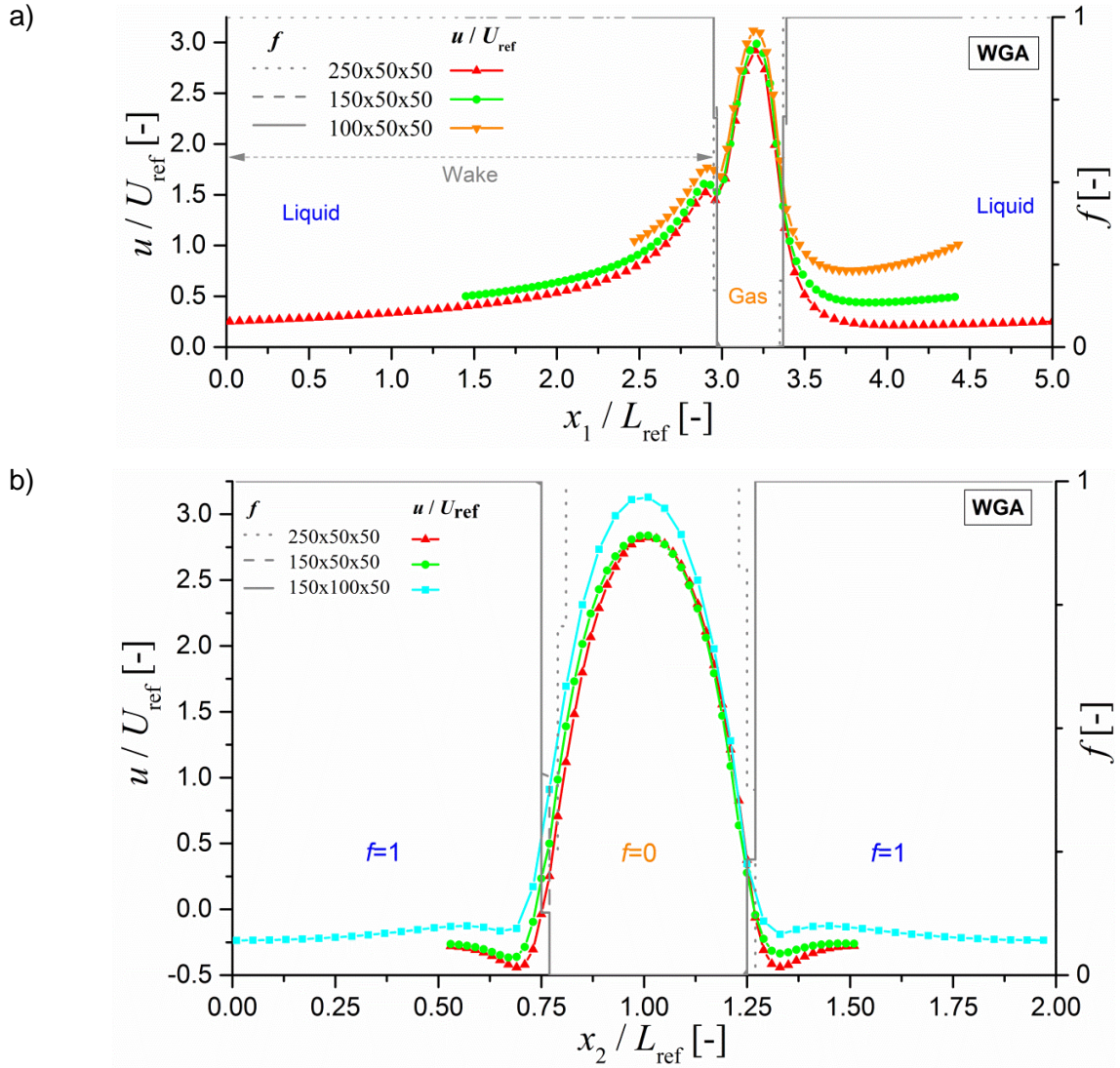
Fig. 11: a) The vertical profile of the vertical velocity component in the middle of the computational domain b) The lateral profile of the vertical velocity component in the middle of the computational domain for Water-Glycerin / Air system.

In Fig. 11 a), the influence of the height of the computational domain or the bubble frequency on the local velocity field is illustrated using the vertical profile of the vertical velocity component in the middle of the computational domain. The minimum value of the liquid velocity in 5×1×1 (L_x / d_B ≈ 10.5) domain is approximately half of the values in 3×1×1 domain (L_x / d_B ≈ 6) and around one fourth of the value in 2×1×1 domain (L_x / d_B ≈ 4). The variation in the liquid velocity also reflects to the values of the maximum velocity in the bubble ($u_{B,max}$) but in a lower magnitude. In 2×1×1 domain, it is only 6 – 7% higher than in 5×1×1 domain. In an even longer domain, the influence may be negligible. However, such a domain would not be applicable for a DNS simulation with fine grid in terms of computational costs and CPU time. For the computational domain 2×1×1, the minimum value of the liquid velocity corresponds to approximately one third

53

of $u_{B,max}$. For the domain 5×1×1 (L_x / d_B ≈ 10.5), this effect reduces to about 10%. By this effect, the rear bubble in the bubble chain enters to the wake of its fore bubble where a positive velocity field exists and therefore the rear bubble accelerates. For L_x / d_B > 10, the minimum liquid velocity in the wake is less than 10% of $u_{B,max}$. This value is a good estimation in simulations where extreme precision is not required.

Chai et al. [178] investigated the wake acceleration effect depending on the vertical distance between rising bubbles for large bubbles (4 – 7 mm) with low aspect ratio (0.6 – 0.7) and presented that the velocity profile in the wake keeps developing until the vertical distance between bubbles is 3 – 5 times of the longer diameter of ellipsoidal bubble. Considering rather spherical bubbles as in this study (cf. Section 3.3.6), these values correspond to approximately L_x / d_B ≈ 4 – 6. With respect to different flow parameters, bubbles sizes and wake structure, this finding of Chai et al. [178] is qualitatively comparable to the results from Fig. 11 a) where for L_x / d_B ≈ 6 the minimum value of the liquid velocity in the wake is less than 20% of $u_{B,max}$.

On the other hand, for the flow between parallel walls there is an interaction of bubbles and liquid between the bubbles in lateral direction as if there is another parallel channel. This liquid region may be named as so-called "bubble-free liquid column". The neighboring bubbles have also influence on the flow and the velocity profiles within the side-liquid slug region. In numerical work, this situation may be interpreted as many parallel single bubbles rising side-by-side. This is naturally not the case in the experiments. In Fig. 11 b), the influence of the lateral distance in the computational domain on the local velocity field is illustrated using the lateral profile of the vertical velocity component in the middle of the computational domain. In the lateral direction, no walls exist and periodic boundary conditions apply. The liquid velocity profiles are negative in the side-liquid slug and stay negative for all cases, which are expected due to non-existing walls. For the computational domain 3×2×1 (L_y / d_B ≈ 4.2) with a doubled lateral distance, $u_{B,max}$ is about 9 – 10% higher than in the computational domains 3×1×1 and 5×1×1 (L_y / d_B ≈ 2.1). The liquid velocity profile in the domain 3×2×1 is flatter and almost constant when it gets far from the phase interface. For two cases with lower lateral distance, the lowest values of the liquid velocity near the phase interface are about twice as low as in the domain with doubled lateral distance. This is due to the stronger mixing of eddies near the bubble in 3×1×1 and 5×1×1 domains than in 3×2×1 domain. Although the magnitude of the liquid velocity values are low in comparison to the values of $u_{B,max}$, the two times wider domain in lateral direction has still influence on $u_{B,max}$ and as a natural consequence also on U_T. For L_y / d_B > 4, the influence of lateral distance on $u_{B,max}$ is less than 10%.

In an experimental setup where a single bubble rising between parallel walls, the parallel plates are located inside of a column / pipe that is limited with its own wall. The velocity profile formed in lateral direction due to these walls may have a different behavior than the velocity profile for bubbles rising so-called side-by-side as in the simulations. Therefore, the influence of lateral distance is only a concern for the numerical study and not comparable with experimental conditions. Contrarily, the influence of vertical distance (bubble frequency) is quantitatively comparable in simulations and experiments.

3.3.4. Influence of viscosity ratio

In Fig. 12, the bubble rise velocities are examined for Case M7 (Table 2) for varied viscosity ratio. Only gas properties were modified to reach various values whereas the liquid viscosity is fixed to its real value. The viscosity ratio is in the range of $1/5 \leq \Gamma_\mu \leq 1$ for a fixed density ratio $\Gamma_\rho = 1/25$. The values of $\Gamma_\mu < 1/5$ require small Δt values less than 10^{-6}. All simulations with $\Gamma_\mu < 1$ are performed based on the case with $\Gamma_\mu = 1$ from the time point at $t = 5t_{ref}$. Here, t_{ref} is non-dimensional time. From the graph, it can be seen that the change of Γ_μ, where the liquid viscosity is fixed and the gas viscosity is varied, has no significant effect on the bubble rise velocity. To date, a number of studies explored the relationships between Γ_μ and U_T [75, 179-181]. It is general practice to neglect the effect of the viscosity of the internal fluid in correlations of terminal velocities. Clift et al. [75] analyzed data from literature for systems with identical Morton number but widely different values of Γ_μ (0.35 to 20). They did not observe any systematic dependency of terminal velocities on Γ_μ, which supports the findings from Fig. 12.

The condition $\Gamma_\mu = 1$ is suitable for numerical calculation and as can be seen from above discussion it has no physical effect on U_T. However, the viscosity change modifies the velocity field inside of the bubble. This fact raises intriguing questions for further analysis of the local velocity profiles. Fig. 13 shows the local profiles in flow direction inside and outside the bubble, along the channel and between the walls. What stands out is that Γ_μ has influence on the velocity profiles in the bubble and in its wake. This effect is especially noticeable between the cases with $\Gamma_\mu = 1$ and $\Gamma_\mu < 1$. As can be seen from Fig. 13 a), the velocity profiles within the bubble presents different structures. This might happen when the intensity of the recirculation in the bubble is altered due to the modified shear stresses and the gradient of friction forces. According to the drag law of Hadamard-Rybczynski, in pure systems with decreasing Γ_μ the drag coefficient applied on the bubble also decreases and this leads the U_T to increase. Since U_T stays constant, assuming that the bubble rising in a linear path in the

simulations then buoyancy, gravity and drag are in balance. Considering the constant density ratio and surface tension with decreasing drag coefficient, the increasing friction force, which tends to compensate the local velocity differences, remains the only reason to sustain this balance. The most interesting aspect of this graph presented in Fig. 13 b) is that for Γ_μ = 1 the velocity profile is parabolic whereas for low Γ_μ (low μ_G) the highest velocity values appear towards the gas-liquid interface.
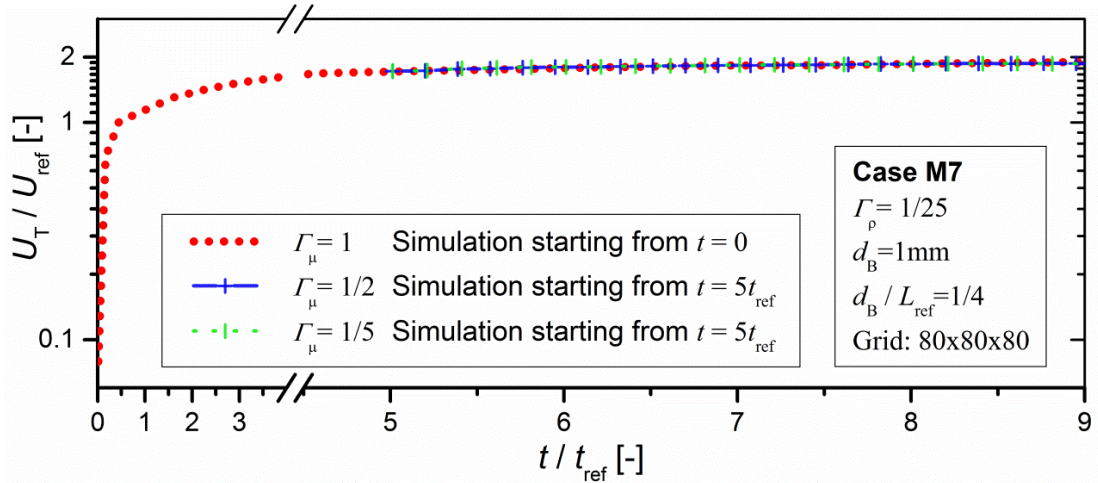

Fig. 12: Effect of viscosity ratio on bubble rise velocity. The evaluated cases are variations of Case M7 in Table 2 and given in Table 14 as M7-SB1 and M7-SB5. Simulations for Γ_μ = 1/2 and 1/5 are started from a time point at quasi-steady-state of the Case M7-SB1 with Γ_μ = 1.

Fig. 13 also shows that the influence of Γ_μ on the velocity profiles in the liquid is accountable only closer to bubble interface. The results in Fig. 13 a) confirms the findings of Clift et al. [75] that internal circulation has influence on the wake formation. It is also interesting about these results that significant velocity values can be observed in the wake of bubble. For a bubble passage, this velocity profile in the wake has influence the U_T. Such an investigation on local velocities is of great importance to understand the wake effect so that the optimum domain size with safe distances can be determined.

Considering the advantages of Γ_μ = 1 for limiting the CPU time, this theoretical parameter was also used for test purposes. However, the low viscosity ratios (Γ_μ < 1) have less influence on the shape of velocity profile whereas U_T is unchanged for both Γ_μ = 1 and Γ_μ < 1. Therefore, the viscosity ratio Γ_μ < 1 is mainly considered in the simulations for validation and analysis purpose.
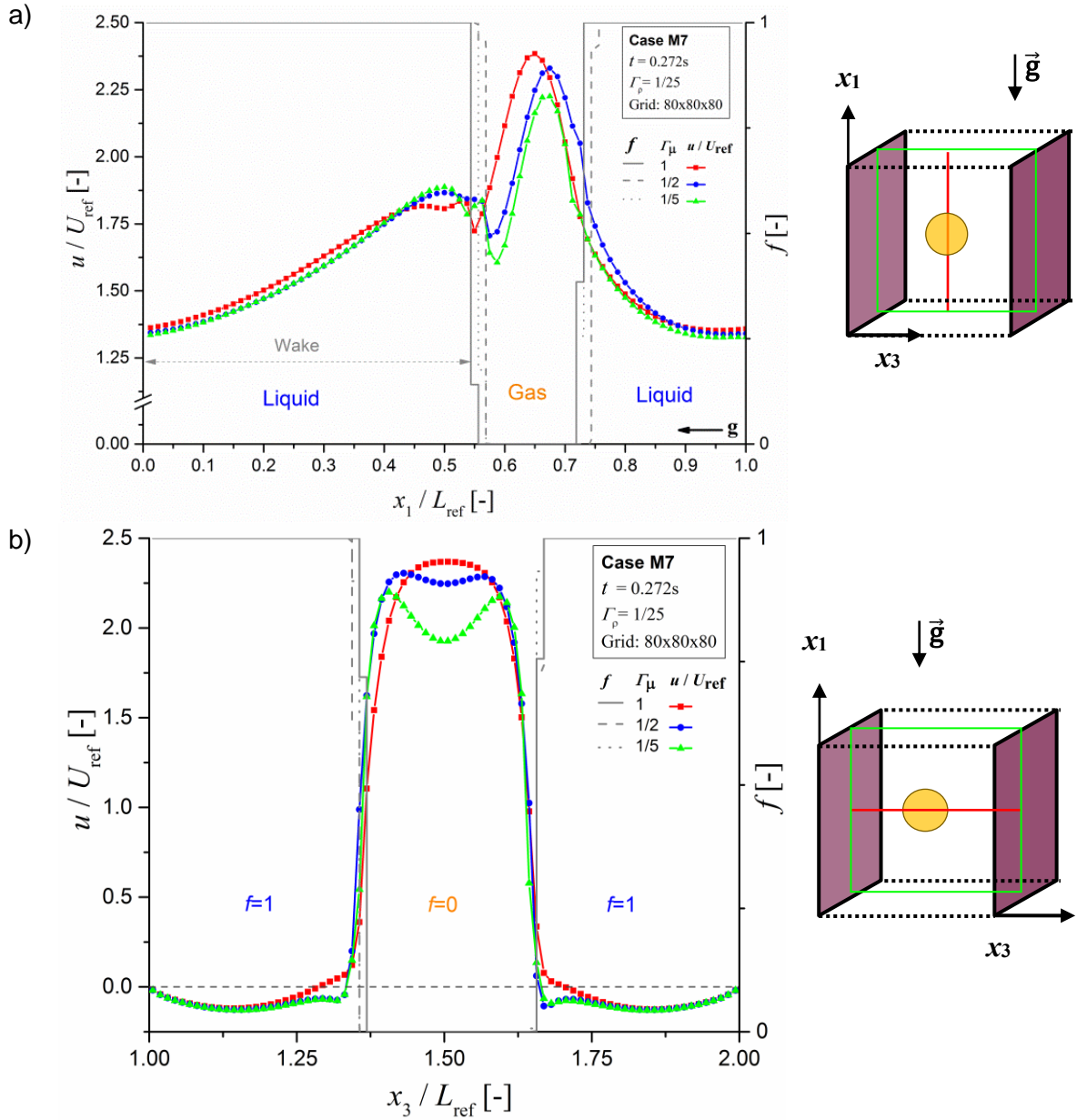
Fig. 13: Effect of viscosity ratio on the vertical velocity profiles in flow direction inside and outside of bubbles. The evaluated cases are variations of Case M7 in Table 2 and given in Table 14 as M7-SB1 and M7-SB5. Simulations for Γ_μ = 1/2 and 1/5 are started from a time point at quasi-steady-state of the Case M7-SB1 with Γ_μ = 1. a) The profiles on a mid-vertical line along the channel. b) The profiles on a mid-horizontal line cutting through the bubble in wall distance. f is the volume fraction, f =0 for gas and f =1 for liquid.

3.3.5. Influence of density ratio

In Fig. 14, the bubble rise velocities are examined for Case M7 (Table 2) for varied density ratio. Only gas properties were modified to reach various values whereas the liquid density is fixed to its real value. The density ratio is in the range of $1/100 \leq \Gamma_\rho \leq$ 1/25 for a fixed viscosity ratio Γ_μ = 1. The values of Γ_ρ < 1/100 require small Δt values less than 10^{-6}.

In Fig. 14, the simulations are performed starting from $t = 0$ for Γ_ρ = 1/25 and 1/50 while for Γ_ρ = 1/100 the simulation is started based on the case with Γ_ρ = 1/25 from a time point where the profile is close to a quasi-steady-state. The terminal bubble velocity shows no deviation for any of the considered values of Γ_ρ. Thus, a gas-to-liquid density ratio of 1/25 is appropriate to obtain results that are independent on the gas density. This density ratio is also typical for real systems under high pressures so that it can be reached in real physical conditions. Additionally, in numerical point of view Γ_ρ = 1/25 provides lower CPU time with a constant value of $\Delta t = 10^{-4}$.
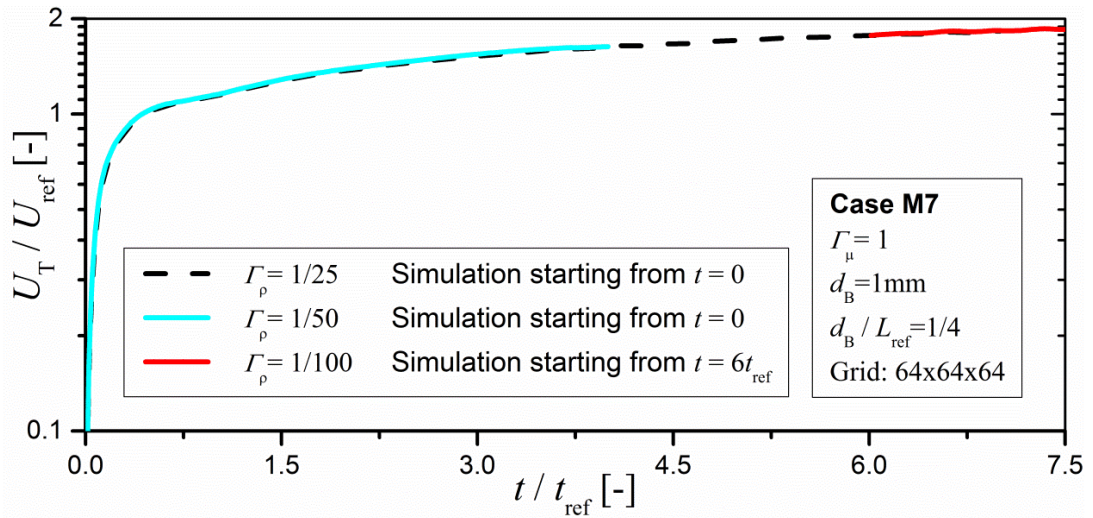

Fig. 14: Effect of density ratio on bubble rise velocity. The cases evaluated are variations of Case M7 in Table 2 and given in Table 14 as M7-SB1, M7-SB3 and M7-SB4. Simulation for Γ_ρ = 1/100 is started from a time point at quasi-steady-state of the Case M7-SB1 with Γ_ρ = 1/25.

3.3.6. Influence of Morton and Eötvös number

Fig. 15 presents the bubble rise velocity profiles and bubble shapes of cases (see Table 2) with different M ($M = g\left(\rho_L - \rho_G\right)\mu_L^4/\rho_L^2\sigma^3$) obtained by changing the surface tension. In the simulation results of M10, M9 and M8 cases from Table 2, more zigzag and helical bubble path as well as more shape oscillations are observed with decreasing M. For the Case M7 with the highest M, the bubble rises almost rectilinear (slightly oscillating). The bubble path influences the velocity profiles as well. In Fig. 15, the steady velocity profiles are plotted only for M7 and at earlier times of M8 while for low M ($M < 10^{-8}$) the instability as well as the terminal velocity of bubbles U_T increases. This effect of low M on the U_T can be anticipated based on the Reynold number change in Fig. 9 and Table 2. These simulations may be compared quantitatively with the

experimental study by Liu et al. [176] where the authors examined the flow structure induced by a chain of gas bubbles in a rectangular bubble column using particle image velocimetry (PIV). They concluded that the variation of bubble rising trajectory associates with the alternation of bubble motions and in general, complex fluid velocity fields present in liquid system of low viscosity (low M) where free vortex, cross flow, and irregular circular flow can be observed. Bubble behaviors such as varied bubble trajectory observed in the simulations and the unsteady velocities of rising bubbles shown in Fig. 15 are similar to the results from the experiments of Liu et al. [176]. The most probable reason for those outcomes observed in both studies is the high intensity of pseudo-turbulence in a low M system. As the measurements of Liu et al. [176] for the liquid pseudo-turbulence in terms of turbulence intensity showed, the pseudo-turbulence is more intense in liquid system with low viscosity (low M). Overall, these results suggest that the cases M8 and M7 with less complex flow are more appropriate for further direct numerical simulations in this work.
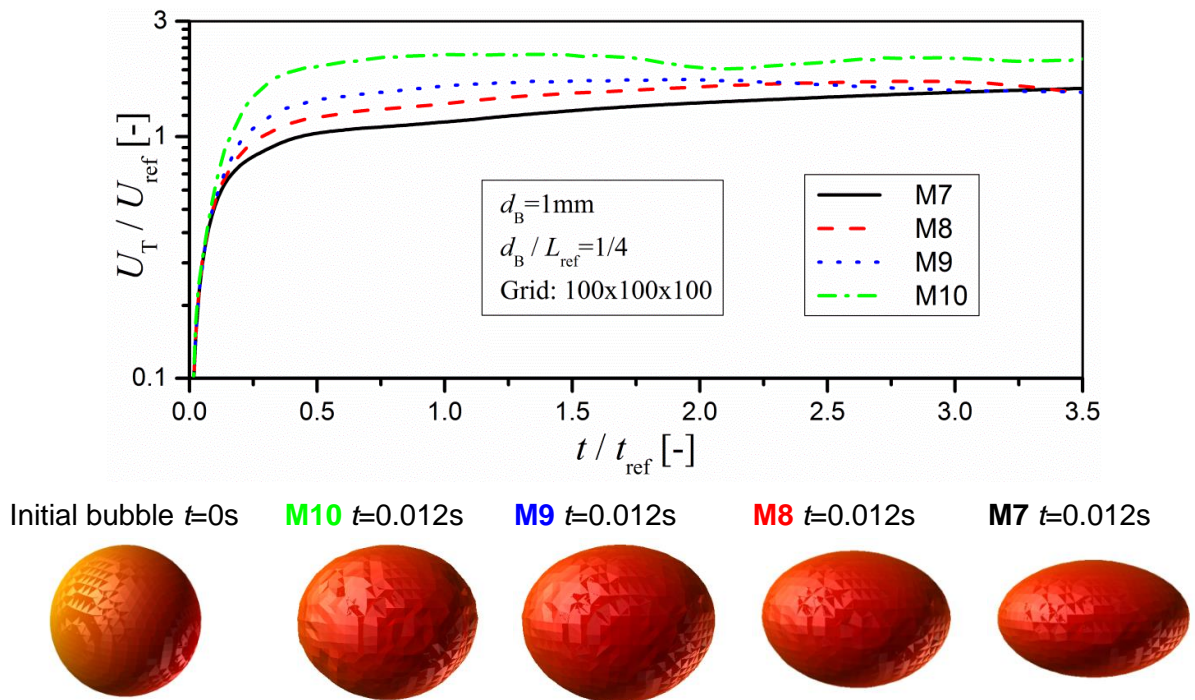
Fig. 15: Effect of M on bubble rise velocity (a) and bubble shape (b) based on the cases in Table 2. Bubble shape of the initial bubble is given at t=0s and bubbles for varied M at the same real time, t=0.012s. Grid: 100×100×100. $\Gamma_\mu = 1$, $\Gamma_\rho = 1/25$. (Bubble sizes may not represent exact proportion).

Clift diagram suggests that the shape of bubbles may be predicted according to Morton and Eötvös numbers. If a bubble is able to keep a geometrically definable shape, then an aspect ratio can be measured based on its altered radiuses. The

relation between aspect ratio of bubbles and Morton and Eötvös numbers for the single bubble cases is represented in Fig. 16. Wellek et al. [182] define a correlation of the mean aspect ratio for single bubbles in contaminated systems in infinite domain as

$$\chi = \frac{1}{1+0.163 E\ddot{o}^{0.757}} \tag{68}$$
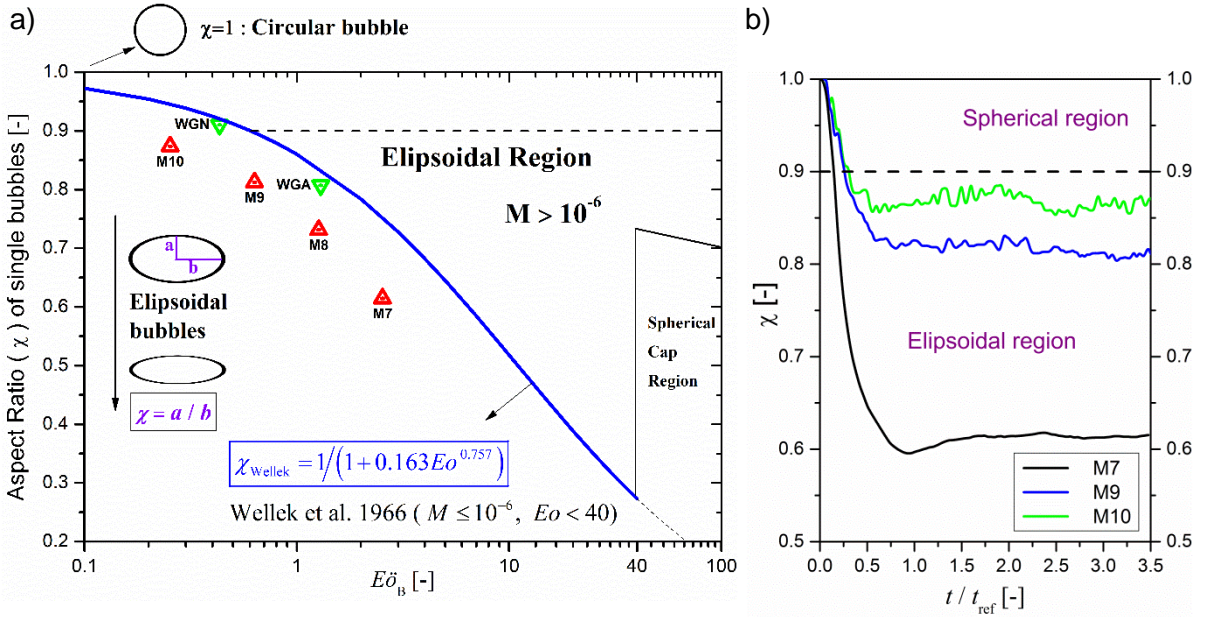
Fig. 16: a) Comparison of mean aspect ratio with correlation from Wellek et al. [182] for drops and bubbles in contaminated systems Clift et al. [75]. b) The change of aspect ratio in time for three cases (M7, M9, M10). The shown cases are given in Table 2 and Table 3.

In Fig. 16 a), the aspect ratio of bubbles obtained from simulations is plotted against the Eötvös number and compared with this correlation. Blue line in Fig. 16 a) represents the correlation for $E\ddot{o} < 40$ and $M \leq 10^{-6}$ and below the dashed line represents the ellipsoidal region. According to Clift et al. [75], "spherical" is defined as bubbles which are closely approximated by spheres if interfacial tension and/or viscous forces are much more important than inertia forces and if the minor to major axis ratio lies within 10% of unity. The term "Ellipsoidal" is generally used to refer to bubbles which are oblate with a convex interface (viewed from inside) around the entire surface. In Fig. 16 a), the aspect ratio values of the test cases (M7, M8, M9, M10) in Table 2 are shown with red triangles. All cases are slightly below the correlation of Wellek et al. [182] plotted in blue color. This is likely due to pure system conditions in simulations. The aspect ratio for M10, M9, WGA and WGN are $\chi > 0.8$, namely the deformation may be considered as insignificant. The almost spherical bubble shapes of M10 and M9 in Fig. 15 b) confirms this result.

In Fig. 16 b), the aspect ratio is plotted against the simulation time. For Case M7, the bubble changes the shape from sphere to ellipsoidal and does not suffer with much oscillation. For Case M10 and M9, the bubble is oscillating so that the bubble shape deforms and never forms a steady shape. The bubble shape predictions in Fig. 16 b) correspond to the real bubble shapes in Fig. 15 b). The shape oscillations with changing M are also similar with those of Liu et al. [176].

3.3.7. Summary of Section 3.3

The single bubble simulations serve as preliminary investigations to identify suitable numerical and physical parameters that allow efficient simulations without compromising the physics. The simulations are performed in a channel bounded with either two or four parallel walls. The influences on the numerical results are investigated in terms of numerical aspects, i.e. grid resolution, time step width, domain size and the physical effects, i.e. density / viscosity and Morton / Eötvös numbers.

The investigations show that a grid resolution of 20 cells per bubble diameter (N_B=20) is appropriate to obtain results that are independent from the mesh size. A coarser grid may cause inaccurate calculation of the interface normal vector and curvature, and thus severe errors regarding velocity calculation. A finer grid provides very close results to those with N_B=20 but requires very high CPU time. This common obstacle can be solved by choosing high time step width (Δt). However, in case of using high values of Δt, the inherent volume conservation is not secured. The loss of bubble volume is observed for $\Delta t > 2\times10^{-4}$. The low values of viscosity ($\Gamma_\mu < 0.2$) and density ratio ($\Gamma_\rho < 0.01$) require finer solution of the flow field and interface and thus low time step width. For values of $\Delta t \leq 10^{-6}$ numerical discrepancies are observed which occur in an unsplit IR-VOF method when the advection of volume fluxes from one cell to another is not calculated properly. Therefore, the time step width is identified as $\Delta t = 10^{-4}$ for the simulations with TURBIT-VOF code in this study. The choice of time step width is crucial for reliable simulations using VOF methods and must be identified individually for each code and software.

Based on the periodic boundary condition in flow direction, a rising single bubble physically represents a chain of identical single bubbles with a well-defined vertical distance. The ratio of vertical distance to bubble diameter $L_x / d_B > 10$ is sufficient to obtain results where the minimum liquid velocity in the wake is less than 10% of maximum velocity value in the bubble $u_{B,max}$. This result is deduced from the simulations performed with the channels lengths $4 \leq L_x / d_B \leq 10.5$. For different channel height, a modified mean velocity profile of the liquid is observed in the bubble wake

related to the passage of consecutive bubbles. In longer channels, the profiles of the bubble rise velocity (U_T) are flatter and lower than the profiles in shorter channels. However, a fully steady state is not observed for any channel height since the vertical distance is not high enough to avoid the influence of wake acceleration. In the reference experiments where L_x / d_B ≈ 525 the flow is in a steady state. On the other hand, in a channel with two parallel walls the periodic boundary conditions are also valid in lateral direction. For the ratio of lateral distance to bubble diameter L_y / d_B > 4, the influence of lateral distance on $u_{B,max}$ is less than 10%.

The change of physical properties has influence on the numerical results. The results of the examined cases indicate that a liquid-to-gas density ratio of 25 (Γ_ρ = 0.04) is appropriate to obtain results that are independent from the density ratio. The change of viscosity ratio Γ_μ with fixed liquid viscosity has no significant effect on the bubble rise velocity U_T. However, with Γ_μ = 1 the velocity profile inside of the bubble and in the bubble wake differs from the profiles computed with the values of Γ_μ < 1. Therefore, the viscosity ratio Γ_μ < 1 is chosen if higher accuracy is required. With these values of physical parameters, the influence of density and viscosity on the velocity profiles in the bubble and in the wake of the bubble is negligible.

The investigations are carried out with varied Morton number $2.2 \times 10^{-10} \leq M \leq 3.86 \times 10^{-7}$ and Eötvös number $0.253 \leq E\ddot{o} \leq 2.539$ by changing the surface tension for a fixed liquid viscosity. The resulting aspect ratio (χ) of the bubbles are in the range of $0.6 < \chi < 0.9$. In the given range, the Eötvös number controls the bubble shape and the Morton number characterizes the motion of bubble. For higher values of $E\ddot{o}$, the bubble shape is more ellipsoidal while for the lowest value of $E\ddot{o}$ the bubble is almost spherical. These observations are in good agreement with the estimations in the literature. The bubble shape and its evaluation for different values of M and $E\ddot{o}$ correspond to the correlations from Wellek et al. [182] as well as to the approximations exhibited in the diagram of Clift et al. [75]. The bubble rise velocity increases with decreasing Morton number. With high Morton number ~10^{-7}, where the bubble shape is ellipsoidal ($\chi \approx 0.62$), the lateral deviations of bubble path are low and the bubble rises almost in a rectilinear line. With low Morton number ~10^{-10} where $\chi \approx 0.85$, more zigzag motion and rotational bubble path are observed and shape oscillations (wobbling) occur. However, it is known from [26] that the lateral motions tend to be suppressed for a bubble shape closer to spherical (χ > 0.9). This means that the lateral motion mentioned here is not related to the aspect ratio but mainly to the shape oscillations such as wobbling which is exhibited in the diagram of Clift et al. [75].

3.4. Comparison with correlations, experiments and simulations

This Section consists of four parts. In the first part, the numerical results for the terminal velocity of the rising single bubbles are compared with the experiments of TUHH and with the correlations from the literature based on the approaches in the literature given in Section 2.2. The second part focuses on the influence of surface contamination and corresponding bubble shape changes on the terminal velocity. In the third part, the results are further discussed by means the drag applied on bubbles. In the last part, the DNS results from TURBIT-VOF are validated with the DNS results provided by the project partner in TU-Darmstadt and those results are compared with the reference experimental data from TUHH for the velocity profiles of the rising single bubbles in a bubble chain.

3.4.1. Terminal velocity

The correlations in literature are mostly valid for so-called unbounded channels. Therefore, a correction factor is applied on the experimental and numerical results in order to account for the solid wall effect based on the approaches in the literature discussed in Section 2.2.4.

According to Eq. (23), for the cases in Table 3, λ takes the value as follows

$$\lambda_{\text{WGA}} \approx 1/2.1 = 0.4767 \tag{69}$$

$$\lambda_{\text{WGN}} \approx 1/2.4 = 0.4187 \tag{70}$$

Fig. 4 shows the terminal Reynolds number and $\left(K_{\text{U}} - 1 \right)$ as functions of $N_{\text{D}}^{1/3}$ and K_{U} can be estimated as a function of $N_{\text{D}}^{1/3}$ and λ of the system. From N_{D} given in Eq.(26), considering the cases in this study given in Table 3 $N_{\text{D,WGA}} = 3194$ and $N_{\text{D,WGN}} = 2140$ so that $N_{\text{D,WGA}}^{1/3} = 14.7$ and $N_{\text{D,WGN}}^{1/3} = 12.8$. The velocity correction factor K_{U} can be approximately calculated by $\left(K_{\text{U}} - 1 \right)$ values estimated from the plot in Fig. 4 as

$$K_{U,\text{WGA}} = U_{\text{T}}^{\infty} / U_{\text{T}} \approx 2.05 \tag{71}$$

$$K_{U,\text{WGN}} = U_{\text{T}}^{\infty} / U_{\text{T}} \approx 1.85 \tag{72}$$

The wall correction factors in Eqs. (71) and (72) for each case are applied on the numerical and experimental bubble rise velocity. However, it must be noted that the correction factor is valid for conversion from circular ducts to unbounded channels. No relation for parallel walls was found in the literature.
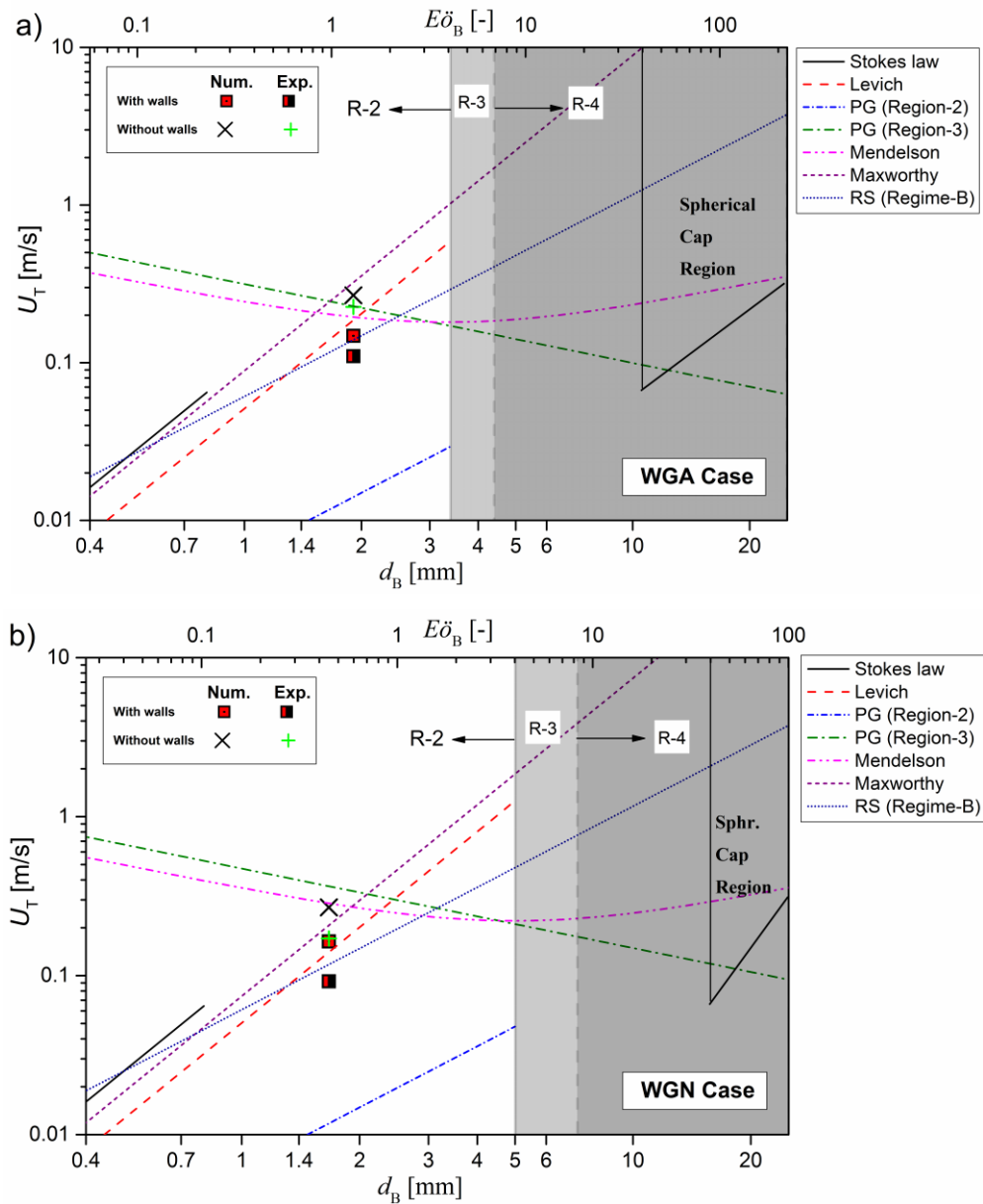
Fig. 17: Bubble rise velocity in dependency of the particle diameter and the corresponding Eötvös numbers. a) WGA b) WGN. (Num.: Numerical results, Exp.: Experimental results, R: Regions shown in Table 1, PG: Peebles and Garber [83], RS: Räbiger and Schlüter [106])

Fig. 17 demonstrates the validation range of the regions based on the Peebles and Garber [83] approach given in Table 1. In Fig. 17, the bubble rise velocity U_T is given in dependency of the particle diameter d_B (below x-axis) and the corresponding Eötvös numbers $Eö_B$ (above x-axis) is given with aspect ratio according to corresponding Eötvös numbers for WGA and WGN cases. The approach from Peebles and Garber [83] in Eq. (7) for Region-3 is a relatively good approximation for both cases. Eq.(6) for Region-2 drastically underestimates the both experimental and numerical findings even though the cases fall into the Region-2 according to Peebles

and Garber [83] classification. Eq. (13) of Mendelson [84] and Eq.(9) of Maxworthy et al. [91] provide close approximations as they promise for being valid in wide range of Morton number. The correlations from Levich [86] in Eq. (8) and Räbiger and Schlüter [106] in Eq. (18) underestimate the velocity values of simulation results. Reminding that the wall effect is considered for circular duct, but the simulations were performed through parallel walls, the qualitative estimation of terminal velocity seems feasible by general formulas rather than restricted one for specific regions.

In Fig. 18, the velocity values, which are calculated from correlations in literature, and the physical properties are converted to the non-dimensional group proposed by Rodrigue [96] using Eq. (11) and Eq. (12), respectively, and the resulted non-dimensional velocity number (V) and the flow number (F) are plotted using Eq. (10) (cf. Section 2.2.2). It is shown that for WGN, Levich [86] and Maxworthy et al. [91] are in good agreement with Rodrigue [96] while Mendelson [84] is underestimated. On the other hand for WGA, Mendelson [84] and Levich [86] are in good agreement but Maxworthy et al. [91] is underestimated. The dimensionless approach of Rodrigue [96] claims to cover a rather wide range of parameters however it doesn't predict the cases in this study.
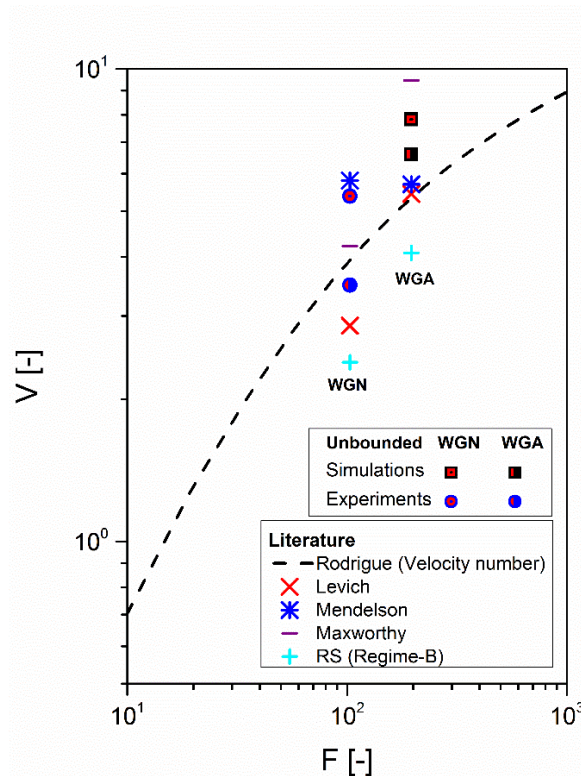

Fig. 18: Comparison of velocities in simulations and experiments with the models in the literature. Wall correction factor is applied for each case in simulations and experiments. V is the velocity number and F is the flow number defined by Rodrigue [96] (cf. Section 2.2.2).

3.4.2. Surface contamination effect

The contaminants accumulated on the phase interface have also a profound effect on the bubble rise velocity due to Marangoni effect (cf. Section 2.2.3) and modified bubble shape. The literature overview for the surface contamination effect of rising bubbles is given in Section 2.2.3. The possible effects on the cases WGA and WGN are discussed here.

Fig. 19 shows the dimensionless terminal velocity U_T^* calculated according to Eq. (14) in dependency of the dimensionless bubble diameter d_B^* calculated by Eq. (15) and presents the four characteristic regimes (A, B, C, D) graphically. These regimes are defined by Räbiger and Schlüter [106] based on the differentiation of bubble shapes. The empirical formula $U_{T,Ar}^* = 0.136 Ar^{0.4266}$ given in Eq. (18) shows reasonable approximation for different cases. It takes almost same value with WGA while underestimating the WGN and M7. Yet it is clear that $U_{T,Ar}^*$ is valid for pure systems flowing through an unbounded and long channel where no bubble frequency effect (due to the interaction between bubbles in chain) on velocity exists. The deviation between two and four walls of WGN cases is visible. The Regime-B of Räbiger and Schlüter [106] corresponds to the Region-2 of Peebles and Garber [83] and both apply similar drag and velocity correlations in their range. For all cases the viscous forces are mostly dominant however due to internal recirculation within the bubble and its intensity, shear stresses at the interface are reduced and the rise velocity increases [84], thus the domination of the inertial forces also increases.
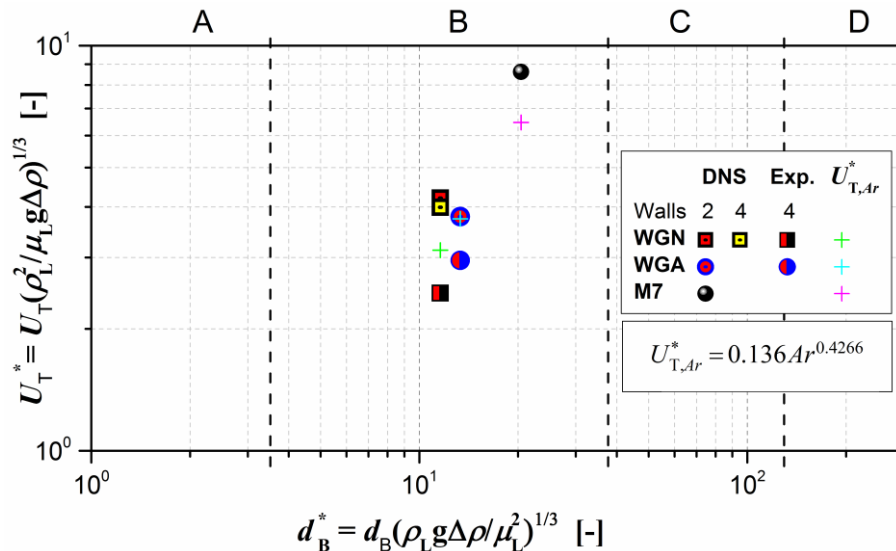

Fig. 19: Dimensionless terminal velocity of gas bubbles U_T^* as given in Eq. (14) in dependency of the dimensionless bubble diameter d_B^* as given Eq. (15). The graph is adopted from Räbiger and Schlüter [106].

The aspect ratio for WGA and WGN is observed as $\chi > 0.8$ (cf. Section 3.3.1, Fig. 16 a). Clift et al. [75] define bubbles and drops in the range of $1 < Re < 600$ as fluid spheres since they remain nearly spherical without significant deformation and exhibit little internal circulation because of high viscosity difference or surface contaminants. In Fig. 19, the results in simulations and experiments differ in terminal velocity values, reminding that no liquid velocity was deducted from the experimental values. These differences for the bubbles with same initial size and remaining spherical (as being in Regime-B and/or Region-2) may be explained by intensity of their internal circulation according to the argument of Clift et al. [75]. As it is discussed in Section 3.3.4, the varied Γ_μ is not the reason for different rise velocity even though it affects the intensity of recirculation as argued in Fig. 13 and Fig. 14. The surface contaminants, not only affecting the internal circulation but also modifying the wake formation, may then be the reason of velocity deviation between experiments and simulations. A type of surfactant Triton X was added into mixture for WGA case therefore the velocity difference is understandable. However, the above discussions suggest that the WGN case may also not be a pure mixture.

Consequences of both the viscous force dominant regime and the surface tension force dominant regime may apply to the cases WGA and WGN. The WGN case is implied to be a pure system while WGA is already contaminated with Triton-X. The experimental evidence shows that U_T does not depend on surfactant concentration [110], shape oscillation would gradually damp down even in a slightly contaminated system. A contaminant can eliminate internal circulation even if the amount of impurity is so small that there is no measurable change in the bulk fluid properties. Thereby it increases the drag significantly and reduces overall mass- and heat-transfer rates drastically [75]. As it is shown in Fig. 20, the calculated C_D in the experiments are significantly higher than the simulation values. This also supports the idea of impurity and contamination effect for both cases. Therefore, regardless from purity attempts in experiments, measured U_T may be expected to be lower than the simulations. In comparison to simulations, the bubbles in experiments are expected to be less deformed due to strong damping effect caused by surfactants and thereby to exhibit less zigzag and helical motions as a result of less scattered of U_T.

3.4.3. Drag model estimation

The rising bubble velocities can also be explained by means of the drag applied on bubbles. Most of the previous studies based on force balance approach calculated the terminal velocity dependent on the drag coefficient.

The conventional correlation for the drag on a sphere in steady motion as "standard drag curve" Clift et al. [75] is given in Fig. 20 where C_D is plotted as a function of Re. Fig. 20 also shows some of the popular correlations for C_D from the literature. The C_D values for cases WGN, WGA and M7 are calculated from the dimensionless definition given by Clift et al. [75] as

$$N_U = Re_T \big/ C_D = 3\rho^2 U_T^3 \big/ 4\Delta\rho g \mu_L \tag{73}$$

Here, Re_T is calculated by the correlation defined for the range of $580 < N_D \leq 1.55 \times 10^{-7}$ and $12.2 < Re \leq 6.35 \times 10^3$ as [75]

$$\log_{10} Re = -1.81391 + 1.34671 \cdot W - 0.12427 \cdot W^2 + 0.006344 \cdot W^3 \tag{74}$$

where $W = \log_{10} N_D$ and N_D is given in Eq. (26).
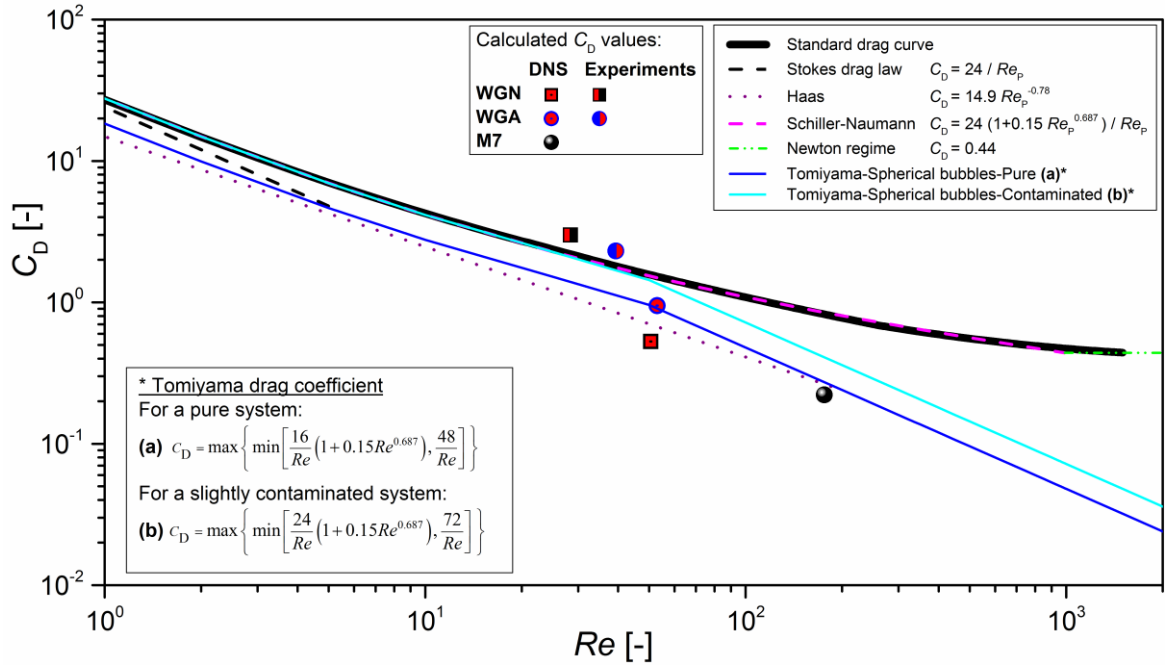
Fig. 20: Drag coefficient of a sphere as a function of Reynolds number. C_D values for the cases are calculated from Eq. (73) given by Clift et al. [75]. The evaluted cases are given in Table 2 and Table 3.

Fig. 20 shows that the experimental results calculated from Eq. (74) are well approximated by the standard drag curve and Tomiyama drag model for contaminated systems in Eq. (66). On the other hand, the DNS results are aligned with the Tomiyama drag model for pure systems in Eq.(64). In Fig. 20, the calculated C_D from the experimental data is significantly higher than the C_D from simulation values for both cases. Such a difference may occur if the purity is not fulfilled in the experiments.

Haberman and Morton [76] explains the "rigidity" of bubbles based on the equality of boundary conditions at the surface: In a contaminated system, the bubble surface attracts and holds a high concentration of particles or molecules of the surface-active substances. The molecules at the surface travel with the bubble and hence give the same boundary conditions as a rigid surface. As the shear forces become larger in comparison to the forces holding the molecules at the surface, "rigidity" at the surface cannot be maintained; circulation inside the bubble ensues and the drag of the bubble becomes smaller as compared to that of a rigid body. As compared to the perfect purity in DNS, the experiments for each system reflect the "rigidity" effect and result high C_D values. The impurity and contamination have influence on not only the WGA case but also the WGN case, which was intended to be pure in experiments.

The "rigidity" also influences the bubble shape. It is known that a flattened particle experiences larger drag force than that acting on an elongated or spherical particle with the same volume as far as the deformation is not so large [183]. The bubbles in the experiments stay always rigid and spherical due to the surfactant effect.

3.4.4. Validation with experiments and another code

Based on the measurements in the reference experiments from TUHH for the mean bubble diameter and the vertical spacing between the bubbles in the bubble chain, the coordinated DNS simulations are performed. The cases based on the experiments (cf. Section 3.2), WGA (water-air-glycerin mixture with the surfactant Triton-X) and WGN (nominally pure water-nitrogen mixture) are simulated with TURBIT-VOF at KIT (cf. Section 2.4.3). On the other hand, the project partner in TU-Darmstadt, the Mathematical Modeling and Analysis Group at CSI (Center of Smart Interfaces) has also simulated the WGN system with the OpenFOAM® solver interFoam [184] which uses an algebraic VOF approach.

In TURBIT-VOF, the Triton-X addition is taken into account via the changed value of the surface tension while the phase interface (in contrast to the experiment) remains fully mobile. For validation, two different computational domains are considered for L_{ref} = 4 mm. In the first one, the computational domain is defined as 5×1×1 (for a 250×50×50 grid) 20×4×4 mm³ with two side walls and periodic boundary conditions in two other directions. It is used for the simulations of WGA and WGN cases with TURBIT-VOF. The experimental setup is a similar vertical plate channel that is located in a cylindrical column where two 25 mm long vertical parallel plates are placed in distance of 4 mm. It is used for the Case WGA experiments. In the second one, the computational domain is defined as 4.5×2.5×1 (for a 288×160×64 grid) for 18×10×4

mm^3 with four side walls and periodic boundary conditions in the flow direction. This setup is used for the simulations of Case WGN with TURBIT-VOF. The experimental setup is a similar but longer rectangular channel of size 1000×10×4 mm^3. It is used for the Case WGN experiments. At the CSI, the simulations are performed for the WGN case in a rectangular channel both for a fully mobile phase interface and also for a partially contaminated and immobile interface using a so-called "stagnant cap" model [185], shortly S.C.M., which models the influence of surfactants on the hydrodynamics. The channel is long enough to minimize the bubble frequency effect due to the interaction between bubbles in chain (cf. Section 3.3.3). Table 4 gives an overview on the domain size applied for the cases in the simulations.

In the experiments, due to surface contamination, the bubble behaves as rigid sphere with an immobile interface where the particles cannot move on the surface. Yet, the surfactant effect is not considered in the simulations and therefore the bubble shape may take another form, i.e. fluid sphere or ellipsoidal bubbles [75]. In order to compare the experimental results with simulations for a contaminated system, surface contamination effects should be taken into account. For this purpose, the modified correlation from Grace et al. [97] is considered. It is used to estimate the contaminated U_T from pure U_T by using a correction factor (Γ) [75] given in Eq. (19). The contamination factor is calculated for the Case WGA, which is contaminated with surfactant Triton X, and for the so-called pure Case WGN in order to compare with the simulations from TU-Darmstadt with OpenFOAM® by using S.C.M. model. For WGA and WGN cases, Eq. (20) takes the value of 1.29 and 0.431; the correction factor (Γ) is read from the plot in Fig. 3 approximately as 0.2 and 1.4, respectively. The contamination coefficient in Eq.(21) is then calculated as 0.85 and 0.72 for WGA and WGN cases, respectively. The contaminated U_T is calculated by substituting the values of Γ, κ_{cont} and the pure terminal velocity from DNS data into Eq.(21).

For the contaminated system (Case WGA), the simulations are performed in computational domains 5×1×1 for a 250×50×50, 3×1×1 for a 150×50×50 grid and 2×1×1 for a 100×50×50. In Fig. 21, U_T is lower for longer channels and its profile comes to steady state faster due to the decreasing influence of bubble frequency. Ideally, the liquid in the wake must be almost stagnant before the following bubble enters to the slug. To eliminate the effect of the vortices in the bubble wake, the vertical distance between two bubbles must be long enough. Based on the findings in Section 3.3.3, the ratio $L_x / d_B > 10$ is identified as an acceptable estimation in terms of the magnitude of the liquid velocity influence on the bubble rise velocity. For the computational domain, 2×1×1 where $L_x / d_B \approx 4.2$, the profile of the bubble rise velocity is approximately 14%

higher than in domain 5×1×1 with $L_x / d_B \approx 10.5$ while the profile of the liquid velocity is twice as high as in domain 5×1×1. Both velocity profiles of the bubble and the liquid are increasing with the time. This is because the effect of the velocity profile of the leading bubble still influential and the liquid slug is not stagnant and therefore the rise velocity of the rear bubble increases slightly but continuously.

In Fig. 21, for the contaminated experimental system, the bubble rise velocity (U_T) calculated with TURBIT-VOF is about 30% higher than the measured value. However, the bubble rise velocity from TURBIT-VOF with the contamination coefficient $\kappa_{cont} U_T$ is only 6 – 10 % higher than the measured values in the experiments. There is no available data regarding the values of mean liquid velocity in the experiments. However, the wake effect is almost eliminated with a high L_x / d_B ratio, which means the liquid velocity in the wake is almost stagnant, and the velocity profiles are in Fig. 21 almost flat, which indicates that the mean liquid velocity in the experiments are negligibly low. Therefore, the velocity profile in the wake that occurs in the simulations is taken into account by a relative velocity $\kappa_{cont} U_T - U_L$, which is used for a better comparison with the experiments. The profile of the relative velocity is as flat as in the experiments and its values are about 3 – 6% higher than in the experiments.
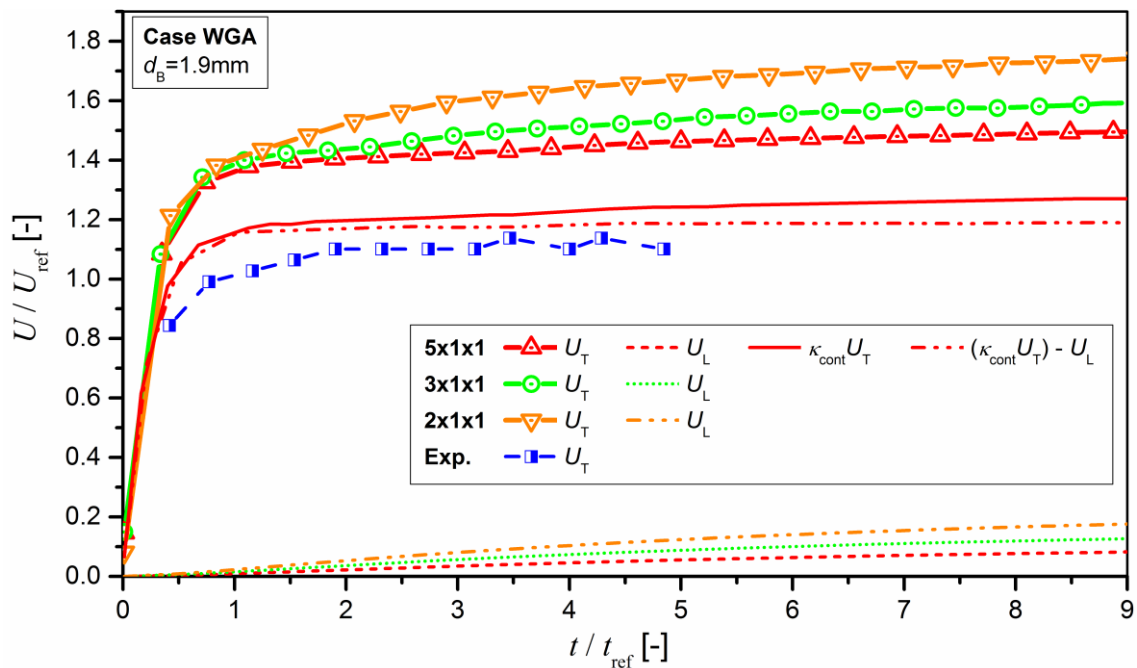

Fig. 21: The bubble rise velocity of WGA system from simulations and experiments. The experimental results represented with blue-dotted-line are provided by IMS in TU-Harmburg in the frame of the Multi-Phase Project.

In Fig. 22, the profiles of bubble rise velocity obtained from the DNS results with TURBIT-VOF (for two and four walls) are compared with the DNS results with OpenFOAM® and the experimental data. Besides, the profiles of the mean liquid velocity, the bubble rise velocity with the contamination coefficient $\kappa_{cont} U_T$, and the relative velocity calculated as $\kappa_{cont} U_T - U_L$ are discussed in the figure. The wake effect and the retarding effect of the surface contamination are taken into account with this relative velocity. For the so-called pure system (no intended surfactant in the WGN system), Fig. 22 shows a comparison of the velocity of a 1.67 mm bubble calculated with TURBIT-VOF and OpenFOAM® and measured at the TUHH. In the four walls case, the bubble deviates from the rectilinear path during the simulation. This is probably due to numerical inaccuracies relevant to the wall contact in lateral y (x_2) direction. In the case of two side walls in TURBIT-VOF, the bubble rises in a straight line and the bubble rise velocity is somewhat (4 – 5%) higher than with four side walls for the straight path, as expected due to the retarding wall effect.

Fig. 22 indicates that the bubble rise velocity is significantly lower in the experiment than predicted by the simulations. The bubble rise velocity in the TURBIT-VOF simulations for two walls is about twice as high as in the experiment. However, it is about 11% higher than in the DNS simulations of the CSI for a free mobile surface (without S.C.M.) in a channel with four side walls. This deviation is plausible due to the double periodic boundary conditions in TURBIT-VOF and the simple periodic boundary conditions in interFoam. The difference is even smaller and almost none compared to the incomplete simulations for four walls in TURBIT-VOF.

With the "stagnant cap" model (S.C.M.), a significant reduction in the U_T (by suppressing the internal circulation in the bubble) is observed in interFoam, which leads to a good agreement with the experimental results. The profile of bubble rise velocity with the contamination coefficient $\kappa_{cont} U_T$ is about 7% higher than the results with S.C.M. for an immobile surface. Since the rectangular channels in the experiments and in the simulations with OpenFOAM® are long enough, the U_T profiles are almost flat and therefore the liquid velocity in the wake is almost stagnant. To account for the wake effect in TURBIT-VOF (L_x / d_B ≈ 12 for 5×1×1 domain), the relative velocity is calculated as $\left(\kappa_{cont} U_T - U_L \right)$. The profile of the relative velocity is about 5% higher than in the DNS simulations of the CSI with S.C.M. This deviation corresponds to the retarding effect due to the four walls setup in interFoam, in contrary to the two walls setup in TURBIT-VOF.

The influence of impurities is very hard to avoid in experiments whereas it is easily eliminated in simulations. The experimental results are expected to depend on the

water quality. The surfactants introduced in the first series of experiments (Case WGA) are still present in the second (nominally pure) series of experiments (Case WGN). The surface-active agents hinder the internal circulation in the bubble and effect the hydrodynamics of the flow. Therefore, the experimental and numerical (DNS) results differ significantly. TURBIT-VOF always assumes a fully mobile interface. For comparison with these experiments, a relative U_T is calculated by applying the correction factor that accounts for the contamination effect and deducting the liquid velocity that accounts for the wake effect. The results from TURBIT-VOF simulations both for the U_T and the relative U_T are very close to those from the DNS simulations of the CSI in interFoam for a free mobile surface (without S.C.M.) and immobile surface (with S.C.M.), respectively.
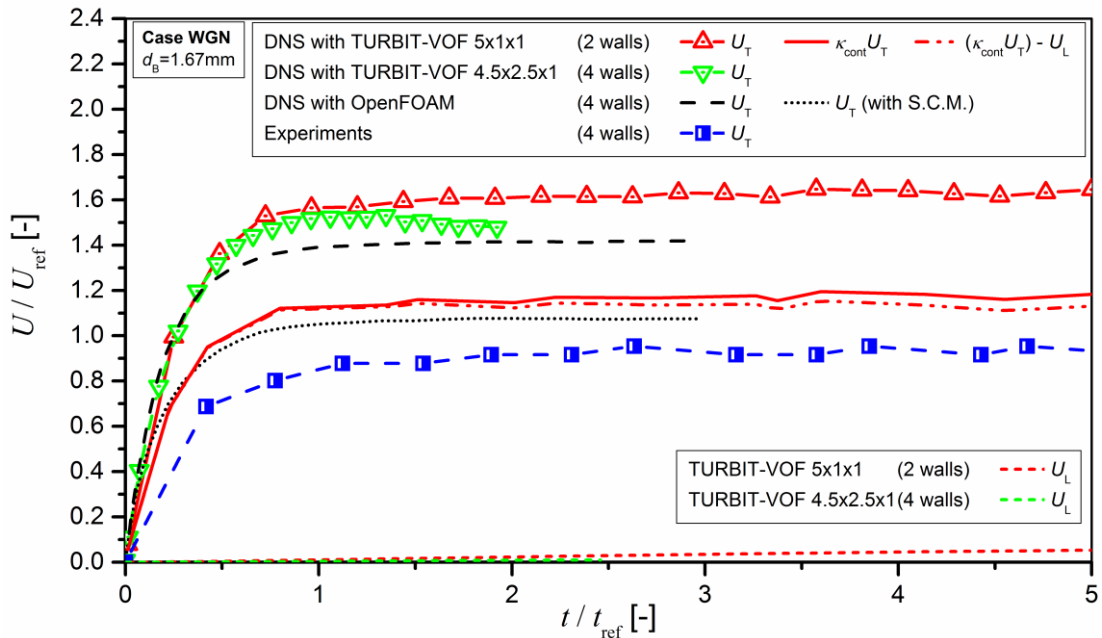

Fig. 22: The bubble rise velocity of WGN system from simulations and experiments. The experimental results represented with blue-dotted-line are provided by IMS in TU-Harmburg and the DNS results with OpenFOAM® represented with black lines are provided by CSI in TU-Darmstadt in the frame of the Multi-Phase Project.

3.4.5. Summary of Section 3.4

The results for the terminal velocity of the rising single bubbles (U_T) are compared with the correlations from the literature, which are mainly valid for unbounded channels. A multiple-step correction calculation from Clift et al. [75] for circular ducts is identified as the most general approach to account for the wall effects in a wide range of non-dimensional parameters $Eö < 40$, $Re > 200$ and $d_B / L_{wall} \leq 0.6$. There is no simple

approach to account for the parallel wall effects in rectangular channels. After a comprehensive review, no universal model is found to approximate U_T. The available models are valid for strictly defined flow parameters. The validation range concept from Peebles and Garber [83] is able to limit the cases examined here to a certain region and the correlations from Mendelson [84] and Maxworthy et al. [91] provide close estimations to simulation and reference experimental results. Räbiger and Schlüter [106] define another validation range approach for U_T based on different bubble shapes which consequently accounts for the purity of system. The surface contaminants affect the internal circulation in the bubble and modify the wake formation, thus, have impact on bubble shape and U_T. Therefore, a correlation from Grace et al. [97] that involves bubble Eötvös number and viscosity ratio of phases is distinguished for calculating a contamination coefficient. This correlation provides reliable results in a code-to-code comparison within this study. Besides, following comparisons of different models for the drag coefficient C_D with numerical results, the model from Tomiyama et al. [102] is identified as suitable for bubble swarm simulations.

The DNS results are further validated with the reference experiments and the DNS results obtained from VOF based code interFoam (an OpenFOAM® solver) using the similar setup and flow properties in the frame of the joint Multi-Phase project. The results from TURBIT-VOF simulations both for the U_T and the relative U_T are very close to those from the DNS simulations of the CSI in interFoam for a free mobile surface (without S.C.M.) and immobile surface (with S.C.M.), respectively. The deviation is 11% and 7%. Besides, the both DNS results that account for the surfactant effects are close to the results from the reference experiments.

3.5. Bubble swarm simulations

This Section is focused on multi-bubble (bubble swarm) simulations, issues encountered before finding useful simulation sets for analysis of turbulence kinetic energy of liquid phase and the method for extending the number of bubbles in a domain to higher values. Part of the results and some figures presented in this Section have been published in Wörner and Erdogan [6]. The bubble swarms are modeled as a group of bubbles in a computational domain with periodic boundary conditions.

Earlier in this Chapter, an extended study of freely rising single bubbles was carried out in terms of numerical and hydrodynamic point of view. Those studies shed light onto important issues for sustaining stable bubble swarm simulations for achieving convergence of statistical data. Based on the study for single bubbles, significant number of DNS calculations for bubble swarms were performed (29 cases among them

are given in Table 15 in the Appendix.A.1) in order to use in analysis of turbulence kinetic energy of liquid phase.

In the simulations, a variety of parameters was chosen as follows: Number of bubbles 4 – 8, bubble diameter d_B 1 – 5 mm, gas content ε_G 1 – 6.5%, Morton number 10^{-7} – 10^{-10}, Eötvös number 0.1 – 10. However, only some of these results are discussed subsequently. In order to identify parameters that allow efficient simulations without compromising the physics, a grid resolution of 20 cells per bubble diameter, a liquid-to-gas density ratio of 25 and a liquid-to-gas viscosity ratio of between 1 and 5 are used to obtain results that are independent from the mesh size as well as the gas density and viscosity.
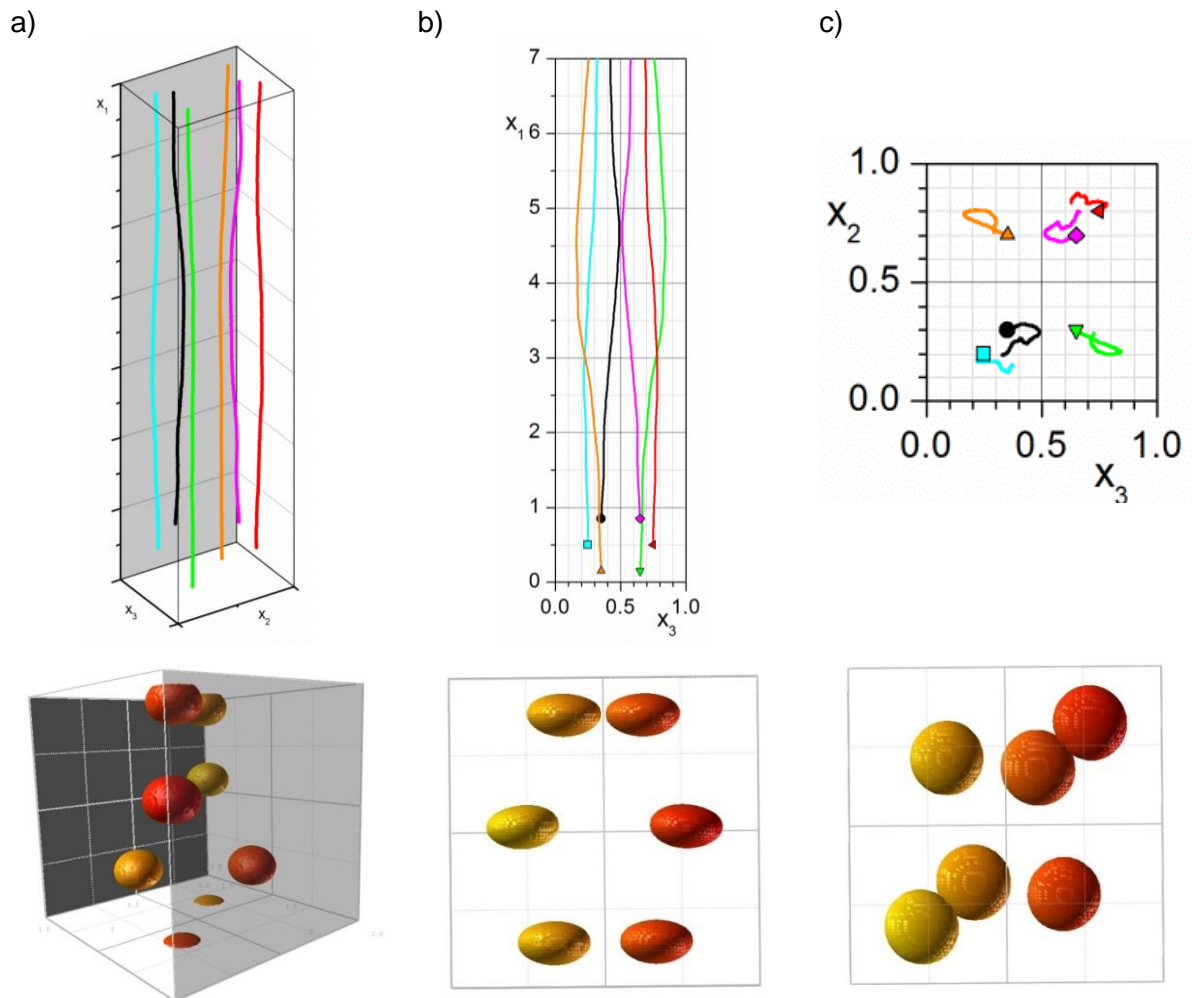
Fig. 23: Trajectories of individual bubbles and captures from simulations for Case No.6 with 6 bubbles in domain given in Table 15 in Appendix.A.1. ε_G = 2.5%, $E\ddot{o}_B$ = 2.5, M = 2.2 × 10^{-7}. a) 3D view. The channel walls are highlighted gray/dark gray. b) x_1-x_3 plane (plane between walls) c) x_2-x_3 plane (above). The symbols represent initial bubble centroid positions.

The bubble-induced velocity fluctuations of the liquid phase are strongly related to the dynamics of bubbles. This is particularly expected in bubble swarm flows where the motion of an individual bubble is more complex. For the later turbulence analysis it is, therefore, advantageous to determine bubble trajectories [26]. Fig. 23 shows the analyses of bubble trajectories for Case No. 6 (see Table 15) in mono-disperse condition, before the coalescence occurs. For this case, it can be seen that the bubbles are no longer spherical and tend to follow a helical path. The initial conditions at $t = 0$ for Case No. 6 are same as the setup explained in Fig. 8 in Section 3.1.

Ilic [26] found that the bubbles move, not only into the adjacent periodic box in the vertical direction through buoyancy, but also in both horizontal directions, wall normal and span-wise, through the dispersion. This movement can be also seen in Fig. 23 b) and c). These lateral movements of bubbles result in the formation of two distinctive bubble populations. Bubbles tend to align at approximately constant distance from the walls making a kind of bubble curtains between the central liquid core and downward flowing liquid layers next to the walls [26].

3.5.1. Issues in DNS of bubble swarms

In multi-bubble simulations in narrow bubble columns two problems occur. The first one concerns the approach of bubbles toward the wall. The second and more severe problem in the context of the present study concerns bubble coalescence. Part of the discussions in this Section are published in Wörner and Erdogan [6].

a) Wall contact problem

When a part of the bubble enters the mesh cell layer that is closest to the wall, the liquid film between the bubble and the wall is not resolved. This may lead to artificial wall contact of the bubble [6]. Fig. 24 a) shows the approach of bubbles toward the wall at an instant time at which the simulation stops. This is because the contact lines, which denote the intersection of the interface between two immiscible fluids with the solid wall, are not calculated in TURBIT-VOF code. To circumvent this problem a grid that is non-equidistant in z-direction with refinement near the side walls is used. Fig. 24 b) shows the influence of this refinement on the same individual bubbles that cause wall contact for equidistant grid. The bubble in non-equidistant meshed domain (red-dashed-line trajectory) rises on a straighter trajectory than that in equidistant meshed domain (blue-line trajectory). By this refinement, the liquid film between the bubble and the wall can be resolved better and the interaction of the interface and the wall is understood correctly.
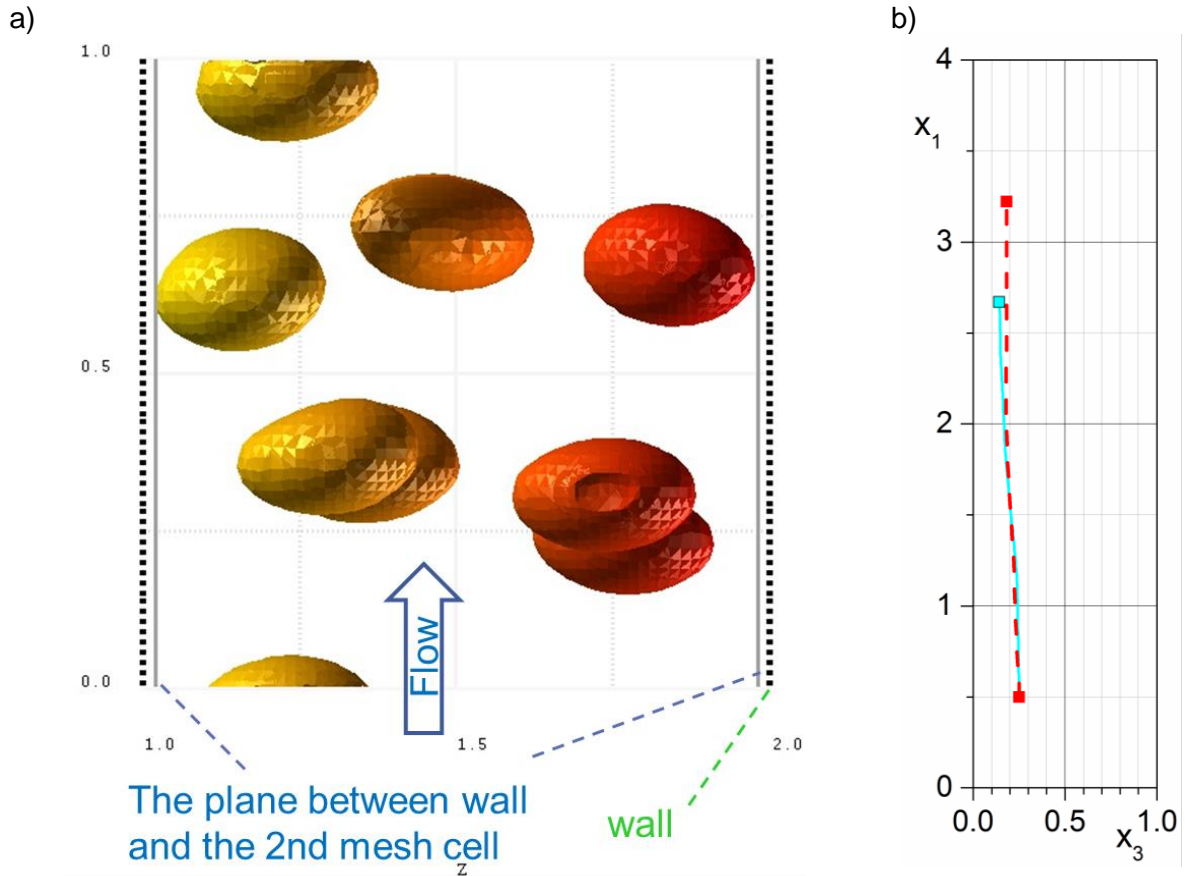
Fig. 24: The approach of bubbles toward the wall for Case No.8 with 8 bubbles in domain given in Table 15 in Appendix.A.1. a) An instant time at which the code stops the simulation when a part of the bubble is between the first and second mesh cell next to the wall. b) Trajectories of same individual bubbles in a domain with equadistant (blue-line trajectory) and non-equadistant grid (red-dashed-line trajectory).

b) Coalescence problem

Coalescence is an unresolved problem in DNS of interfacial flows as some methods (e.g. front- tracking) suppress it while others like VOF lead to artificial coalescence [47]. In the VOF method in this work, coalescence is initiated when the distance between two bubbles is less than the size of a mesh cell [6] and is therefore grid-dependent [5]. To limit the physical complexity problem, the investigations within in this study aim at mono-disperse bubbly flows. Bubble coalescence is therefore unwanted. In the DNS studies of Ilic et al. [20], mono-disperse conditions could be preserved for $M \geq 3{\times}10^{-6}$ and $Eö_B \leq 3.065$ with void fractions up to 6.4% (up to eight bubbles, $\mu_G / \mu_L = 1$, $\rho_G / \rho_L = 1/2$). Here, in this work, the DNS computations are performed for various conditions with similar values of the Eötvös number but for smaller values of the Morton number. It has been found that for lower Morton numbers the probability for coalescence in the simulations is significantly increased [5, 6].
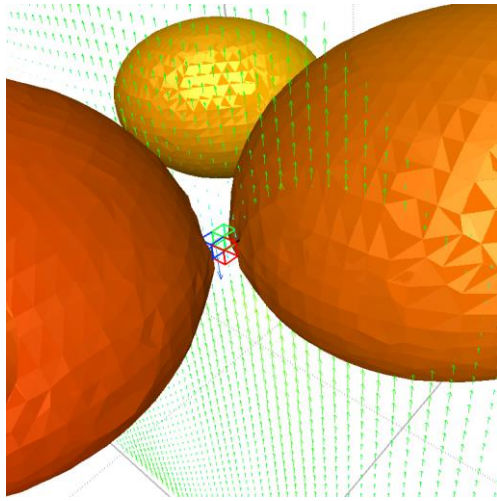
a) t = 0.0593 s   b) t = 0.0595 s
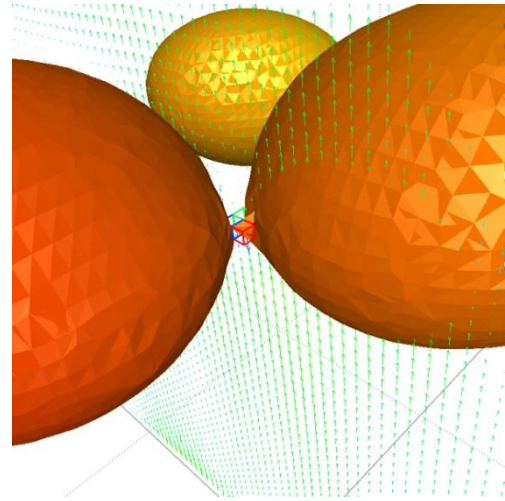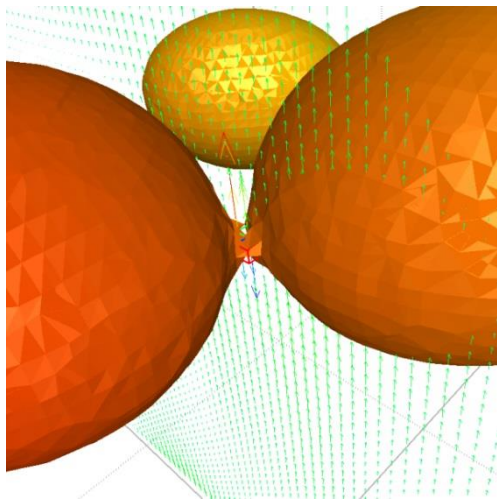
c) t = 0.0597 s   d) t = 0.0598 s
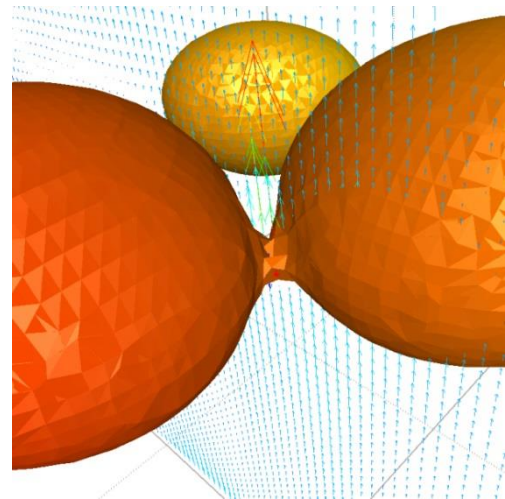
Fig. 25: Illustration of the coalescence of two bubbles at four different time points (Morton number M = 2.8×10^{-7}, Eötvös number $E\ddot{o}$ = 1.265, Case No.11 with 8 bubbles in domain given in Table 15 in Appendix.A.1). When two bubbles approach (a) and the distance between them becomes smaller than a mesh width, the two interfaces make a bond (b) and form a gas bridge (c), which increases in time (d) and leads to coalescence. The small boxes between the bubbles indicate single mesh cells. The vertical vector field in flow direction is shown in coloured scale. Taken from Wörner and Erdogan [6].

Fig. 25 shows the close-up visualizations of a small section in a bubble swarm simulation (M = 2.8×10^{-8}, $E\ddot{o}_B$= 1.265) with eight bubbles at four consecutive slightly different instants in time. (For more frames of this visualization over a longer period, see Fig. 53 in the Appendix.A.2). When the distance between two bubbles becomes

less than one mesh cell (Fig. 25 a)) both two interfaces connect (Fig. 25 b)) and form a gas bridge (Fig. 25 c)) that grows in time (Fig. 25 d)) and finally leads to coalescence. Since the spatial resolution of the gas bridge is only a few mesh cells, the estimation of interface normal vector and curvature is rather inaccurate and leads to large erroneous velocity vectors (Fig. 25 c) and d)). It is obvious that the initialization of the coalescence process depends on the mesh size. Numerical coalescence can be prevented by using a separate VOF function for each bubble [186]. Such an approach is applied within the Multi-Phase project in the simulations of the TU-Darmstadt. However, the associate computational effort strongly increases with the number of bubbles.

3.5.2. Selected simulation cases

The overall void fraction is a critical issue in the bubble swarm simulations. Mono-disperse flows, which represent a useful restriction for the analysis of the k_L equation, are main interest in this work and bubble coalescence is therefore unwanted. To avoid coalescence, only selected results from the total of 29 different DNS cases (given in Table 15 in Appendix.A.1) with the rather low gas holdup of 2.1% and 2.5% in the domain are considered here. From many tests, a gas holdup ε_G of about 2.5 % is found as a reasonable upper limit for preserving mono-disperse flow in the simulations within this study. However, coalescence occurs occasionally even for lower values of ε_G. In the present set-up, ε_G depends on the ratio d_{eq} / L_{wall} and on the number of bubbles within the cubic domain. Here, $L_{wall} = L_{ref} = 5d_B$ is chosen. The number of bubbles within the computational domain is either five or six. This corresponds to an overall gas content of ε_G = 2.1% and 2.5 %, respectively. The discussions in this Section have been published in Erdogan and Wörner [5].

The direct numerical simulations and the analysis of the transport equation of liquid phase turbulence kinetic energy are motivated from the work of Ilic [20, 26]. In those works, the simulations were performed for Morton numbers (M) in the range of $3\times10^{-2} - 3\times10^{-6}$ and the Eötvös number $E\ddot{o}$ = 3.065 with the density ratio $\Gamma_\rho = \rho_G$ / ρ_L = 1/2 and the viscosity ratio $\Gamma_\mu = \mu_G$ / μ_L = 1. The bubble Reynolds number (Re) was in the range 1 − 90. In this study, the simulations are extended to lower values of the Morton number M and a wide range of the Eötvös number $E\ddot{o}$ and thus to higher values of Re as well as more realistic density and viscosity ratios. Numerical simulations for bubble swarms are performed for two scenarios, where some parameters are varied while others are fixed, see Table 5 and Table 6. The values of the liquid density slightly differ for Scenario A and B while the gas-to-liquid density ratio is always ρ_G/ρ_L = 1/25.

The liquid viscosity is in the range 0.44 mPas ≤ μ_L ≤ 5 mPas, the surface tension is in the range 0.0028 N/m ≤ σ ≤ 0.028 N/m. These variations yield values of the Morton number in the range 2.2×10^{-8} ≤ M ≤ 3.1×10^{-7}. The cases contain five and six bubbles and the volume-equivalent bubble diameter is in the range 1 mm ≤ d_B ≤ 3 mm, which corresponds to Eötvös numbers in the range 0.747 ≤ $E\ddot{o}_B$ ≤ 2.625. The cases with $M \approx 10^{-7}$ are started from spherical bubbles with both, liquid and gas at rest. Instead, the cases for $M \approx 10^{-8}$ are started from simulations runs with $M \approx 10^{-7}$. For most cases, the simulations have already achieved statistically steady flow conditions. A mean value of the bubble Reynolds number, Re_B, which is in the range 35 – 230 is calculated from the mean velocity of bubbles in the swarm. As expected, Re_B increases for scenario A with increase of d_B and $E\ddot{o}_B$, and increases for scenario B with decrease of the Morton number.

Table 5:   Scenario A - Cases with variation of $E\ddot{o}_B$ and ε_G and following fixed parameters: ρ_L = 867 kg/m³, μ_L = 5 mPas, σ = 0.028 N/m, M = 3.1×10^{-7}, μ_G/μ_L = 1/3. Non-equidistant grid with 100 × 100 × 120 cells. Adapted from Erdogan and Wörner [5].

Case	A1	A2	A3	A4
Number of bubbles	5	5 (3)	5	6 (4)
d_B [mm]	1.6	2.0	3.0	2.0
ε_G [%]	2.1	2.1	2.1	2.5
$E\ddot{o}$	0.747	1.167	2.625	1.167
Re_B (mean)	35	55	115	60
Coalescence	No	No (Later 2 times)	No	2 times

Table 6:   Scenario B - Cases with variation of the Morton number and following fixed parameters: 6 bubbles, ρ_L = 752 kg/m³, ε_G = 2.5%, d_B = 1 mm, $E\ddot{o}_B$ = 2.53, σ = 0.0028 N/m, μ_G/μ_L = 1. Equidistant grid with 100 × 100 × 100 cells. Adapted from Erdogan and Wörner [5].

Case	B-M7	B-M8
Number of bubbles	6	6
μ_L [mPas]	0.79	0.44
M	2.2×10^{-7}	2.2×10^{-8}
Re_B (mean)	125	230
Coalescence	No	No

The Scenario A includes four simulations with five or six bubbles for three different bubble diameters in the range of 1.6 – 3 mm and the fixed parameters ρ_L = 867 kg/m³, μ_L = 5 mPas, σ = 0.028 N/m, μ_G/μ_L = 1/3. In all simulations, the ratio d_{eq} / L_{ref} = 1/5 is fixed so that with variation of d_B, the wall distance L_{ref} and the volume of the

computational domain $(L_{ref})^3$ also vary. The Cartesian grid consists of 100 × 100 × 120 mesh cells. It is equidistant in x- and y-direction but non-equidistant in z-direction with finer cells near the walls to resolve the liquid film between bubbles and walls better. From Case A1 to A3, $E\ddot{o}_B$ increases and accordingly the bubble shape changes from almost spherical to ellipsoidal. For Case A1 and A3 the flow stays mono-disperse whereas in Case A2 and Case A4 coalescence occurs two times between different bubble couples. Case A2 is averaged over the time interval both with mono-disperse and bi-disperse flow. Case A4 is averaged only over the time interval during bi-disperse flow with four bubbles exists in the later part of the simulation, where the two larger bubbles having the double volume of the two smaller bubbles. The number of bubbles in Table 6 refers to the initial conditions of the simulation. The value in brackets for the cases with coalescence indicates the remaining number of bubbles after the coalescence. Gas holdup of Case A4 is ε_G = 2.5% while that of other cases in Scenario A are $\varepsilon_G = 2.1\%$.

The Scenario B includes two simulations with six bubbles for a bubble diameter of 1 mm and the fixed parameters ρ_L = 752 kg/m³, σ = 0.0028 N/m, μ_G/μ_L = 1. The Cartesian grid consists of 100 × 100 × 100 mesh cells and is equidistant in all directions. The gas holdup ε_G = 2.5% and the Eötvös number $E\ddot{o}$ = 2.53 are also fixed. The Morton number is varied from 2.2×10^{-8} to 2.2×10^{-7} due to different liquid viscosities (μ_L = 0.79 and 0.44 mPas).

3.5.3. Domain replication

In Fig. 26, on the right side, it is illustrated how a single domain is replicated to multiple domains and transform to a bubble column, as shown on the left side of the figure. For the DNS calculations with multiple bubbles, to limit the computation time until a statistically steady state is reached and to improve the statistical evaluation in general, the following strategy is applied. First, a simulation with 4 − 8 bubbles in a small domain was performed till the statistically steady state. The DNS data on the last time points were then replicated in the both periodic directions. This increases the computational domain and the number of bubbles by a factor of four where the gas content remains the same. The simulations were then continued for the four-fold larger computational domain (with more degrees of freedom for the relative arrangement of the bubbles) till a statistically steady state which can be evaluated. This procedure is tested in Chapter 4 and the results are reliable.
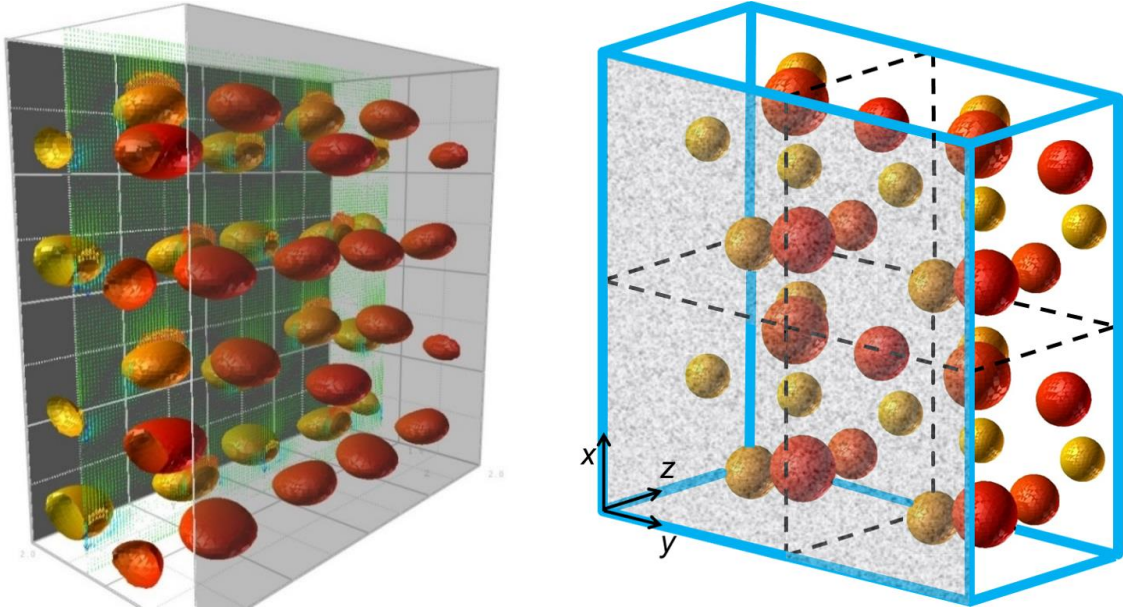
Fig. 26: Left: A view from the simulations (replicated domain of Case B-M7, Table 6). Right: An illustration of replicating the domain in the direction of periodic boundary conditions in order to increase number of bubbles.

3.5.4. Summary of Section 3.5

For the bubble swarm simulations, the values of liquid viscosity and surface tension between gas and liquid are in the range of 0.44 mPas ≤ μ_L ≤ 5 mPas and 0.0028 N/m ≤ σ ≤ 0.028 N/m, respectively. These values yield the Morton number between 2.2×10^{-8} ≤ M ≤ 3.1×10^{-7} and the Eötvös numbers in the range of 0.747 ≤ $E\ddot{o}$ ≤ 2.625. The bubble swarm simulations are performed in a domain with an overall gas content of ε_G = 2.1% and 2.5 % containing five or six bubbles with the volume equivalent bubble diameter 1 mm ≤ d_B ≤ 3 mm.

DNS of bubble swarms suffer from imprecise treatment of coalescence, which is – depending on the numerical method – either completely suppressed or artificially enhanced [6]. In the bubble swarm simulations, numerical coalescence occurs related to the mesh size and the VOF method. The process takes place mainly within a single mesh cell. Using a separate VOF function for each bubble [186] is recommended in the literature to circumvent numerical coalescence but this requires high computational effort depending on the number of bubbles. Alternatively, the physical and numerical parameters must be limited to preserve mono-disperse flow in the simulations. In this work, the void fraction in the domain is limited to 2 – 2.5 %. Despite the limitations, coalescence still occurs occasionally. To avoid the coalescence the ratio of the wall distance to the bubble diameter L_{wall} / d_B > 5 is another necessary condition. To maintain the rectilinear bubble trajectory with least possible lateral motions the Morton

number is chosen between $2.2 \times 10^{-8} \leq M \leq 3.1 \times 10^{-7}$ whereas the Eötvös number is in the range of $0.747 \leq E\ddot{o} \leq 2.625$.

Another problem in multi-bubble simulations is the approach of bubbles toward the wall. This problem is avoided by using a grid that is non-equidistant in wall direction with refinement near the side walls to resolve the liquid film between the bubble and the wall. The ratio of $L_{wall} / d_B > 5$ is also important to avoid wall contact of bubbles if the liquid film between bubble and wall are not well resolved.

The number of bubbles is increased using a domain replication methodology. In this study, the computational domain with up to 64 bubbles are obtained but because of required time step width and high CPU effort only the simulation up to 24 bubbles are further performed and analyzed for the turbulence kinetic energy. A grid resolution of 20 cells per bubble diameter and a liquid-to-gas density ratio of 25 are used to obtain results that are independent from the mesh size and the density of gas. The gas-to-liquid viscosity ratio is $\Gamma_\mu \leq 1$.

4. Analysis of Turbulence Kinetic Energy Equation of Liquid Phase

This Chapter presents the evaluation of the DNS results of the bubble swarm simulations for development of improved turbulence models for the Euler-Euler two-fluid model. The focus here is on the transport equation for TKE of the liquid (k_L-equation given in Eq. (34)), which is the cornerstone in the statistical k-ε turbulence models commonly used for industrial applications. The methodological approach is explained in Section 2.5.4. Some part of the results and figures presented in this Chapter have been published in Erdogan and Wörner [5].

Hereafter, the DNS results from Section 3.4.5 are used to analyze k_L-equation and to develop improved closure assumptions on this basis. For this purpose, first, the profiles and budget of k_L, which is obtained by evaluation of all terms in Eq. (34) from the DNS data, is discussed. Then, the DNS results for the interfacial term I_{kL} is compared with four closure relations from literature. This so-called a-priori-testing allows us to identify suitable models and propose potential improvements. The recommended model for I_{kL} is tested in the two-fluid model computations in Chapter 5.

4.1. Distribution of kinetic energy

In Fig. 27, the wall-normal profiles of the turbulence kinetic energy of the liquid for the six cases in Table 5 and Table 6 are plotted. It can be seen that for Scenario-A, the maximum value of k_L and the integral of k_L profiles over the channel increase with the increase of d_B and $E\ddot{o}_B$. For Scenario-B, both values increase with the decreasing liquid viscosity and Morton number. For each scenario, k_L increases with increase of the bubble Reynolds number. However, a comparison of Case B-M7 and Case B-M8 with Case A4 shows that in the former two cases k_L is lower although Re_B is higher. This may be attributed to the different values of the viscosity ratio, which notably influences the liquid velocity in the bubble wake (cf. Section 3.3.4) [5].

Between the cases A2 and A4 it is difficult to make a certain comparison in terms of void fraction since for Case A4 coalescence occurs two times between different bubble couples thus eventually two initial size and two bubbles with double volume exist in the time interval of the statistical analysis. In Fig. 27, if we pay attention to the curve with light blue circles (Case A4), we can realize the influence of the different bubble sizes in the bi-disperse flow. The kinetic energy curve is not symmetrical since the main interfacial term is higher at certain regions depending on the higher void fraction of the merged bubbles. For other cases, almost symmetrical curves appear

even though slight changes are visible. This is because the evaluation period in a statistically steady state is not yet sufficient [5].
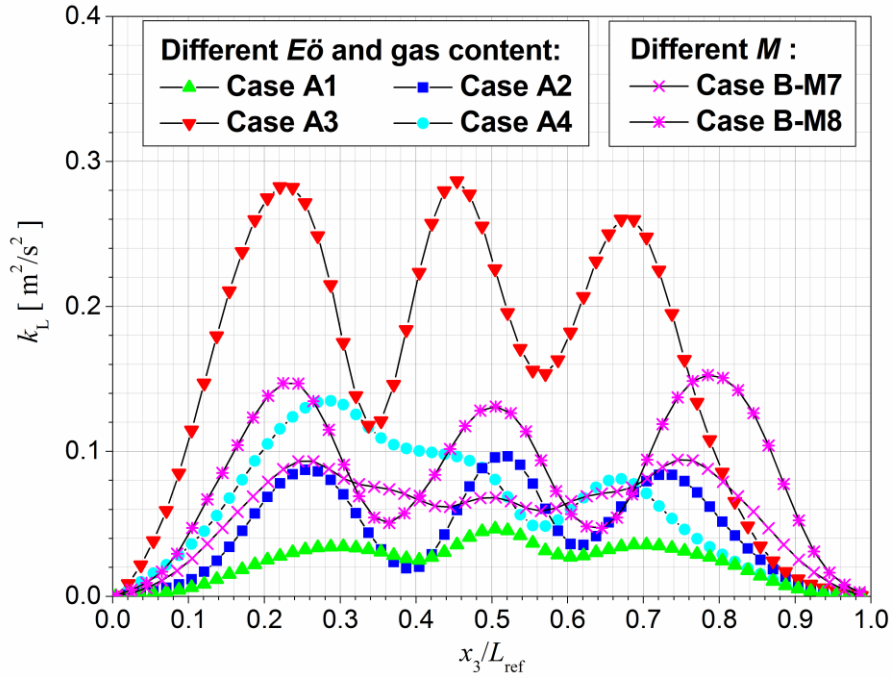

Fig. 27: Kinetic energy of liquid velocity fluctuations generated by bubble rise through liquids for the selected cases Scenario A in Table 5 and Scenario B in Table 6. In the Scenario A cases, the $E\ddot{o}_B$ (0.747 for A1, 1.167 for A2 and A4, 2.625 for A3) and ε_G (2.1% for A1, A2, A3 and 2.5% for A4) are varied while $M = 3.1\times10^{-7}$ is fixed. In the Scenario B cases, the M is varied (2.2×10^{-7} for B-M7 and 2.2×10^{-8} for B-M8) while the ε_G = 2.5%, $E\ddot{o}_B$ = 2.53 are fixed. Figure is taken from Erdogan and Wörner [5].

Fig. 28 shows the components of the averaged mean liquid velocity for the bubble swarms in Case B-M7. The vertical component of the mean liquid velocity in flow direction $u_{L,1}$ is higher than the ones in horizontal directions, $u_{L,2}$ and $u_{L,3}$. The velocity profiles are not symmetrical since the flow is not in an exact steady state. Periodic boundary conditions are applied for x_1- and x_2-directions. However, the structure of the liquid flow in x_2-direction strongly depends on the number of suspended bubbles and therefore is more complex. The profiles, where the domain is replicated in flow direction and lateral direction, are well matching with the profiles of the initial domain.

The root-mean-square (r.m.s) of liquid velocity fluctuations induced by motion of bubble swarms through liquid in each direction are given in Fig. 29, where the profiles of initial domain are compared with two different replicated domains: 2x1x1 where the domain is replicated only in flow direction and 2x2x1 where the replication is applied both in flow and lateral direction. The results for both replicated domains reflect are

very close to the initial domain. In Fig. 29 the fluctuations in the vertical direction strongly dominate the ones in the lateral and span-wise directions. The magnitude of the profiles in span-wise direction is higher than the one in the wall-normal direction.
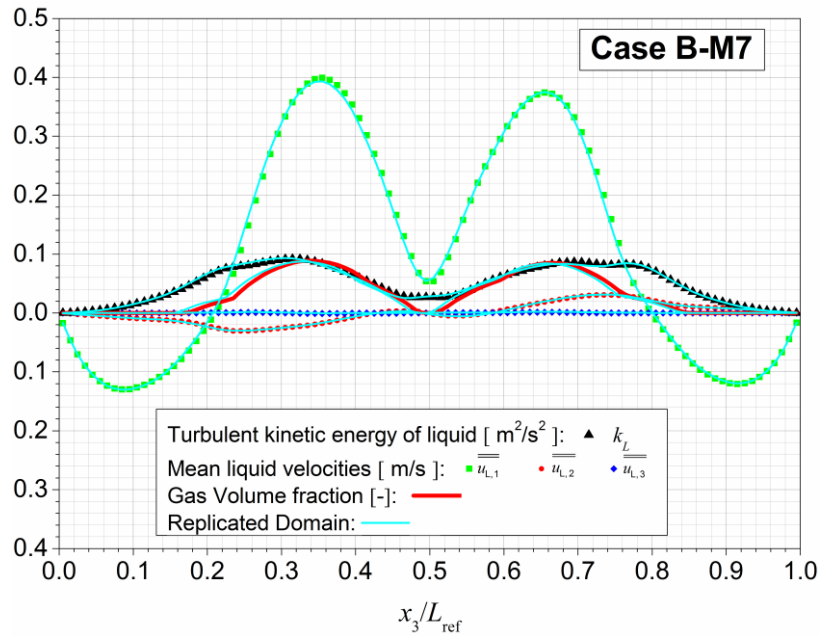
Fig. 28: Wall normal profiles of the turbulence kinetic energy of the liquid and mean liquid velocities for Case B-M7 given in Table 6 in comparison with replicated domain 2x2x1 (24 bubbles).
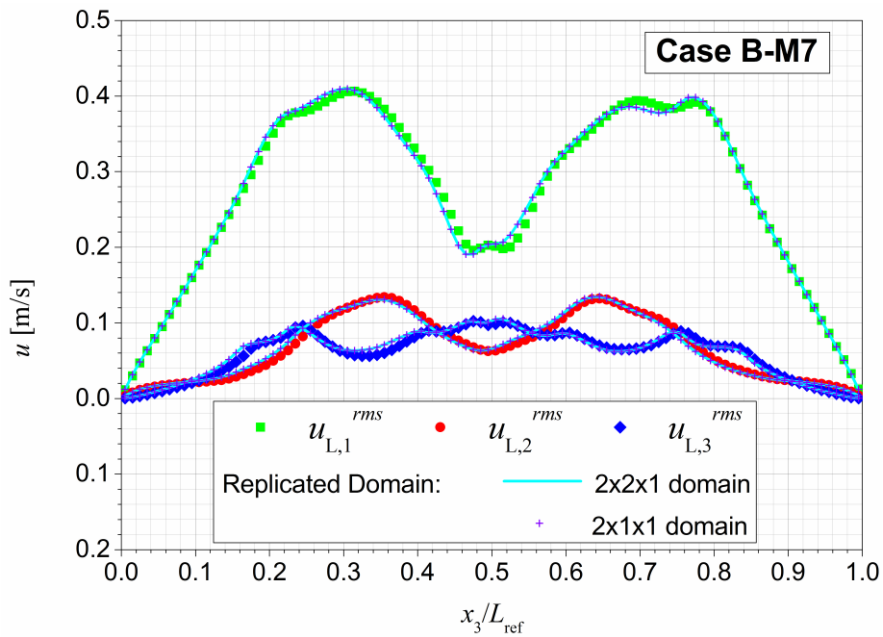

Fig. 29: Root mean square of liquid velocity fluctuations induced by motion of bubble swarms through liquid for Case B-M7 given in Table 6 in comparison with replicated domain 2x1x1 (12 bubbles) and 2x2x1 (24 bubbles).

4.2. Budget of k_L-equation

In this Section, the budget of k_L-equation, which is obtained by evaluating the Eq. (34) from the DNS data for the selected cases, is discussed. Except for the unsteady term, all terms are evaluated in accordance with the averaging method described in Section 2.4.4 (see more about it in Ilic [26]). The profile of the convection term on the left side of equation Eq. (34) was also evaluated, but it is not shown here since the values are negligibly small, compared to the other terms.
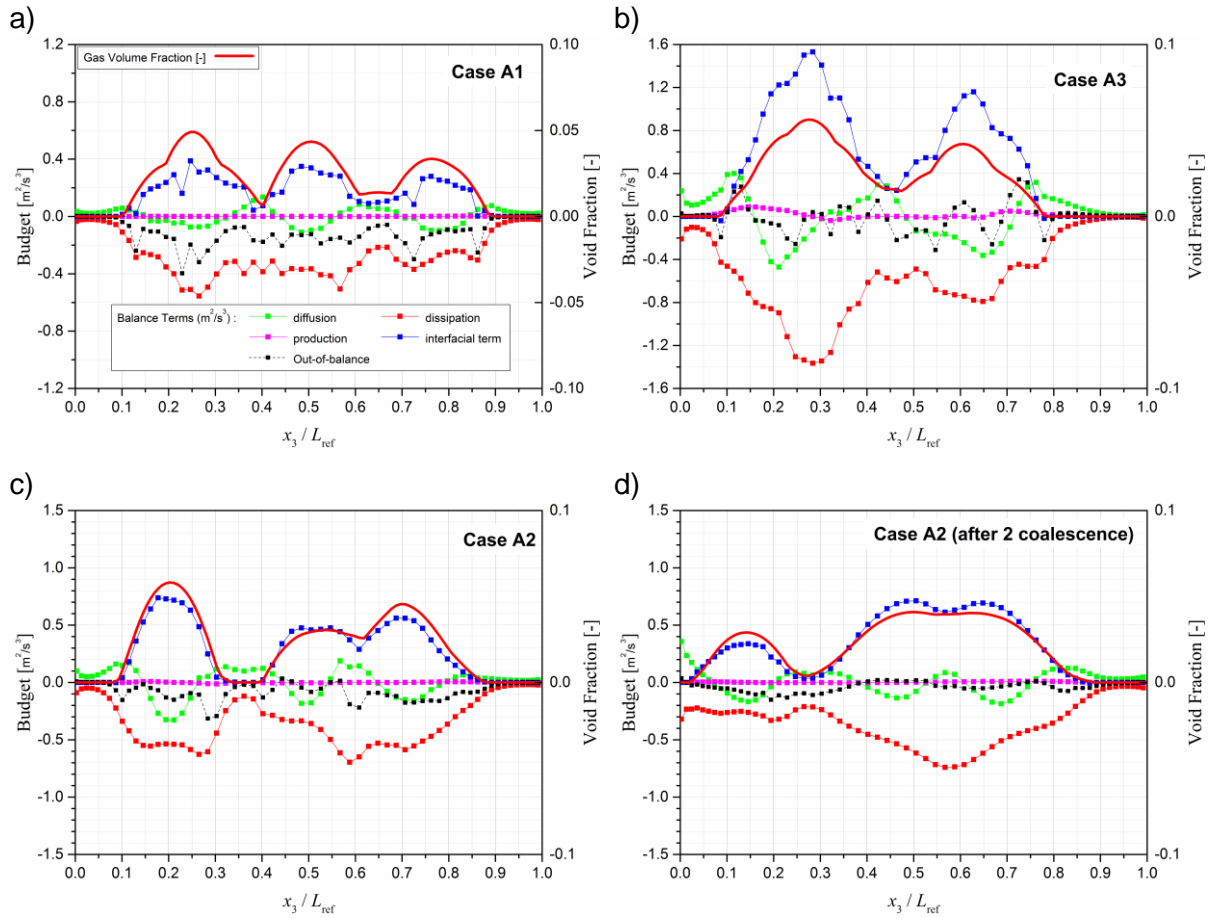
Fig. 30: Budget of the exact k_L-equation for Case A1 (a), Case A3 (b), Case A2 (c) and Case A2 after two coalescence (d). The cases are given in Table 5.

Fig. 30 and Fig. 31 show the wall normal profiles of the mean gas content and the four closure terms on the right side of equation Eq. (34) as evaluated from the DNS data for the cases A1, A2, A3 and B-M7. The sum of four closure terms is indicated as the "out of balance term", O_{kL}. This term should be close to zero for a statistically fully developed flow. For a statistically not fully developed flow, O_{kL} represents essentially the unsteady term in Eq. (34). O_{kL} also includes all inaccuracies based on the numerical evaluation of the other terms. For the cases evaluated in this study, the

magnitude of O_{kL} is always much smaller than that of the maximum balance terms, such as the dissipation term ε and the interfacial source term I_{kL}. This indicates that the statistical evaluation is sufficiently reliable.

For Case B-M7, all profiles in Fig. 31 are very symmetrical, which is because the six bubbles in this case rise relatively straight without big interaction among themselves. For the Case A1, A2 and A3 in Fig. 30 a), b), c), the profiles are much more asymmetrical due to the uneven number of bubbles. In Fig. 30 d), the asymmetry increases due to two coalescence. Also shown in the figures is the profile of the mean gas volume fraction α_G. On the parts where the bubbles with higher volumes appear, the high α_G values can be observed. It is zero in the regions close to the lateral walls (where the liquid flows downwards so that the lift force is directed away from the wall) and takes local values up to 9% (Case B-M7) and 6% (Case A3), although the overall gas holdup is only 2.5% and 2.1%, respectively.
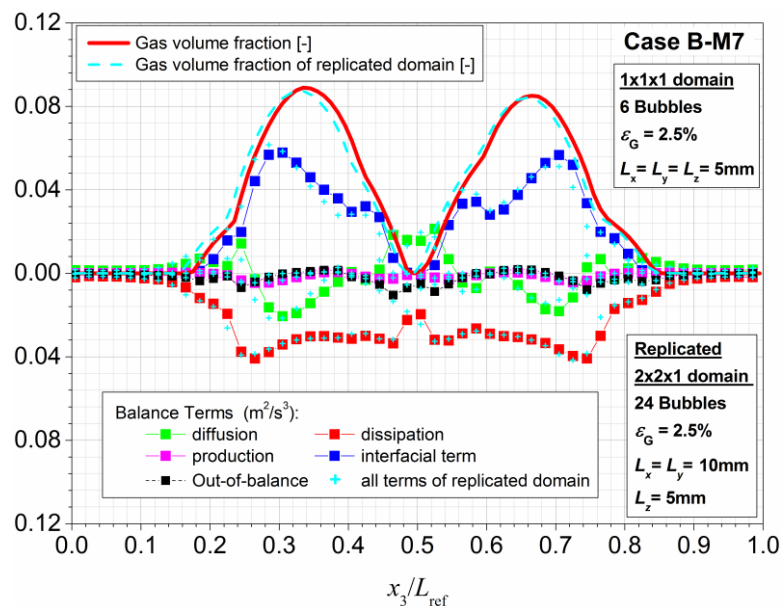
Fig. 31: Budget of the exact k_L-equation for Case B-M7 given in Table 6. The balance terms are demonstrated before (6 bubbles) as well as after replication of the domain (24 bubbles) in x and y direction. Figure is taken from Erdogan and Wörner [5].

Fig. 31 also shows the budget of the exact k_L-equation for Case B-M7 as the initialized domain as well as the replicated domain where the computational domain is enlarged and the number of bubbles is multiplied by a factor of four while the gas content remains the same. The replicated domain for Case B-M7 is demonstrated in Fig. 26 a). The simulations were then continued for the four-fold larger computational domain and the results were evaluated. The profiles after replication process nearly

match with the initial domain. The magnitude of the curves is reflected qualitatively and almost quantitatively. The test was successful as four times higher number of bubbles could be obtained without high computing times. The ideal comparison of replication method could be with a domain initially with 24 bubbles. However, such a test causes unacceptable computing time and therefore it was ruled out. The replication method offers important advantages for analysis of the budget of turbulence kinetic energy for higher number of bubbles in the domain.

The interfacial term, I_{kL}, contains the specific interfacial area a_i and is thus specific for two-phase flows. Since the interfacial term is related to the presence of the bubbles and their relative velocity, its shape strongly resembles the shape of the average bubble volumetric fraction α_G [29]. Comparing the profile of I_{kL} with that of α_G shows that I_{kL} has large positive values in regions with high void fraction and is zero in regions always occupied by liquid. This indicates that the rising bubbles create velocity fluctuations in the bubble wakes and thereby pseudo-turbulence. Clearly, I_{kL} is the main source of liquid turbulence kinetic energy whereas production by shear stresses P_{kL} is negligible [5]. The same results are reported in [26].
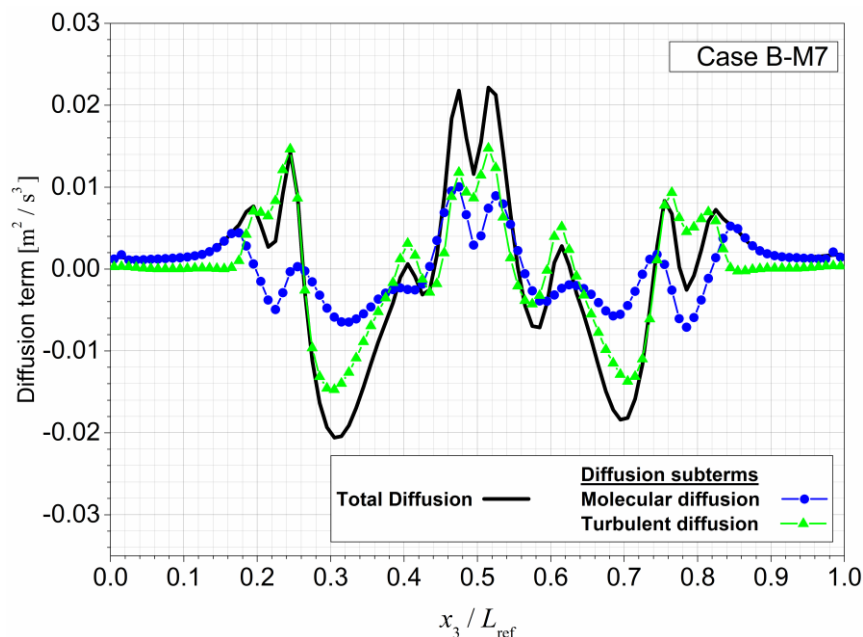
Fig. 32: Diffusion term in the exact k_L-equation for Case B-M7 given in Table 6.

The magnitude of the dissipation rate of k_L is very large in two-phase regions but is non-zero in pure liquid regions close to the walls. Thus, production and dissipation are not in local equilibrium. Instead, molecular and turbulent diffusion D_{kL} redistribute the surplus of production in regions of high void fractions toward regions of low or zero

void fraction. So to say, diffusion processes transport the energy generated by bubble interfaces from the two-phase regions towards the single-phase regions [5]. The diffusion term $D_{k\mathrm{L}}$ in the exact k_{L}-equation is shown in Fig. 32 for Case B-M7. It consists of two sub-terms: one molecular (first term) and one turbulent term (second term). The profiles of both sub-terms have complex distributions and the turbulent part dominates over the molecular part. Molecular and turbulent diffusion transports the energy generated by bubble interfaces from the two-phase region towards the single-phase regions.

Santarelli and Fröhlich [28] and Santarelli et al. [29] investigated the turbulence kinetic energy budget in a vertical turbulent channel flow configuration with realistic density difference by employing data obtained from Euler-Lagrange Direct Numerical Simulations. They addressed the dynamics of bubbles in a channel flow with background turbulence that is different from the rising bubbles in a quiescent fluid in this dissertation. They showed that the $O_{k\mathrm{L}}$ term is almost zero everywhere for a single-phase case, as expected. For the bubble swarm case, its magnitude is only around 10% of the dissipation term, which is the largest in magnitude. For the cases in this study, the magnitude of $O_{k\mathrm{L}}$ is also much smaller than the maximum balance term which is generally the dissipation term ε. Similar to this study, they also showed that the dissipation term ε presents a local minimum at the same position of the maximum of $I_{k\mathrm{L}}$ and there is a balance between the interfacial term and the dissipation term whereas the production is negligible.

4.3. Interfacial turbulence transfer

In this section, the profile of the exact interfacial term in the k_{L} equation as evaluated from the DNS data with profiles predicted for $I_{k\mathrm{L}}$ by different models are compared. This so-called a-priori test will allow identifying promising model approaches as well as model deficiencies and, on this basis, to develop model improvements. Since the interfacial term $I_{k\mathrm{L}}$ constitutes the main source of k_{L}, this term should be modelled properly [5]. In literature, several models have been proposed for closure of this term, see e.g. [14].

Closure assumptions from literature relate the interfacial term in various ways to the rate of work performed by hydrodynamic forces [14, 26]. The most important hydrodynamic force is the drag force F_{D}. By taking the product of F_{D} with the relative velocity between the phases, the rate of the work done by F_{D} is obtained as

$$W_{\mathrm{D}} = F_{\mathrm{D}}\left|\bar{\bar{u}}_{\mathrm{rel}}\right| = \frac{3}{4}C_{\mathrm{D}}\frac{\alpha_G \rho_L}{d_B}\left|\bar{\bar{u}}_{\mathrm{rel}}\right|^3 \tag{75}$$

The relative velocity is computed as

$$\overline{\overline{u}}_{\text{rel}} = \overline{\overline{u}}_{\text{G}} - \overline{\overline{u}}_{\text{L}} \tag{76}$$

Table 7: Models from the literature for the interfacial term I_{kL} in the k_L-equation.

Reference	Mentioned name	Model for the interfacial term I_{kL}
Ishii and Mishima [187]	Ishii-model	W_{D}
Olmos et al. [136]	Olmos-model	$0.75 \cdot W_{\text{D}}$
Lahey [24]	Lahey-model	$\left[(1 + C_{\text{D}}^{4/3}) / 3 C_{\text{D}} \right] \cdot W_{\text{D}}$
Pfleger and Becker [137]	Pfleger-model (PB)	$1.44(1 - \alpha_G) \cdot W_{\text{D}}$

In Table 7 four different models from literature are listed. Those models are later tested against the DNS data. They relate I_{kL} differently but linear to W_{D}. In the model of Ishii and Mishima [187] the interfacial term is $I_{kL} = W_{\text{D}}$, while the models of Olmos et al. [136], Lahey [24], Pfleger and Becker [137] all include a prefactor. In the Lahey-model, the prefactor is not constant but a function of C_{D}, whereas in the Pfleger-model it is a function of α_{G}. The drag coefficient C_{D} in Ishii-model, Lahey-model and Olmos-model are evaluated from [103] as $C_{\text{D}} = (2/3) E\ddot{o}_{\text{B}}^{0.5}$. For Eötvös numbers in the range $0.747 - 2.625$ we obtain from this correlation drag coefficients in the range of $0.576 \leq C_{\text{D}} \leq 1.08$. The constant value $C_{\text{D}} = 0.44$ in the Pfleger-model is valid for flow around a rigid sphere at Reynolds number $Re_{\text{B}} > 1000$ while for our cases Re_{B} is much lower and in the range $35 - 230$ [5]. Initially in this work, (see Erdogan and Wörner [5]), the interfacial term models were analyzed based on the approach originally given in their related papers. For models Ishii (given as LL by Erdogan and Wörner [5]) and Olmos, if $C_{\text{D}} = (2/3) E\ddot{o}_{\text{B}}^{0.5}$ is inserted in Eq. (75) then d_{B} cancels so that the influence of coalescence on I_{kL} only occurs via the volumetric fraction α_{G}. Thus, the models that define I_{kL} proportional to W_{D} with $C_{\text{D}} = (2/3) E\ddot{o}_{\text{B}}^{0.5}$ do not account at all for the influence of the bubble diameter and its change. For the Pfleger-model this is not the case since C_{D} is constant, hence, the value of d_{B} in Eq. (75) is still in charge. The Pfleger-model provided the best fit for all cases in [5].

Extending the work in Erdogan and Wörner [5], one unique drag law proposed by Tomiyama et al. [102] for clean systems in Eq. (64) is considered to allow for a better comparison of the models for the analysis of the interfacial turbulence transfer. Thus, all the models define I_{kL} proportional to W_{D} and account for the influence of the bubble diameter and its change. The model is repeated here for convenience:

$$C_D = \max\left\{\min\left[\frac{16}{Re}\left(1+0.15Re^{0.687}\right), \frac{48}{Re}\right], \frac{8}{3}\frac{E\ddot{o}}{E\ddot{o}+4}\right\} \qquad (77)$$

Tomiyama drag model has been verified for a wide parameter range. It is also tested in Section 3.4.3 for the single bubble cases and provided satisfactory results. Some of drag coefficient models from the literature are also discussed in Section 2.5.2. Furthermore, it is interesting to see in Fig. 33 that the profiles of $\alpha_G C_D$ resulted as different terms of Tomiyama drag model for the different DNS cases. Fig. 33 shows that Eq. (77) results for Case A1 as the first term $C_D = 16\left(1+0.15Re^{0.687}\right)\big/Re$ (Schiller-Naumann with Hadamard-Rybzinsky bubble correction), for Case A2 it is partly the first and partly the second term $C_D = 48/Re$ from Levich [86] (for potential flow for spherical fluid particles), and for Case A3 it is the third term $C_D = \left(8/3\right)\left(E\ddot{o}/E\ddot{o}+4\right)$ (for deformed and spherical cap bubbles). It should be noted that the bubble diameter of the originally mono-disperse flow is applied in Eq. (75) and for the determination of Eötvös number, Reynolds number and consequently the Tomiyama drag model, even for the cases with coalescence. An alternative, which is not investigated here, would be to use the "Sauter mean diameter" approach.
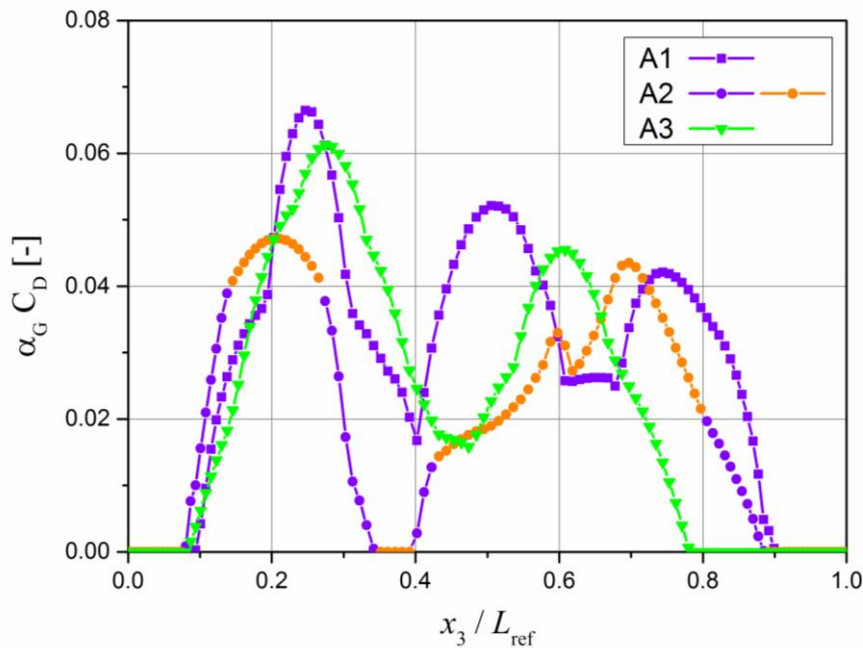
Fig. 33: Profiles of $\alpha_G C_D$ for the Case A1, A2 and A3. The color coding refers to the three terms in the right-hand-side of Eq. (75) purple = term 1, orange = term 2, green = term 3.

Fig. 34 shows the wall normal profiles of the I_{kL} (solid lines, left scale) and the local gas content (dashed orange line, right scale). Based on the described procedure,

the profiles predicted from the models in Table 7 (colored solid lines with symbols) were determined for I_{kL} and compared with the exact profiles from the DNS data (black solid line) for the mono-disperse Case A1 (a), Case A2 (b), Case A3 (c) and Case A4 (d). In the figures, the models for the interfacial term are normalized with liquid density in order to be compatible with the exact formulation as defined in TURBIT-VOF [26]. The black solid line in Fig. 34 corresponds to the blue line representing the interfacial closure term in Fig. 31. It is noted that for Case A2, the profiles in the figure are evaluated for the time interval of mono-disperse flow and the first coalescence occurs shortly after. This means that the distance between two bubbles that will cause coalescence is very low (at $x_3/L_{ref} \approx 0.6$) and therefore the flow is unstable, which can be realized from the DNS profiles.

The closest approximation to the DNS curve is obtained by the Olmos-model for cases A1, A2 and A3. For Case A4, where the coalescence occurs, the Olmos-model gives an acceptable match with the magnitude of interfacial term for the mono-disperse ($x_3/L_{ref} < 0.3$) part of the curve while for the bi-dispersed ($x_3/L_{ref} > 0.3$) part underestimates it. If we consider the volume-equivalent diameter of two coalesced bubbles for calculation of F_D, due to inverse proportion the value of I_{kL} would be 26% lower [5], which means I_{kL} gets closer to the Olmos-model at the location of the coalesced bubbles (at $x_3/L_{ref} \approx 0.5 - 0.7$). The Ishii-model and in particular the Pfleger-model overestimate I_{kL} for all cases and the Lahey-model slightly underestimates it except Case A2.

Qualitatively, all four models reflect the bias caused by coalescence although the initial d_B value is used for $E\ddot{o}_B$ in C_D to calculate I_{kL}, not d_B after coalescence. For Case A4, none of the models can reflect the magnitude of the curve (at $x_3/L_{ref} \approx 0.35$), where a second coalescence is approaching. This is because the coalescence causes a strong variation of bubble trajectories and fluctuations, which has an adverse effect on accuracy of the statistical evaluation of the k_L-equation. On the contrary, the bubbles in case of mono-disperse flow demonstrate almost rectilinear trajectories and thus the flow is in a quasi-steady state where the fluctuations are also almost stable.

Overall, all models investigated here yield a profile similar in shape but different in magnitude. The Pfleger-model is valid for higher bubble Reynolds numbers. Among them Olmos-model is the best fit. Lahey-model is the second closest model since it reflects the magnitude of the curves locally. The Olmos-model and Lahey-model, in combination with the drag correlation of Tomiyama, yield satisfactory agreement with the profiles of the exact interfacial term for different cases and thus can be used for the two-fluid simulations in this study.
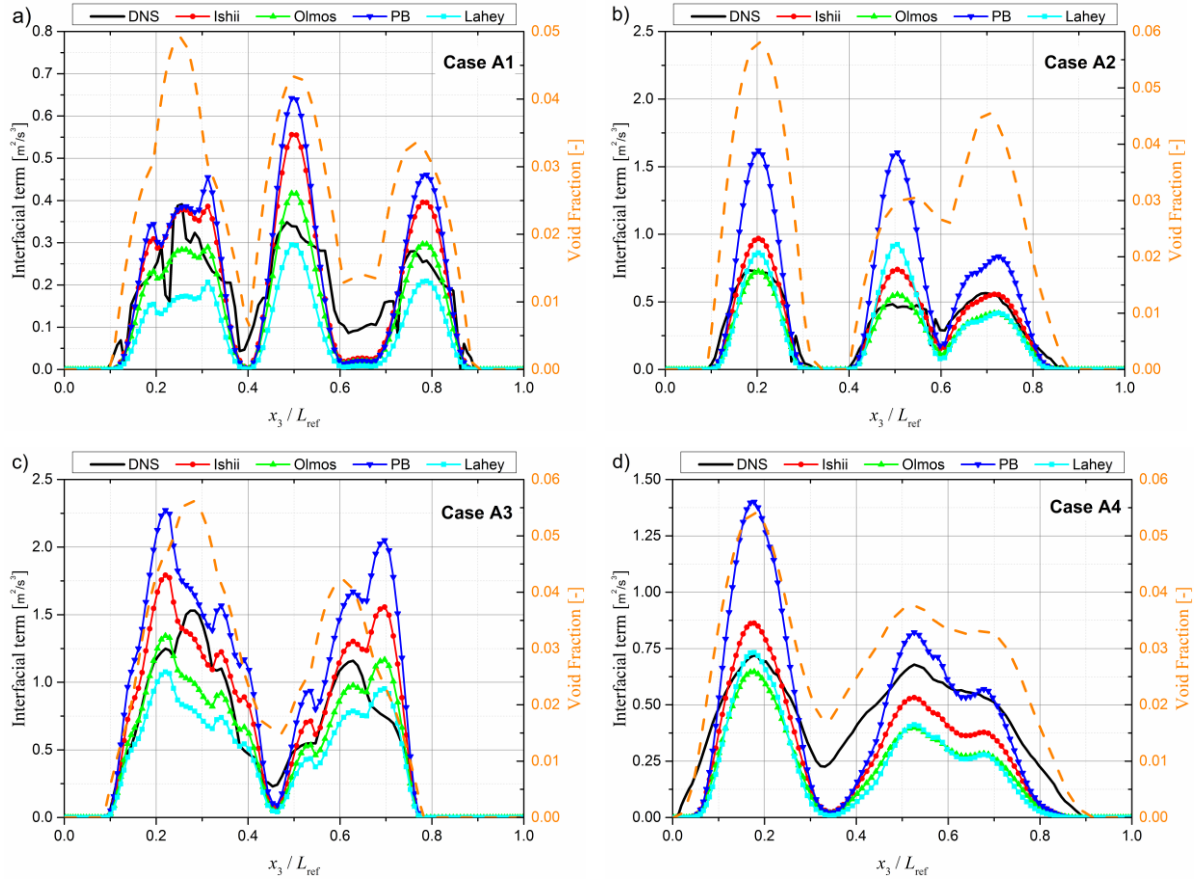
Fig. 34: Predictions of interfacial turbulence transfer by engineering models for Case A1 (a), Case A2 (b), Case A3 (c) and Case A4 with coalescence (d). The solid orange line is the void fraction. The models for the interfacial term are normalized with liquid density. The figures are based on the similar figures from Erdogan and Wörner [5] but averaged at further time points here.

The Case A2 and A3 are exactly same cases but only with different bubble diameter. In Erdogan and Wörner [5] Case A2 and A3 are compared with Pfleger-model. The plot is not repeated here, however, comparing the Fig. 34 b), c) one can see that less interfacial area is present with smaller bubbles (Case A2) and therefore they create less interfacial turbulence than bigger ones (Case A3). For Case A3, lateral motion of bubbles occurs by the increase of Re_B and therefore the interfacial term does not become zero in most part of the domain except near wall regions [5].

In their work, Santarelli and Fröhlich [28] and Santarelli et al. [29] considered bubbles of fixed spherical shape with low Eötvös number, rising in contaminated water in a much larger domain. The authors assessed the model performances in the literature by means of the DNS data. The drag coefficient different for each simulation was obtained by a formula as in Roghair et al. [188]. The common models considered in both work are the Olmos-model, Pfleger-model and Ishii-model. They considered Ishii-model as later improved version by Troshko and Hassan [22]. In Santarelli et al.

[29], for a single test case, the Ishii-model overestimates the interfacial term by around 17% while in Fig. 34 it is between 15% up to 50% locally. A similar deviation is also observed in Ilic et al. [19]. The Pfleger-model yields an over-estimation of around 80% for the case of Santarelli et al. [29] while the Olmos-model provides an underestimation of $I_{k\mathrm{L}}$ by 12%. The Olmos-model, the best fit in Fig. 34, in mono-disperse regions underestimates the $I_{k\mathrm{L}}$ by max. 12-13% locally, but generally by less than 10%. Overall, also in their results all models yield a profile fairly similar in shape compared to the DNS data whereas the magnitude can differ substantially [29]. They also proposed a model by fitting the available data for their simulations but it is only valid for that specific case.

4.4. Summary

The development of improved turbulence closure relations for bubble-driven flows is hindered by the lack of detailed experimental data on the various closure terms in the turbulence kinetic energy equation. Direct numerical simulations of bubble swarms can provide such data. For the model development, extensive direct numerical simulations for bubble swarms are performed within a sub-region of a flat bubble column. From the DNS data, the liquid phase turbulence kinetic energy k_L and its analytical transport equation are evaluated. The statistical analysis of k_L profiles show that the maximum value of k_L and the integral of k_L profiles over the channel increases with i) the increasing d_B and $E\ddot{o}_\mathrm{B}$ for a fixed liquid viscosity and Morton number and ii) the decreasing liquid viscosity and Morton number for a fixed d_B and $E\ddot{o}_\mathrm{B}$.

The evaluation of the individual terms in the k_L equation indicates that the main source term for the turbulence kinetic energy is due to the interaction of interfaces. In bubble columns, the large-scale liquid recirculation generates shear-induced turbulence (especially near the walls) which is superposed to the BIT. However, for the conditions examined here the production due to shear stresses is negligible. Production and dissipation are not in local equilibrium. Therefore, molecular and turbulent diffusion redistribute the surplus of production of k_L from regions of high to low void fractions or, another way of saying, from the two-phase regions towards the single-phase regions. The results for the budget of k_L equation are consistent with the investigations from the literature [26, 28, 29].

In its modeled form, the k_L equation is a cornerstone for CFD simulations of bubbly flows with statistical turbulence models based on the Euler-Euler approach. Here, the DNS results are used for a priori-testing of closure assumptions for the interfacial term in the k_L equation. This so-called a-priori-testing allows us to identify

suitable models and to propose potential improvements.

The models from Olmos et al. [136] and Lahey [24] identified as suitable models for the closure of the interfacial term $I_{k\mathrm{L}}$, as they are relatively good agreement with the DNS data. The Olmos-model with its linear dependency on the drag coefficient C_D due to constant prefactor is more suitable than the Lahey model with its non-linear dependency on C_D. The evaluation of models for the interfacial term is restricted to a single drag model to allow for a comparison independent from C_D. The generic model from Tomiyama [102] for clean systems is verified for a wide parameter range and utilized for calculations. It is interesting to see that the profiles of $\alpha_\mathrm{G}C_\mathrm{D}$ for the different DNS cases result from different terms in the equation of C_D. For one case, C_D is calculated with two terms in the Tomiyama drag model.

Strong variation of bubble trajectories and fluctuations due to coalescence has influence on the accuracy of the statistical evaluation of the k_L-equation. All the tested models reflect the tendency of the interfacial term (even for coalescence) on the magnitude of the curves qualitatively, but not quantitatively. The Olmos-model is the closest model for reflecting coalescence. Using the volume-equivalent diameter of coalesced bubbles for calculation of the interfacial term provide better estimations after the coalescence.

5. Euler-Euler Simulations of a Bubble Column

In this Chapter, firstly the numerical code used for the simulations, the test column which is the basis for the simulations and the methodology of data analysis are explained. Later, the results and analysis of Euler-Euler simulations are discussed.

5.1. Set-up and procedures

5.1.1. Industrial DN330 bubble column reactor

The Euler-Euler simulations are performed based on the experimental studies [189, 190] by Evonik Industries and the Helmholtz-Zentrum Dresden-Rossendorf (HZDR). The gas holdup and the bubble size distribution are investigated for an industrial high-pressure bubble column reactor of Evonik Industries AG in Marl (Germany). The stainless-steel bubble column (DN330) has a 5 m height (liquid level: 3.88 m) and a diameter of 0.33 m. With the chosen column diameter, it was aimed to reduce the wall effects. The sketch of the test facility is shown in Fig. 35. In the industrial bubble column, the gas (nitrogen) and liquid phase (cumene or deionized water) are operated in co-current upward flow. The gas is introduced to the column by a perforated plate sparger (352 × 1 mm^2 holes) (see Fig. 36), leaves the column at the top and the liquid is circulated by a pump. For this bubble column, experiments were performed with a gas superficial velocity in the range of 0 to 0.05 m/s at low superficial liquid velocities of 0.008 and 0.018 m/s for operating temperatures and pressures up to 75 °C and 36 bar [189, 190]. Radial profiles of local gas content at 2.23 m height were measured by high-resolution gamma-ray computed tomography (GammaCT) and wire-mesh sensor (WMS) which were developed by the HZDR (for details see [191, 192]). Circular dimensions of the DN330 bubble column are given in Table 8.

Table 8:   Circular dimensions of the DN330 bubble column and inlets / outlets.

|	Diameter (m)	Cross sectional area (m^2) ($A=\pi D^2/4$)	
Bubble column	0.330	A_{column}	= 0.08553
Gas inlet	0.233	$A_{G,inlet}$	= 0.04263
Holes at gas inlet	0.001(x352)	$A_{G,hole}$	= 0.0004524
Liquid inlet	0.024	$A_{L,inlet}$	= 0.00159
Gas outlet	0.045	$A_{G,inlet}$	= 0.0002765
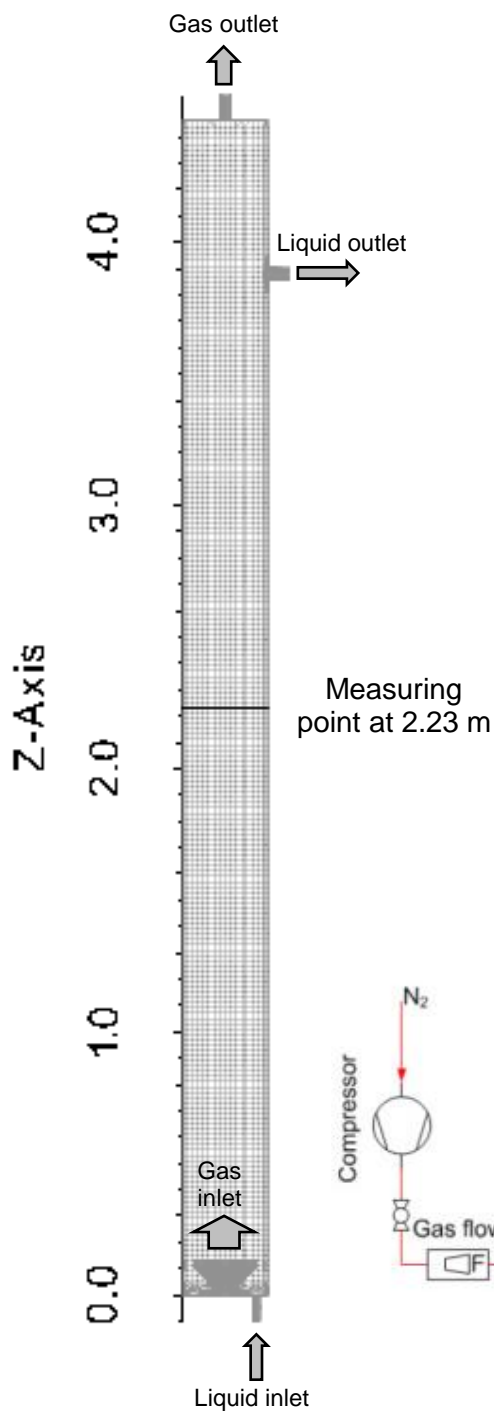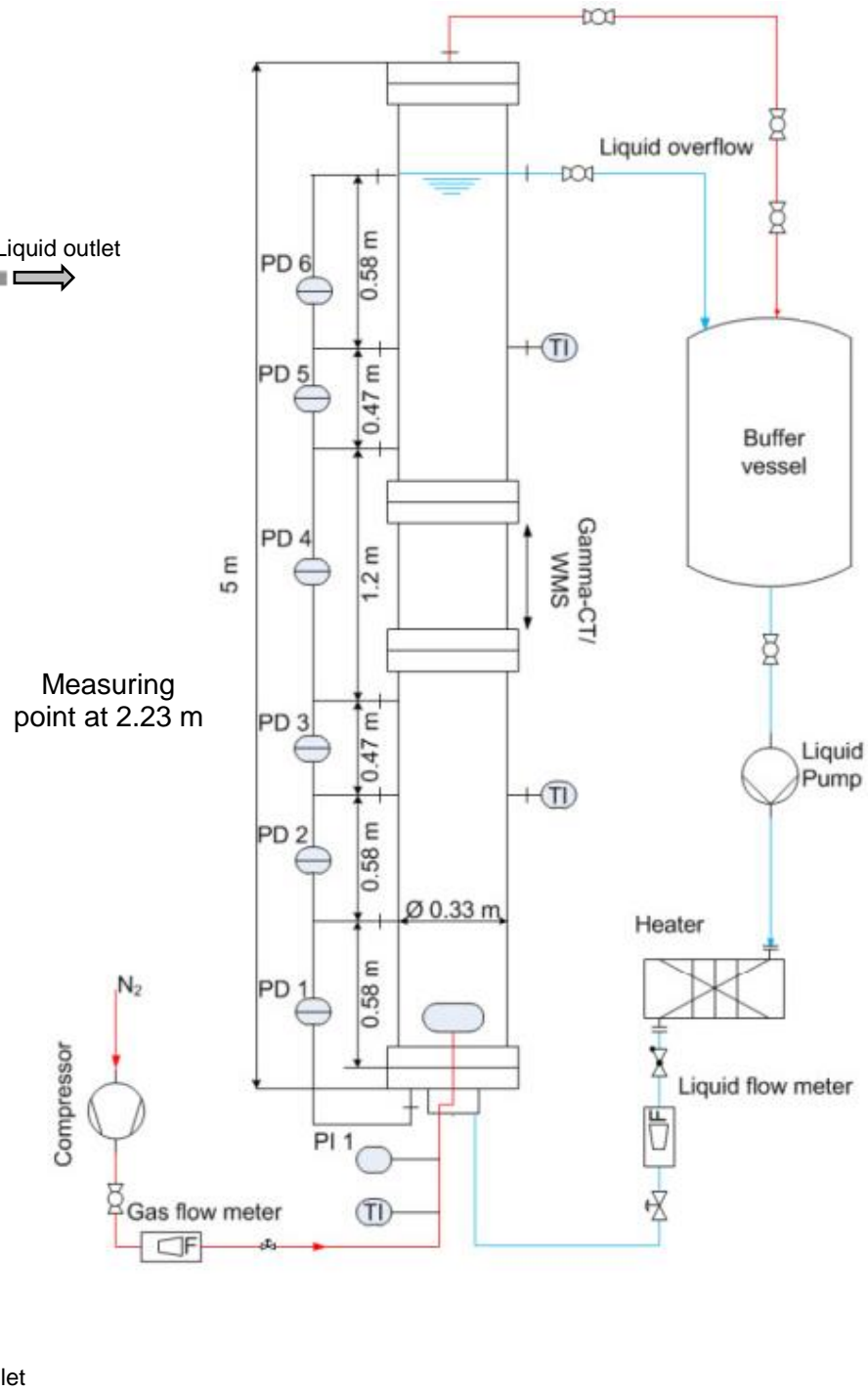
Fig. 35: a) DN330 bubble column geometry for Euler-Euler simulations. The measuring point for simulations is shown with a bolded line at 2.23 m. b) Sketch of the industrial DN330 bubble column of Evonik Industries AG (Marl, Germany) [189, 190]
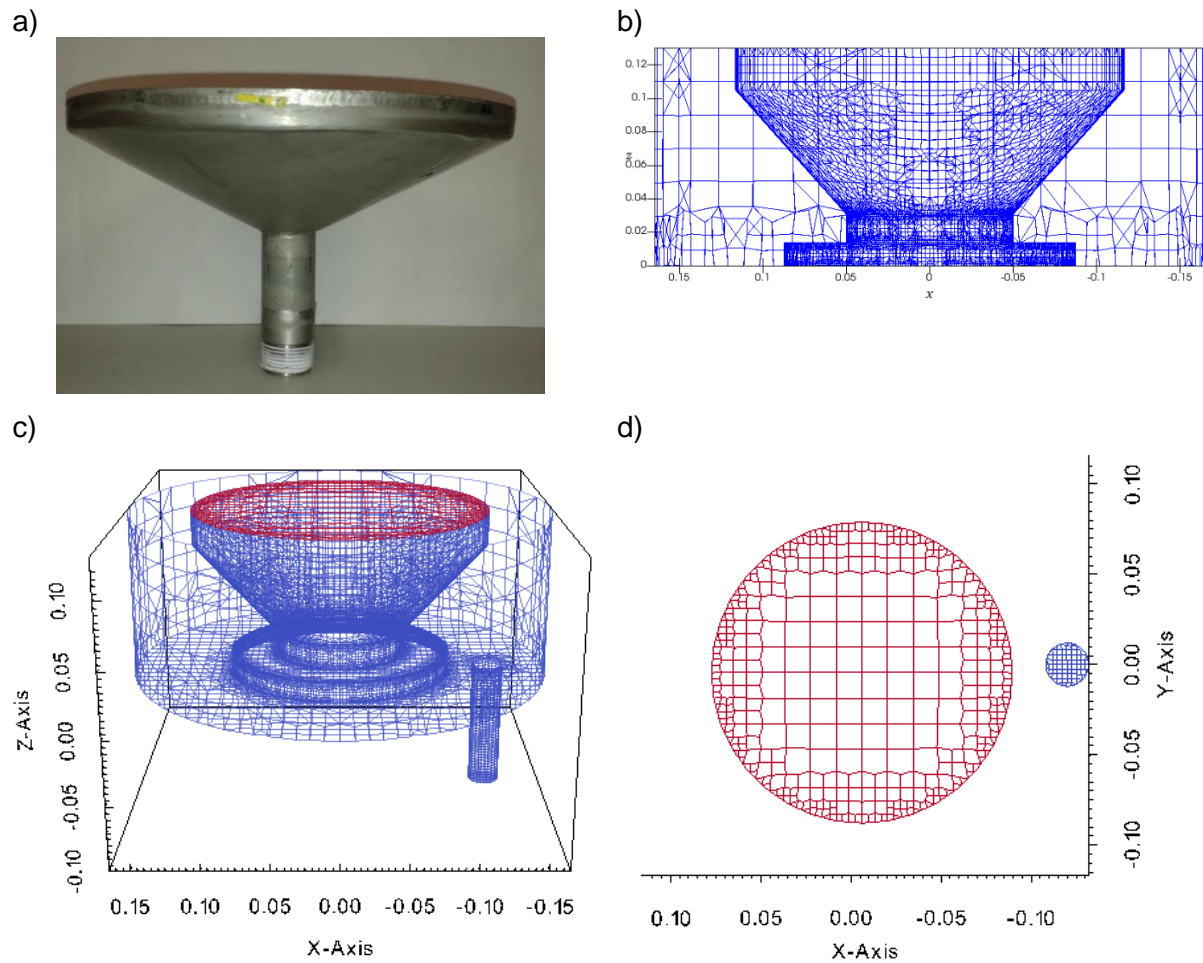
Fig. 36 Perforated plate sparger a) Sparger used in experiments (Photo provided by A. Bieberle, HZDR), b) Geometrical representation of the sparger in E-E simulations (2D), c) Gas (red) and liquid inlet in E-E simulations (3D), d) Gas (red) and liquid (blue) inlet in E-E simulations (view from above). Dimensions of the perforated plate sparger are provided in Table 8.

5.1.2. Numerical set-up

For Euler-Euler simulations, the cases at different conditions were selected from the experimental study based on variety of numerical tests. The gas superficial velocities are in the range of $0.0014 \leq U_{G,0} \leq 0.0056$ m/s and the superficial liquid velocities are in the range of $0.0083 \leq U_{L,0} \leq 0.0175$ m/s. The operating temperature is 23 °C $\leq T \leq$ 70 °C and pressure is in the range of 1 bar $\leq p \leq$ 36 bar. The physical properties and initial conditions for the cases are given in Table 9 and Table 10.

The superficial velocities measured in experiments cannot be used as inlet parameters. For numerical purpose, the inlet and outlet geometry of DN330 are designed as smeared surfaces and the velocity values are ought to be converted according to cross-sectional area. Hence, the superficial velocities are converted into

the inlet velocities by calculating the volumetric flow rate (Q) across the cross-sectional area ($A=\pi D^2/4$) given in Table 8 for each inlet and outlet as

$$Q_G = u_{G,\text{inlet}}\alpha_{G,\text{inlet}}A_{G,\text{inlet}} = U_{G,0}A_{\text{column}} = u_{G,\text{outlet}}\alpha_{G,\text{outlet}}A_{G,\text{outlet}} \tag{78}$$

$$Q_L = u_{L,\text{inlet}}\alpha_{L,\text{inlet}}A_{L,\text{inlet}} = U_{L,0}A_{\text{column}} \tag{79}$$

Here, α is the gas fraction for each phase at the corresponding inlet or outlet. The liquid inlet and the gas outlet are open pipe and therefore $\alpha_{L,\text{inlet}}$ and $\alpha_{G,\text{outlet}}$ are always equal to 1. The inlet velocity $u_{L,\text{inlet}}$ for liquid phase is then calculated from the balance of Eq. (79) and the outlet velocity $u_{G,\text{outlet}}$ for gas phase is calculated from the balance of Eq. (78). However, for the $u_{G,\text{inlet}}$ in Eq. (78) first $\alpha_{G,\text{inlet}}$ must be known. The gas is sparged to the column through the 352 holes each with a 1 mm^2 cross sectional area. In order to represent the geometry with holes as a smeared surface the inlet gas fraction is calculated as

$$\alpha_{G,\text{inlet}} = \frac{352 A_{\text{hole}}}{A_{G,\text{inlet}}} = \frac{352(0.001)^2\,\pi/4}{(0.233)^2\,\pi/4} = 0.0064838 \tag{80}$$

The calculated $u_{L,\text{inlet}}$, $u_{G,\text{inlet}}$ and $u_{G,\text{outlet}}$ are the initial velocity values for E-E simulations. The corresponding velocity values are given in Table 10. These values are entered in the *U.air* and *U.water* files under "*0*" folder in OpenFOAM®. The values of k and ε, which must be given as inlet conditions, are obtained from the turbulence intensity T_i and characteristic length L by means of the correlations explained in Section 5.1.3 and the results of the calculations are given in Table 11.

In the first test simulations, the gas outlet velocity is calculated with the velocity inlet/outlet boundary condition of OpenFOAM® while setting the outlet pressure boundary condition to a fixed value. However, the simulation did not converge. As the superficial velocity across the cross-section and the inlet velocities are known from the experiments, the gas velocity at the outlet is easily calculated from the volumetric flow rate by Eq.(78). Therefore, the velocity is set to the calculated fixed value $u_{G,\text{outlet}}$ for each case at the gas outlet and the pressure is defined as the fixedFluxPressure [193] boundary condition where the pressure is evaluated by the flux on the boundary which is specified by the velocity boundary condition. This means that the pressure is calculated according to the velocity input.

The three-dimensional geometry of the DN330 bubble column for the simulations and the grid were provided by Evonik Industries. The liquid at rest without gas content was determined as initial condition. The bubble diameter is set to d_B = 4 mm at 1 bar according to the peak of measured bubble size distribution in experiments [189]. At

18.5 and 36 bar, experimental information about the bubble diameter is not available for the selected flow conditions in this work. Bubble diameter in bubble columns were studies by many authors [194-196], extensively reviewed by Rollbusch et al. [197] and investigated in the "Multi-Phase" project via the experiments [190]. The authors found that d_B is smaller at elevated pressures. At 18.5 bar the bubble diameter is in the range of $2.25 \leq d_B \leq 4$ mm and at 36 bar the $d_B = 2.25$ mm. The constant bubble size is important for the initial conditions however depending on the operating conditions the d_B is modified during the simulation due to bubble break-up and coalescence. Thus, the average bubble size is expected to be smaller at elevated pressures and temperatures [197, 198].

Table 9: Physical parameters of water, cumene and nitrogen (N_2) in the Euler-Euler simulations. The values were obtained via measurements from the experiments within the Multi-Phase Project. Surface tension (σ) data are only available for low temperature (23 °C). Therefore, same values are also used for high temperature (70 °C).

		Water		Water-N_2	Cumene		Cumene-N_2	N_2	
p (bar)	T (°C)	ρ (kg/m³)	μ (Pa.s) ($\times10^{-4}$)	σ (N/m)	ρ (kg/m³)	μ (Pa.s) ($\times10^{-4}$)	σ (N/m)	ρ (kg/m³)	μ (Pa.s) ($\times10^{-4}$)
1	23	997.05	8.50	0.0715	867.16	7.90	0.0260	1.13	0.178
	70	974.84	4.05		820.49	4.27		0.97	0.198
18.5	23	997.83	8.50	0.0687	876.91	7.90	0.0255	20.9	0.181
	70	975.62	4.05		825.85	4.27		17.8	0.201
36	23	998.62	8.50	0.0671	869.65	7.90	0.0252	40.8	0.184
	70	976.39	4.05		828.73	4.27		34.6	0.204

Table 10: Initial conditions for the E-E Simulations.

Scenario	Water - N$_2$	p (bar)	T (°C)	d_B (mm)	l_{kL}	C_D	$U_{L,0}$ (m/s)	$U_{G,0}$ (m/s)	$u_{L,inlet}$ (m/s)	$u_{G,inlet}$ (m/s)	$u_{G,outlet}$ (m/s)
	Case A (Base)	1	23	4	Lahey	S-N	0.0084	0.0056	1.588	1.733	0.301
A	Case A1	1	23	4	**Olmos**	S-N	0.0084	0.0056	1.588	1.733	0.301
	Case A2	1	23	4	**2xLahey**	S-N	0.0084	0.0056	1.588	1.733	0.301
	Case B (Base)	18.5	23	2.25	Lahey	S-N	0.0084	0.0055	1.588	1.702	0.295
	Case B1	18.5	23	2.25	**Olmos**	S-N	0.0084	0.0055	1.588	1.702	0.295
	Case B2	18.5	23	2.25	**2xLahey**	S-N	0.0084	0.0055	1.588	1.702	0.295
	Case B3	18.5	23	**3**	Lahey	S-N	0.0084	0.0055	1.588	1.702	0.295
	Case B4	18.5	23	**4**	Lahey	S-N	0.0084	0.0055	1.588	1.702	0.295
B	Case B5	18.5	**70**	2.25	Lahey	S-N	0.0084	0.0055	1.588	1.702	0.295
	Case B6	18.5	23	2.25	Lahey	S-N	0.0084	**0.0034**	1.588	1.052	0.183
	Case B7	18.5	23	2.25	Lahey	S-N	0.0084	**0.0014**	1.588	0.433	0.075
	Case B8	18.5	23	2.25	Lahey	S-N	**0.0175**	0.0055	3.300	1.702	0.295
	Case B9	18.5	23	2.25	Lahey	**To**	0.0084	0.0055	1.588	1.702	0.295
	Case B10	18.5	23	2.25	**Olmos**	**To**	0.0084	0.0055	1.588	1.702	0.295
	Case C1 (Base)	36	23	2.25	Lahey	S-N	0.0084	0.0055	1.588	1.702	0.295
C	Case C2	36	23	2.25	Lahey	S-N	0.0083	**0.0039**	1.569	1.207	0.209
	Case C3	36	23	2.25	Lahey	S-N	0.0084	**0.0014**	1.588	0.433	0.075
	Cumene - N$_2$										
	Case D1	1	70	2.93	Lahey	S-N	0.0082	**0.0068**	1.550	2.105	0.365
D	Case D2	18.5	70	2.94	Lahey	S-N	0.0082	**0.0061**	1.550	1.888	0.328
	Case D3	36	70	2.94	Lahey	S-N	0.0082	**0.0054**	1.550	1.671	0.290

Case A, Case B and Case C1 are designed as base cases for other cases with same initial. The initial conditions differing from the base cases are bolded. Abbreviations: p: pressure, T: temperature, d_B: bubble diameter, l_{kL}: interfacial term, C_D: drag model, U_0: superficial velocity, u: inlet or outlet velocity S-N: Schiller-Naumann drag model [101] , To: Tomiyama drag model [102].

Table 11: Boundary conditions as input parameters for the Euler-Euler Simulations.

Pressure	Temperature	Case	Water			N_2		
			k (m²/s²)	ε (m²/s³)	ν_{turb} (m²/s)	k (m²/s²)	ε (m²/s³)	ν_{turb} (m²/s)
1 bar	23 °C	A, A1, A2	4.3×10^{-3}	2.7×10^{-2}	6.0×10^{-5}	2.3×10^{-2}	8.23	5.8×10^{-6}
18.5 bar	23 °C	B, B1, B2, B3, B4, B9, B10	4.3×10^{-3}	2.7×10^{-2}	6.0×10^{-5}	1.0×10^{-2}	2.63	3.9×10^{-6}
		B6				4.6×10^{-3}	7.4×10^{-1}	2.6×10^{-6}
		B7				9.8×10^{-4}	7.2×10^{-2}	1.2×10^{-6}
		B8	1.5×10^{-2}	0.89	1.1×10^{-4}	1.0×10^{-2}	2.63	3.9×10^{-6}
	70 °C	B5	3.6×10^{-3}	2.1×10^{-2}	5.5×10^{-5}	1.1×10^{-2}	2.91	4.1×10^{-6}
36 bar	23 °C	C1	4.3×10^{-3}	2.7×10^{-2}	6.0×10^{-5}	9.2×10^{-3}	2.07	3.7×10^{-6}
		C2				5.0×10^{-3}	0.84	2.7×10^{-6}
		C3				3.0×10^{-3}	0.37	2.1×10^{-6}
			Cumene					
1 bar	70 °C	D1	3.6×10^{-3}	2.2×10^{-2}	5.6×10^{-5}	3.5×10^{-2}	15.1	7.1×10^{-6}
18.5 bar		D2				1.4×10^{-2}	3.82	4.5×10^{-6}
36 bar		D3				9.5×10^{-3}	2.18	3.7×10^{-6}

5.1.3. Boundary conditions

The detailed boundary condition information is required to operate the model equations for k and ε and to initialize the simulations until the flow come to a steady and stable state. Therefore, the distributions of k and ε must be given as inlet conditions. However, measurements of both quantities are rarely available. Possible approaches could be: (1) using the values of k and ε from the literature [113] or (2) obtaining rough approximations for the inlet distributions of k and ε from the turbulence intensity T_i, characteristic length L and the turbulence length scale (mixing length) l, by means of the correlations explained below. The latter was considered in this work because the boundary conditions are calculated from real parameters of the operating fluids.

The turbulence length scale l is a physical quantity related to the size of the large eddies that contain the energy in turbulent flows. In fully developed duct flows, l, is restricted by the size of the duct, since the turbulent eddies cannot be larger than the duct. An approximate relationship between l and the physical size of the duct is [199]

$$l = 0.07L \tag{81}$$

The factor of 0.07 is based on the maximum value of the mixing length in fully-developed turbulent pipe flow, where L is the diameter of the pipe [199]. For a circular tube, the hydraulic diameter is the diameter of the tube.

$$D_\mathrm{H} = \frac{4A}{P} = \frac{4\left(\pi D^2 / 4\right)}{\pi D} = D \tag{82}$$

where A is the cross-sectional area and P is the wetted perimeter of the cross-section. Therefore, in a channel of non-circular cross-section, L can be defined as the hydraulic diameter, $L=D_\mathrm{H}$ [199].

The turbulent dissipation rate can be determined by the length scale from this relationship

$$\varepsilon = \left(C_\mu\right)^{3/4} \frac{k^{3/2}}{l} \tag{83}$$

Here C_μ is 0.09 and constant. The transport equations of the standard k-ε model contain five adjustable constants [121], which are given in Table 12.

Table 12: Coefficients of the turbulence models.

C_μ	C_1	C_2	σ_k	σ_c
0.09	1.44	1.92	1.00	1.30

Turbulence intensity T_i is defined as the average root mean square (r.m.s.) velocity given in Eq.(32), which is divided by a reference mean flow velocity, and is linked to the turbulence kinetic energy k

$$T_i = \frac{u_{rms}}{u_{mean}} \equiv \frac{\sqrt{\overline{u'^2}}}{u_{mean}} \tag{84}$$

Here, u_{rms} is the r.m.s. of the turbulent velocity fluctuations at a particular location over a specified period of time and u_{mean} is the average of the velocity at the same location over same time period. By substituting $\overline{u'^2}$ from Eq. (33) into Eq. (84) then

$$T_i = \frac{(2k/3)^{1/2}}{u_{mean}} \tag{85}$$

When the velocities only in flow direction (for example x component) is accounted for, then Eq. (33) becomes

$$k = \frac{\overline{u'^2_x}}{2} \tag{86}$$

and from Eq. (84) and Eq. (86) the turbulence intensity for x component is then

$$T_i = \frac{u_{rms}}{u_{mean}} = \frac{(2k)^{1/2}}{u_{mean}} \tag{87}$$

In practice many authors seem not to use the three components of average r.m.s. velocity for applying the turbulence intensity (see Eq. (85)) but instead prefer using only flow direction component as in Eq.(87). The turbulence kinetic energy k can be defined by T_i from Eq. (87) as

$$k = \frac{1}{2}\left(u_{mean} T_i\right)^2 \tag{88}$$

At the core of a fully-developed duct flow, the turbulence intensity can be estimated from the following formula derived from an empirical correlation for pipe flows [199]:

$$T_i \equiv \frac{u'}{u} = 0.16\left(Re_{D_H}\right)^{-1/8} \tag{89}$$

where the Reynolds number is defined by the hydraulic diameter

5.1.4. Modelling for two-fluid simulations

The formulation of the inter-phase momentum transfer term and the two-phase turbulence model is the main feature of the two-fluid methodology because it depends on the exact nature of the flow [135]. The two-fluid simulations are performed with OpenFOAM® and the top-level solver *twoPhaseEulerFoam* is used as solver.

Models for turbulence:

The results in Section 4.3 from the investigation of interfacial term in the exact k_L-equation via DNS had revealed that the models for the interfacial term defined by Lahey [24] and Olmos et al. [136] yield a reasonable-satisfactory agreement with the profiles of the exact interfacial term for different cases. In OpenFOAM® two variations of $k\text{-}\varepsilon$ turbulence model approaches are available: the standard $k\text{-}\varepsilon$ model [121] and the so-called basic-mixture turbulence model according to the work of Rusche [131, 135]. The details for both approaches are explained in Section 2.3.4.

The standard $k\text{-}\varepsilon$ model with the extension of the interfacial term from the work of Lahey [24] is named as *LaheyKEpsilon*. It solves the turbulence kinetic energy equations including bubble-generated turbulence (interfacial term) for the continuous (liquid) phase, i.e. for k_L and ε_L. The source files of the model are available online on the website of the OpenCFD Ltd. [200]. In the Lahey [24], the interfacial term is given as:

$$I_{\text{kL}}^{\text{Lahey}} = 0.25(1 + C_{\text{D}}^{4/3})\alpha_G \frac{\rho_L u_{\text{rel}}^3}{d_B} \tag{90}$$

The mixture $k\text{-}\varepsilon$ model is called *mixtureKEpsilon* [201] and solves the equations for the mixture of two phases, i.e. k_m and ε_m. The basic structure of the model is based on Behzadi et al. [131]. It uses the Lahey-model [24] as interfacial term same as in *LaheyKEpsilon*. Both models use the standard set of model coefficients (see Table 12). However, the choice of the turbulence model has a major impact on the stability of the calculations with *twoPhaseEulerFoam*. With the *LaheyKEpsilon* model, convergence problems occurred often while simulating a bubble column, so that *twoPhaseEulerFoam* did not provide a solution. In contrast, the convergence behavior and stability when using the *mixtureKEpsilon* model are significantly better. This observation was made both at Evonik and at KIT. For this reason, all simulations with *twoPhaseEulerFoam* for cases involving Lahey-model [24] as BIT term are performed by using the *mixtureKEpsilon* turbulence model. In the course of this study, an additional model, the Olmos-model is implemented in OpenFOAM® as *OlmosKEpsilon* by applying *mixtureKEpsilon* base. The simulations with these two types of BIT models

are performed up to a steady-state condition. In the Olmos et al. [136], the interfacial term is given as:

$$I_{\text{kL}}^{\text{Olmos}} = 0.75 \frac{3}{4} C_{\text{D}} \alpha_G \frac{\rho_L u_{\text{rel}}^3}{d_B} \tag{91}$$

The *LaheyKEpsilon* model considers the effective viscosity $v_{\text{L}}^{\text{eff}}$ approach in Eq.(43) as a sum of the usual turbulent viscosity, the molecular viscosity and the eddy viscosity model of Sato [114, 115] due to bubbles. On the other hand, in *mixtureKEpsilon* model the effective viscosity is modelled without the bubble-induced eddy viscosity from Sato [114, 115] and uses a mixture turbulent viscosity as in Eq. (44). This means *LaheyKEpsilon* allows for the BIT by both viscosity model as well as the interfacial term. For *mixtureKEpsilon* model, the turbulence response function C_{t} affects the k_{m} and ε_{m} as well as the turbulent eddy viscosity v_{m}^{t}. However, for small values of the density ratio ρ_G / ρ_L and for small gas holdup α_G the influence of C_{t} negligibly small. Therefore, the mixture quantities take the form of the liquid phase when approaching the limiting case of the density ratio and gas fraction, i.e. $k_{\text{m}} \approx k_{\text{L}}$, $\varepsilon_{\text{m}} \approx \varepsilon_{\text{L}}$ and $v_{\text{m}}^{\text{t}} \approx v_{\text{L}}^{\text{t}}$. Therefore, the difference between *LaheyKEpsilon* and *mixtureKEpsilon* in terms of the k and ε values appears to be rather small for the cases investigated in this study.

Models for the interfacial momentum transfer:

It is found in Section 4.3 that each of the Olmos-model and Lahey-model in combination with the drag correlation of Tomiyama [102] yields a reasonable-satisfactory agreement with the profiles of the exact interfacial term for different cases and thus is chosen to be used for the two-fluid simulations in this study. However, the results of simulations with the implemented Tomiyama drag model in OpenFOAM® exhibited unphysical behavior and convergence problems. Therefore, the Schiller-Naumann [101] drag model as given in Eq. (63) is further used in E-E simulations. The interfacial forces applied in a bubbly flow are discussed in Section 2.5.2. The models used in the E-E simulations are listed in Table 13.

Table 13: Applied models in the Euler-Euler Simulations with OpenFOAM®.

Category	Applied Model
Turbulence (RANS Model)	mixtureKEpsilon, OlmosKEpsilon
aspectRatio	Tomiyama
drag	SchillerNaumann, Tomiyama with swarmCorrection-Tomiyama
virtualMass	constantCoefficient=0.5
lift	LegendreMagnaudet
wallLubrication	none
turbulentDispersion	constantCoefficient=0.5

5.1.5. Data Evaluation

In the experiments within the "Multi-Phase" project, Rollbusch et al. [190] performed the experimental study for the DN330 bubble column reactor. Some of their gas holdup measurements are used for comparison with the numerical results. For a reliable comparison, the measurement and data evaluation methods in experimental and numerical way must be consistent.

For exhibiting results of this analysis, an azimuthal averaging procedure is performed on the measuring plane at 2.23 m height (see Fig. 37). The cross-section was divided into 10 annular segments (polygonal) and the radial distributions were calculated by averaging each property in each segment over a steady time interval. The azimuthally averaged radial profiles are then normalized by the column radius (r_{10}/R, r_9/R, …, r_1/R) and plotted from centerline to the wall allowing a simpler quantitative comparison.

Overall gas holdup (ε_G) is usually defined as the ratio of gas volume to total volume in the column. This method yields to an easy way of estimating holdups by measuring the initial (stagnant) liquid height in the column $H_{G,0}$ and the gassed liquid height H_G [190]. Thus ε_G is given as

$$\varepsilon_G = \frac{H_G - H_{G,0}}{H_G}$$

(92)

Based on the uncertainty problems for the measurement of H_G in the experiments, a manometric method was chosen for the gas holdup measurements where the pressure differences (Δp) between two points ($\Delta h = H_G - H_0$) are considered [190] as

$$\varepsilon_G = 1 - \frac{\Delta p}{\rho_L g \Delta h}$$

(93)

Here, H_0 is the lowest gassed liquid height in the column. Depending on the location

of the sparger and the distribution of gas bubbles, H_0 level can be taken as of the bottom of the column until somewhere above the sparger. At the experimental conditions, the pressure difference was measured by the level measurement of glass capillaries and the gas holdups are then calculated according to the ratio of the difference of liquid level capillaries and distance between two points of measurement.
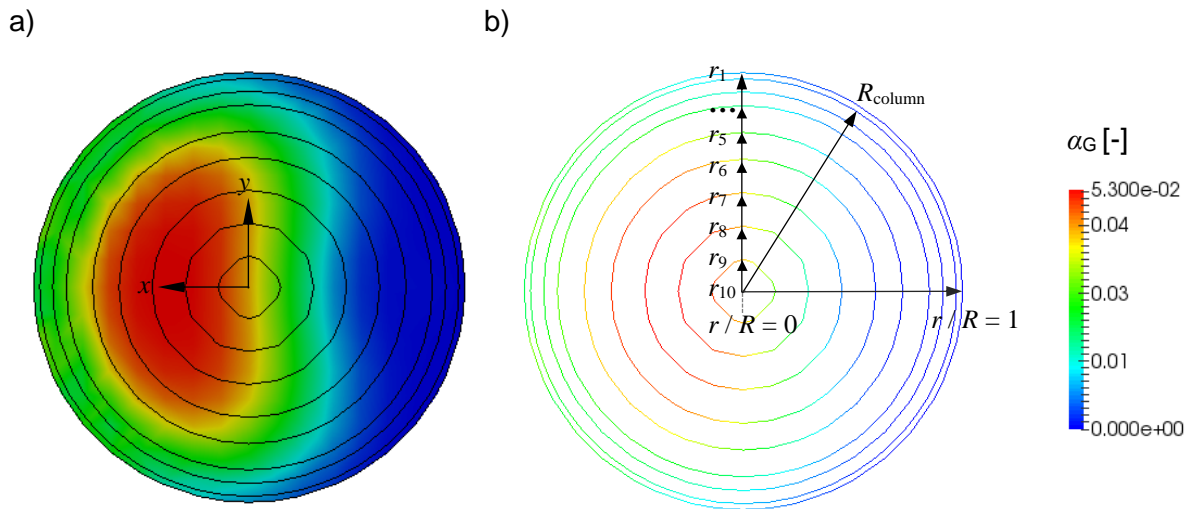

Fig. 37: Annular segments used for azimuthal averaging for each flow property. As an example, the local volumetric gas fraction α_G is exhibited on the plane at 2.23 m in two differen representations, a) over the surface b) the circular-like polygonal lines. Here, R_{column}=165 mm, r_1=164 mm, r_2=160 mm, r_3=150 mm, r_4=140 mm, r_5=120 mm, r_6=100 mm, r_7=75 mm, r_8=50 mm, r_9=25 mm, r_{10}=1 mm.

Under numerical conditions, the pressure can be obtained precisely so that Eq. (93) is directly applicable. Fig. 38 shows the gas holdups based on E-E simulation results for Case B (Table 10 in page 102). The green lines represent the calculated overall gas holdups according to Eq. (93) for data at different heights of the gassed liquid whereas the black lines are calculation from the Paraview for the sections between H_0 and H_G. The blue lines are calculated according to Eq. (92) and the right axis represented by red color shows the mean local gas holdups (α_G) on a cross-sectional plane at different H_G. As H_0 three values were used: H_0=0 where is the bottom line of the column, H_0=0.13005 m slightly above the sparger which placed at 0.13 m and H_0=0.26 m above the sparger in order to see the influence of measurement point on the gas holdup values.

Based on the evaluation of α_G it is possible to see the transition from the gas-liquid mixture to full liquid part above the column. Within this transient region, the green lines of Eq. (93) are almost aligned with each other, the black line of Paraview

calculation above H_0=0.13005 m is the closest to green line, above H_0=0.26 m is slightly above whereas H_0=0 is drastically below. This clarifies that the measurement point at H_0=0.13005 m is the most reasonable point. In order not to leave a suspicion, the results were also investigated for other cases and it proved that these results are not a coincidence. For the brevity, the results for other cases are not shown here. Nevertheless, the gas holdup via Paraview are also be calculated above H_0=0 for the further investigations. This is because the measurements were performed in the experiments for the entire column namely above H_0=0 [190].
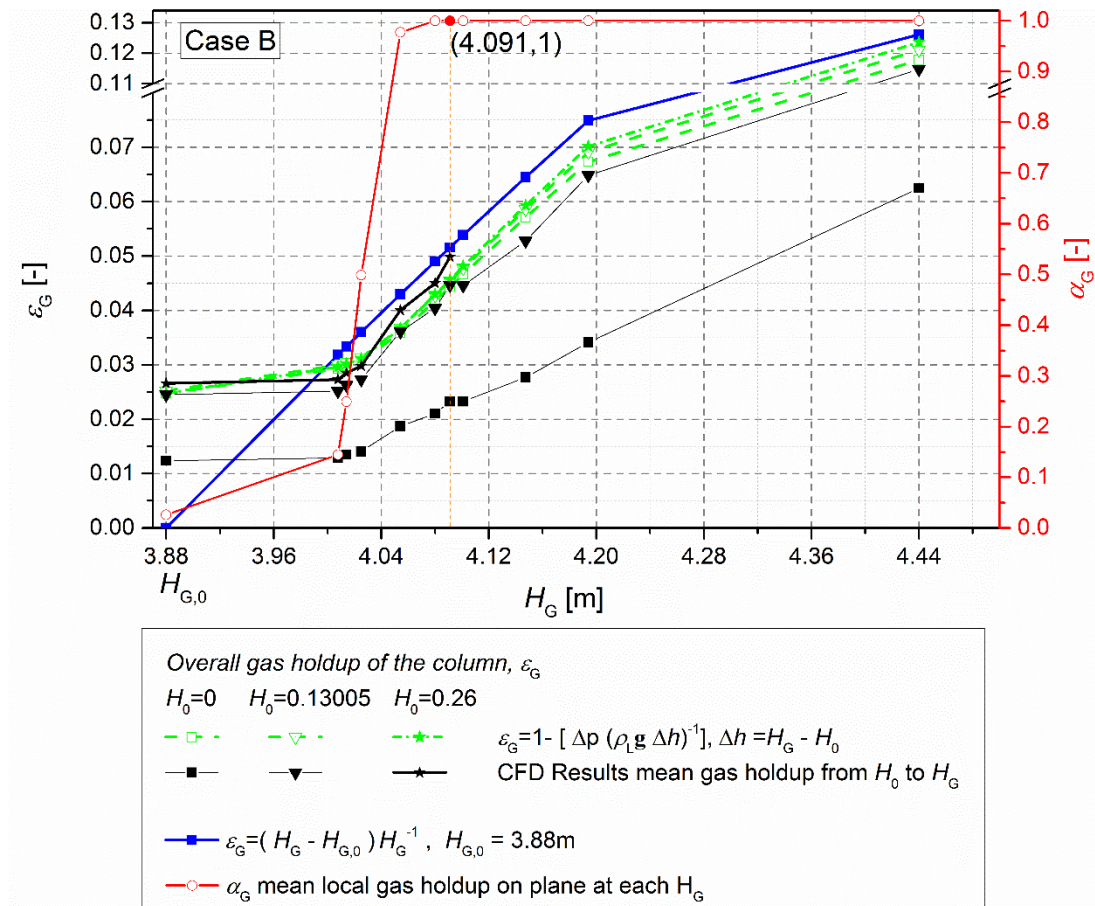
Fig. 38: Procedure for evaluation of overall gas holdup ε_G (Case B).

5.2. Results of the Euler-Euler Simulations

The importance of the interfacial term as the main source of exact k_L-equation is discussed in Chapter 4. In this section, primarily, the influence of the interfacial term (I_{kL}) on the turbulence kinetic energy (k_m-equation of the mixture k-ε model) is discussed and the radial gas content profiles provided from experiments are compared with the

simulation results. Furthermore, the local gas holdup (α_G), mean liquid and gas velocities (u_L, u_G) and turbulence kinetic energy (k_m) are studied for the varied liquid properties (water and cumene) and bubble diameter (d_B) under various operating conditions such as pressure (p), temperature (T) and superficial velocities ($U_{L,0}$, $U_{G,0}$). Performance of the implemented Olmos-model (*OlmosKEpsilon*) for the interfacial term in *twoPhaseEulerFoam* solver and the drag model of Tomiyama are also demonstrated in the following section. The cases studied are given in Table 10 (page 102) and the details of the studied flow parameters and models are given in Table 9 (page 101).

E-E simulations are performed for four scenarios given in Table 10, where the pressure is fixed for each scenario while other parameters are varied. Scenario A, B and C are based on Water - N_2 at 1, 18.5, 36 bar pressure, respectively, while Scenario D is based on Cumene - N_2. The results are discussed mostly around the cases of Scenario-B (Case B 1-9) since the several tests have been performed for those cases. The base cases of each scenario are started from where both liquid and gas at rest and simulated until the distribution of local gas fraction over time is stable. For saving computational costs and CPU time, the other cases are started from simulation runs of base cases at a steady state. The further calculations are performed by changing models or parameters until steady-state conditions are reached. This method is used unless otherwise is stated.

5.2.1. Flow structure

Fig. 39 shows the gas content in the vertical center plane of the DN330 bubble column for a test case in three different sections. In this case, the nitrogen bubbles are rising in deionized water at 18.5 bar and the turbulence model is double of the Lahey model. In the lower quarter of the bubble column (up to a height of about 1 m), the gas distribution is strongly asymmetrical. This is due to the radial displacement of the liquid feed. The velocity vectors for the liquid in Fig. 39 c) shows that in the lower part of the bubble column a recirculation region is formed leaning against one side of the wall. This recirculation region disappears from a height of about 1 m, so that the gas distribution becomes significantly more symmetrical (with higher values in the middle and lower values near the wall). However, the gas content is not fully rotationally-symmetrical in the upper half of the bubble column as well, and the lateral influence of the liquid feed and resulting liquid motion is recognizable.
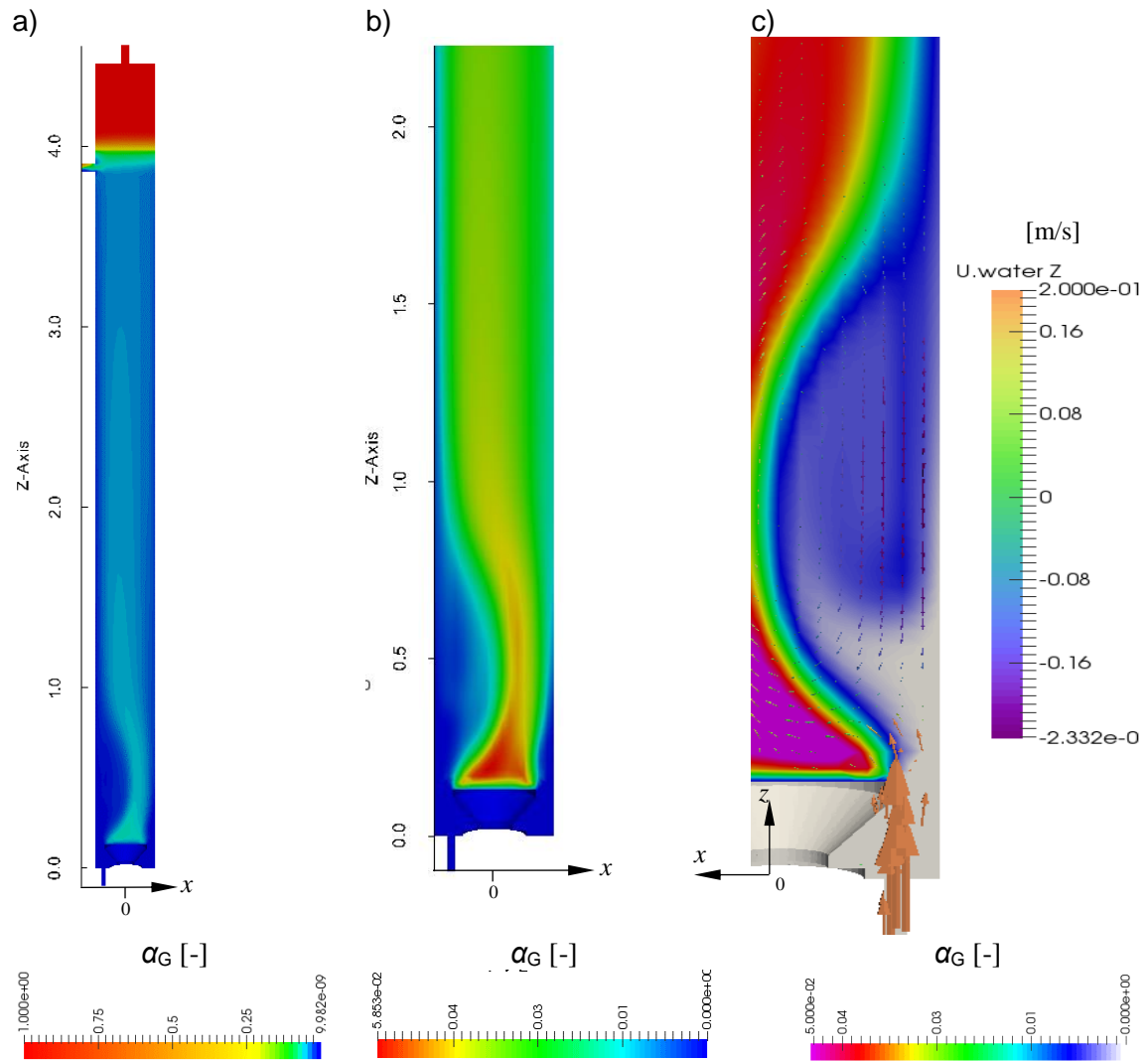
Fig. 39: Contour plots of the volume fraction of gas (α_G) in the vertical center plane of the bubble column DN330 for deionized water-nitrogen system at 18.5 bar a) Whole bubble column, b) lower half of the bubble column, c) lower quarter of the bubble column with velocity field of the liquid. (This case is only for the purpose of preliminary study and not further investigated).

Fig. 40 exhibits the vertical cross section, illustrating the volumetric gas fraction (α_G) and the gas phase velocity (u_G) contours for the Case B (Base) at different times after its start-up. The lower part is filled with water at $t = 0$ s, while the upper part (above 3.88 m) is filled with gas. Marschall et al. [157] examined the flow structure of a rectangular and a cylindrical bubble column in the frame of k-ε based E-E simulations by using the top-level solver *bubbleFoam* in OpenFOAM® software. Their results show similarities with Fig. 40. Initially, when gas enters the bubble column a bubble plume evolves (Fig. 40 a), $t = 5$ s); an asymmetric distribution within the bubble plume can be observed (Fig. 40 a), $t = 10$ s). The liquid level increases by rising bubble plume and the plume reaches to upper part filled with gas at $t = 20$ s (Fig. 40 b)). After $t = 20$ s

(Fig. 40 a)), on the bottom part, the liquid feed starts pushing the bubble plume against contrary side of the wall while the plume begins to oscillate and deviates from its central position. This deviation is caused by the wall effect hindering the central bubble plume in its lateral movement [157]. Starting from t = 90 s (Fig. 40 a), b)), a recirculation region is formed on the upper part of the column and finally at t = 390 s the radially displaced plume and the recirculation region becomes steady although the gas content is not fully rotationally-symmetrical and the lateral influence of the liquid feed is still recognizable. Due to lateral lift, large and small bubbles are radially separated [157] in the bubble swarm. Mostly large bubbles are aligned at t < 120 s in the center of swarm and at t > 120 s on the left-upper radially displaced part exhibiting a high rising velocity; taking high gas fraction values. The radial separation occurs within the radially displaced swarm where the gas fraction increases from outer to the centerline of the displaced region. The gas fraction decreases near the column wall in the recirculation region.

Fig. 41 shows the profiles of turbulence kinetic energy k_m, local gas holdup α_G and liquid velocities ($u_{L\,x,y,z}$) for Case B. The profiles are based on the data on a line in x-direction in the middle of a cross-section at different heights, i.e H=2.97 m and H=2.23 m. Near the walls, u_z values tend to decrease due to the presence of the pipe wall [202]. The void fraction α_G takes large positive values on the left side of the channel. These dense rising bubbles create velocity fluctuations in the liquid, increase the liquid velocity in flow direction and causes pseudo turbulence of liquid phase. That is why the u_z and k_m have large positive values in regions with high void fraction as well and they decrease in regions occupied by less gas where α_G has small values. This means that the liquid phase turbulence kinetic energy is mainly produced by the rising gas bubbles and it diffuses from regions of high α_G toward regions with low α_G. This finding confirms the DNS results. At a scale, the energy containing turbulent eddies are smoothened out by viscos effects which reduces their mechanical energy. In Fig. 41 a) on the r.h.s., α_G makes a peak and goes to zero. This behavior is because of examining only a certain point rather than an average of many points and it exhibits that the investigation of parameters at a certain line is not very reliable for any comparison study, neither with experiments nor with literature. Therefore, the radial distribution method by using the azimuthal averaged data as explained in Section 5.1.3 helps to minimize the effect of irregular data distribution for comparisons.

a) volumetric gas fraction α_G [-]

z

x

0.000e+00   0.01   0.03   0.04   5.300e-02

t =0s   5s   10s   15s   20s   30s   60s   90s   120s   180s   300s   390s

b) gas phase velocity u_G [m/s]

z

x

0.000e+00   0.2   0.4   0.6   8.000e-01
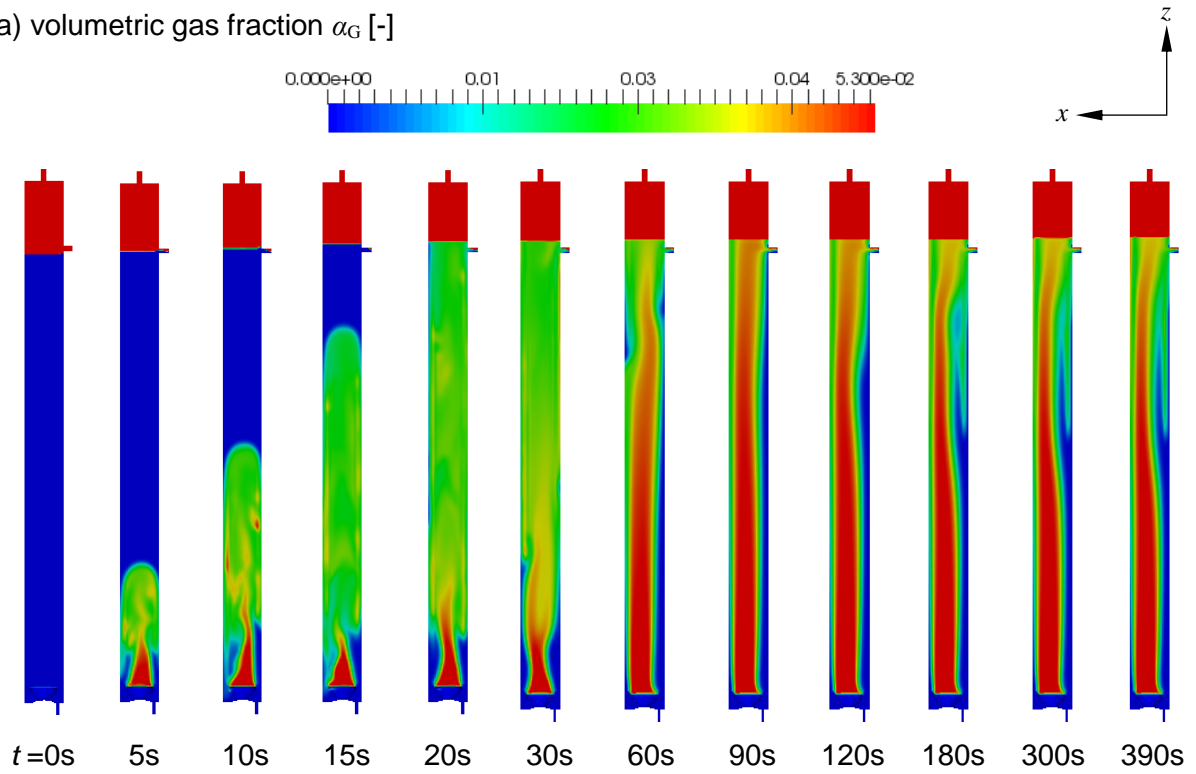
t =0s   5s   10s   15s   20s   25s   60s   90s   120s   180s   300s   390s
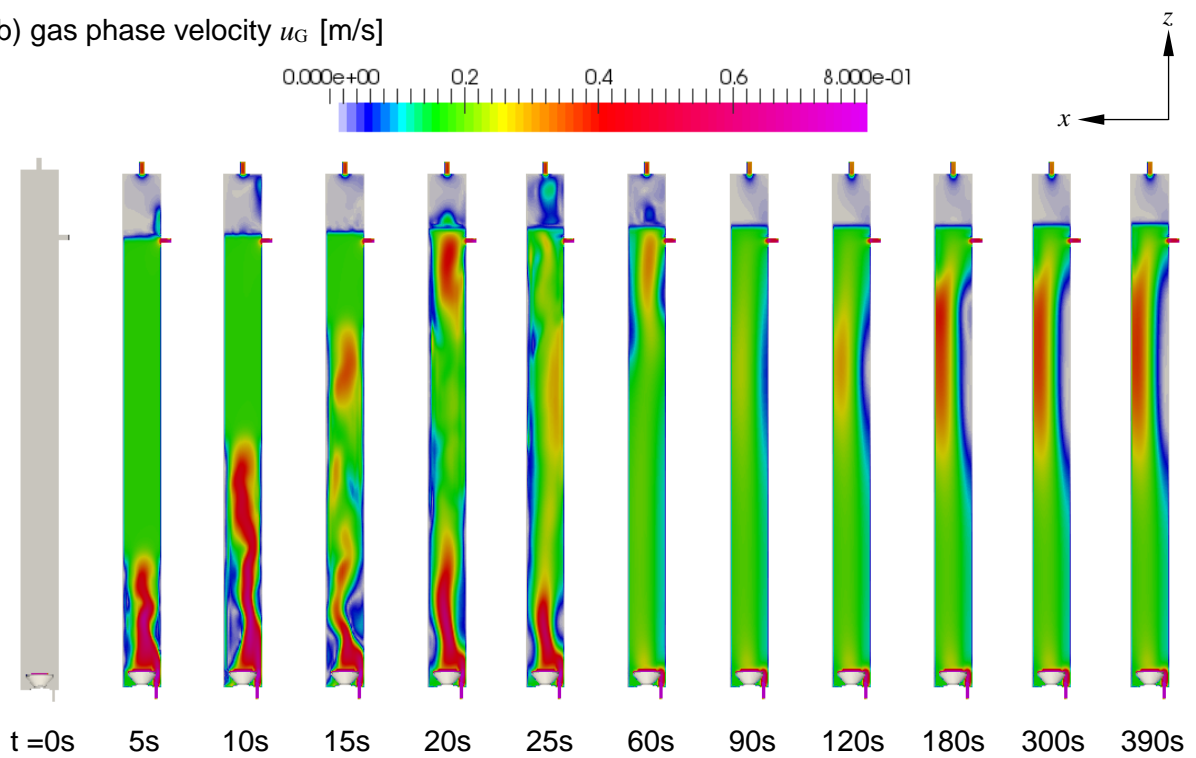
Fig. 40: Simulation results for Case B. a) volumetric gas fraction α_G, b) gas phase velocity u_G.
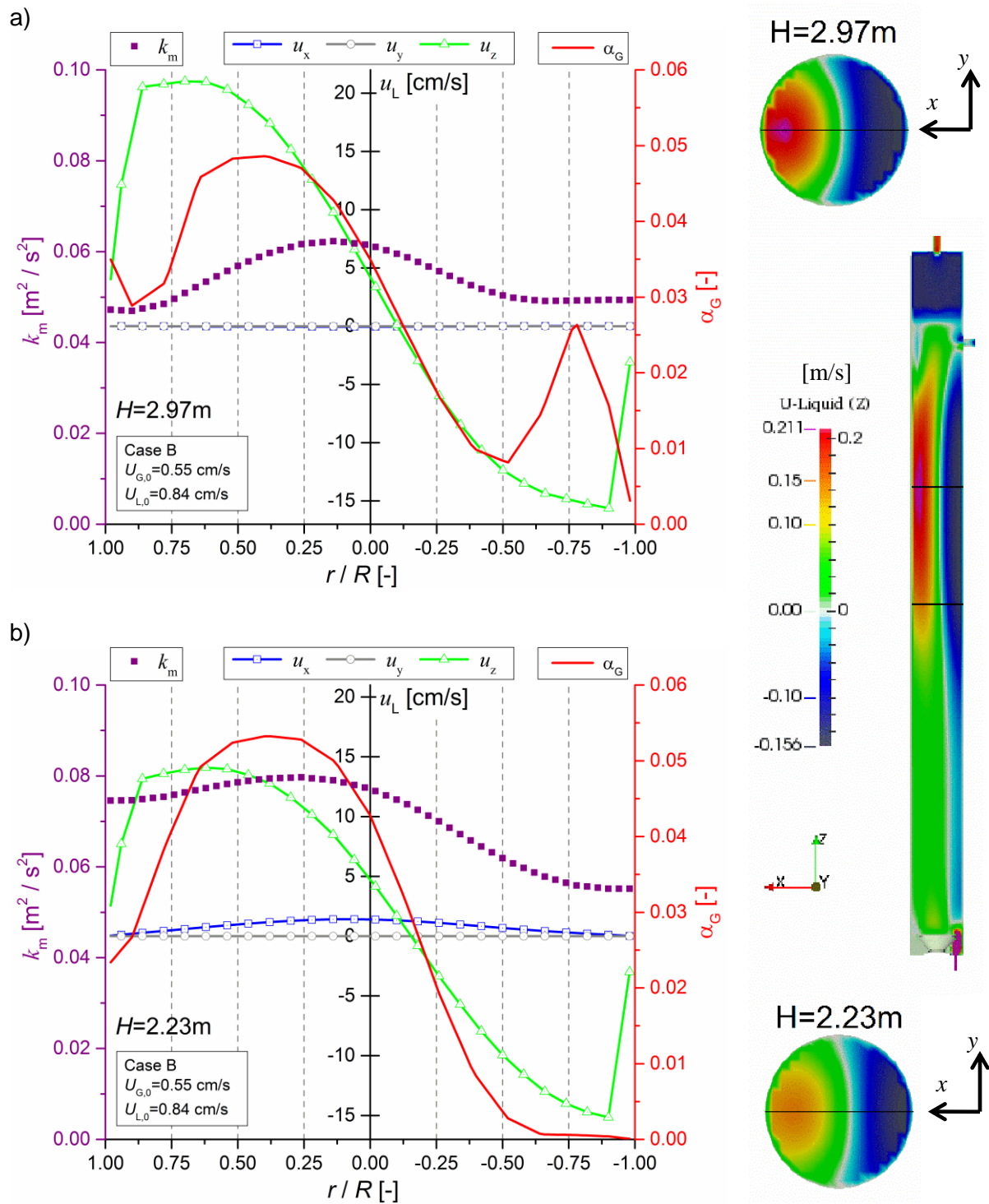
Fig. 41: Profiles of turbulence kinetic energy k_m, local gas holdup α_G and liquid velocities in three directions ($u_{L\ x,y,z}$) on a cross-section at different heights for Case B. a) H=2.97 m, b) H=2.23 m. On r.h.s the bubble column and the cross-sections are shown as color mapped.

5.2.2. General results

In Fig. 42 a), the turbulence kinetic energy k_m which is calculated by using the mixture k-ε model is plotted against the local gas volume fraction α_G at different pressures. Hosokawa and Tomiyama [202] measured turbulence intensities and Reynolds stresses of bubble-induced pseudo turbulence in air–water laminar bubbly flows within a vertical pipe of 20 mm diameter. They showed that the distributions of turbulence kinetic energy (TKE) roughly correspond to the void distributions, which shows that TKE is induced by the bubbles. Similar to the results of Hosokawa and Tomiyama [202], the distribution of k_m corresponds to the α_G distribution for all cases in a linear trend. The increase in α_G increases the number of BIT eddies, and therefore, increases the interaction between BIT eddies and based on this linear dependency TKE can be modeled as a linear function of the local void fraction [202].
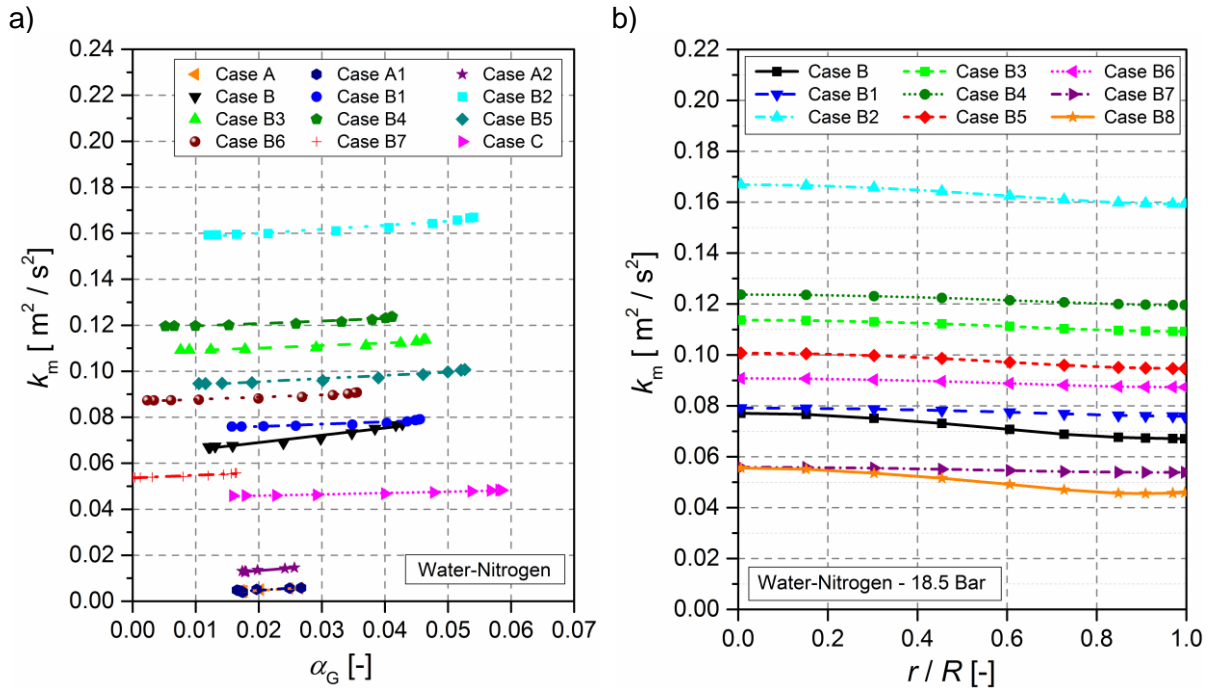
Fig. 42: a) Turbulence kinetic energy k_m plotted against the local gas volume fraction α_G at different pressures b) Radial distributions of k_m for cases at 18.5 bar. The radial profiles are obtained from azimuthally averaged data on the measuring plane at a height of H=2.23 m.

Fig. 42 b) radial distributions of turbulence kinetic energy are shown for the Scenario-B cases at 18.5 bar (cf. Table 10 in page 102). All the curves have similar trend; higher in the column center and decrease closer to the wall. The numbered cases differ from the base Case B in terms of the BIT model l_{kL} (B1, B2), the bubble diameter d_B (B3, B4), the temperature T (B5), the gas superficial velocity $U_{G,0}$ (B6, B7) and the liquid superficial velocity $U_{L,0}$ (B8). All these parameters are somehow

connected and have influence on the TKE profiles in terms of magnitude. For example, d_B and T modifies Re_B as well as the C_D and thus l_{kL}. With increasing T from 23 °C to 70 °C, the viscosity of water decreases to its half and thus increases Re_B so that C_D decreases as well. The relation of changing parameter with C_D and thus l_{kL} are plotted in Fig. 56 given in Appendix B, where it can be seen that the distribution of TKE correspond to the void distributions. Further in Fig. 42 b), the k_m decreases with the increasing liquid superficial velocity, i.e. $U_{L,0}$ = 0.0084m/s (Case B) and $U_{L,0}$ = 0.0175m/s (Case B8). It must be noted that with the decreasing gas superficial velocity, i.e. $U_{G,0}$ = 0.0055m/s (Case B), $U_{G,0}$ = 0.0034m/s (Case B6) and $U_{G,0}$ = 0.0014m/s (Case B7), the k_m increases for Case B6 but decreases for Case B7.

Fig. 43 shows the radial distribution of relative velocity for the Scenario-B cases. Except cases B3 and B4 with varied d_B, the relative velocity remains constant over the cross-section except the near wall region where the gas velocity decreases due to presence of the wall as Hosokawa and Tomiyama [202] presented the similar results in their experiments. For Case B3 d_B=3 mm and Case B4 d_B=4 mm whereas for other cases d_B=2.25 mm. An increasing relative velocity by increasing bubble diameter is observed here. It is known that the bigger bubbles rise with higher bubble velocity [190].
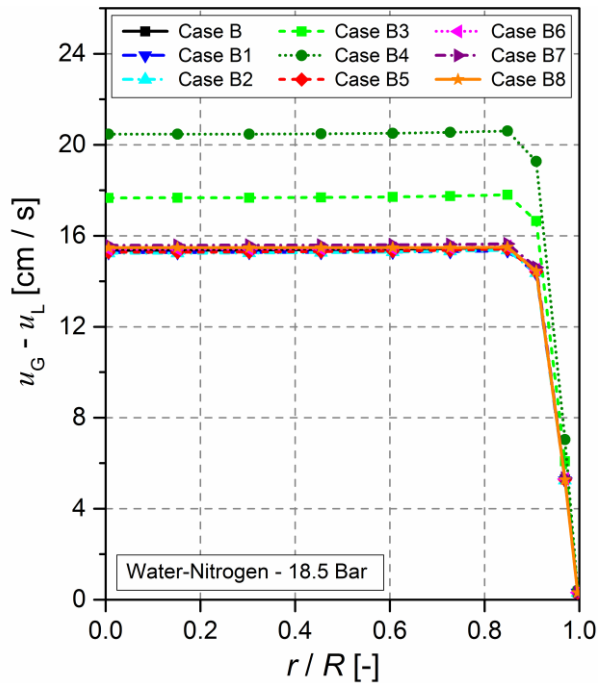
Fig. 43: Radial distribution of relative velocity for cases at 18.5 bar. The radial profiles are obtained from azimuthally averaged data on the measuring plane at a height of H=2.23 m.

5.2.3. Local gas holdup

In the frame of the joint work in the Multi-Phase project, Bieberle et al. [189] determined the radial profiles and the cross-sectional distribution of local gas holdup in the bubble column. The measurement is made on a plane at 2.23 m height and the data is averaged in each annular segment. The radial profiles of local gas content were measured by high-resolution gamma-ray computed tomography (GammaCT) and wire-mesh sensor (WMS). The experimental set-up is explained in Section 5.1.1. The experimental data is only available for radial distributions of local gas holdup (α_G). In this section, the numerical data is compared with the experiments and further investigated in terms of the axial component of mean liquid and gas velocities (u_L, u_G) and turbulence kinetic energy (k_m).

For a fully developed upward flow in a bubble column, large and small bubbles are radially separated in the bubble swarm due to lateral lift. The large bubbles are aligned in the core region and increase the rise velocity and gas fraction whereas in the near wall region a liquid film is formed and mostly small bubbles are gathered and decrease the gas fraction [157]. Besides, the experimental study from Zhou et al. [203] for a circular pipe shows that the runs with cap-bubbly, slug, and churn-turbulent flows have center peaked void profiles since large bubbles (cap, slug, and churn bubbles) concentrate in the pipe center region in upward two-phase flows.

Fig. 44 a) presents the numerical and experimental data for nitrogen in water and organic fluid cumene. The numerical results for the cumene system are close to experimental data within the range of 10 – 15 %. Besides, the flat profile α_G is represented well although the curves behave different in the near-wall region. For the water system, the deviation is too high. The profile of the water system in the experiments is rather flat in the region of r / R < 0.5 whereas the profile in the simulations is rather parabolic.

According to the experimental data plotted in the figure, the α_G for the cumene system is higher while the radial difference is much lower than the water system. The high gas holdup in cumene is connected to the smaller bubble sizes during the operation due to lower surface tension and viscosity, which suppresses coalescence and therefore, the rise velocity of the bubbles is smaller [189]. This argument can also be observed in Fig. 44 b) where the gas velocity of cumene system is lower and flatter than the water system. The reason of low radial difference of cumene system is again the existence of smaller bubbles which are more evenly distributed along the radial coordinate than the bubbles formed in water, which are denser in the middle of the column [190]. Hence, the α_G profiles of water system are steeper than the cumene

system. However, the velocity profile of water system is flatter in the core region where α_G is high. This inversely proportional distribution of the velocities to α_G is related to BIT, which flattens the velocity distribution due to the momentum mixing by eddies [202]. On the other hand, for cumene system the flattened distribution of the velocities, which is directly proportional to the α_G, can be attributed to the momentum transfer (mainly due to the drag force) between bubbles and liquid [202]. Thus, the turbulence kinetic energy for water system is higher than the cumene system. Fig. 44 c) shows that the water system produces about ten times more turbulence kinetic energy than the cumene system. The radial difference of k_m distribution is very low in comparison to gas holdup and velocity values. For water system near the wall BIT is non-zero even where there are nearly no bubbles. This is due to the diffusion of TKE from a high void fraction region to no void fraction region [202]. Nevertheless, there is a linear relation of TKE with α_G and u_G. In Fig. 45, the square of local superficial gas velocities $J_G^2 = (\alpha_G u_G)^2$ is plotted against turbulence kinetic energy k_m for different cases of water system with different $U_{G,0}$ and cumene system at different pressure. A linear equation in the slope intercept form can be defined for each case. Hence, TKE can be modeled as a linear function of α_G and u_G independent from pressure, gas superficial velocities and temperature for the investigated systems and cases in this study.
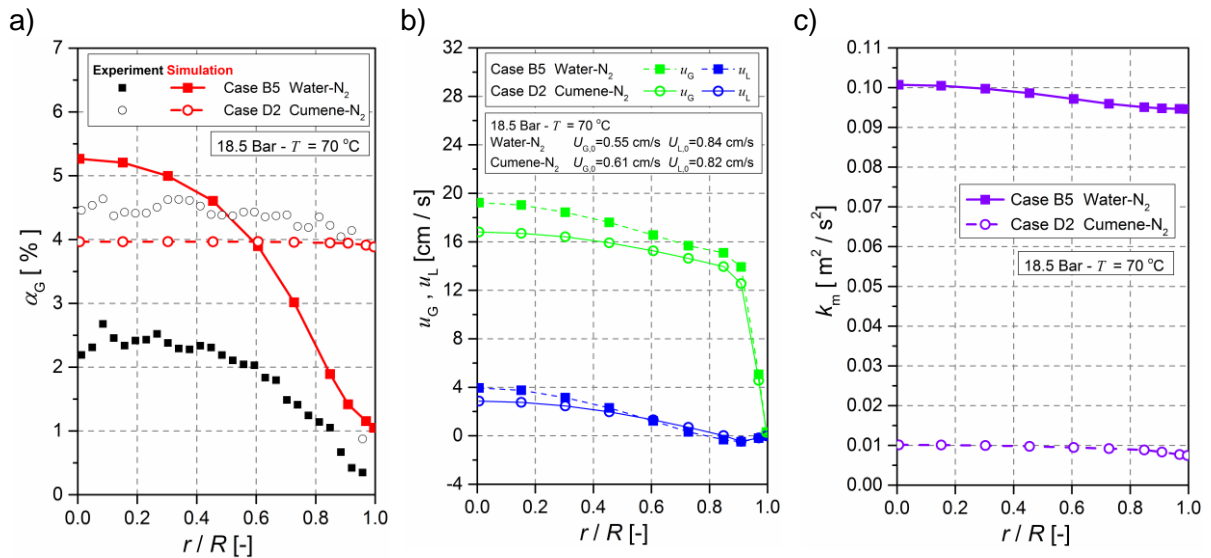

Fig. 44: The azimuthally averaged radial profiles of α_G on a plane in the center of the bubble column at a height of H=2.23 m and the experimental results. The cases are presented at 18.5 bar pressure and T=70 °C for different liquid properties.

The radial profile of gas holdup gives idea about the flow regime as well. The flat radial profile indicates that the column is operated either in a homogeneous flow regime or in a transition flow regime (from the homogeneous to the heterogeneous regime)

[189]. The homogeneous regime occurs at superficial gas velocities $U_{G,0} < 5 – 8$ cm/s [4]. The transition between the homogeneous and the heterogeneous flow can usually be observed at about $U_{G,0} \approx 5 – 7$ cm/s if the reactor diameter is not too small [204]. Another flow regime is defined by Tchowa Medjiade et al. [205] for superficial gas velocities $U_{G,0} \leq 2$ cm/s, at ambient pressure, which occurs by discontinuous bubble release, when the gas velocity is too low for continuous bubble formation from the sparger. However, such a discontinuity is not reported in the experiments.
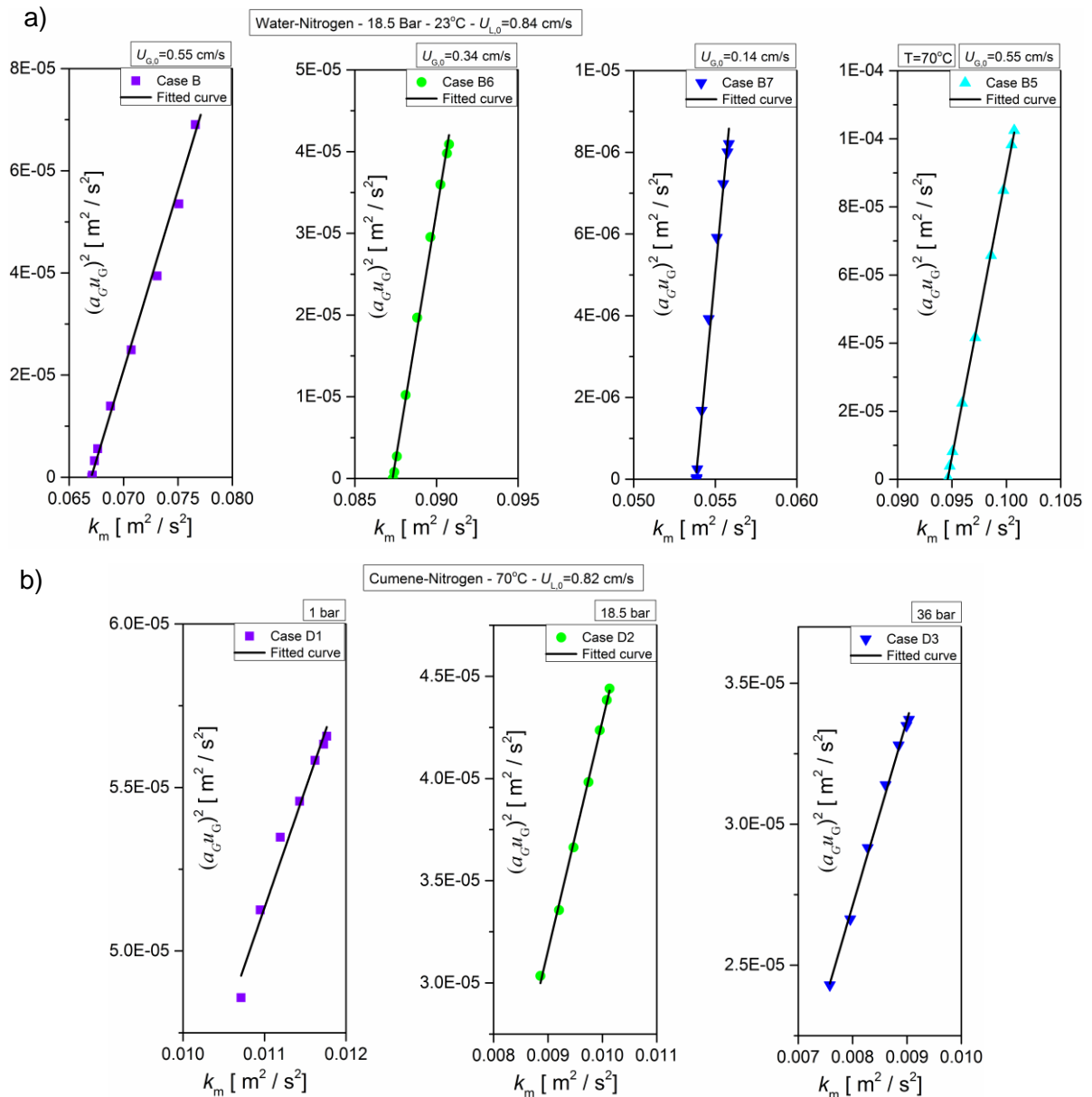
Fig. 45: The square of local superficial gas velocity $J_G^2 = (\alpha_G u_G)^2$ versus k_m. a) Water – N_2 for different $U_{G,0}$, and T b) Cumene – N_2 for different pressure. The near wall values are omitted in the plots for cumene system. The plotted data are based on the azimuthally averaged radial values of α_G, u_G and k_m on the measuring plane at a height of H=2.23 m.
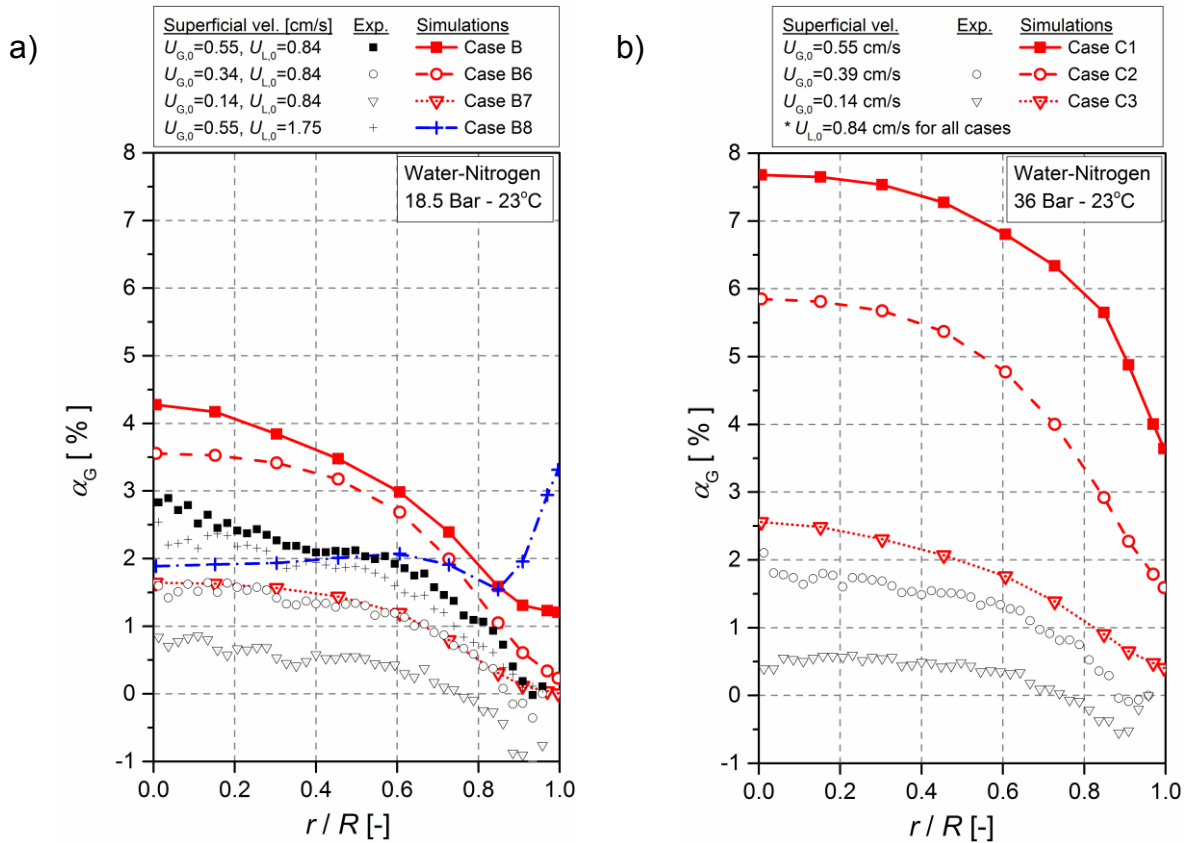
Fig. 46: The azimuthally averaged radial profiles of α_G on a plane in the center of the bubble column at a height of H=2.23 m and the experimental results. The cases are presented at T=23 °C a) for 18.5 bar with different gas and liquid superficial velocities and b) for 36 bar with different gas and liquid superficial velocities.

Fig. 46 a) and b) show α_G profiles for varied gas and liquid superficial velocities compared with the experimental results at 18.5 bar and 36 bar. At lower $U_{G,0}$, α_G profiles are flatter and lower as also shown in the experimental study of [196]. This means at higher $U_{G,0}$, more gas is gathered in the center of the column than near the wall region, which is caused by an increase in liquid circulation due to higher gas velocities [197]. The effect of pressure on local gas holdup can be observed by comparing the cases with corresponding $U_{G,0}$ side by side. It can be seen that α_G increases with rising pressure. However, several authors reported [197] that the influence of pressure is very low at low gas superficial velocities. On the other hand, overall gas holdups ε_G increase with rising pressure as it is also observed in the experiments by Rollbusch et al. [190]. In terms of the parabolic-like shape, the profiles of numerical results reflect the experimental results. At elevated pressure, the numerical results are 3 – 5 times higher than the experiments. The deviation is relatively low at 18.5 bar but still not reasonable. In the center of the column, it is 45% more than experiments for Case B while the values for Case B6 and B7 are more than double of the experiments. The deviation increases closer to the wall. Negative values of α_G in the experiments are

naturally not physical. This might be related to the calculation methodology during the measurements.

In Fig. 46 a), the profiles of Case B8 with $U_{L,0}$ = 1.75 m/s reflect the experimental results in the core region of the column in $r / R < 0.4$. In the part of $r / R \approx 0.4 - 0.6$, the curves increase slightly, and then start decreasing until $r / R \approx 0.85$ and again increasing in the near wall part of $r / R > 0.85$ until reaching the wall. The numerical results are similar to those reported by Zhou et al. [203] except the void fraction values at the wall. The authors performed experiments in a circular pipe with about 50 mm diameter and for a bubbly flow run with $U_{L,0}$ = 1.95 m/s observed a uniform void fraction profile except a near-wall peaking (starting from approximately r / R = 0.7 to 0.95) that decreases at the wall. Considering the above-mentioned experiments, in Fig. 46 a) the α_G profile at the wall (after $r / R > 0.95$) must have decreased. Such behavior at the wall is also observed in Fig. 48 a) for the α_G profiles of the cases at 1 bar. On the other hand, non-physical α_G values at the wall are observed from the contour plots during the data evaluation for the Case B8.

More plots and discussions regarding the influence of pressure change as well as the influence of different bubble diameters in gas holdups and turbulence kinetic energy, and further investigation of axial evaluation of local gas holdup are presented in Appendix B.

5.2.4. Influence of BIT model

In this Section, the radial distribution of local parameters such as gas holdup, gas and liquid velocity and the turbulence kinetic energy are analyzed based on the varied BIT models. The investigations in Chapter 4 show that the Olmos-model [136] and Lahey-model [24] given for the interfacial term are both in relatively good agreement with the DNS data. The Lahey-model in Eq.(90) was already implemented in OpenFOAM® while the model of Olmos in Eq.(91) is implemented during this research. In principle, the model of Olmos has a constant prefactor and therefore a linear dependency on the drag coefficient C_D while the Lahey-model has a non-linear dependency on C_D, as given in Table 7. Euler-Euler simulations showed that the Olmos-model provides a slightly more homogenous flow structure than the Lahey-model.

The influence of the BIT models on local gas holdup, velocity profiles and the turbulence kinetic energy is studied by comparing the Olmos-model with the Lahey-model and a doubled prefactor version of the Lahey-model in Eq.(90) where the prefactor is taken as 0.5 instead of 0.25. Fig. 47 shows the contour plots of the slices

in the middle of the bubble column at 2.23 m, as an example for Scenario-B cases. In Fig. 48 b), these contour plots are then azimuthally and over the period $t = 200 - 300$ s averaged so that the radial profiles allow a simpler quantitative comparison. Fig. 48 depicts the radial distributions of local gas holdup (α_G), axial component of mean liquid and gas velocities (u_L, u_G) and turbulence kinetic energy (k_m) at 1 bar (a) and 18.5 bar (b), for the Scenario-A and Scenario-B cases given in Table 10 (page 102).
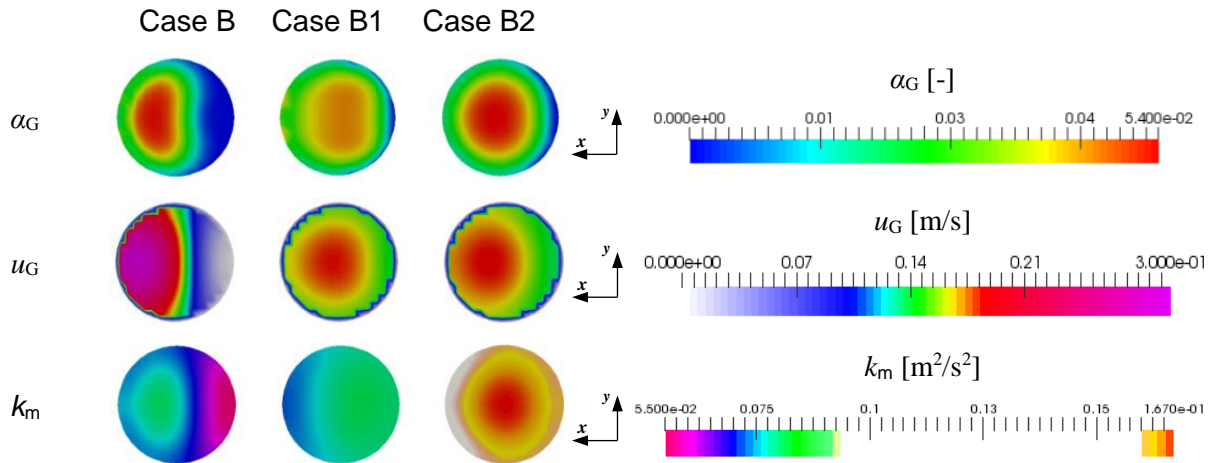
Fig. 47: Contour plots of the measurement plane at a height of H=2.23 m. The related properties from top to bottom: α_G, u_G, k_m.

Fig. 48 a) shows the simulation results at 1 bar. The inset graph for α_G present more details for the curves with a logarithmic scale of y-axis. The results for local gas holdup α_G is in good agreement with the experiments in the center of the bubble column (at $r / R < 0.3$) where the profiles are rather flat. The α_G profiles from simulations are flat even further in the region of $r / R < 0.6$. Unphysical α_G values at the wall can be observed from the contours of the local gas holdup for Case A in Fig. 54 given in the Appendix.B.1. In the outer region of the column at $r / R > 0.3$, the numerical results are greatly above the experiments. At $r / R \approx 0.6$ they decrease first (as observed in the inset graph) and then at $r / R \approx 0.85$ increase sharply near the wall and reach their maximum value on the wall. The experimental curve on the other hand always decreases in $r / R > 0.3$ in direction to the wall. The velocity profiles of gas and liquid are uniform except the near wall region, where the gas velocity drops rapidly at $r / R \approx$ 0.9. Similar liquid velocity profiles are reported by Zhou et al. [203]. Comparable to the numerical results in Fig. 48 a), the authors indicated that the relatively uniform distribution of the void fraction in the bulk flow helps developing uniform liquid-phase turbulence structure in the pipe center region [203]. The influence of the varied BIT models can be seen in the inset graph. The Olmos-model exhibits higher slope where

r / *R* > 0.3 and a deeper low peak where *r* / *R* > 0.85. On the other hand, the k_m values increase more than double, around three times more, when the value of the prefactor in the model for l_{kL} is doubled. The Olmos-model is slightly lower in the core region and slightly higher in the wall direction in *r* / *R* > 0.6. The k_m values, excluding the Case A2 with doubled l_{kL}, are relatively low, nearly negligible. Shi et al. [206] measured the liquid-phase turbulence in air-water two-phase flows for a circular flow channel with an inner diameter of about 25 mm at room temperature and 1 bar pressure using particle image velocimetry. The authors presented that for the bubbly flows with low void fractions less than 3%, the turbulence structure is similar to single-phase flow with peak values in the near-wall region. The low TKE profiles of the cases at 1 bar in Fig. 48 a) reflect this statement.

All three cases exhibit similar peak near the wall so that the reason of this behavior may be related to the models chosen in the simulations. It must be noted that the simulations are performed without consideration of the wall lubrication force which defines repulsive force between bubbles and the pipe wall [159]. In their numerical and experimental study for bubbly flows for water and air at atmospheric pressure and room temperature, Hosokawa and Tomiyama [159] investigated the effect of wall lubrication force model on gas holdup and observed better predictions without wall lubrication. In their results, close to the wall at *r* / *R* ≈ 0.85 the α_G curve exhibits a peak similar to the ones in Fig. 48 a), but afterwards drastically reduces at the wall unlike the ones in Fig. 48 a). The same behavior is also observed by Antal et al. [158] in their void fraction profiles for co-current upflow. The results in near-wall region are difficult to estimate and must be investigated further.

For Scenario-B cases in Fig. 48 b), the computed α_G profiles overestimate the measured α_G significantly by 50% and more. The minimum and maximum values of α_G for each measurement point are also shown in the figure. The Lahey-model provides the closest results to the experiments although in the core region even the minimum α_G value is not able to estimate the experimental data. After *r* / *R* > 0.3 some lower values of α_G get closer to and lower from the experimental curve. For the Olmos model, parabolic shape of the α_G profile is alike with the measured profile from *r* / *R* = 0.4 to 0.6. However, the magnitude of its curve including the minimum measured values is higher than the experiments. The reason for the deviation may be the flow structure. In the experiments [189, 190], a liquid film is formed near the wall and the flow structure is more homogenous and symmetrical in radial direction contrary to the simulations, although they are in a steady state. The radial averaging method used in the experiments may also lead to a deviation between numerical and experimental results.
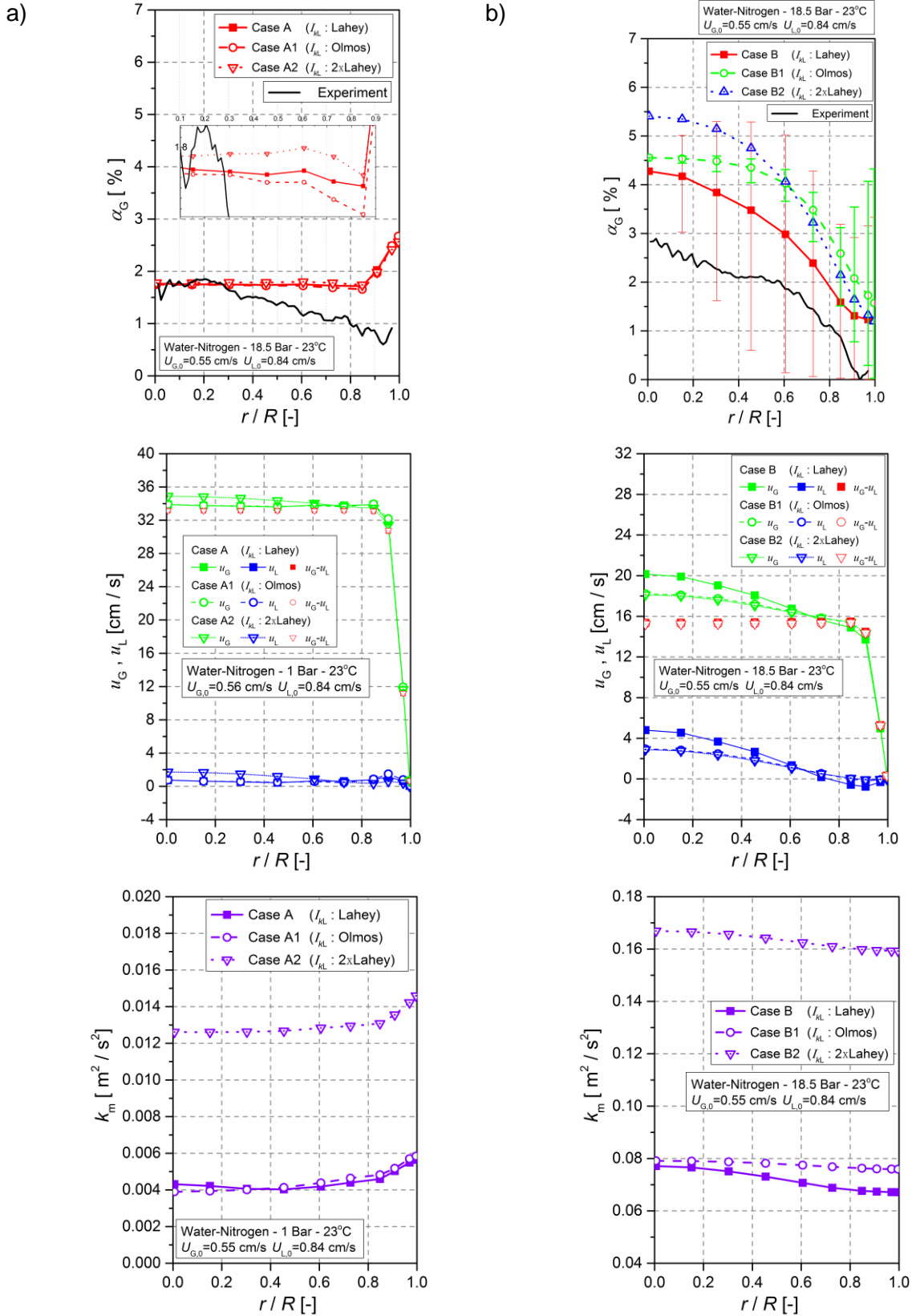
Fig. 48: Azimuthally averaged radial profiles of α_G; u_L, u_G; k_m in the center of the bubble column at a height of H=2.23 m with Olmos and simple and doubled Lahey interfacial term I_{kL} at T=23 °C. Comparison with experimental results for α_G. a) Scenario-A with p = 1 bar, Cases A, A1, A2. b) Scenario-B with p = 18.5 bar, Cases B, B1, B2.

The increase in α_G in a core peeking profile accelerates the velocity in the core region due to the momentum transfer between bubbles and liquid. The velocity profiles are consistent with the α_G profiles when this momentum transfer between the phases is stronger than the mixing due to BIT then [202]. In Fig. 48 b), Case B and Case B2 with doubled l_{kL}, each has a core peeking α_G profile but contrarily rather flat velocity profile. According to Hosokawa and Tomiyama [202], this implies that the BIT flattens the velocity distribution due to the momentum mixing by eddies. This means for the cases here, the BIT is dominant. The u_G and u_L profile of Case B2 are lower in the core region (r / R < 0.65), where α_G takes higher values, but higher in the near wall region in comparison to Case B. It means that Case B2 has even flatter profiles than Case B. This indicates the clear influence of the stronger BIT model as it can also be depicted from the profiles of k_m in Fig. 48 b) that the k_m values increase more than double when the value of the prefactor in the model for l_{kL} is doubled. On the other hand, in the case of the Olmos-model, k_m distribution over the cross-section in Fig. 47 is more homogenous than the Lahey-model. Therefore, the radial difference of k_m values for the Olmos-model is very small. The difference between the Olmos and Lahey models on k_m is low in the core region and increases closer to the wall.

For all cases in Fig. 48 a) and b), the radial distribution of relative velocity remains constant over the cross-section except the near wall region, where u_G tends to decrease. Similar results are also discussed in Hosokawa and Tomiyama [202]. For Scenario-B cases, the liquid velocities are upwards in the central region and downwards near the column wall. The correlation between α_G and k_m is proportional. Increase in α_G also increases TKE.

5.2.5. Overall gas holdup

Prediction of gas holdup is essential for the design of bubble column reactors. Several authors developed correlations to calculate the amount of gas holdup. For a detailed overview of available correlations see Krishna et al. [207]. In the experimental study of Rollbusch et al. [190] in the frame of the Multi-Phase project, they reviewed some of these approaches to compare with the bubble columns investigated in the project. It is noted that many of the correlations are based on experiments with water, which is most often not of interest for industrial production plants, and correlations suited for the prediction of holdups in organic material are very rare. The appropriate correlation to predict gas holdup must account for column diameter, different liquid properties and gas density. Those criteria are met by the equations from Zehner [208, 209] as identified in Krishna et al. [207]. Zehner's [208] correlation predicted a

decrease of holdups with column diameter which is about the same magnitude as observed in the experiments [190].

In his earlier work, Zehner [209] extended the improved circulation cell model originally suggested by Joshi and Sharma [210] by substituting circulation cells with crosswise on top of each other aligned vortex-cylinder-couples. In this alternative form, an upward flow is always available in the centerline of column. The centerline velocity of the liquid phase is always directed upwards and the liquid velocity near the wall is directed downwards. Most of the bubbles move upwards with the liquid whereas the near wall regions the liquid moves in the opposite direction and entrains some bubbles. As a result, a difference in gas holdups occurs which causes a pressure difference that is relieved by pressure losses due to liquid movement [190, 209]. Based on the pressure difference Zehner [209] defined an equation which calculates the maximum centerline velocity of the liquid phase as

$$w_{c,L} = \left(\frac{1}{2.5} \frac{\rho_L - \rho_G}{\rho_L} U_{G,0} g D \right)^{1/3}$$

(94)

where $U_{G,0}$ is the gas superficial velocity, D is the column diameter.

In a later study, Zehner [208] demonstrated the gas-liquid interactions for bubble columns on the basis of dispersion coefficient, volumetric mass transfer coefficient and gas holdup and defined correlations for those parameter. Zehner's correlation [208] to predict gas holdups is based on the liquid centerline velocity and given as

$$\varepsilon_G = \frac{U_{G,0}/w_{bs}}{\left[1 + 4 \left(\frac{U_{G,0}}{w_{bs}} \right)^{2/3} \left(\frac{w_{c,L}}{w_{bs}} \right) \right]^{0.5}}$$

(95)

where w_{bs} is the slip velocity of the biggest stable single bubble. The correlations from Mersmann [107] can be applied for the calculation of w_{bs}. The velocity correlation for the biggest single stable fluid particle is given as [107]

$$w_b = 1.55 \left(\frac{\sigma g (\rho_L - \rho_G)}{\rho_L^2} \right)^{0.25} \left(\frac{\rho_G}{\rho_L} \right)^{1/24}$$

(96)

For liquid to gas viscosity ratio $\mu_L / \mu_G \approx 10 \text{-} 200$, the maximum rise velocity of a single fluid particle is given as [107]

$$w_{max} = 2 \left(\frac{\sigma g (\rho_L - \rho_G)}{\rho_L^2} \right)^{0.25}$$

(97)

The cases in this work remain in the given range 10 – 200. At $T = 23$ °C for Water - N_2 $\mu_L/\mu_G \approx 47$ and for Cumene - N_2 $\mu_L/\mu_G \approx 44$. The simplified version of the correlation in Eq. (96) is utilized by Rollbusch et al. [190] referring to Zehner [208] and given as

$$w_{b,simple} = 1.55 \left(\frac{\sigma g (\rho_L - \rho_G)}{\rho_L^2} \right)^{0.25} \tag{98}$$

All the correlations for w_{bs} depend on the liquid and gas density and the surface tension. These parameters are dependent on temperature and pressure. Therefore, the velocity correlations must be calculated accordingly. In Fig. 49, the ε_G is calculated by Zehner's correlation [208] based on the correlations from Eqs. (94), (98), (96) and (97). The liquid and gas density values are taken from Table 9 (page 101) for three different pressures; 1 bar corresponds to Scenario-A, 18.5 bar to Scenario-B and 36 bar to Scenario-C cases. For the correlations $w_{b,simple}$ and w_{max}, which differs only by the prefactor, no major deviation is observed at different pressures. However, the line for w_b is clearly above the lines for 18.5 bar and 36 bar.
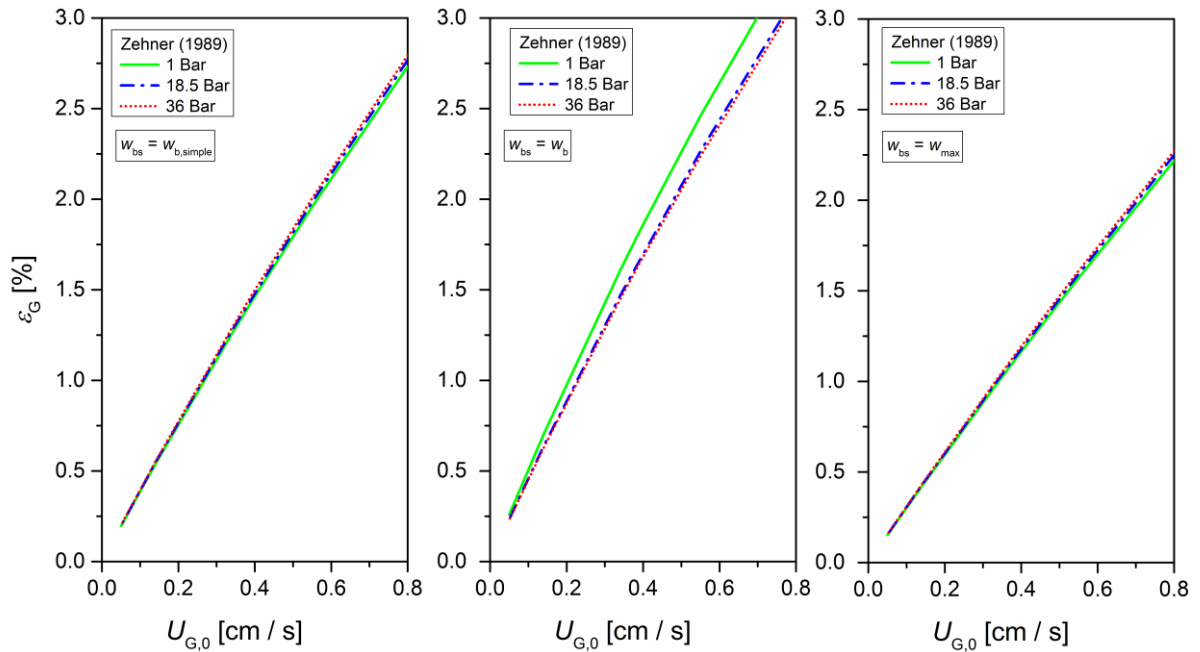
Fig. 49: Overall gas holdups ε_G calculated by Zehner's correlation [208] with w_{bs} values $w_{b,simple}$, w_b, w_{max} (from left to right) at three different pressures 1, 18.5, 36 bar.
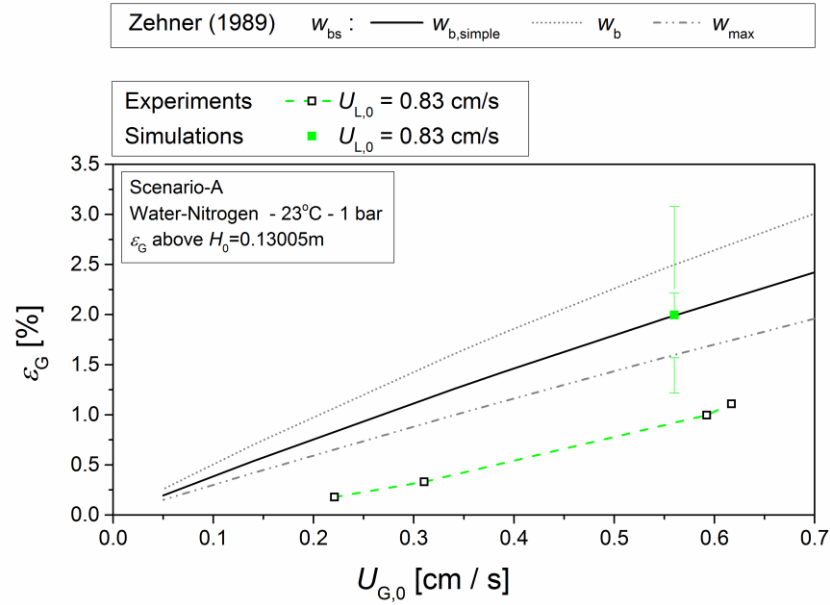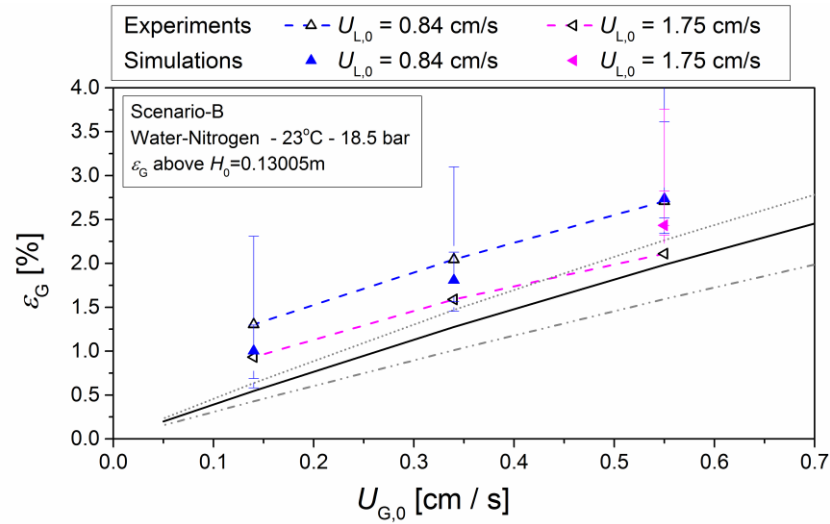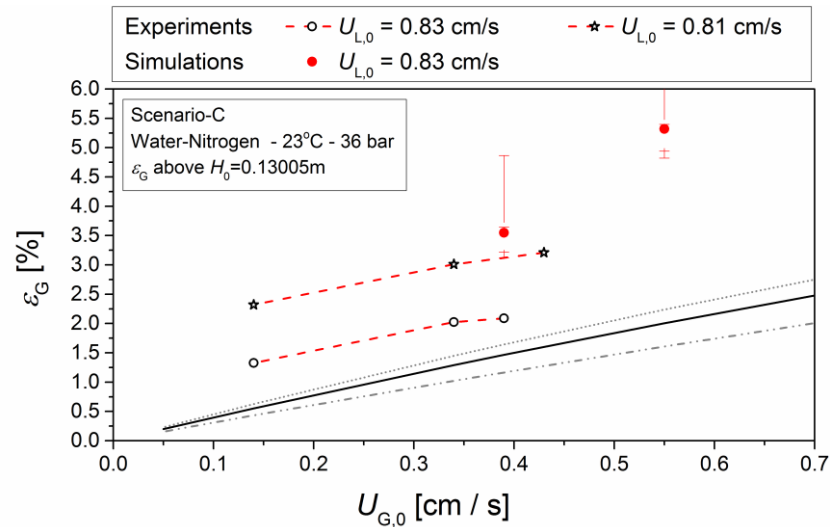
Fig. 50: Overall gas holdups ε_G from E-E simulations above H_0=0.13005 m, ε_G from the experiments and ε_G calculated by Zehner's correlation [208] with varied w_{bs} values for Scenario A, B, C cases.

Fig. 50 shows overall gas holdup ε_G from E-E simulations and experiments at T = 23 °C and 1, 18.5 and 36 bar pressure. The ε_G from E-E simulations account for the part above the lowest gassed liquid height H_0 = 0.13005 m, which represents slightly above the sparger. In Fig. 50 b) the liquid superficial velocity $U_{L,0}$ is varied by almost doubling while in a) and c) $U_{L,0}$ is almost fixed. The literature values are calculated with Zehner's ε_G correlation [208] in Eq. (95). The $w_{c,L}$ is calculated by the formula in Eq. (94) while w_{bs} is calculated by different correlations from Eqs. (98), (96) and (97). The numerical results are presented as the averaged ε_G together with maximum, minimum and upper/lower quartile values shown with connected horizontal lines.

In Fig. 50 a) and c), the simulation results for Scenario-A and Scenario-C cases are above the experimental results. In Fig. 50 a), the only case for Scenario-A fits perfectly to the ε_G with $w_{bs} = w_{b,simple}$. In Fig. 50 c), the calculated lines underestimate the Scenario-C results as well as the experiments. In Fig. 50 b), the Scenario-B cases with the doubled $U_{L,0}$ and varied $U_{G,0}$ are presented. The mean ε_G from simulations at high $U_{G,0}$ has a perfect fit with experimental data. However, with decreasing $U_{G,0}$ the simulations underestimate the experimental line with a deviation up to ca. 22%. On the other hand, the upper quartile values of cases with lower $U_{G,0}$ match with the experimental result. For the doubled $U_{L,0}$, only a single numerical case is available, and it overestimates the experiments. None of the calculated holdups matches the measured holdups exactly. However, the numerical results reflects a similar inclination as the calculated ε_G with $w_{bs} = w_b$ whereas for the experiments $w_{bs} = w_{b,simple}$ presents closer inclination.

In Fig. 51, H_0 = 0 is considered as measurement level for simulations. This means the whole column including the below part of the sparger is taken into account. By this measuring point, the ε_G values are about half of the plotted values in Fig. 50. For brevity in the graph, the calculated ε_G lines are only plotted for 18.5 bar properties. It is noted in Fig. 49 that only the calculated ε_G line with w_b at 1 bar differs from the plotted w_b line for 18.5 bar. Different from Fig. 50 b), another set of experimental data for 18.5 bar is shown in Fig. 51. Even for the same initial conditions such as $U_{L,0}$ and $U_{G,0}$, different measurement data are available in the experiments. It can be seen from the figure that the simulation cases, depending on the used turbulence model, are closer to those experimental values with a 10 – 15 % deviation at $U_{G,0} > 0.3$. The Scenario-B cases are then predicted well by the calculated ε_G with $w_{bs} = w_{max}$ whereas the Scenario-C cases by the calculated ε_G with $w_{bs} = w_b$. The prediction is better at lower values of $U_{G,0}$. All correlations overestimate the Scenario-A case as well as the related experiments. The closest correlation is ε_G with $w_{bs} = w_{max}$ as also discussed by Rollbusch et al. [190],

who showed that ε_G with $w_{bs} = w_{max}$ predicts bubble velocities of nitrogen in cumene with outstanding accuracy at 1 bar ≤ p ≤ 36 bar whereas the measure bubble velocities of nitrogen in water are about 10% different from the calculation at 1 bar ≤ p ≤ 18.5 bar. However, the provided experimental results plotted in Fig. 51 reflects only the tendency qualitatively but not quantitively. The deviation is around 30 – 40 %. The measurement techniques and measurement level play an important role for the comparative study. Based on the result here, the ε_G results for the measurement level H_0 = 0 exhibit more reliable results, both against experiments and the correlations.
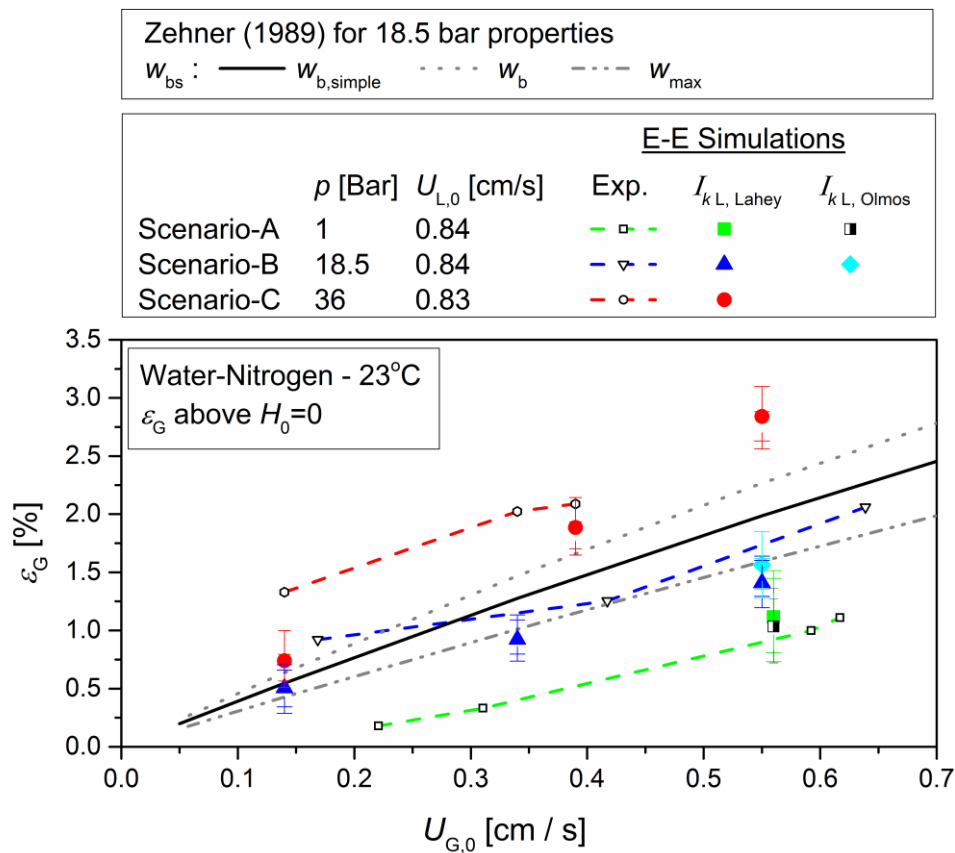
Fig. 51: Overall gas holdups ε_G from E-E simulations above H_0=0 for different turbulence models, ε_G from the experiments and ε_G calculated by Zehner's correlation [208] with varied w_{bs} values for the scenarios A, B, C.

Fig. 51 also shows the influence of the turbulence model applied in the E-E simulations. All the cases plotted in the figure applied Schiller-Naumann drag model. For Scenario-A case, the mean gas holdup computed from the simulations with the Olmos-model is 7% less than the one with the Lahey-model. Thus, the ε_G with the Olmos-model takes a closer value to the experimental line. The ε_G with the Lahey-model overestimates the experimental line ca. 23% while the deviation of ε_G with the

Olmos-model is 13%. For Scenario-B case, the mean ε_G obtained from the simulations with the Olmos-model takes a 11% higher value than the one with the Lahey-model. Thus, the ε_G with the Olmos-model takes a closer value to the experimental line. The ε_G with the Lahey-model underestimates the experimental line ca. 18% while the deviation of ε_G with the Olmos-model is only 9%. In general, the Olmos-model effects the results for a better approximation. If the Olmos-model affects the other cases of Scenario-B similarly around 7 – 10 %, the simulation results would fit the blue dashed lines of experiments perfectly. Besides, the ε_G with $w_{bs} = w_{max}$ predicts the mean gas holdup with the new implemented Olmos-model for both examined cases. The calculated ε_G with $w_{bs} = w_{max}$ predicts the numerical results at $U_{G,0} = 0.4$ as well.

As a summary, the measurement level for simulations at H_0 = 0 gives better results even though the section below sparger where almost no bubble exists is also taken into account. Therefore, the mean gas holdup decreases around 40 – 50% in comparison to the measurements at H_0 = 0.13005 m. By this decrease, the numerical results fit the calculated ε_G as well as the experimental data. A reasonable prediction of numerical results is observed with the correlations $w_{bs} = w_{b,simple}$ and $w_{bs} = w_{max}$. In terms of experimental comparison, at low superficial gas velocity values larger deviations between experiments and simulations are observed since it is more difficult to measure holdups at gas fluxes of low magnitude [190]. Rollbusch et al. [190] also indicates that larger deviations occur when holdups are predicted in water because of possible impurities present in the experimental facility during the measurements. Nevertheless, the numerical results simulated by using the Olmos turbulence model and measured above H_0 = 0 are very close to the experimental data with a deviation of 9 – 13 %. This result is very satisfactory.

Fig. 52 presents the overall gas holdup from the simulations for nitrogen in water and cumene and the predicted gas holdups calculated by Zehner's ε_G correlation [208] with $w_{bs} = w_{b,simple}$ and $w_{bs} = w_{max}$. The cases form scenarios A, B, C and D are presented in the graph at T = 23 °C and different pressures. All the cases that are shown here used Schiller-Naumann drag model and varied turbulence models. The drag model from Tomiyama is not included in the results because of convergence problems during the simulations with this drag model. The gas holdup is measured above H_0=0.

Fig. 52 a) shows that the gas holdup at 18.5 bar and 36 bar both for nitrogen in water and cumene is predicted within 25% range by the correlation $w_{bs} = w_{b,simple}$. All cases at 18.5 bar are 25% underestimated and all Water-N_2 cases at 36 bar are 25% overestimated. Cumene case at 36 bar exhibits the closest gas holdup prediction among all. On the other hand, the prediction of holdups at 1 bar both in water and

cumene is failed. The Water-N_2 case at 18.5 bar enters this range with consideration of the new implemented Olmos-model for BIT. In the inset plot, the difference between the Lahey-model and the Olmos-model is shown in detail where the case with Lahey-model is out of the given range while the Olmos-model with its maximum value very close to the predicted line. At 1 bar, the case with Olmos-model gets far from the range.

In Fig. 52 b), the gas holdup with $w_{bs} = w_{max}$ correlation is able to predict the holdups at 18.5 bar in cumene and water. The case with the Olmos-model is predicted with high accuracy. The holdup in cumene at 36 bar is also perfectly predicted whereas the results in water at the same elevated pressure are completely underestimated as it was also shown in the experiments by Rollbusch et al. [190]. They explained this result based on the addition of small tracer substances that changed water quality. However, the numerical simulations account for the pure system and the results are still same as their observation. Hence, the water quality due to traces is not the reason for the deviation. It must be noted that these velocity correlations are improved based on other correlations and experimental measurements and thus limited to certain parameter range and operating conditions.

Based on the findings above, the Zehner correlation [208] for gas holdup with the velocity correlation of Mersmann [107] w_{max} is applicable for holdups in organic liquids at elevated pressures (18.5 and 36 bar) and in deionized water at 18.5 bar. The prediction is highly accurate for the cases investigated here. The choice of Olmos-model for the turbulence production due to bubbles is also an important factor for the reliable results. The numerical findings and experimental findings are also aligned. Therefore, the outcome of this validation study is consistent and satisfactory.
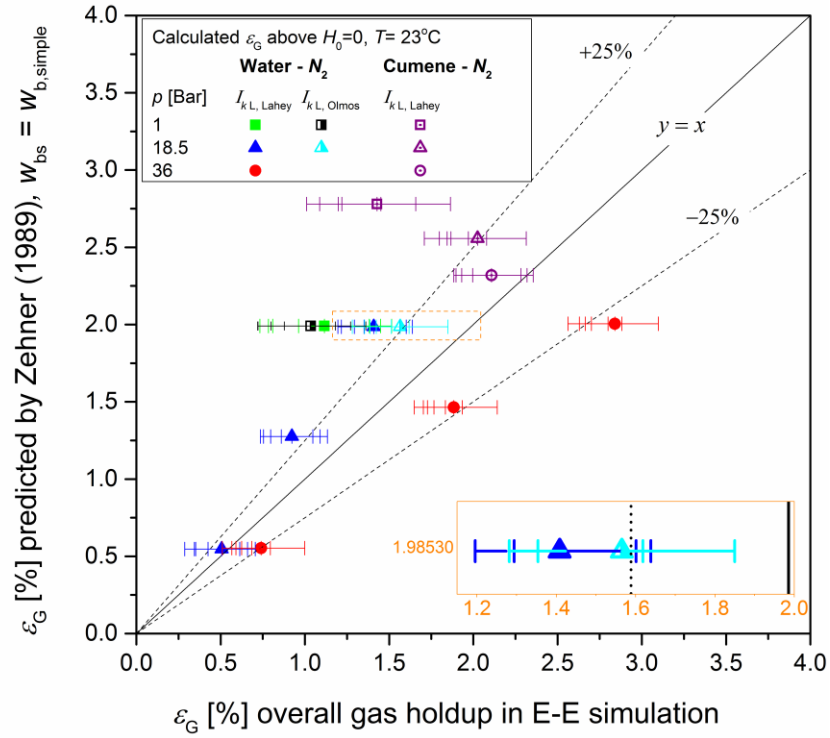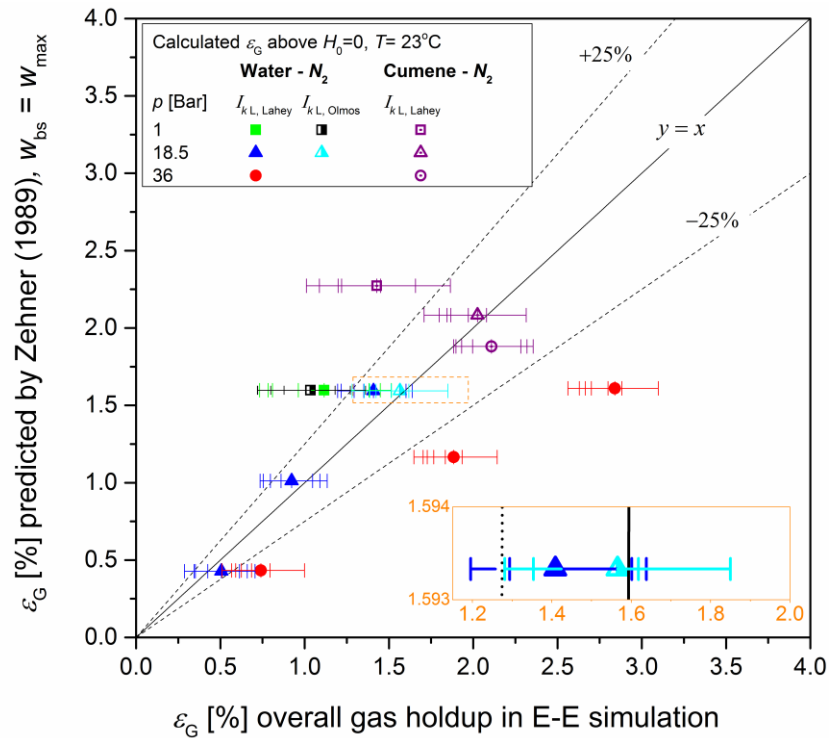
Fig. 52: Overall gas holdup from the simulations and predicted gas holdups. Prediction by the model of Zehner [208] and by applying the bubble velocity a) $w_{bs} = w_{b,simple}$ b) $w_{bs} = w_{max}$. The inset plots are closeup of the marked areas in each graph. $y = x$ represents the parity.

5.2.6. Summary

Eulerian two-fluid simulations with statistical turbulence models in bubble columns often ignore the complex physics of the turbulence and adopt standard single-phase closure laws and coefficients. The concept of a priori testing of model assumptions for closure terms is certainly useful for the development of improved models. However, it does not consider that in practical CFD computations the quantities entering into the model – e.g. the mean void fraction and velocity profiles – are influenced by the model itself, as it is part of the governing equations and, therefore, affect the solution for the mean quantities. Since this feedback is non-linear, the a posteriori testing of any potential model refinement in full E-E simulations is necessary and validation by experiments is mandatory [6]. The joint work in the project provides the unique opportunity to validate such an implementation with pilot-scale bubble columns. Therefore, different from the previous studies, the improved BIT models are applied for industrial purpose and verified for a test bubble column.

In this context, an industrial bubble column DN330 with 4 m height and 0.33 m diameter is computed with the two-fluid model in OpenFOAM® using the twoPhaseEulerFoam solver. The standard k-ε model [121] and the so-called basic-mixture turbulence model (the mixture k-ε model) [131, 135] are utilized. The results for the k and ε using those models are very close for the cases investigated in this study. The turbulence kinetic energy (TKE) is analyzed along with the local (α_G) and overall (ε_G) gas holdups, and the velocity profiles of gas (u_G) and liquid (u_L) phase. Industrial bubble columns are operated at elevated pressures and high temperatures. Organic liquids are of main interest for industrial processes. Therefore, in the simulations various industrial operating conditions are considered such as pressure 1 bar ≤ p ≤ 36 bar and temperature 23 °C ≤ T ≤ 70 °C. Nitrogen in deionized water and nitrogen in organic cumene are used as gas-liquid systems. Gas superficial velocities vary in the range of $0.0014 \leq U_{G,0} \leq 0.0056$ m/s.

The variation of turbulence model, pressure, temperature and superficial velocities have no influence on relative velocity of gas and liquid. The relative velocity remains constant over the cross-section except the near wall region, where u_G tends to decrease. The correlation between α_G and k_m is proportional. Increase in α_G also increases TKE. A linear relation of k_m with $\alpha_G u_G$ is identified for each case examined in this work.

The influence of the interfacial term in the turbulence kinetic energy equation is examined using the turbulence models from Olmos et al. [136] and Lahey [24], which are identified through the assessment of the balance equation for turbulence kinetic

energy of the liquid phase (the exact k_L equation) based on DNS data of bubble swarms. The Lahey model was already available in the OpenFOAM®. In the course of this study, the Olmos-model is implemented (OlmosKEpsilon) as an extension to the mixture k-ε model.

It is deduced from the examined radial profiles that the BIT is dominant in the flow. The velocity profiles are flattened due to the mixing by eddies in the central region of the bubble column where more bubbles exist. This behavior is especially obvious when the value of the prefactor in the interfacial term is doubled while the turbulence kinetic energy increases more than double. This means that the influence of the BIT model is more significant on the flow than expected. The influence of turbulence model both on azimuthally averaged radial profiles of the local gas holdup α_G and that of the velocity profiles of phases (u_G and u_L) is minor at normal pressure 1 bar while it is noticeable at 18.5 bar. This is because, for the bubbly flows at atmospheric pressure with low void fractions less than 3%, the turbulence structure is similar to single-phase flow [206] and thus the bubble-induced turbulence is nearly negligible at 1 bar. With the Olmos-model, the gas bubbles are distributed more symmetrically over the cross-section and the distribution of TKE is more homogenous than with the Lahey-model. Therefore, the radial difference of k_m values for the Olmos-model is very small. The Olmos-model has a promising influence on overall gas holdup of the bubble column for a deionized water-nitrogen system where ε_G is 7% lower at 1 bar and 11% higher at 18.5 bar in comparison to the Lahey-model. This leads to a closer value to the experimental data with deviation of 13% and 9%, respectively.

It is known that for a fully developed upward flow in a bubble column, large and small bubbles are radially separated in the bubble swarm due to lateral lift where the large bubbles are aligned in the core region and small bubbles in the near wall region [157]. According to the bubble distribution data from experiments, the bubbles are smaller in the cumene than in the water. Small bubbles are produced due to lower surface tension and viscosity of cumene system, which suppresses coalescence [189]. The simulation results are able to reflect the characteristic of liquid systems. The large bubbles formed in water are denser in the middle of the column and thus the gas fraction and velocity are locally higher than the organic system. However, the average gas content over the cross-section is higher for the cumene system. This is because the smaller bubbles in cumene are more evenly distributed along the radial coordinate. Hence, the α_G profiles are flat. The analysis of exact k_L equation in this study shows that larger bubbles cause more turbulence kinetic energy. The TKE for the water system is about ten times more than that for the organic system. It is also interesting

to see that, in the near-wall region, TKE is non-zero even there are nearly no bubbles. This is due to the diffusion of TKE from the central region with high void fraction to near-wall region with low void fraction [202]. This characteristic of TKE is also observed in the budget of the exact k_L equation.

The numerical results for the local gas holdup α_G are compared with the reference experiments by project partners for the same bubble column. In particular, at high pressures, the measured α_G values for deionized water-nitrogen system are significantly overestimated by the simulation for most of the cases examined here. The parabolic shape of the measured α_G profile is better approximated by the Olmos-model at 18.5 bar. For normal pressure, the numerical results are in good agreement with the experiments only in the core of the bubble column. Closer to the wall, the numerical data take values greatly above the experiments. For the cumene-nitrogen system at 70 °C, the numerical results are close to experimental data with a deviation in the range of 10 – 15 %. On the other hand, the simulation results of water-nitrogen system for overall gas holdup ε_G are close to the experimental values with a deviation of approximately 10 – 15 % at 1 bar, 18.5 bar and partially at 36 bar. For the latter pressure, the deviation increases for the lower values of gas superficial velocity.

The CFD data are further compared with the correlations from the literature for the estimation of overall gas holdup ε_G. The Zehner approach [208] for ε_G is applied using the three different velocity correlations for the slip velocity of bubble from Mersmann [107], $w_{b,simple}$ from Eq.(98), w_b from Eq.(96) and w_{max} from Eq.(97). All correlations overestimate the numerical as well as the experimental results for 1 bar. The ε_G values of all cases at 18.5 bar and 36 bar both for nitrogen in water and cumene are predicted within the 25% range of the correlation for the slip velocity of bubble $w_{b,simple}$. For the nitrogen in water at 36 bar, the closest approach at lower values of $U_{G,0}$ is calculated with w_b for the biggest single stable fluid particle. The simulation results of the deionized water system at 18.5 bar and the organic cumene liquid system at elevated pressures (18.5 and 36 bar) are predicted well by the calculated ε_G using w_{max}, which is valid for $\mu_L/\mu_G \approx 10\text{-}200$. The systems examined here fall into this range. The predictions with w_{max} at 18.5 bar are highly accurate. With the choice of Olmos-model, the simulation results are even closer to the predicted line with w_{max}. The Zehner correlation [208] for ε_G is able to predict both systems at elevated pressures with up to 25% deviation when the slip velocity is calculated with $w_{b,simple}$, whereas it is able to predict both systems at 18.5 bar precisely when the slip velocity is calculated with w_{max}.

6. Conclusions and Outlook

This Chapter concludes the thesis in two Sections. The first one summarizes the conclusions of this work and the second one makes suggestions for future work.

6.1. Conclusions

The dissertation presents numerical investigations of bubble-driven two-phase flows at various scale to develop adequate closure relations for the bubble-induced turbulence (BIT). For this purpose, two computational methods are used: Direct Numerical Simulations (DNS) and Euler-Euler (E-E) approach (also called two-fluid model). The DNS is employed on small scale from single bubble to bubble swarms to determine the closure for the interfacial term in the balance equation of liquid phase turbulence kinetic energy, k_L. Two suitable models for the interfacial term are identified and utilized for the k-ε based CFD simulations of industrial bubble columns using OpenFOAM®. The models provide accurate and efficient results for the engineering computations. The new model implemented in OpenFOAM® has positive impacts.

Although this study focuses on the development of improved turbulence models, the findings contribute in several ways to understanding of numerical analysis of two-phase flows. Comprehensive DNS investigations for single bubbles revealed that a grid resolution of 20 cells per bubble diameter, a liquid-to-gas density ratio of 25 and a gas-to-liquid viscosity ratio of $\Gamma_\mu < 1$ are appropriate to obtain results that are independent from the mesh size, the gas density and the gas viscosity, respectively. The vertical distance of bubbles must be at least 10 times of bubble diameter (L_x / d_B > 10) to minimize the influence of the wake acceleration that modifies the velocity profile in the wake.

The bubble swarm simulations provide insights for limitations of numerical study of bubbly flows. The numerical coalescence is displayed frame-by-frame as it takes place mainly within a single mesh cell. To avoid coalescence, the best practices in this work for bubble swarms in a certain range of Morton and Eötvös numbers $2.2 \times 10^{-8} \leq M \leq 3.1 \times 10^{-7}$ and $0.747 \leq E\ddot{o} \leq 2.625$ suggest a limitation of the void fraction to 2 – 2.5 % and a definition of the wall distance to be at least 5 times bubble diameter. Taken together, this may provide the rectilinear bubble trajectory and least possible lateral motions. Using the domain replication methodology, the number of bubbles is increased up to 64 bubbles in a larger computational domain while the void fraction is preserved. The simulations up to 24 bubbles are further analyzed for the turbulence kinetic energy. Thereby, the present study extends the DNS study of Ilic [26], which

was for up to eight bubbles with $M > 3 \times 10^{-6}$, to higher number of bubbles in a wide range of $E\ddot{o}$ and Re for lower M values, down to $M = 2.2 \times 10^{-10}$ for single bubbles and $M = 2.2 \times 10^{-8}$ for bubble swarms.

The concept of a priori testing of model assumptions for closure terms in the balance equation of liquid phase turbulence kinetic energy k_L is necessary for the development of improved models. The DNS data of bubble swarms is used for the statistical analysis of k_L profiles. In bubble columns, the large-scale liquid recirculation generates shear-induced turbulence (especially near the walls) which is superposed to the BIT. For the conditions examined here, the production due to shear stresses is negligible. The main source term for the turbulence kinetic energy is the interfacial term. Production and dissipation are not in local equilibrium. Therefore, molecular and turbulent diffusion redistribute the surplus of production of k_L from regions of high to low void fractions or, another way of saying, from the two-phase regions towards the single-phase regions. The results for the budget of k_L equation are consistent with the findings from the literature [26, 28, 29].

The investigations for the closure of the interfacial term $I_{k\mathrm{L}}$ in the k_L equation disclose two models that are in a good agreement with the DNS data: The Olmos-model from Olmos et al. [136] and the Lahey-model from Lahey [24]. The Olmos-model is implemented in OpenFOAM® as an extension to the mixture k-ε model [131, 135] and named as OlmosKEpsilon. Both models are utilized for CFD simulations using the twoPhaseEulerFoam solver in OpenFOAM®.

The CFD study complements the solution procedure by engineering simulations that are designated to reflect various industrial operating conditions. In practical CFD computations, the quantities entering into the model – e.g. the mean void fraction and velocity profiles – are influenced by the model itself, as these quantities are part of the governing equations and, thus, affect the solution for the mean quantities. A-posteriori testing of potential model refinement in E-E simulations is therefore necessary and further validation by experiments is mandatory [6]. For this purpose, the identified turbulence models are proved for an industrial bubble column. The results for the void fraction (or gas holdup) are validated with experimental data and correlations from literature. The turbulence kinetic energy (k_m) is studied in detail and the most of findings are supported by previous studies in literature.

A linear relation of turbulence kinetic energy with the local void fraction (α_G) and mean gas velocity (u_G) is identified for each case examined in this work. Further studies with a greater focus on mathematical modelling could produce correlations of k_m depending on $(\alpha_\mathrm{G} u_\mathrm{G})^2$. Regarding another aspect of local cross-sectional analysis, the

average gas content in organic cumene is higher whereas the rise velocity of bubbles is lower than in water. The numerical findings corroborate the experimental results and the deductions of Bieberle et al. [189], who suggested that the smaller bubbles are formed in the cumene than in the water due to lower surface tension and viscosity, which suppresses the coalescence yielding low bubble rise velocity. Moreover, the radial separation of large and small bubbles due to lateral lift is rather uniform for cumene owing to the low bubble size distribution. The further investigations of radial profiles reveal that the influence of bubble size and coalescence is significant on the bubble-induced turbulence. The larger bubbles in water generate about ten times more turbulence kinetic energy than the organic system.

The CFD investigations prove that the bubble-induced turbulence is dominant in the flow. Consistent with the DNS results, the E-E simulations confirm the strong association between the turbulence kinetic energy and the interfacial term I_{kL} as the main source. It is interesting to note that the turbulence kinetic energy increases more than double when the value of the prefactor in the model for I_{kL} is doubled.

In terms of the turbulence models, the analysis for the flow quantities computed with the Olmos-model indicates that the cross-sectional distribution of the void fraction is smoother and the radial differences in the turbulence kinetic energy profiles are almost negligible in comparison to the simulations with the Lahey-model. The choice of turbulence model has a minor influence on the local void fraction and the velocity profiles at normal pressure (1 bar) while it is noticeable at 18.5 bar.

For the water-nitrogen system at 23 °C, the simulation results of overall gas holdup ε_G for higher values of the gas superficial velocity are close to the reference experiments with a deviation of approximately 9 – 15 %. Using the Olmos-model has improved the numerical results at 1 bar and 18.5 bar around 50 % compared to those with the Lahey-model. In general, the measured α_G values are significantly overestimated by the simulations particularly at high pressures. For the organic cumene-nitrogen system at 70 °C for 18.5 bar pressure, the numerical results for α_G are close to experimental data with a deviation in the range of 10 – 15 %.

At the final stage, the CFD simulations are validated by the correlations from literature. The Zehner correlation with the slip velocity of bubble from Mersmann [107] (w_{max}) is identified as an applicable approach for the estimation of overall gas holdup ε_G in industrial bubble columns, i.e. using organic liquids, operating at elevated pressures. The simulation results of the water-nitrogen system at 18.5 bar and the cumene-nitrogen system at elevated pressures (18.5 and 36 bar) are predicted well by the calculated ε_G using w_{max}. The predictions with w_{max} at 18.5 bar are highly accurate.

The results with the Olmos-model are even closer to the predicted line with w_{max}. Moreover, another correlation for the slip velocity from Mersmann [107], $w_{b,simple}$ provides an approximation up to 25% deviation at elevated pressures.

6.2. Outlook

This dissertation contributes to the understanding of turbulence modelling in bubbly flows and the use of CFD as a tool for design of industrial scale bubble columns. This study presents a full picture of numerical investigation of bubbly flows from a single bubble to industrial scale. Therefore, it has been one of the first attempts to examine various scale of bubbly flows numerically using different approaches and involving systematic validation of the models for each scale. The findings will be of interest to future numerical studies in the field and the insights may be of assistance to comparative studies for industrial bubble columns using CFD. The methodology in this study establishes a framework for the development of models for bubble-induced turbulence in bubble columns. This research has a number of important implications for future practice.

In the Multi-Phase project, experimental data were available only for gas holdup. The validations have been carried out for one size pilot-scale bubble column. For a systematic validation study of gas-liquid flows in bubble columns, a complete experimental data set is necessary (i.e. measurement of bubble size distribution, void fraction profiles, mean liquid and gas velocity profiles, profiles of turbulence kinetic energy in one experiment). Further investigation and experimentation, using a wide range of column diameter, varied operating conditions and production-scale bubble columns is strongly recommended. The measurement methods in experimental and numerical study must be aligned. On the other hand, a numerical research for further improvement of the two-fluid model in twoPhaseEulerFoam solver of OpenFOAM® would be worthwhile for the numerical stability of the simulations for bubble columns under industrial conditions.

In general, the experimental data obtained in a lab-scale bubble column may represent the industrial-scale reactors in terms of similar mixing and fluid dynamics [211]. However, a variety of scale-up criteria, for example size of bubble column and type of sparger, must be taken into account. As more research involving the combination of experiments and CFD is required [212], a study comparing the lab-scale and the production-scale bubble columns may help for acquiring a better understanding of the scale-up of bubble columns.

Further model improvements for the closure of interfacial term are required for

general approaches. A study with more focus on mathematical modelling of turbulence models is therefore suggested. A greater focus on numerical coalescence phenomenon could produce interesting findings that ensure mono-disperse flow. In the current work, mean bubble diameter of originally mono-disperse flow is used for calculating the Eötvös and Reynolds numbers, the drag model and the model for interfacial term, even in case of coalescence. In future investigations, it might be possible to use a different approach to determine the bubble diameter. Other options could be to use the "Sauter mean diameter", to consider an approach that accounts for the bubble size distribution or to apply population balance models where bubble breakup and coalescence are essential. Tailored studies are needed for each of the suggested alternatives.

The current study provides comprehensive analysis of the budget of exact equation liquid phase turbulence kinetic energy. The assessment of the k_{L} profiles indicates that the gain of turbulence kinetic energy is mainly caused by the interfacial term and it is redistributed by the diffusion term from regions of high void fractions to low void fractions. There are still many unanswered questions about the diffusion term. As presented briefly in this work, it consists of molecular and turbulent diffusion where the turbulent part dominates over the molecular part. Both sub-terms have complex distributions of the profiles and thus require a detailed investigation. By applying a similar procedure as in the current work, it is possible to use the DNS data to develop improved models for the diffusion term as well as other closure terms in the equation of liquid phase turbulence kinetic energy.

Appendix A.   DNS

A.1. Tables of the simulations

Tables for single bubble simulations and bubble swarm simulations are given in this section.

Table 14: Single bubble simulations - Computational set-up specified for DNS.

	M7-SB1 (M7)	M7-SB2	M7-SB3	M7-SB4	M7-SB5	M7-SB6	M8	M9	M10
L_{ref}	4 mm	6 mm	4 mm	4 mm	4 mm	4 mm	4 mm	4 mm	4 mm
U_{ref}	0.1m/s	0.1 m/s	0.1 m/s	0.1 m/s	0.1 m/s	0.1 m/s	0.1 m/s	0.1 m/s	0.1 m/s
Computational domain size	1x1x1 2x1x1	1x1x1	1x1x1	1x1x1	1x1x1 2x1x1	1x1x1 2x1x1	1x1x1	1x1x1	1x1x1
Grid	$64^3, 80^3, 100^3$, 128x64x64, 64x64x80.	100^3	64^3	64^3	80^3 and 128x64x64	$64^3, 80^3$ and 128x64x64	100^3	100^3	100^3
Mesh cells per d_B	16,20,25,16,20	16.6	16	16	20, 16	16, 20, 16	25	25	25
Equivalent d_B	0.25	0.1667	0.25	0.25	0.25	0.25	0.25	0.25	0.25
d_B	1 mm	1 mm	1 mm	1 mm	1 mm	1 mm	1 mm	1 mm	1 mm
d_B / L_{ref}	1/4	1/6	1/4	1/4	1/4	1/4	1/4	1/4	1/4
Num. of bubbles	1	1	1	1	1	1	1	1	1
ε_G	0.818%	0.24%	0.818%	0.818%	0.818%	0.818%	0.818%	0.818%	0.818%
ρ_G / ρ_L	1/25	1/25	1/100	1/50	1/25	1/25	1/25	1/25	1/25
μ_G / μ_L	1	1	1	1	1/2, 1/5	1/10	1	1	1
M	2.22×10^{-7}	2.22×10^{-7}	2.22×10^{-7}	2.22×10^{-7}	2.22×10^{-7}	2.22×10^{-7}	2.77×10^{-8}	3.47×10^{-9}	2.22×10^{-10}
$E\ddot{o}_B$	2.529	2.529	2.608	2.582	2.529	2.529	1.265	0.632	0.253
$E\ddot{o}_{ref}$	40.468	91.054	41.733	41.312	40.468	40.468	20.234	10.117	4.047
We_{ref}	10.743	16.114	10.743	10.743	10.743	10.743	5.371	2.685	1.0743
Re_{ref}	380.76	571.14	380.76	380.76	380.76	380.76	380.76	380.76	380.76
Time step width	10^{-4}	10^{-4}	10^{-4}	10^{-4}	10^{-4}	10^{-4}	10^{-4}	10^{-4}	10^{-4}
Initial conditions	Stagnant	Stagnant	M7-SB1	Stagnant	M7-SB1	M7-SB1	Stagnant	Stagnant	Stagnant

Table 15: An overview of bubble swarm simulations performed and used in this study. N_{Bubble}: Number of bubbles, Grid: a: 64 × 64 × 64, b: 80 × 80 × 80, c: 100 × 100 × 100, d: 120 × 120 × 120, e: 100 × 100 × 120. N_B: Mesh cells per bubble diameter. L_{wall}: Wall distance, d_b: Bubble diameter, ε_G: Gas content, M: Morton number, $E\ddot{o}_B$: Bubble Eötvös number, C: Coalescence, y: yes, n: no, n/a: Not available (The information about coalescence is not available since these cases are not further evaluated due to numerical artifacts and following unphysical behavior). *: Due to non-equidistant grid N_B is minimum 20.

														(A4)		(A2)	(A3)		(A1)				(B-M7)	(B-M8)					
Case No.	1	2	3	4	5	6	7	8	9	10	11	12	13	14	15	16	17	18	19	20	21	22	23	24	25	26	27	28	29
N_{Bubble}	4	4	4	4	4	6	6	8	8	8	8	8	8	6	6	5	5	6	5	5	5	5	6	6	6	6	6	6	6
Grid	b	c	a,b,c	c	d	c	d	a	b	c	c	b	d	e	e	e	e	e	e	e	e	e	d	d	d	d	d	d	d
N_B	20	20	16,20,25	20	20	20	20	16	20	20	25	10	20	20*	20*	20*	20*	20*	20*	20*	20*	20*	20	20	20	20	20	20	20
d_B / L_{wall}	1/4	1/5	1/4	1/5	1/6	1/5	1/6	1/4	1/4	1/5	1/4	1/8	1/6	1/5	1/5	1/5	1/5	1/5	1/5	1/5	1/5	1/5	1/5	1/5	1/5	1/5	1/5	1/5	1/5
d_B[mm]	1	1	1	1	1	1	1	1	2	1	1	0.5	1	2.0	0.5	2	3	2	1.6	5	4	3	1	1	1	1	1	2	0.5
ε_G [%]	3.2	1.6	3.2	1.6	1.0	2.5	1.4	6.5	6.5	3.3	6.5	0.8	1.9	2.5	2.5	2.1	2.1	2.5	2.1	2.1	2.1	2.1	2.5	2.5	2.5	2.5	2.5	2.5	2.5
log M	-7	-7	-8	-8	-8	-7	-8	-7	-7	-7	-8	-8	-8	-7	-10	-7	-7	-7	-7	-7	-7	-8	-7	-8	-9	-10	-7	-7	-7
$E\ddot{o}_B$	2.5	2.5	1.2	1.2	1.2	2.5	1.2	2.5	10	2.5	1.2	1.2	1.2	1.2	0.1	1.2	2.6	1.2	0.7	7.3	4.7	2.6	2.5	2.5	2.5	2.5	2.5	10	0.6
C	y	y	y	y	y	y	n/a	y	y	y	y	y	n/a	y	n/a	y	n	y	n	n/a	n/a	n/a	n	n	n/a	n/a	n/a	n/a	n/a

145

A.2. Coalescence process

$t_1 = 0.0592$ s $t_1 + t_x$ $t_1 + 2t_x$ $t_1 + 3t_x$

$t_1 + 4t_x$ $t_1 + 5t_x$ $t_1 + 6t_x$ $t_1 + 7t_x$
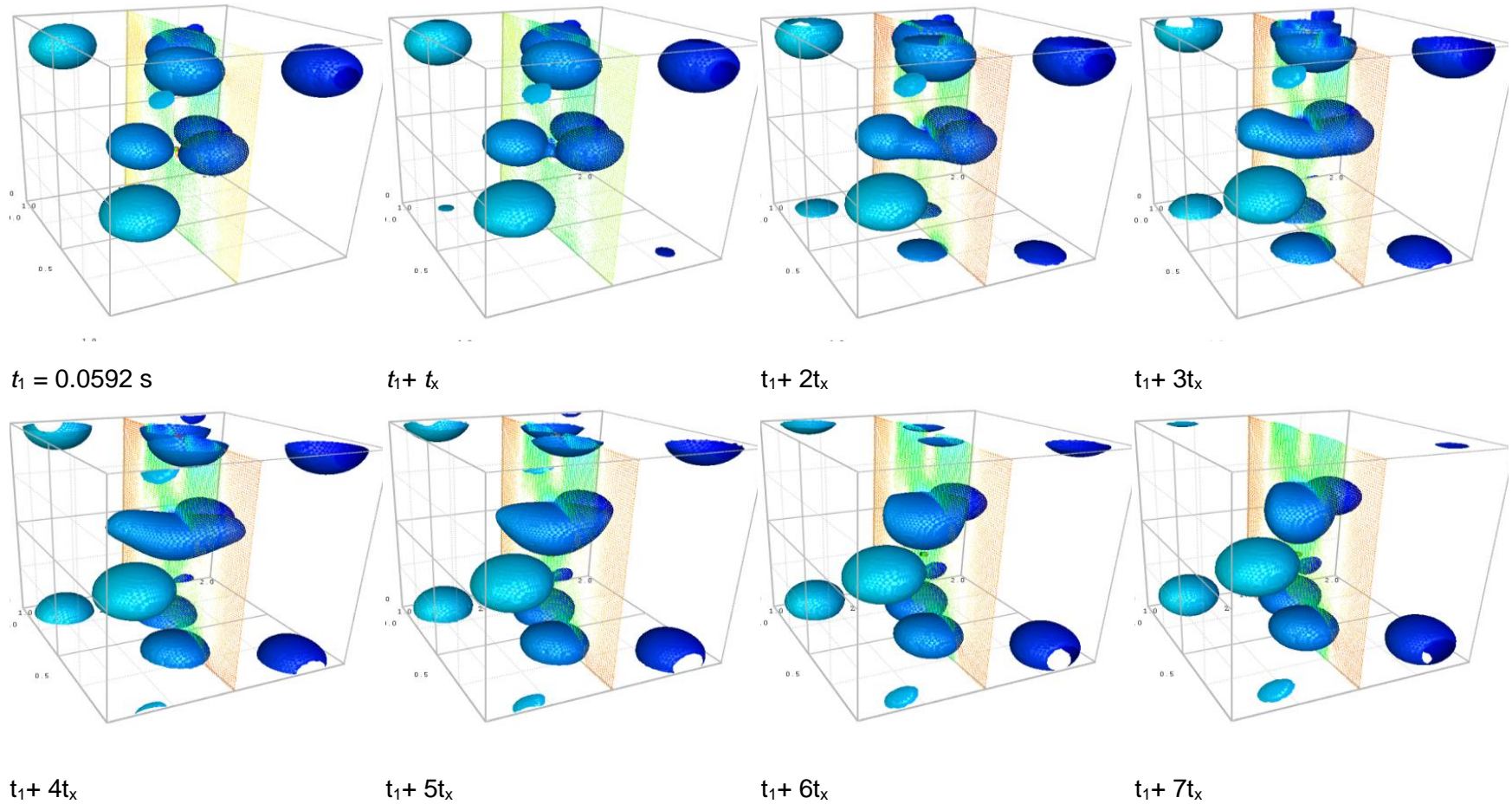
Fig. 53: Coalescence process of two bubbles at eight different instants in time. The first instant is at $t_1 = 0.0592$ s and each instant of time is $t_x = 0.8$ ms. ahead from the previous one. Case No.11 with 8 bubbles in domain is given in Table 15. The vertical vector field in flow direction is shown in coloured scale. This process is discusse in Section 3.5.1 and given as a close-up view in Fig. 25 over a shorter period.

Appendix B. E-E Simulations

B.1. Local gas holdups

Fig. 54 shows the contour plots of slices at different heights. For Case A at 2.23 and 3.30 m, the α_G values changes sharply near the wall, which are locally much higher or much lower than the center of the column. This is not a physical but a numerical problem and occurred for all cases at 1 bar. For Case B, the transition is smooth and local gas holdup values are lower near the wall.
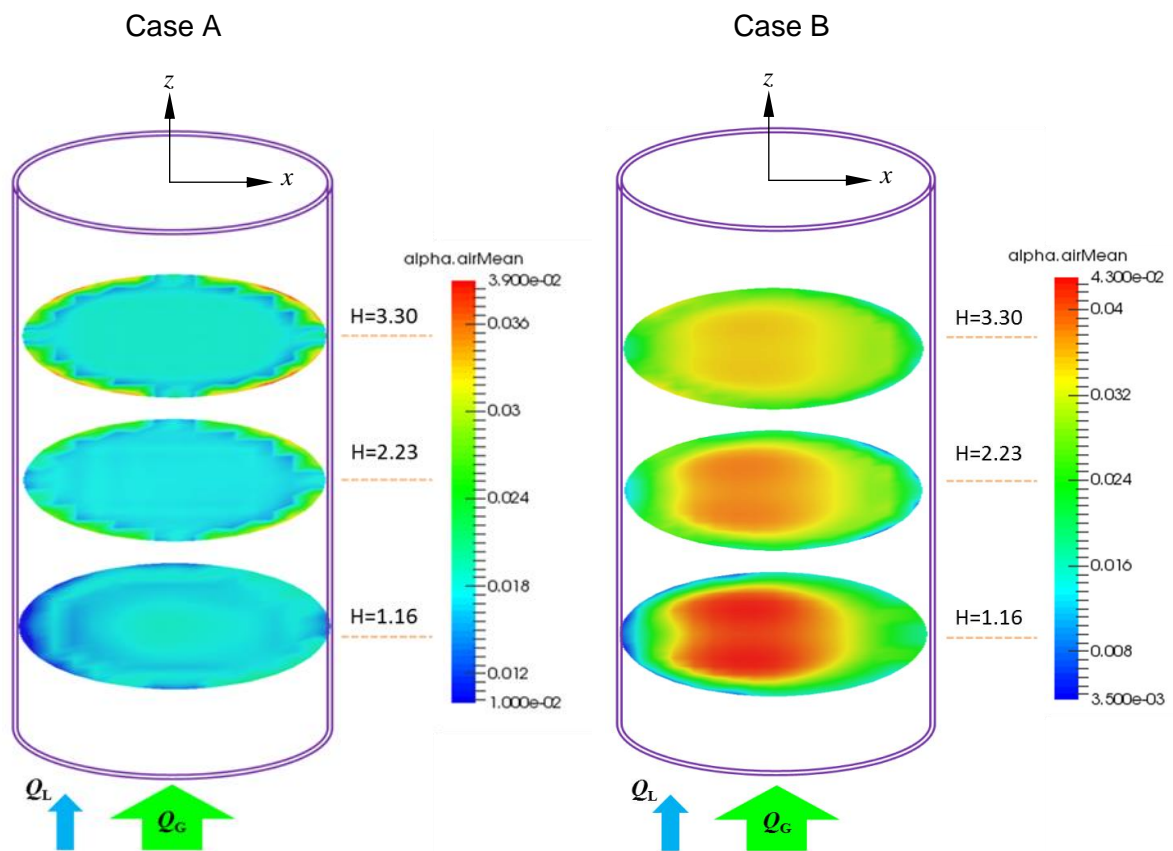
Fig. 54: Contour plots for α_G of slices at different heights in the column. H=1.16 m, 2.23 m, 3.30 m. T=23 °C, $U_{L,0}$=0.84 cm/s, $U_{L,0}$=0.54 cm/s. Left: Case A at 1 bar; Right: Case B 18.5 bar.

Influence of bubble diameter

The "Multi-Phase" Project is focused on mono disperse flow and thus the gas fed into liquid through the sparger is set to a constant diameter. For the E-E simulations a certain bubble diameter is required as input. During the operation of the bubble column different size of bubbles are in action. This approximate bubble diameter is obtained in the experiments via bubble size distribution based on the average bubble size in the

column [189]. In Fig. 55, the influence of initial d_B on the turbulence kinetic energy k, the velocity profiles u_L, u_G and the gas holdup is studied by comparing the cases with d_B =2.25 mm, 3 mm and 4 mm using the Lahey-model as the l_{kL}.

The velocity changes are not consistent with the gas holdup. Although the Case B3 and B4 take core peaking profiles with very low α_G near the wall, their velocity profiles are flattened due to the dominating BIT [202]. Thus, the k_m is higher for those cases with higher initial d_B, the mixing of eddies is distributed over the cross-section and TKE diffuses from a high α_G region to low α_G region. This is the reason of low radial difference on k_m profiles, which are non-zero even where there are nearly no bubbles. The relative velocity (u_G - u_L) is not constant but increases by increasing initial d_B (as discussed in Fig. 43).

The varied bubble diameter modifies the drag force and the drag coefficient C_D. The interfacial term l_{kL} is then modified depending on modified C_D. In Fig. 56 a), l_{kL} increases by increasing d_B higher in the core region and lower near the wall region, although the higher bubble diameter tends to decrease the drag force. However, since the relative velocity increases with increasing d_B, considering the cubic effect of the relative velocity in Eq.(75), the profiles from Fig. 56 a) are logical. The bigger bubbles with higher l_{kL} cause higher turbulence kinetic energy as it is seen in Fig. 55 c).
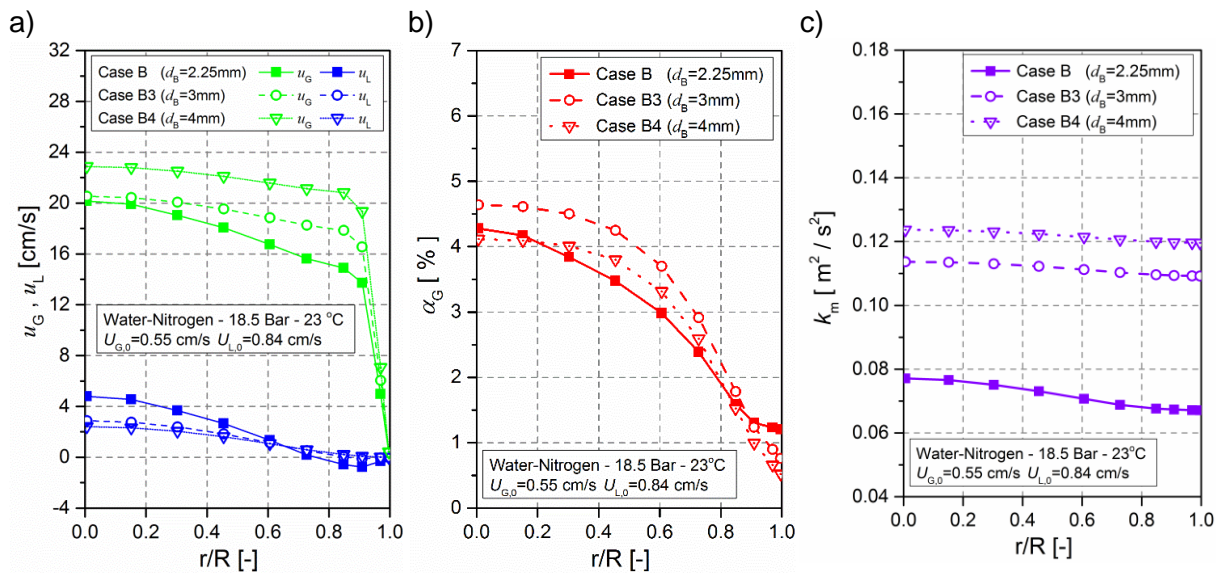
Fig. 55: Azimuthally averaged radial profiles of (a) u_L and u_G, (b) α_G and (c) k_m in the center of the bubble column for 18.5 bar at T=23 °C with different bubble diameter, i.e. d_B=2.25 mm (Case B), d_B=3 mm (Case B3) and d_B=4 mm (Case B4).
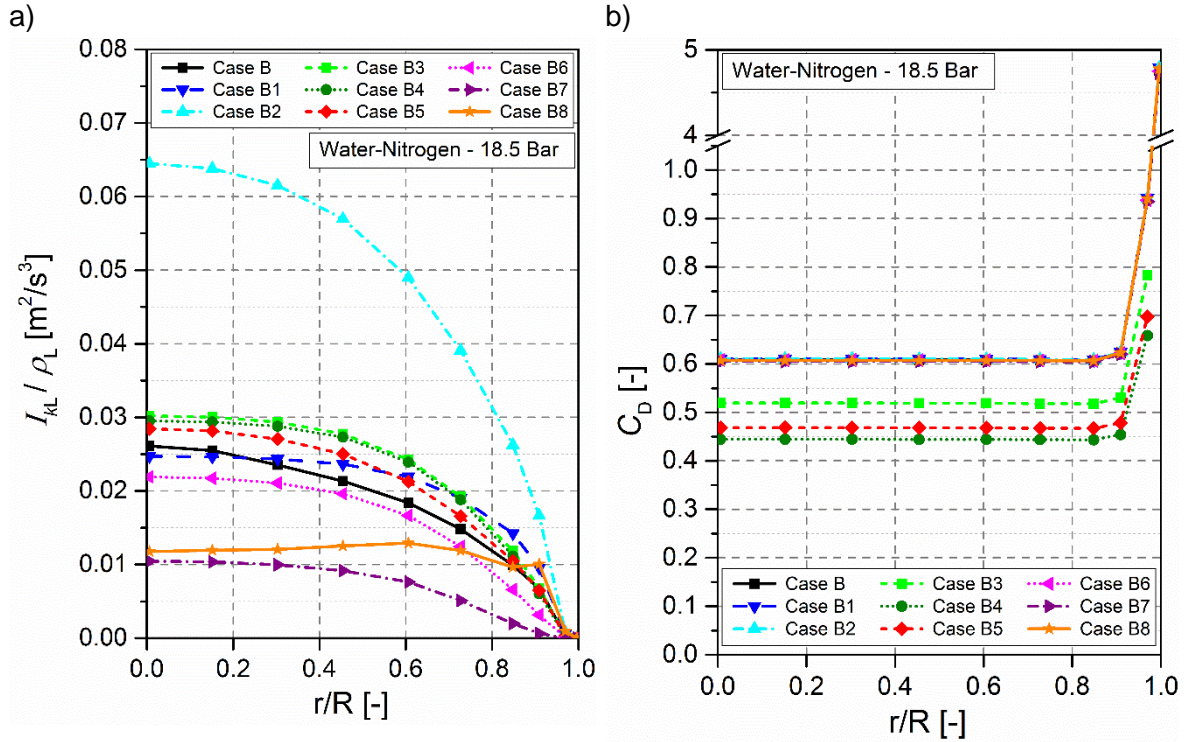
Fig. 56: Radial profiles of I_{kL} (a) and C_D (b) calculated from u_L, u_G, α_G and flow parameters according to Table 7 and Eq.(75) for Water-N_2 cases at 18.5 bar.

Influence of pressure

Euler-Euler simulations were performed for varied pressures of 1, 18.5 and 36 bar using the Lahey-model as the I_{kL}. Fig. 57 shows the radial distributions of local gas holdup (α_G), turbulence kinetic energy (k) and axial component of mean liquid and gas velocities (u_L, u_G) for different pressures (Case A, B and C). High pressure increases the gas density (ρ_G) significantly as well as the liquid density (ρ_L) but negligibly. Besides, the surface tension between the phases (σ) decreases at higher pressure. Smaller bubble diameter was considered in simulations for high pressures due to the experimental findings mentioned in Section 5.1.2. Initial bubble size is constant and d_B=4 mm for 1 bar and d_B=2.25 mm for 18.5 and 36 bar.

Rollbusch et. al. [197] carried out an extended review on the bubble columns operated under industrially relevant conditions and highlighted that d_B is smaller at elevated pressures [194-196]. According to Lin et al. [198], the increased pressure leads to an increase in gas holdup which is explained by a reduced stable bubble size and thus a retarding effect on bubble coalescence and lower bubble rise velocity [197]. This forms an explanation to the high volumetric gas fraction α_G at high pressures in Fig. 57. Especially for Case B and C with the same initial d_B the difference of α_G is up to 80-85%. This is related to the decreased bubble size in Case C due to a delay in

bubble break-up and coalescence [194]. Thus, the lowest gas velocity u_G occurs at the highest α_G for 36 bar whereas the highest gas velocity u_G occurs at the lowest α_G distribution for 1 bar. The change of axial gas velocity is not proportional to the change of α_G when pressure changes.

For Case B and Case C, the liquid velocity profiles in the core region are steeper where the α_G is also high. The corresponding steep profile for each case is because the core peaking profile of α_G causes acceleration of the liquid in the core region due to the momentum transfer between bubble and liquid [202]. The characteristic near-wall downward flow of a vertical bubble column can be observed in the wall region.
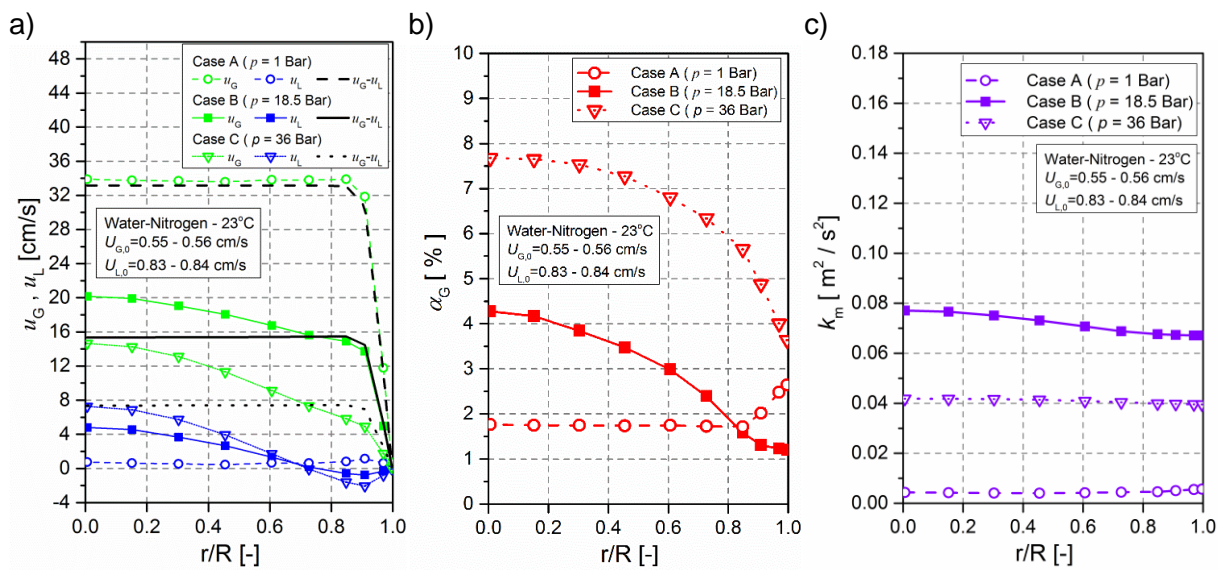
Fig. 57: Azimuthally averaged radial profiles of (a) u_L and u_G, (b) α_G and (c) k_m in the center of the bubble column at different pressures, i.e. 1 bar (Case A), 18.5 bar (Case B) and 36 bar (Case C).

Bibliography

1. Deckwer, W.-D., *Bubble column reactors*. 1992, Chichester; New York: Wiley.

2. Kantarci, N., F. Borak, and K.O. Ulgen, *Bubble column reactors*. Process Biochemistry, 2005. **40**: p. 2263-2283.

3. Besagni, G., F. Inzoli, and T. Ziegenhein, *Two-Phase Bubble Columns: A Comprehensive Review*. ChemEngineering, 2018. **2**. Artn. 13.

4. Joshi, J.B., *Computational flow modelling and design of bubble column reactors*. Chemical Engineering Science, 2001. **56**: p. 5893-5933.

5. Erdogan, S. and M. Wörner. *Analysis and modelling of liquid phase turbulence kinetic energy equation in bubbly flows via direct numerical simulation*. in *2nd Int. Symp. Multiscale Multiphase Process Engineering (MMPE-2)*. 2014. Hamburg, Germany: p. 430-435.

6. Wörner, M. and S. Erdogan, *Toward Improved Closure Relations for the Turbulent Kinetic Energy Equation in Bubble-Driven Flows*. Chemie Ingenieur Technik, 2013. **85**: p. 1131-1136.

7. Lance, M. and J. Bataille, *Turbulence in the Liquid-Phase of a Uniform Bubbly Air Water-Flow*. Journal of Fluid Mechanics, 1991. **222**: p. 95-118.

8. Hosokawa, S. and A. Tomiyama, *Turbulence modification in gas-liquid and solid-liquid dispersed two-phase pipe flows*. International Journal of Heat and Fluid Flow, 2004. **25**: p. 489-498.

9. Serizawa, A., I. Kataoka, and I. Michiyoshi, *Turbulence structure of air-water bubbly flow—II. local properties*. International Journal of Multiphase Flow, 1975. **2**: p. 235-246.

10. Drew, D.A. and S.L. Passman, *Theory of multicomponent fluids*. 1999, New York; London: Springer-Verlag.

11. Prosperetti, A. and G. Tryggvason, *Computational methods for multiphase flow*. 2007, Cambridge: Cambridge University Press.

12. Ishii, M. and T. Hibiki, *Thermo-fluid dynamics of two-phase flow*. 2006, New York; London: Springer.

13. Ma, T., *A contribution to turbulence modelling in bubbly flows*. 2017. Dissertation, Technische Universität Dresden, Dresden, Germany.

14. Zhang, D., N.G. Deen, and J.A.M. Kuipers, *Numerical simulation of the dynamic flow behavior in a bubble column: A study of closures for turbulence and interface forces*. Chemical Engineering Science, 2006. **61**: p. 7593-7608.

15. Dhotre, M.T., B. Niceno, and B.L. Smith, *Large eddy simulation of a bubble column using dynamic sub-grid scale model.* Chemical Engineering Journal, 2008. **136**: p. 337-348.

16. Tabib, M.V., S.A. Roy, and J.B. Joshi, *CFD simulation of bubble column - An analysis of interphase forces and turbulence models.* Chemical Engineering Journal, 2008. **139**: p. 589-614.

17. Silva, M.K., M.A. d'Avila, and M. Mori, *Study of the interfacial forces and turbulence models in a bubble column.* Computers & Chemical Engineering, 2012. **44**: p. 34-44.

18. Theofanous, T.G. and J. Sullivan, *Turbulence in two-phase dispersed flows.* Journal of Fluid Mechanics, 1982. **116**: p. 343-362.

19. Ilic, M., M. Wörner, and D.G. Cacuci, *Balance of liquid-phase turbulence kinetic energy equation for bubble-train flow.* Journal of Nuclear Science and Technology, 2004. **41**: p. 331-338.

20. Ilic, M., M. Wörner , and D.G. Cacuci. *Investigations of liquid phase turbulence based on direct numerical simulations of bubbly flows.* in *NURETH-11*. 2005. Avignon, France: Paper No. 22.

21. Kataoka, I. and A. Serizawa, *Basic Equations of Turbulence in Gas-Liquid 2-Phase Flow.* International Journal of Multiphase Flow, 1989. **15**: p. 843-855.

22. Troshko, A.A. and Y.A. Hassan, *A two-equation turbulence model of turbulent bubbly flows.* International Journal of Multiphase Flow, 2001. **27**: p. 1965-2000.

23. Debertodano, M.L., R.T. Lahey, and O.C. Jones, *Development of a K-Epsilon Model for Bubbly 2-Phase Flow.* Journal of Fluids Engineering-Transactions of the Asme, 1994. **116**: p. 128-134.

24. Lahey, R.T., *The simulation of multidimensional multiphase flows.* Nuclear Engineering and Design, 2005. **235**: p. 1043-1060.

25. Morel, C. *Turbulence modelling and first numerical simulations in turbulent two-phase flows.* in *Proc. 11th Symp. on Turbulent Shear Flows.* 1997. Grenoble, France. **3**: p. 10-15.

26. Ilic, M., *Statistical analysis of liquid phase turbulence based on direct numerical simulations of bubbly flows* 2006. Wissenschaftliche Berichte. FZKA 7199. Von der Fakultät für Maschinenbau der Universität Karlsruhe (TH) genehmigte Dissertation. Karlsruhe: Forschungszentrum Karlsruhe GmbH.

27. Wörner, M., B.E. Ghidersa, M. Ilic, and D.G. Cacuci, *Volume-of-fluid method based numerical simulations of gas-liquid two-phase flow in confined geometries.* La Houille Blanche - International Water Journal, 2005: p. 91-104.

28.   Santarelli, C. and J. Fröhlich, *Direct Numerical Simulations of spherical bubbles in vertical turbulent channel flow. Influence of bubble size and bidispersity.* International Journal of Multiphase Flow, 2016. **81**: p. 27-45.

29.   Santarelli, C., J. Roussel, and J. Fröhlich, *Budget analysis of the turbulent kinetic energy for bubbly flow in a vertical channel.* Chemical Engineering Science, 2016. **141**: p. 46-62.

30.   Ma, T., C. Santarelli, T. Ziegenhein, D. Lucas, and J. Fröhlich, *Direct numerical simulation–based Reynolds-averaged closure for bubble-induced turbulence.* Physical Review Fluids, 2017. **2**. Artn. 034301.

31.   Ma, T., D. Lucas, S. Jakirlić, and J. Fröhlich, *Progress in the second-moment closure for bubbly flow based on direct numerical simulation data.* Journal of Fluid Mechanics, 2019. **883**. Artn. A9.

32.   Mühlbauer, A., M.W. Hlawitschka, and H.-J. Bart, *Models for the Numerical Simulation of Bubble Columns: A Review.* Chemie Ingenieur Technik, 2019. **91**: p. 1747-1765.

33.   Becker, M., M. Tuinier, P. Rollbusch, M. Ludwig, R. Franke, M. Grünewald, and M. Schlüter, *BMBF-Projekt „Multi-Phase".* Chemie Ingenieur Technik, 2013. **85**: p. 989-991.

34.   Esmaeeli, A. and G. Tryggvason, *A direct numerical simulation study of the buoyant rise of bubbles at O(100) Reynolds number.* Physics of Fluids, 2005. **17**. Artn. 093303.

35.   Esmaeeli, A. and G. Tryggvason, *Direct numerical simulations of bubbly flows Part 2. Moderate Reynolds number arrays.* Journal of Fluid Mechanics, 1999. **385**: p. 325-358.

36.   Esmaeeli, A. and G. Tryggvason, *Direct numerical simulations of bubbly flows. Part 1. Low Reynolds number arrays.* Journal of Fluid Mechanics, 1998. **377**: p. 313-345.

37.   Bunner, B. and G. Tryggvason, *Dynamics of homogeneous bubbly flows Part 1. Rise velocity and microstructure of the bubbles.* Journal of Fluid Mechanics, 2002. **466**: p. 17-52.

38.   Bunner, B. and G. Tryggvason, *Dynamics of homogeneous bubbly flows Part 2. Velocity fluctuations.* Journal of Fluid Mechanics, 2002. **466**: p. 53-84.

39.   Bunner, B. and G. Tryggvason, *Effect of bubble deformation on the properties of bubbly flows.* Journal of Fluid Mechanics, 2003. **495**: p. 77-118.

40.   Sabisch, W., *Dreidimensionale numerische Simulation der Dynamik von aufsteigenden Einzelblasen und Blasenschwärmen mit einer Volume-of-Fluid-Methode.* 2000. Wissenschaftliche Berichte. FZKA 6478. Karlsruhe: Forschungszentrum Karlsruhe GmbH.

41. Sabisch, W., M. Wörner, G. Grötzbach, and D.G. Cacuci. *3D volume-of-fluid simulation of a wobbling bubble in a gas-liquid system of low Morton number*. in *Proc. of the 4th Internat. Conf. on Multiphase Flow - ICMF*. 2001. New Orleans, Louisiana, USA: Paper No. 244.

42. Wörner, M., W. Sabisch, G. Grötzbach, and D.G. Cacuci. *Volume-averaged conservation equations for volume-of-fluid interface tracking*. in *Proc. of the 4th Internat. Conf. on Multiphase Flow - ICMF*. 2001. New Orleans, Louisiana, USA: Paper No. 245.

43. Öztaskin, M.C., M. Wörner, and H.S. Soyhan, *Numerical investigation of the stability of bubble train flow in a square minichannel.* Physics of Fluids, 2009. **21**. Artn. 042108.

44. Özkan, F., M. Wörner, A. Wenka, and H.S. Soyhan, *Critical evaluation of CFD codes for interfacial simulation of bubble-train flow in a narrow channel.* International Journal for Numerical Methods in Fluids, 2007. **55**: p. 537-564.

45. Erdogan, S., M. Wörner, and H.S. Soyhan, *Modeling the diffusion-free liquid phase residence time distribution of Taylor flow by the unit cell concept: Progress and limitations.* Chemical Engineering Journal, 2012. **200**: p. 380-390.

46. Ghidersa, B.E., M. Wörner, and D.G. Cacuci, *Exploring the flow of immiscible fluids in a square vertical mini-channel by direct numerical simulation.* Chemical Engineering Journal, 2004. **101**: p. 285-294.

47. Wörner, M., *Numerical modeling of multiphase flows in microfluidics and micro process engineering: a review of methods and applications.* Microfluidics and Nanofluidics, 2012. **12**: p. 841-886.

48. Ekambara, K., M.T. Dhotre, and J.B. Joshi, *CFD simulations of bubble column reactors: 1D, 2D and 3D approach.* Chemical Engineering Science, 2005. **60**: p. 6733-6746.

49. Sokolichin, A., G. Eigenberger, and A. Lapin, *Simulation of buoyancy driven bubbly flow: Established simplifications and open questions.* AIChE Journal, 2004. **50**: p. 24-45.

50. Jakobsen, H.A., H. Lindborg, and C.A. Dorao, *Modeling of bubble column reactors: Progress and limitations.* Industrial & Engineering Chemistry Research, 2005. **44**: p. 5107-5151.

51. Sokolichin, A., G. Eigenberger, A. Lapin, and A. Lubbert, *Dynamic numerical simulation of gas-liquid two-phase flows - Euler/Euler versus Euler/Lagrange.* Chemical Engineering Science, 1997. **52**: p. 611-626.

52. van Wachem, B.G.M. and A.E. Almstedt, *Methods for multiphase computational fluid dynamics.* Chemical Engineering Journal, 2003. **96**: p. 81-98.

53. Buwa, V.V., D.S. Deo, and V.V. Ranade, *Eulerian-Lagrangian simulations of unsteady gas-liquid flows in bubble columns.* International Journal of Multiphase Flow, 2006. **32**: p. 864-885.

54. Lain, S., D. Bröder, M. Sommerfeld, and M.F. Göz, *Modelling hydrodynamics and turbulence in a bubble column using the Euler-Lagrange procedure.* International Journal of Multiphase Flow, 2002. **28**: p. 1381-1407.

55. Crowe, C.T., M. Sommerfeld, and Y. Tsuji, *Multiphase flows with droplets and particles.* 1998, Boca Raton, Fla.; London: CRC Press.

56. Marschall, H., R. Mornhinweg, A. Kossmann, S. Oberhauser, K. Langbein, and O. Hinrichsen, *Numerical Simulation of Dispersed Gas/Liquid Flows in Bubble Columns at High Phase Fractions using OpenFOAM (R) Part I - Modeling Basics.* Chemical Engineering & Technology, 2011. **34**: p. 1311-1320.

57. Ishii, M., *Two-fluid model for two-phase flow.* Multiphase Science and Technology, 1990. **5**: p. 1-63.

58. Chen, P., *Modeling the Fluid Dynamics of Bubble Column Flows.* 2004. PhD Thesis, The Sever Institute of Washington University, Saint Louis, Missouri, USA.

59. Chen, P., J. Sanyal, and M.P. Dudukovic, *CFD modeling of bubble columns flows: implementation of population balance.* Chemical Engineering Science, 2004. **59**: p. 5201-5207.

60. Ekambara, K., K. Nandakumar, and J.B. Joshi, *CFD Simulation of Bubble Column Reactor Using Population Balance.* Industrial & Engineering Chemistry Research, 2008. **47**: p. 8505-8516.

61. Liao, Y.X., D. Lucas, E. Krepper, and M. Schmidtke, *Development of a generalized coalescence and breakup closure for the inhomogeneous MUSIG model.* Nuclear Engineering and Design, 2011. **241**: p. 1024-1033.

62. Laborde-Boutet, C., F. Larachi, N. Dromard, O. Delsart, and D. Schweich, *CFD simulation of bubble column flows: Investigations on turbulence models in RANS approach.* Chemical Engineering Science, 2009. **64**: p. 4399-4413.

63. Vaidheeswaran, A. and T. Hibiki, *Bubble-induced turbulence modeling for vertical bubbly flows.* International Journal of Heat and Mass Transfer, 2017. **115**: p. 741-752.

64. Khan, Z., V.H. Bhusare, and J.B. Joshi, *Comparison of turbulence models for bubble column reactors.* Chemical Engineering Science, 2017. **164**: p. 34-52.

65. van Wijngaarden, L., *On Pseudo Turbulence.* Theoretical and Computational Fluid Dynamics, 1998. **10**: p. 449-458.

66.   Riboux, G., F. Risso, and D. Legendre, *Experimental characterization of the agitation generated by bubbles rising at high Reynolds number.* Journal of Fluid Mechanics, 2010. **643**: p. 509-539.

67.   Martinez-Mercado, J., C.A. Palacios-Morales, and R. Zenit, *Measurement of pseudoturbulence intensity in monodispersed bubbly liquids for 10 < Re < 500.* Physics of Fluids, 2007. **19**. Artn. 103302.

68.   Risso, F. and K. Ellingsen, *Velocity fluctuations in a homogeneous dilute dispersion of high-Reynolds-number rising bubbles.* Journal of Fluid Mechanics, 2002. **453**: p. 395-410.

69.   Mercado, J.M., D.C. Gomez, D. Van Gils, C. Sun, and D. Lohse, *On bubble clustering and energy spectra in pseudo-turbulence.* Journal of Fluid Mechanics, 2010. **650**: p. 287-306.

70.   Risso, F., V. Roig, Z. Amoura, G. Riboux, and A.M. Billet, *Wake attenuation in large Reynolds number dispersed two-phase flows.* Philosophical Transactions of the Royal Society a-Mathematical Physical and Engineering Sciences, 2008. **366**: p. 2177-2190.

71.   Roghair, I., J.M. Mercado, M.V. Annaland, H. Kuipers, C. Sun, and D. Lohse, *Energy spectra and bubble velocity distributions in pseudo-turbulence: Numerical simulations vs. experiments.* International Journal of Multiphase Flow, 2011. **37**: p. 1093-1098.

72.   Mazzitelli, I.M. and D. Lohse, *Evolution of energy in flow driven by rising bubbles.* Physical Review E, 2009. **79**. Artn. 066317.

73.   Ilic, M., M. Wörner , and D.G. Cacuci. *Evaluation of energy spectra in bubble driven liquid flows from direct numerical simulations*. in *6th International Conference on Multiphase Flow*. 2007. Leipzig, Germany: PS1-11.

74.   Figueroa- Espinoza, B. and R. Zenit, *Clustering in high Re monodispersed bubbly flows.* Physics of Fluids, 2005. **17**. Artn. 091701.

75.   Clift, R., J.R. Grace, and M.E. Weber, *Bubbles, drops, and particles*. 1978, New York: Academic Press.

76.   Haberman, W.L. and R.K. Morton, *An experimental investigation of the drag and shape of air bubbles rising in various liquids / by W. L. Haberman and R. K. Morton*. 1953, Washington, D.C.: Navy Department, The David W. Taylor Model Basin.

77.   Brauer, H., *Grundlagen der Einphasen- und Mehrphasenströmungen*. 1971, Aarau: Verlag Sauerländer.

78.   Kulkarni, A.A. and J.B. Joshi, *Bubble formation and bubble rise velocity in gas-liquid systems: A review.* Industrial & Engineering Chemistry Research, 2005. **44**: p. 5873-5931.

79. Tomiyama, A., G.P. Celata, S. Hosokawa, and S. Yoshida, *Terminal velocity of single bubbles in surface tension force dominant regime.* International Journal of Multiphase Flow, 2002. **28**: p. 1497-1519.

80. Magnaudet, J. and I. Eames, *The motion of high-Reynolds-mumber bubbles in inhomogeneous flows.* Annual Review of Fluid Mechanics, 2000. **32**: p. 659-708.

81. Batchelor, G.K., *An introduction to fluid dynamics.* 1967, Cambridge, UK: Cambridge University Press.

82. Davies, R.M. and G. Taylor, *The Mechanics of Large Bubbles Rising through Extended Liquids and through Liquids in Tubes.* Proceedings of the Royal Society of London Series a-Mathematical and Physical Sciences, 1950. **200**: p. 375-390.

83. Peebles, F.N. and H.J. Garber, *Studies on the Motion of Gas Bubbles in Liquids.* Chemical Engineering Progress, 1953. **49**: p. 88-97.

84. Mendelson, H.D., *Prediction of Bubble Terminal Velocities from Wave Theory.* AIChE Journal, 1967. **13**: p. 250-253.

85. Haas, U., H. Schmidt-Traub, and H. Brauer, *Flow Round Spherical Bubbles with Internal Circulation.* Chemie Ingenieur Technik, 1972. **44**: p. 1060-1068.

86. Levich, V.G., *Physicochemical hydrodynamics.* 1962, Englewood Cliffs, N.J., USA: Prentice-Hall.

87. Moore, D.W., *Velocity of Rise of Distorted Gas Bubbles in a Liquid of Small Viscosity.* Journal of Fluid Mechanics, 1965. **23**: p. 749-766.

88. Moore, D.W., *The Rise of a Gas Bubble in a Viscous Liquid.* Journal of Fluid Mechanics, 1959. **6**: p. 113-130.

89. Moore, D.W., *The Boundary Layer on a Spherical Gas Bubble.* Journal of Fluid Mechanics, 1963. **16**: p. 161-176.

90. Rodrigue, D., *Drag coefficient-Reynolds number transition for gas bubbles rising steadily in viscous fluids.* Canadian Journal of Chemical Engineering, 2001. **79**: p. 119-123.

91. Maxworthy, T., C. Gnann, M. Kurten, and F. Durst, *Experiments on the rise of air bubbles in clean viscous liquids.* Journal of Fluid Mechanics, 1996. **321**: p. 421-441.

92. Raymond, F. and J.M. Rosant, *A numerical and experimental study of the terminal velocity and shape of bubbles in viscous liquids.* Chemical Engineering Science, 2000. **55**: p. 943-955.

93. Smolianski, A., H. Haario, and P. Luukka, *Numerical study of dynamics of single bubbles and bubble swarms.* Applied Mathematical Modelling, 2008. **32**: p. 641-659.

94.   Abou-El-Hassan, M.E., *Correlations for Bubble Rise in Gas-Liquid Systems*. Encyclopedia of Fluid Mechanics. Vol. 3. 1986, Houston: Gulf Publishing.

95.   Rodrigue, D., *Generalized correlation for bubble motion.* AIChE Journal, 2001. **47**: p. 39-44.

96.   Rodrigue, D., *A general correlation for the rise velocity of single gas bubbles.* Canadian Journal of Chemical Engineering, 2004. **82**: p. 382-386.

97.   Grace, J.R., T. Wairegi, and T.H. Nguyen, *Shapes and Velocities of Single Drops and Bubbles Moving Freely through Immiscible Liquids.* Transactions of the Institution of Chemical Engineers, 1976. **54**: p. 167-173.

98.   Maneri, C.C., *New Look at Wave Analogy for Prediction of Bubble Terminal Velocities.* AIChE Journal, 1995. **41**: p. 481-487.

99.   Jamialahmadi, M., C. Branch, and H. Müller-Steinhagen, *Terminal Bubble Rise Velocity in Liquids.* Chemical Engineering Research & Design, 1994. **72**: p. 119-122.

100.   Bothe, M. and M. Schlüter, *Modeling Parameters for Bubbly Flows.* Chemie Ingenieur Technik, 2013. **85**: p. 1023-1035.

101.   Schiller, L., Naumann, A., *A Drag Coefficient Correlation.* Z. Ver. Dtsch. Ing., 1933. **77**: p. 318.

102.   Tomiyama, A., I. Kataoka, I. Zun, and T. Sakaguchi, *Drag coefficients of single bubbles under normal and micro gravity conditions.* Jsme International Journal Series B-Fluids and Thermal Engineering, 1998. **41**: p. 472-479.

103.   Ishii, M. and N. Zuber, *Drag Coefficient and Relative Velocity in Bubbly, Droplet or Particulate Flows.* AIChE Journal, 1979. **25**: p. 843-855.

104.   Frumkin, A. and V. Levich, *O Vliyanii Poverkhnostno-Aktivnykh Veshchestv Na Dvizhenie Na Granitse Zhidkikh Sred (On the effect of surfactants on movement at the boundary of liquid media).* Zhurnal Fizicheskoi Khimii (Russian Journal of Physical Chemistry), 1947. **21**: p. 1183-1204.

105.   Green-Start-LLC, *Improving Plant Aeration Using Gas Infusion Technology*. [last access 2020 05 March]. Available from: https://www.mi-wea.org/docs/Brown%20-%20Hoogerwerf%20-%20WWAdCon%20Presentation.pdf.

106.   Räbiger, N. and M. Schlüter, *VDI Heat Atlas*. 2nd ed. VDI-Buch. 2010, Berlin, Heidelberg: Springer-Verlag.

107.   Mersmann, A., *Design and Scale-up of Bubble and Drop Columns.* Chemie Ingenieur Technik, 1977. **49**: p. 679-691.

108. Aybers, N.M. and A. Tapucu, *Studies on the drag and shape of gas bubbles rising through a stagnant liquid.* Wärme - und Stoffübertragung, 1969. **2**: p. 171-177.

109. Lunde, K. and R.J. Perkins, *Shape oscillations of rising bubbles.* Applied Scientific Research, 1998. **58**: p. 387-408.

110. Zhang, Y.Q. and J.A. Finch, *A note on single bubble motion in surfactant solutions.* Journal of Fluid Mechanics, 2001. **429**: p. 63-66.

111. Uno, S. and R.C. Kintner, *Effect of Wall Proximity on the Rate of Rise of Single Air Bubbles in a Quiescent Liquid.* AIChE Journal, 1956. **2**: p. 420-425.

112. Collins, R., *Effect of a Containing Cylindrical Boundary on Velocity of a Large Gas Bubble in a Liquid.* Journal of Fluid Mechanics, 1967. **28**: p. 97-112.

113. Versteeg, H.K. and W. Malalasekera, *An introduction to computational fluid dynamics : the finite volume method*. 2nd ed. 2007, Harlow: Prentice Hall.

114. Sato, Y., M. Sadatomi, and K. Sekoguchi, *Momentum and Heat-Transfer in 2-Phase Bubble Flow .1. Theory.* International Journal of Multiphase Flow, 1981. **7**: p. 167-177.

115. Sato, Y. and K. Sekoguchi, *Liquid Velocity Distribution in Two-Phase Bubble Flow.* International Journal of Multiphase Flow, 1975. **2**: p. 79-95.

116. Kataoka, I., *Local Instant Formulation of 2-Phase Flow.* International Journal of Multiphase Flow, 1986. **12**: p. 745-758.

117. Sokolichin, A. and G. Eigenberger, *Applicability of the standard k-epsilon turbulence model to the dynamic simulation of bubble columns: Part I. Detailed numerical simulations.* Chemical Engineering Science, 1999. **54**: p. 2273-2284.

118. Bothe, D., H. Shirzadi, and H.J. Warnecke, *Evaluations of Euler-Euler simulations of bubble columns based on numerical tracer experiments.* Chemical Engineering Research & Design, 2007. **85**: p. 1491-1496.

119. Gimbun, J., *Assessment of the turbuelnce models for modelling of bubble column.* Journal of the Institution of Engineers, Malaysia, 2009. **70**: p. 57-64.

120. Ekambara, K. and M.T. Dhotre, *CFD simulation of bubble column.* Nuclear Engineering and Design, 2010. **240**: p. 963-969.

121. Launder, B.E. and D.B. Spalding, *The numerical computation of turbulent flows.* Computer Methods in Applied Mechanics and Engineering, 1974. **3**: p. 269-289.

122. Davidson, L., *An Introduction to Turbulence Models.* 1997. Report 97/2. Göteborg, Sweden: Chalmers University of Technology Department of Thermo and Fluid Dynamics.

123. Hosokawa, S., T. Suzuki, and A. Tomiyama, *Turbulence kinetic energy budget in bubbly flows in a vertical duct.* Experiments in Fluids, 2012. **52**: p. 719-728.

124. Lu, J.C. and G. Tryggvason, *Effect of bubble deformability in turbulent bubbly upflow in a vertical channel.* Physics of Fluids, 2008. **20**. Artn. 040701.

125. Lu, J.C. and G. Tryggvason, *Numerical study of turbulent bubbly downflows in a vertical channel.* Physics of Fluids, 2006. **18**. Artn. 103302.

126. Liao, Y.X. and D. Lucas, *A literature review on mechanisms and models for the coalescence process of fluid particles.* Chemical Engineering Science, 2010. **65**: p. 2851-2864.

127. Liao, Y.X. and D. Lucas, *A literature review of theoretical models for drop and bubble breakup in turbulent dispersions.* Chemical Engineering Science, 2009. **64**: p. 3389-3406.

128. Rzehak, R. and E. Krepper, *Bubble-induced turbulence: Comparison of CFD models.* Nuclear Engineering and Design, 2013. **258**: p. 57-65.

129. Kendil, F.Z., E. Krepper, A.B. Salah, D. Lucas, and A. Mataoui, *Numerical study of a bubble plume generated by bubble entrainment from an impinging jet.* Nuclear Engineering and Design, 2011. **241**: p. 4111-4121.

130. Boussinesq, J., *Théorie de l'écoulement tourbillonnant et tumultueux des liquides dans les lits rectilignes à grande section, par M. J. Boussinesq,... (-Second mémoire : Étude des régimes graduellement variés.).* 1897, Paris: Gauthier-Villars et fils.

131. Behzadi, A., R.I. Issa, and H. Rusche, *Modelling of dispersed bubble and droplet flow at high phase fractions.* Chemical Engineering Science, 2004. **59**: p. 759-770.

132. Jones, W.P. and B.E. Launder, *Prediction of Laminarization with a 2-Equation Model of Turbulence.* International Journal of Heat and Mass Transfer, 1972. **15**: p. 301-314.

133. Lee, S.L., R.T. Lahey, and O.C. Jones, *The Prediction of Two-Phase Turbulence and Phase Distribution Phenomena Using a k-ε Model.* Japanese Journal of Multiphase Flow, 1989. **3**: p. 335-368.

134. Gosman, A.D., C. Lekakou, S. Politis, R.I. Issa, and M.K. Looney, *Multidimensional Modeling of Turbulent 2-Phase Flows in Stirred Vessels.* AIChE Journal, 1992. **38**: p. 1946-1956.

135. Rusche, H., *Computational fluid dynamics of dispersed two-phase flows at high phase fractions.* 2002. PhD Thesis, Imperial College of Science, Technology and Medicine, London, UK.

136. Olmos, E., C. Gentric, and N. Midoux, *Numerical description of flow regime transitions in bubble column reactors by a multiple gas phase model.* Chemical Engineering Science, 2003. **58**: p. 2113-2121.

137. Pfleger, D. and S. Becker, *Modelling and simulation of the dynamic flow behaviour in a bubble column.* Chemical Engineering Science, 2001. **56**: p. 1737-1747.

138. Hirt, C.W. and B.D. Nichols, *Volume of fluid (VOF) method for the dynamics of free boundaries.* Journal of Computational Physics, 1981. **39**: p. 201-225.

139. Rider, W.J. and D.B. Kothe, *Reconstructing volume tracking.* Journal of Computational Physics, 1998. **141**: p. 112-152.

140. Rudman, M., *Volume-tracking methods for interfacial flow calculations.* International Journal for Numerical Methods in Fluids, 1997. **24**: p. 671-691.

141. Pilliod, J.E. and E.G. Puckett, *Second-order accurate volume-of-fluid algorithms for tracking material interfaces.* Journal of Computational Physics, 2004. **199**: p. 465-502.

142. Marschall, H., S. Boden, C. Lehrenfeld, C.J. Falconi D., U. Hampel, A. Reusken, M. Wörner, and D. Bothe, *Validation of Interface Capturing and Tracking techniques with different surface tension treatments against a Taylor bubble benchmark problem.* Computers & Fluids, 2014. **102**: p. 336-352.

143. Sabisch, W., M. Wörner, G. Grötzbach, and D.G. Cacuci, *Dreidimensionale numerische Simulation von aufsteigenden Einzelblasen und Blasenschwärmen mit einer Volume-of-Fluid Methode.* Chemie Ingenieur Technik, 2001. **73**: p. 368-373.

144. Wörner, M., B. Ghidersa, and A. Onea, *A model for the residence time distribution of bubble-train flow in a square mini-channel based on direct numerical simulation results.* International Journal of Heat and Fluid Flow, 2007. **28**: p. 83-94.

145. Wörner , M., B. Ghidersa, and A. Shahab. *Numerical study of bubble train flow in a square vertical mini-channel: influence of the length of the flow unit cell.* in *5th Int. Conf. Multiphase Flow, ICMF'04.* 2004. Yokohama, Japan: Paper No. 154.

146. Kececi, S., M. Wörner, A. Onea, and H.S. Soyhan, *Recirculation time and liquid slug mass transfer in co-current upward and downward Taylor flow.* Catalysis Today, 2009. **147**: p. 125-131.

147. Keskin, O., M. Wörner, H.S. Soyhan, T. Bauer, O. Deutschmann, and R. Lange, *Viscous Co-Current Downward Taylor Flow in a Square Mini-Channel.* AIChE Journal, 2010. **56**: p. 1693-1702.

148. Erdogan, S. and M. Wörner, *Numerical Investigation and Analytical Modeling of Liquid Phase Residence Time Distribution for Bubble Train Flow in a Square Mini-Channel.* 2009. Wissenschaftliche Berichte. FZKA 7490. Karlsruhe: Forschungszentrum Karlsruhe GmbH.

149. Onea, A., M. Wörner, and D.G. Cacuci, *A qualitative computational study of mass transfer in upward bubble train flow through square and rectangular mini-channels.* Chemical Engineering Science, 2009. **64**: p. 1416-1435.

150. Wörner, M., *Computational Study on Scaling of Co-Current Downward Taylor Flow in Small Square Channels of Three Different Sizes.* Journal of Chemical Engineering of Japan, 2013. **46**: p. 335-341.

151. Ishii, M., *Thermo-fluid dynamic theory of two-phase flow*. 1975, Paris: Eyrolles.

152. Weller, H.G., *Derivation, Modelling and Solution of the Conditionally Averaged Two-Phase Flow Equations.* 2005. Tech. Rep. TR/HGW/02. OpenCFD Ltd.

153. Marschall, H., *Towards the Numerical Simulation of Multi-Scale Two-Phase Flows.* 2011. Dissertation, Technische Universität München, Munich, Germany.

154. Hill, D.P., *The Computer Simulation of Dispersed Two-Phase Flows.* 1998. PhD Thesis, University of London, London, UK.

155. Tomiyama, A., *Struggle with computational bubble dynamics.* Multiphase Science and Technology, 1998. **10**: p. 369-405.

156. Legendre, D. and J. Magnaudet, *The lift force on a spherical bubble in a viscous linear shear flow.* Journal of Fluid Mechanics, 1998. **368**: p. 81-126.

157. Marschall, H., R. Mornhinweg, A. Kossmann, S. Oberhauser, K. Langbein, and O. Hinrichsen, *Numerical Simulation of Dispersed Gas/Liquid Flows in Bubble Columns at High Phase Fractions using OpenFOAM (R) Part II - Numerical Simulations and Results.* Chemical Engineering & Technology, 2011. **34**: p. 1321-1327.

158. Antal, S.P., R.T. Lahey, and J.E. Flaherty, *Analysis of Phase Distribution in Fully-Developed Laminar Bubbly 2-Phase Flow.* International Journal of Multiphase Flow, 1991. **17**: p. 635-652.

159. Hosokawa, S. and A. Tomiyama, *Multi-fluid simulation of turbulent bubbly pipe flows.* Chemical Engineering Science, 2009. **64**: p. 5308-5318.

160. Weller, H.G., G. Tabor, H. Jasak, and C. Fureby, *A tensorial approach to computational continuum mechanics using object-oriented techniques.* Computers in Physics, 1998. **12**: p. 620-631.

161. Greenshields, C.J., *OpenFOAM User Guide*. 3.0.1 ed. 2015, England: CFD Direct Ltd., OpenFOAM Foundation Ltd.

162. Greenshields, C.J., *OpenFOAM Programmer's Guide*. 3.0.1 ed. 2015, England: CFD Direct Ltd., OpenFOAM Foundation Ltd.

163. *OpenFOAM User Guide - Version 8*. [last access 2020 07 March]; CFD Direct Ltd. Available from: https://cfd.direct/openfoam/user-guide/.

164. Cai, X., *Interface-Resolving Simulations of Gas-Liquid Two-Phase Flows in Solid Structures of Different Wettability.* 2016. Dissertation, Karlsruhe Institute of Technology (KIT), Karlsruhe, Germany.

165. Patankar, S.V. and D.B. Spalding, *A calculation procedure for heat, mass and momentum transfer in three-dimensional parabolic flows.* International Journal of Heat and Mass Transfer, 1972. **15**: p. 1787-1806.

166. Jasak, H., *Error Analysis and Estimation for the Finite Volume Method with Applications to Fluid Flows.* 1996. PhD Thesis, Imperial College of Science, Technology and Medicine, London, UK.

167. *OpenFOAM User Guide - A.1 Standard solvers*. [last access 2020 07 March]; OpenCFD Ltd. Available from: https://www.openfoam.com/documentation/user-guide/standard-solvers.php.

168. Ubbink, O., *Numerical prediction of two fluid systems with sharp interfaces.* 1997. PhD Thesis, Imperial College of Science, Technology and Medicine, London, UK.

169. Magolan, B., N. Lubchenko, and E. Baglietto, *A quantitative and generalized assessment of bubble-induced turbulence models for gas-liquid systems.* Chemical Engineering Science: X, 2019. **2**: p. 100009.

170. Bhusare, V.H., M.K. Dhiman, D.V. Kalaga, S. Roy, and J.B. Joshi, *CFD simulations of a bubble column with and without internals by using OpenFOAM.* Chemical Engineering Journal, 2017. **317**: p. 157-174.

171. Rzehak, R. and S. Kriebitzsch, *Multiphase CFD-simulation of bubbly pipe flow: A code comparison.* International Journal of Multiphase Flow, 2015. **68**: p. 135-152.

172. Otromke, M., *Implementation and Comparison of Correlations for interfacial Forces in a Gas-Liquid System within an Euler-Euler Framework.* 2013. Master Thesis, Fakultät für Verfahrens- und Chemietechnik, Hochschule Mannheim, Mannheim, Germany.

173. Hosokawa, S. and A. Tomiyama. *Effects of Bubbles on Turbulent Flows in Vertical Channels*. in *7th International Conference on Multiphase Flow*. 2010. Tampa, FL USA: Keynote - No. 9.

174. Chai, X. and X. Cheng, *Wake acceleration effect on spherical bubbles aligned in-line.* Progress in Nuclear Energy, 2015. **80**: p. 74-79.

175. Chai, X., X. Liu, J. Xiong, and X. Cheng, *Numerical investigation of bubble wake properties in the moving liquid with LES model.* Journal of Nuclear Science and Technology, 2016. **53**: p. 1870-1880.

176. Liu, Z.L., Y. Zheng, L. Jia, and Q.K. Zhang, *Study of bubble induced flow structure using PIV.* Chemical Engineering Science, 2005. **60**: p. 3537-3552.

177. Chai, X., *Numerical study of the wake acceleration effect using CFD approach.* 2014. Dissertation, Karlsruhe Institute of Technology (KIT), Karlsruhe, Germany.

178. Chai, X., I. Otic, and X. Cheng, *A new drag force model for the wake acceleration effect and its application to simulation of bubbly flow.* Progress in Nuclear Energy, 2015. **80**: p. 24-36.

179. Thorsen, G. and S.G. Terjesen, *On the Mechanism of Mass Transfer in Liquid-Liquid Extraction.* Chemical Engineering Science, 1962. **17**: p. 137-148.

180. Thorsen, G., R.M. Stordalen, and S.G. Terjesen, *On Terminal Velocity of Circulating and Oscillating Liquid Drops.* Chemical Engineering Science, 1968. **23**: p. 413-426.

181. Hamielec, A.E., *Studies of fluid flow and mass transfer in drops.* 1960. PhD Thesis, University of Toronto, Toronto, Canada.

182. Wellek, R.M., A.K. Agrawal, and A.H. Skelland, *Shape of Liquid Drops Moving in Liquid Media.* AIChE Journal, 1966. **12**: p. 854-862.

183. Oguro, Y., M. Makino, and O. Sano, *Passage of a Small Air Bubble through a Circular Pore across the Plate of Finite Thickness.* Journal of the Physical Society of Japan, 2010. **79**. Artn. 084402.

184. Deising, D., *Modelling and Numerical Simulation of Species Transfer in Bubbly Flows using OpenFOAM.* 2019. Dissertation, Technische Universität Darmstadt, Darmstadt, Germany.

185. Fleckenstein, S. and D. Bothe, *Simplified modeling of the influence of surfactants on the rise of bubbles in VOF-simulations.* Chemical Engineering Science, 2013. **102**: p. 514-523.

186. Coyajee, E. and B.J. Boersma, *Numerical simulation of drop impact on a liquid-liquid interface with a multiple marker front-capturing method.* Journal of Computational Physics, 2009. **228**: p. 4444-4467.

187. Ishii, M. and K. Mishima, *2-Fluid Model and Hydrodynamic Constitutive Relations.* Nuclear Engineering and Design, 1984. **82**: p. 107-126.

188. Roghair, I., Y.M. Lau, N.G. Deen, H.M. Slagter, M.W. Baltussen, M.V. Annaland, and J.A.M. Kuipers, *On the drag force of bubbles in bubble swarms at intermediate and high Reynolds numbers.* Chemical Engineering Science, 2011. **66**: p. 3204-3211.

189. Bieberle, A., M. Schubert, P. Rollbusch, M. Becker, E. Schleicher, and U. Hampel. *Tomographic imaging of gas holdup distribution in pressurized bubble columns*. in *2nd International Symposium on Multiscale Multiphase Process Engineering*. 2014. Hamburg, Germany: p. 262-267.

190. Rollbusch, P., M. Becker, M. Ludwig, A. Bieberle, M. Grünewald, U. Hampel, and R. Franke, *Experimental investigation of the influence of column scale, gas density and liquid properties on gas holdup in bubble columns.* International Journal of Multiphase Flow, 2015. **75**: p. 88-106.

191. Bieberle, A., H.U. Harting, S. Rabha, M. Schubert, and U. Hampel, *Gamma-Ray Computed Tomography for Imaging of Multiphase Flows.* Chemie Ingenieur Technik, 2013. **85**: p. 1002-1011.

192. Schlusemann, L., G.H. Zheng, and M. Grünewald, *Measurement of Phase Distribution in Bubble Columns.* Chemie Ingenieur Technik, 2013. **85**: p. 997-1001.

193. *OpenFOAM User Guide - A.4 Standard boundary conditions*. [last access 2020 07 March]; OpenCFD Ltd. Available from: https://www.openfoam.com/documentation/user-guide/standard-boundaryconditions.php.

194. Schäfer, R., C. Merten, and G. Eigenberger, *Bubble size distributions in a bubble column reactor under industrial conditions.* Experimental Thermal and Fluid Science, 2002. **26**: p. 595-604.

195. Lin, T.J. and L.S. Fan, *Heat transfer and bubble characteristics from a nozzle in high-pressure bubble columns.* Chemical Engineering Science, 1999. **54**: p. 4853-4859.

196. Kemoun, A., B.C. Ong, P. Gupta, M.H. Al-Dahhan, and M.P. Dudukovic, *Gas holdup in bubble columns at elevated pressure via computed tomography.* International Journal of Multiphase Flow, 2001. **27**: p. 929-946.

197. Rollbusch, P., M. Bothe, M. Becker, M. Ludwig, M. Grünewald, M. Schlüter, and R. Franke, *Bubble columns operated under industrially relevant conditions - Current understanding of design parameters.* Chemical Engineering Science, 2015. **126**: p. 660-678.

198. Lin, T.J., K. Tsuchiya, and L.S. Fan, *Bubble flow characteristics in bubble columns at elevated pressure and temperature.* AIChE Journal, 1998. **44**: p. 545-560.

199.   *FLUENT 6.3 User's Guide*. Version 6.3 ed. 2006: Fluent Inc.

200.   *OpenFOAM: API Guide v1912: LaheyKEpsilon Directory Reference*.
         [last access 2020 05 March]; OpenCFD Ltd. Available from:
         https://www.openfoam.com/documentation/guides/latest/api/dir_65113bc1
         bb0d4fec08fc461cd17bd951.html.

201.   *OpenFOAM: API Guide v1912: mixtureKEpsilon Directory Reference*.
         [last access 2020 05 March]; OpenCFD Ltd. Available from:
         https://www.openfoam.com/documentation/guides/latest/api/classFoam_1
         _1RASModels_1_1mixtureKEpsilon.html.

202.   Hosokawa, S. and A. Tomiyama, *Bubble-induced pseudo turbulence in
         laminar pipe flows.* International Journal of Heat and Fluid Flow, 2013.
         40: p. 97-105.

203.   Zhou, X., X. Sun, and Y. Liu, *Liquid-phase turbulence measurements in
         air-water two-phase flows over a wide range of void fractions.* Nuclear
         Engineering and Design, 2016. **310**: p. 534-543.

204.   Deckwer, W.-D., Y. Louisi, A. Zaidi, and M. Ralek, *Hydrodynamic
         Properties of the Fischer-Tropsch Slurry Process.* Industrial &
         Engineering Chemistry Process Design and Development, 1980. **19**: p.
         699-708.

205.   Tchowa Medjiade, W., A. Rosenbaum Alvaro, and A. Schumpe, *Flow
         regime transitions in a bubble column.* Chemical Engineering Science,
         2017. **170**: p. 263-269.

206.   Shi, S., D. Wang, Y. Qian, X. Sun, Y. Liu, and A. Tentner, *Liquid-phase
         turbulence measurements in air-water two-phase flows using particle
         image velocimetry.* Progress in Nuclear Energy, 2020. **124**. Artn. 103334.

207.   Krishna, R., J.M. van Baten, and M.I. Urseanu, *Scale effects on the
         hydrodynamics of bubble columns operating in the homogeneous flow
         regime.* Chemical Engineering & Technology, 2001. **24**: p. 451-458.

208.   Zehner, P., *Multiphase flows in gas-liquid reactors* DECHEMA-Monogr.,
         1989. **114**: p. 215-232.

209.   Zehner, P., *Impuls-, Stoff-und Wärmetransport in Blasensäulen*
         Verfahrenstechnik, 1982. **16**: p. 347-351.

210.   Joshi, J.B. and M.M. Sharma, *Circulation Cell Model For Bubble-
         Columns.* Transactions of the Institution of Chemical Engineers, 1979. **57**:
         p. 244-251.

211.   Besagni, G., L. Gallazzini, and F. Inzoli, *On the scale-up criteria for
         bubble columns.* Petroleum, 2019. **5**: p. 114-122.

212.   Shaikh, A. and M. Al-Dahhan, *Scale-up of Bubble Column Reactors: A
         Review of Current State-of-the-Art.* Industrial & Engineering Chemistry
         Research, 2013. **52**: p. 8091-8108.

Nomenclature

Roman Symbols

A	Cross sectional area	[m^2]
a_i	Specific interfacial area	[m^{-1}]
A_i	Interfacial area concentration	[-]
C_t	Turbulence response coefficient	[-]
D	Diameter of channel or column or pipe or hole	[m]
d_B	Bubble diameter	[m]
D_H	Hydraulic diameter	[m]
D_{kL}	Diffusion term in turbulence kinetic energy equation	[m^2 s^{-3}]
$\hat{\mathbf{e}}$	unit normal vector	[-]
f	Liquid volumetric fraction within a mesh cell	[-]
$\mathbf{F}$	Force per unit volume	[N m^{-3}]
F_D	Magnitude of drag force per unit volume	[N m^{-3}]
$\mathbf{g}$	Gravity vector	[m s^{-2}]
g	Gravitational acceleration	[m s^{-2}]
H	Height	[m]
H_0	The lowest gassed liquid height in the column	[m]
$\mathbf{I}$	Unit tensor	[-]
I_{kL}	Interfacial term in turbulence kinetic energy equation	[m^2 s^{-3}]
J_G	Local superficial gas velocity	[m s^{-1}]
k	Turbulence kinetic energy for single phase flow	[m^2 s^{-2}]
k_G	Turbulence kinetic energy of gas phase	[m^2 s^{-2}]
k_L	Turbulence kinetic energy of liquid phase	[m^2 s^{-2}]
k_m	Turbulence kinetic energy of phase mixture	[m^2 s^{-2}]

167

K_U	Velocity correction factor for rigid spheres	[-]
l	Turbulent mixing length	[m]
L	Length	[m]
L_{ref}	Reference length	[m]
$\mathbf{\hat{n}}_i$	Unit normal vector to interface	[-]
N_B	Mesh cells per bubble diameter	[-]
N_{cell}	Number of mesh cells	[-]
N_D	A number used for the estimation of terminal velocity [75]	[-]
O_{kL}	Out-of-balance term in turbulence kinetic energy equation	[m^2 s^{-3}]
p	Pressure	[Pa]
P	Wetted perimeter	[m]
P^*	Non-dimensional reduced pressure	[-]
P_{kL}	Production term in turbulence kinetic energy equation	[m^2 s^{-3}]
Q	Volumetric flow rate	[m^3 s^{-1}]
r	Radius	[m]
R	Radius of column	[m]
$\mathbf{R}$	Reynolds stress tensor	[m^2 s^{-2}]
t	Time	[s]
T	Temperature	[°C]
T_i	Turbulence intensity	[-]
u	Velocity	[m s^{-1}]
$\mathbf{u}$	Velocity field	[m s^{-1}]
$U_{G,0}$	Superficial velocity of gas phase	[m s^{-1}]
U_L	Velocity of liquid medium surrounding a single bubble	[m s^{-1}]
$U_{L,0}$	Superficial velocity of liquid phase	[m s^{-1}]
U_{ref}	Reference velocity	[m s^{-1}]
U_T	Terminal velocity of a rising bubble in liquid medium	[m s^{-1}]

$\mathbf{v}$	Velocity field within a mesh cell	[m s^{-1}]
$\mathbf{v}_\mathrm{m}$	Center-of-mass velocity within a mesh cell	[m s^{-1}]
w_b	Velocity of the biggest single stable fluid particle	[m s^{-1}]
w_bs	Slip velocity of the biggest stable single bubble	[m s^{-1}]
$w_\mathrm{c,L}$	Maximum centerline velocity of the liquid phase	[m s^{-1}]
W_D	Rate of the work done by drag force per unit volume	[J s^{-1} m^{-3}]
w_max	Maximum rise velocity of a single fluid particle	[m s^{-1}]
X	Phase indicator function	[-]
x, y, z	Cartesian co-ordinates	[m]

Greek Symbols

α	Volume fraction	[-]
α_G	Local gas holdup	[-]
α_L	Mean liquid volumetric fraction	[-]
Γ	Correction factor for estimating terminal velocity	[-]
Γ_μ	Gas to liquid viscosity ratio	[-]
Γ_ρ	Gas to liquid density ratio	[-]
Δ	Difference	[-]
ε	Dissipation rate of k	[m^2 s^{-3}]
ε_G	Overall gas holdup	[-]
θ	Non-dimensional time	[-]
κ^{*}	Curvature	[-]
κ_cont	Contamination coefficient	[-]
λ	Ratio of bubble diameter to wall distance	[-]
μ	Dynamic viscosity	[Pa s]
ν	Kinematic viscosity	[m^2 s^{-1}]

σ	Surface tension		[N m^{-1}]
$\sum$	Summation		[-]
τ	Shear stress tensor		[Pa]
Φ_{mean}	Steady mean component		[-]
φ	Arbitrary quantity		[-]
ρ	Density		[kg m^{-3}]
χ	Bubble aspect ratio		[-]

Non-dimensional numbers

Ar	Archimedes number	$d_{\text{p}}^3 \cdot g \cdot \rho_{\text{L}} \cdot \Delta\rho / \mu_{\text{L}}^2$
C_{D}	Drag coefficient	$\dfrac{F_{\text{D}}}{\dfrac{1}{2} \cdot \rho_{\text{L}} \cdot A \cdot u_{\text{rel}}^2}$
$E\ddot{o}$	Eötvös number	$g \cdot \Delta\rho \cdot d_{\text{B}}^2 / \sigma$
Eu	Euler number	$\Delta p / \rho_{\text{L}} \cdot u^2$
F	Flow number	$g\left(\rho^5 \cdot d_{\text{B}}^8 / \sigma \cdot \mu^4\right)^{1/3}$
Fr	Froude number	$g \cdot d_B / u^2$
K_{F}	Liquid number	$\rho_{\text{L}} \cdot \sigma^3 / g \cdot \mu_{\text{L}}^4$
M	Morton number	$g \cdot \Delta\rho \cdot \mu_{\text{L}}^4 / \rho_{\text{L}}^2 \cdot \sigma^3$
Re	Reynolds number	$\rho_{\text{L}} \cdot U_{\text{T}} \cdot d_{\text{B}} / \mu_{\text{L}}$
V	Velocity number	$U_{\text{T}}\left(\rho^2 \cdot d_{\text{B}}^2 / \sigma \cdot \mu\right)^{1/3}$
We	Weber number	$\rho_{\text{L}} \cdot L \cdot u^2 / \sigma$

Subscripts

axial	Axial direction
B	Bubble
cont	Contaminated
cell	Mesh cell
D	Drag
eff	Effective
G	Gas phase
i	Liquid phase quantities at the gas-liquid interface
inlet	Quantity at the inlet
L	Liquid phase or Lift
m	Mixture
max	Maximum
mean	Mean component
outlet	Quantity at the outlet
ref	Reference
rel	Relative
rms	Root mean square
turb	Turbulent
T	Terminal
TD	Turbulent dispersion
VM	Virtual mass
wall	wall related
x, y, z	Cartesian co-ordinates
1	Vertical direction
2	Span-wise (lateral) direction
3	wall-normal direction

Superscripts

*	Non-dimensional
eff	Effective
mol	Molecular
rms	Root mean square
t	Turbulent
T	Transposition
φ	Phase indicator

Overbar Symbols

$\bar{\varphi}$	Averaged component
$\bar{\bar{\varphi}}$	Phase-weighted (conditional) averaged component
φ'	Fluctuating component (fluctuations)
$\overline{\varphi'}$	Averaged fluctuating component
$\overline{(\varphi')^2}$	Variance of time averaged fluctuating component
$\sqrt{\overline{\varphi'^2}}$	Root mean square of time averaged fluctuating component

List of Abbreviations

2D	Two dimensional
3D	Three dimensional
BIT	Bubble induced turbulence
CF	Color function
CFD	Computational Fluid Dynamics

CSI   Center of Smart Interfaces of TU-Darmstadt

DNS   Direct Numerical Simulations

E-E   Euler-Euler

E-L   Euler-Lagrange

EPIRA   Exact Plane Interface Reconstruction Algorithm

GammaCT   High-resolution gamma-ray computed tomography

HZDR   Helmholtz-Zentrum Dresden-Rossendorf

IMS   Institute of Multiphase Flows of TUHH

IR   Interface reconstruction

KIT   Karlsruhe Institute of Technology

LES   Large eddy simulation

MUSIG   Multiple Size Group

N_2 Nitrogen

p.b.c   periodic boundary conditions

PB   Model for interfacial term from Pfleger and Becker [137]

PDF   Probability distribution function

PIV   Particle image velocimetry

PLIC   Piecewise Linear Interface Calculation

RANS   Reynolds-Averaged Navier-Stokes

RNG   Re-Normalization Group

RSM   Reynolds stress model

S.C.M.   Stagnant Cap Model

S-N   Schiller-Naumann drag model [101]

SST   Shear Stress Transport

TKE   Turbulence kinetic energy

To   Tomiyama drag model [102]

TUHH   Hamburg University of Technology

VOF	Volume-of-Fluid Method
WGA	Water-Glycerin-Air system
WGN	Water-Glycerin-Nitrogen system
WMS	Wire-mesh sensor

List of Figures

List of Tables